An Investigation of the Coral Sea with an Ocean General Circulation Model

A Thesis submitted by

Rowan David Hughes M.Sc. (*JCUNQ*)

in fulfillment for the requirements of the degree of Doctor of Philosophy

at James Cook University of North Queensland
in the Department of Civil and Systems Engineering

December 1993

Access to This Thesis

I, the undersigned, the author of this thesis, understand that James Cook University of North Queensland will make it available for use within the University Library and, by microfilm or other means, allow access to users in other approved libraries. All users consulting this thesis will have to sign the following statement:

> " In consulting this thesis I agree not to copy or closely paraphrase it in whole or in part without the written consent of the author; and to make proper written acknowledgement for any assistance which I have obtained from it."

Beyond this, I do not wish to place any restriction on access to this thesis.

R.D. Hughes

Declaration

I declare that this thesis is my own work and has not been submitted in any form for another degree or diploma at any university or other institution of tertiary education. Information derived from the published or unpublished work of others has been acknowledged in the text and a list of references is given.

R.D. Hughes

Abstract

An ocean general circulation model covering the global domain is used to determine the flow regimes of the southwest Pacific, and the relationship between the Indonesian throughflow (IT), the East Australian Current (EAC) and the Coral Sea dynamics. A number of physical oceanographic surveys in the Coral Sea, using newly acquired acoustic Doppler current profiling instrumentation, show this area to be rather more complex than was at first thought. Earlier investigations of the Coral Sea led to the conclusion of a closed cyclonic gyre as the dominant pattern. The model shows a subsurface western boundary current, the New Guinea Coastal Undercurrent (NGCU), which begins on the Australian east coast near 16°S and circulates along the coast of Papua New Guinea. The field surveys confirm the existence of this current and show the average volume to be about $25\,Sv$, being in fair agreement with the model. The observed flow turns northwards at the eastern tip of Papua New Guinea and is probably the source of the Vityaz Strait throughflow. An additional strong current is predicted to lie north of New Ireland during winter, and strong westwards flows through St. George's Channel have already been observed. The bifurcation of the South Equatorial Current (SEC) occurs between 14°S and 23°S, at varying depths along the Australian coast. The southern branch forms the EAC and the northwards flow forms the NGCU. The bifurcation has a notable baroclinic component with more of the deep water moving northwards. The Great Barrier Reef Undercurrent, flowing northwards in the Queensland Trough, is a deeper component of the SEC that bifurcates around the Queensland Plateau, while the shallower southwards flowing EAC originates from the surface bifurcation near 15°S. The model NGCU is found to retroflect eastwards at 140°E during summer, whence it forms the equatorial undercurrent, in good agreement with historical surveys. However, during winter, the model NGCU flows further to the west where it encounters Halmahera Island, which deflects the current northwards to near 3°N, and it then finally retroflects again to form the Equatorial Undercurrent. If this island is moved southwards in the model, or removed, the NGCU supplies more than half the IT during winter, which is in direct contradiction to all observations. It is asserted that it is Halmahera Island which is the sole cause of the NGCU's

non–participation in the IT, and not the broader scale dynamics. The model IT is found to be sensitive to modifications of the Antarctic Circumpolar Current (ACC), while the South Pacific wind stress perhaps does no more than seasonally modulate the throughflow. If the world model has its southern wall at 64°S the IT is about $15\,Sv$ during spin–up, but falls to $10\,Sv$ after relaxation is switched off. With the wall at 75°S the IT remains fairly steady during all phases on integration. Thus, it is assumed that the ACC has a primary role in driving the IT. Sverdrup models predict that the IT is driven by the South Pacific wind stress since there is a $16\,Sv$ northwards residual in the curl of the wind stress field. It is postulated that the basic assumptions of Sverdrup models are violated to some extent by real and modelled ACC. The ACC effectively sets the depth–averaged pressures at the southern tips of both Africa and South America, so the single reference pressure set in Sverdrup models in not a valid assumption. A survey in September–91 by the *R.V. Franklin* (Fr0791) found intense offshore flows originating from the EAC at about 24°S, moving to more than $500\,km$ off the coast. This is well north of the EAC's normal departure latitude (33°S), and no such findings appear to have been reported before this survey. Using Smagorinsky viscosity in the model, intense gyres that are elongated against the western boundary are found to develop, but only if the boundary itself is meridional. Haney & Wright (1975) reported this behaviour in a barotropic quasigeostrophic model with a rectangular domain, but they concluded that it constituted an unrealistic numerical mode. However, intense recirculations of the EAC are apparent in the Fr0791 data and in the data of the March–60 cruise of the *H.M.A.S. Gascoyne* (Ga0260). The model gyres are very similar to the observations, and it is concluded that they have at least some degree of realism.

Acknowledgements

This project and thesis would not have been possible without the financial support of my family. Partial funding was provided by a student stipend from the Australian Institute of Marine Science. My supervisors, Lance Bode (JCUNQ) and Derek Burrage (AIMS), spent much time in reading and correcting my hastily written words.

Derek organized, obtained funding for, and led the field expeditions Fr0690 and Fr0791. Lance, Craig Steinberg (AIMS), and the *R.V. Franklin* crew spent many days on the CTD "chain gang". The late Stan Hayes, as well as Linda Mangum (PMEL), provided access to the TEW data. Cray Research (Australia) Pty. Ltd. and the Australian National University Supercomputer Facility provided valuable machine time.

Contents

List of Figures

List of Tables

Chapter 1

Introduction

The circulation of the western South Pacific is poorly understood, since comparatively few oceanographic surveys have been conducted in this area, and this state of affairs is exacerbated by the fact that the area has arguably one of the most complex ocean flow regimes found anywhere. Australian oceanographic investigators have been equipped with acoustic Doppler current profiling (ADCP) facilities since 1985, and conductivity temperature depth (CTD) facilities since 1981, and only now is a more detailed understanding of this area's flow patterns emerging. Investigations around the Tasman Sea area in the 1960s and 70s used geomagnetic–electro–kinetograph, sonar submarine drifters and satellite tracked surface drifters, as well as the more usual dynamic height analysis from discrete sampling, i.e., Nansen and Niskin bottles. More modern methods have only been used around the Coral and Solomon Seas since the latter 1980s, and only to a very limited extent. Previous studies of the Coral and Solomon Seas areas have used only dynamic height analysis from discrete sampling and simple drifters (Yamanaka, 1973) to gain an idea of gross features of water movements. Investigations of the Tasman Sea have generally used the best available experimental methods for the time, although the total number of measurements has been small. There are very few long–term continuous oceanographic records of any part of Australia's near waters. Fig. 1.1 shows the geographical area of interest for the present study, and the 1, 2 and 4 km isobaths.

The East Australian Current (EAC) is an eddying western boundary current that flows polewards along the east coast of Australia and is the return path for the equatorwards Sverdrup flow of the central South Pacific gyre. It is generally thought to begin near 20°S on the Australian coast and then flows southwards to

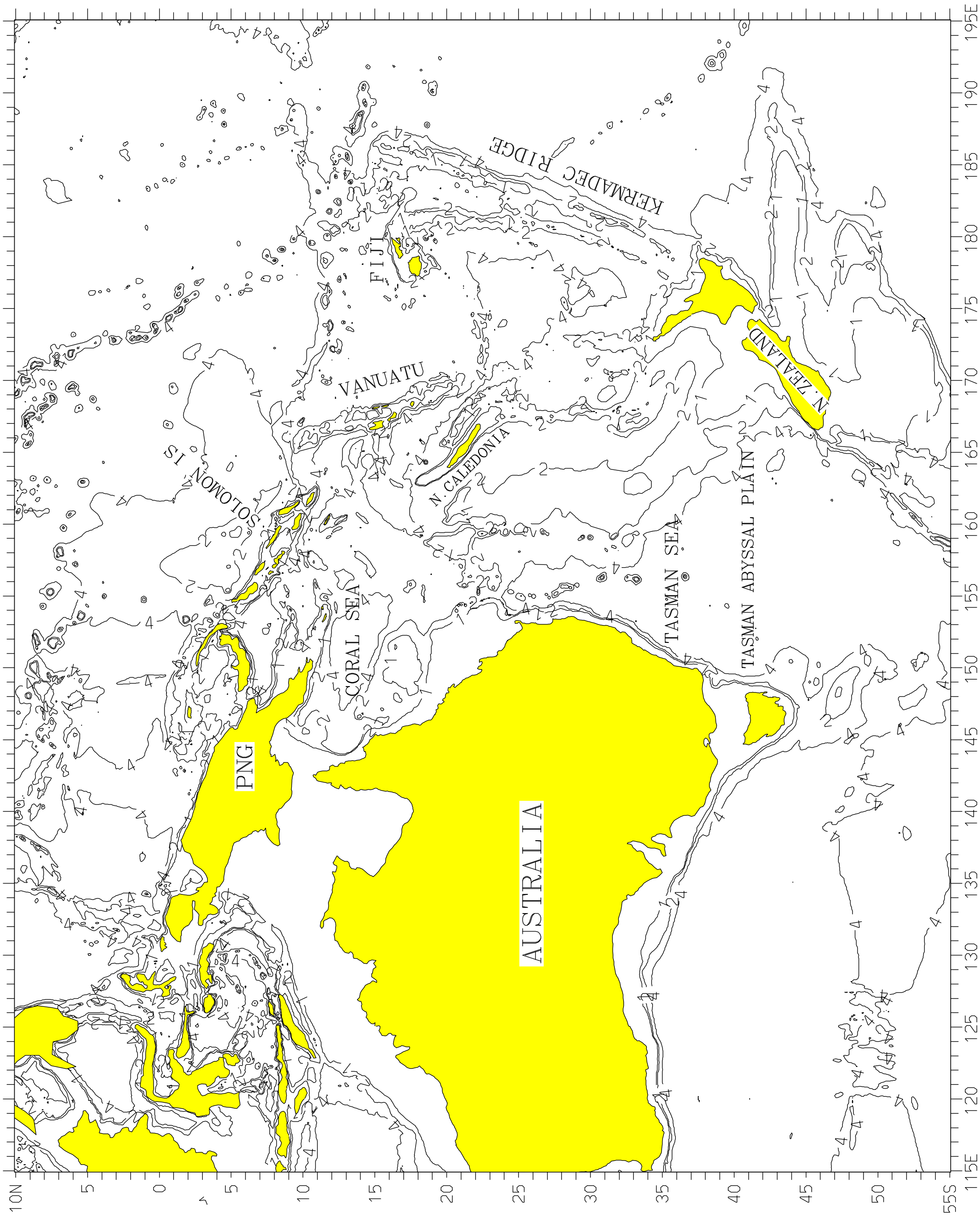

Figure 1.1: **:** [rotated] Geography of the western South Pacific, and isobaths (km). The Tasman, Coral and Solomon (8°S:155°E) Seas are cut–off from the deeper Pacific by submarine ridges. The deepest opening is 2700 m between the Solomons and Vanuatu. The Kermadec Ridge. is 2000 m deep just north of New Zealand, but shoals to about 500 m near Fiji. Halmahera I. is at 1°N:128°E.

about 33°S, where it abruptly departs to flow zonally towards the northern tip of New Zealand. Hamon (1965) estimates its nett annually–averaged volume flux to be about $25 \times 10^6\, m^3 s^{-1}$ (25 *Sverdrups*), although individual measurements range between $10\, Sv$ *northwards* (Thompson & Veronis, 1980) to $50\, Sv$ southwards. Its general seasonal trend is for intensification during the austral summer. Since it flows polewards along the Australian coast, warmer tropical waters are carried southwards and then offshore at 33°S to form the Tasman Front. While this front is fairly well defined, the total meridional surface temperature variation is not large, only about 2°C, in contrast with other poleward boundary currents like the Gulf Stream. Large warm cored eddies are formed by pinch–offs of the EAC, a little south of the departure latitude, and they meander up and down the coast, move eastwards, or are occasionally re–incorporated back into the EAC. The Tasman Sea area dynamics are perhaps the best understood of all of Australia's nearby waters, yet it is virtually unknown in comparison with the body of knowledge that exists for northern hemisphere oceans, for example the North Atlantic. Bennett (1983) provides a short but very useful review of most findings for the Tasman Sea.

The Coral Sea area had received less attention by investigators until roughly the last decade, but even so, the total number of comprehensive wide–scale surveys performed over the Coral and Solomon Seas is still fewer than twenty. Several early investigations found large volume fluxes entering the Coral Sea but the presence of western boundary currents, other than the EAC, appears not to have been postulated. Thompson & Veronis (1980) found fluxes of up to $40\, Sv$ entering from the east and departing northwards to the Solomon Sea. The spatial coarseness of their sampling stations would not have permitted the identification of a western boundary current. The inflow from the east is the South Equatorial Current (SEC). They postulated that this circulation is driven by the local wind stress of the Coral Sea, but this seems unlikely given the magnitude of the flow and the relatively small area. The findings presented in that work have often been regarded with a little scepticism since a zonal transect across the Tasman Sea actually showed the EAC to be flowing northwards. For the Coral Sea, Scully–Power (1973) found flows a little smaller than those of Thompson & Veronis, but in the same directions. Andrews & Clegg (1989) show a $6\, Sv$ cyclonic circulation in the western Coral Sea and a northwards flow of $17\, Sv$ into the Solomon Sea.

Pickard *et al.* (1977) provide a review of the findings of all the early investigators: Takahashi (1960), Wyrtki (1961b, 1962ab), Donguy *et al.* (1970) and Scully-Power (1973). The overall consensus is that of a clockwise gyre in the northern Coral Sea, with an inflow from the SEC, and an outflow into the Solomon Sea. It is thus reasonable to expect large current regimes which transport mass away from this area and it is reasonable also to assume that this would be manifested as a western boundary current. A link between the Coral Sea and the equatorial undercurrent was first suggested by Tsuchiya (1968, 1981) and more recently by additional investigators (Tsuchiya *et al.*, 1989; Lindstrom *et al.*, 1990; Godfrey *et al.*, 1993), indicating that the Coral Sea gyre is part of a much wider flow regime. The exact route that the Coral Sea outflux takes through the islands that comprise Papua New Guinea (PNG) and the Solomons still awaits observational validation. The WEPOCS expedition (Lindstrom *et al.*, 1987) found a substantial westwards flux, $8\,Sv$, through the narrow Vityaz Strait between PNG and New Britain. More recent current meter data suggest that the throughflow is 14–20 Sv, and is fairly steady (E. Lindstrom, private communication).

Numerical ocean general circulation models can provide a simple and effective short–cut around this lack of historical knowledge, and this was the motivation for the commencement of the present project. The lack of any real understanding of the Coral and Solomon Seas regimes also provides an opportunity for numerical models to take the lead over empirical knowledge, in contrast with the northern hemisphere oceans where much was known about the general circulation features before numerical models came into widespread use. The modelling community is now focusing its attention more on the mesoscale and microscale behaviour of the oceans, in an attempt to gauge its effect on the long–term behaviour of large–scale flows. Such a study would be nigh on impossible on an experimental basis. Large world and hemisphere models (e.g., Semtner & Chervin, 1988, 1992; Webb, 1991) with very fine grid resolutions have been developed. These include the Coral Sea and southwest Pacific, although they have used somewhat smoothed bathymetry and most islands have been submerged. This is done to greatly improve the execution efficiency on vector computers and to overcome numerical errors, particularly in the barotropic stream function. Such tasks require many weeks of processor time on the world's largest supercomputers, so there is an unwillingness to vary model parameters and basin shapes for sensitivity analysis.

The original intention of this project was to implement a fine resolution (0.25°) regional model of the Coral Sea, utilizing only moderate computer resources, in a similar fashion to Robinson & Walstad's (1987) open boundary model of Gulf Stream ring formations. This would have allowed a great deal of variation in model parameters while still being economical. The Cox–Bryan code (Cox, 1984) was chosen since it is well established, includes islands and has had some limited use with open boundaries. Small domain open boundary primitive equation models can only be integrated for a maximum of several weeks (model time) for reasons discussed below. However, it quickly became apparent that the data necessary to set the open boundaries was not available for the local Coral Sea area, in contrast with the northwestern Atlantic. The grid domain was then increased to cover the Pacific, to 43°S, since several Australia–South America oceanic transects are available (e.g., Stommel *et al.*, 1973), in conjunction with the Levitus (1982) data set. Flows through the Indonesian passages are always observed to be southwards, i.e., out of the Pacific, hence it was assumed that data would not be necessary for this open boundary. At that time only modest computational resources were available, so the Pacific basin model's grid resolution had to be reduced to 1°. It was then assumed that the open boundaries were suitably distant from the Coral Sea so that uncertainties in the boundary data would be of little consequence.

One of the major problems still unresolved for modelling, using the primitive equations (PE), is that of open boundary conditions. For most other formulations the problem of open boundaries has essentially been solved, or at least they appear to easily accept the information provided at the boundary. The PEs were shown to be ill-conditioned by Charney *et al.* (1950), with respect to open boundaries, and essentially no progress has been made since then, for the analytic case. Bennett & Kloeden (1981) used a fairly simple analysis to show that the hyperbolic contributions to the PEs are the cause of the trouble, and that instabilities grow from areas where characteristic lines are tangential to an open boundary. This leads to a build–up of wave energy at the boundaries, since the artificial boundary dynamics do not permit perfect transmission out of the domain. In the practical sense, progress has been slow and no truly successful model (for long time scales) has yet been devised. The FRAM model (Fine Resolution Antarctic Model; Webb, 1991) uses an open boundary at 23.875°S and is stable over long–term integrations. The open boundary formulation is that of Stevens (1990). FRAM results near the open boundary are mediocre, especially in the vicinity of the EAC, yet this is generally considered to be the most successful open boundary PE model yet devised. Inflow boundary variables are simply assigned fixed values and internal velocities are usually determined from geostrophy. The barotropic stream function is assigned fixed values on inflow sections, but it is much more difficult to determine appropriate outflow values. The radiation condition of Camerlengo & O'Brien (1980) was used in the Pacific basin model.

The Pacific basin model did not work correctly despite a great deal of experimentation and became unstable only after a few months of integration. Its domain was similar to that shown in Fig. 1.2, but only over the Pacific and with the open boundaries at 43°S and across the Indonesian Passages. Inflow sections of the open boundaries worked reasonably well but instabilities quickly developed at the outflow sections near the east coast of Australia, and the Indonesian passages. The future direction of open boundary formulations in primitive equation models seems unclear at this time. The nesting method being developed by Spall & Holland (1991) shows promise but will probably not be implemented widely because of the imminent availability of much more powerful computers. Within the next three years it should be possible to implement world models with $15\,km$ (0.14°) grid resolutions, while improvements in the solution methods will permit even finer resolutions (Killworth *et al.*, 1991; Smith *et al.*, 1992; Dukowicz & Smith, 1992).

Perhaps the most important consideration in modelling the South Pacific is the fact that it is not closed. FRAM is the only true open boundary PE model which works over long time scales. However, it forces the nett barotropic flux to be zero around its northern border, i.e., the stream function can vary along this border but its value on the Australian coast is set to zero, thus eliminating any Indonesian throughflow. The Community Modelling Effort's (CME) models of the North Atlantic set barotropic flux to zero at all points across the southern border but, in a sense, the border is open for baroclinic flows. A solid wall is placed south of the equator and diffusion and relaxation are greatly increased immediately to the north of it. This is termed an active–diffusive wall, or pumping sponge layer. The zero nett flux is realistic for the North Atlantic since it is nearly closed to the north. This CME method is apparently fairly successful (Boning *et al.*, 1991; Bryan & Holland, 1989), but it does not constitute a true open boundary formulation.

The Indonesian throughflow (IT), which is observed to attain at least 21 Sv (Fieux *et al.*, 1993), must be supplied entirely from the Southern Ocean, via the Pacific, and this will certainly distort the Sverdrupian dynamics and modify South Pacific western boundary currents. Godfrey & Golding (1981) demonstrate that the IT, EAC and possible PNG boundary currents have interdependent dynamics. For all of the model variations used in this project, the flow patterns of the North Pacific were relatively robust and results differed little. In the North Pacific (also Atlantic and Southern Oceans) the nett flux across any line of latitude is zero while for the South Pacific it must be equal to the IT, approximately 20 Sv northwards. The objective of this project was to establish the flow regime of the Coral Sea, and since this probably has an extreme dependence on phenomena at distant locations, it became clear that any open boundary formulation was unlikely to succeed, leaving aside the mathematical problems.

After these initial failures a decision was made to formulate a much larger basin model with solid boundaries that included active–diffusive layers. Only limited vector machine resources were available at this time, but the acquisition of a powerful workstation improved the situation greatly. Solid boundaries would eliminate the problematic barotropic flows and sponge layers would be used to induce baroclinic flows with the correct temperature and salinity characteristics. The detrimental effects of unrealistic solid walls can be mitigated by placing them at locations where the barotropic component is expected to be small. Only northern hemisphere oceans have such convenient locations, so the walls were placed in areas where it was considered that they would cause the least distortion of the western South Pacific. The new domain covered the Pacific and much of the Indian and Southern Oceans. Cyclic east–west boundaries permitted a portion of the Antarctic Circumpolar Current (ACC) to proceed unhindered around a partial Antarctica, and a pumping sponge layer in the Indian Ocean absorbed the IT. Fig. 1.2 shows the grid outline; the hatched areas show where sponge layers were located.

The southern wall was placed at 56°S which severely truncated the ACC. This problem was partially remedied by compressing the 56°S to 66°S climatology into

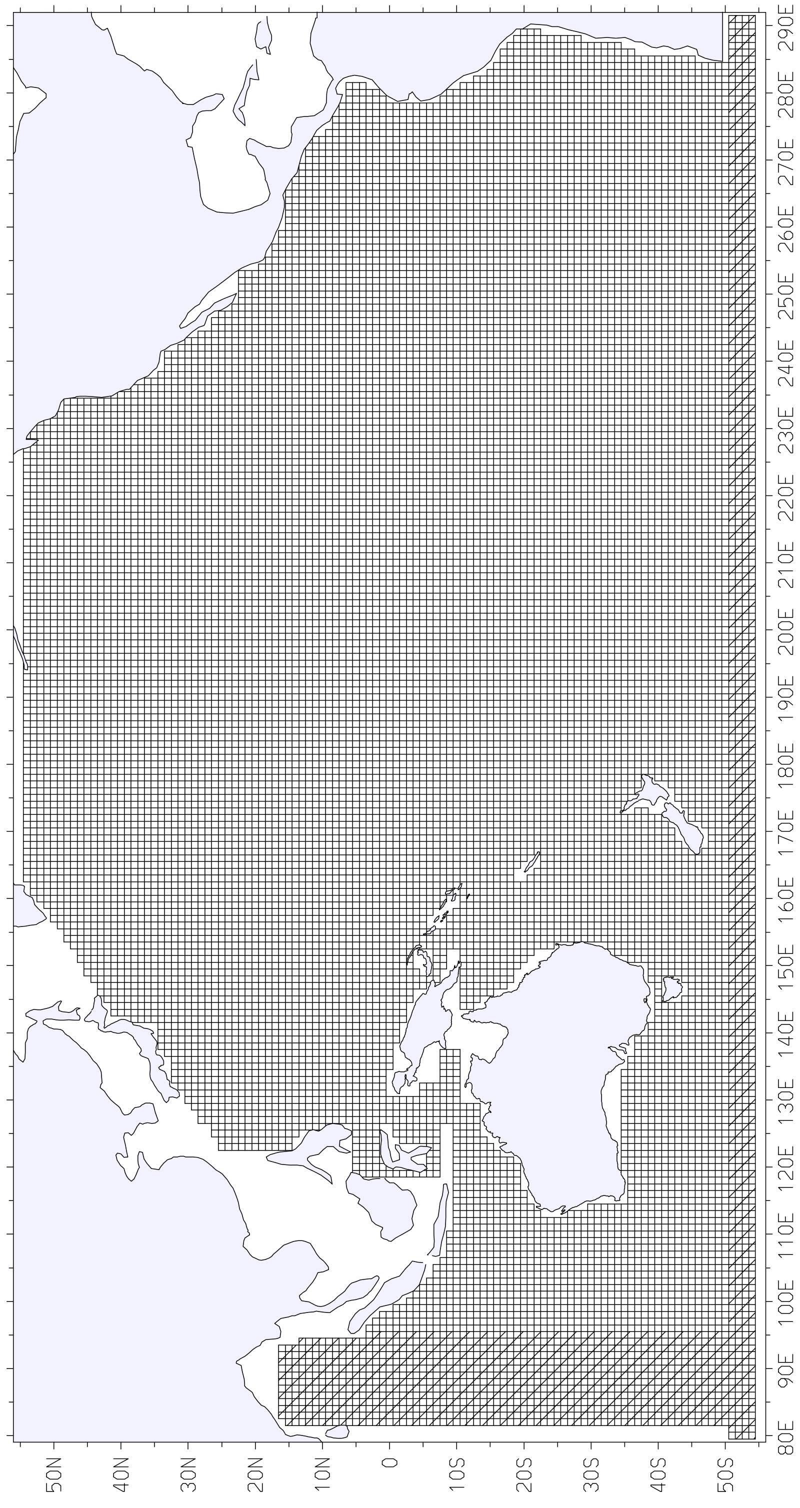

Figure 1.2: **:** [rotated] Outline of the old Pacific–Indian basin model grid. The horizontal grid resolution is 1°. The first row (J=1) is at 55.5°S and the top row (J=112) is at 55.5°N. The first column (I=1) is at 79.5°E and the last column (I=213) is at 291.5°E. The southern sections are cyclic, i.e., outflows at 292°E immediately become inflows at 80°E. Pumping sponge layers are shown hatched.

the bottom few latitude rows. Integration was performed for several decades using the acceleration techniques of Bryan (1984), which effectively implies several centuries. Results for the North Pacific were in reasonable agreement with conventional wisdom but the South Pacific results could not be judged, since there is not a corresponding body of historical knowledge. The ACC attained only 65 Sv, but this was not considered to be pertinent to the IT or Coral Sea dynamics, at the time. During the initial integration phases the IT seemed acceptable at 15 Sv, but as model time progressed it began to steadily fall and was only 2 Sv at the end of twenty years. Correspondingly, the EAC was about 15 Sv during the early phases, but rose steadily as the IT fell. A western boundary current of about 25 Sv flowed counterclockwise around the coast of PNG and reached the Indonesian passages. Vityaz St. was open in this model and all of the PNG boundary current passed through it. Upon arriving at the Indonesian passages the PNG boundary current supplied more than half of the IT. As the EAC increased in strength and the IT decreased, the PNG boundary current decreased as well, but the rate of decrease was a good deal less. This behaviour is reasonably well explained by the Sverdrupian calculations of Godfrey & Golding (1981) which show that the nett fluxes of the EAC and IT should be approximately inversely proportional to each other.

If the IT, in reality, depends only on the South Pacific wind stress, as asserted by several workers (see Godfrey, 1989), then the 56°S wall should not have greatly affected the throughflow, at least not after a lengthy period of integration. It was then decided to use a global domain with zonal walls at 65°S and 65°N and cyclic east-west boundaries. Again, the IT was not robust and gradually fell from 15 Sv to 10 Sv in less than a decade of model time. The southern wall was then moved to 75°S and the robustness problem was virtually eliminated. This was then finalized as the grid geometry to be used in the project. The grid outline is shown in Fig. 1.3. These latitudinal limits are the same as those used by Semtner & Chervin in their world model, which does have a realistic IT (or at least one that is currently thought to be realistic). The results presented in this thesis are derived from the world model. The modelling strategies used are similar to those in the Semtner & Chervin model, but with only a 1° horizontal spacing and seventeen vertical layers. The current model does have more islands than that of Semtner & Chervin (seven versus three) which leads to some accuracy

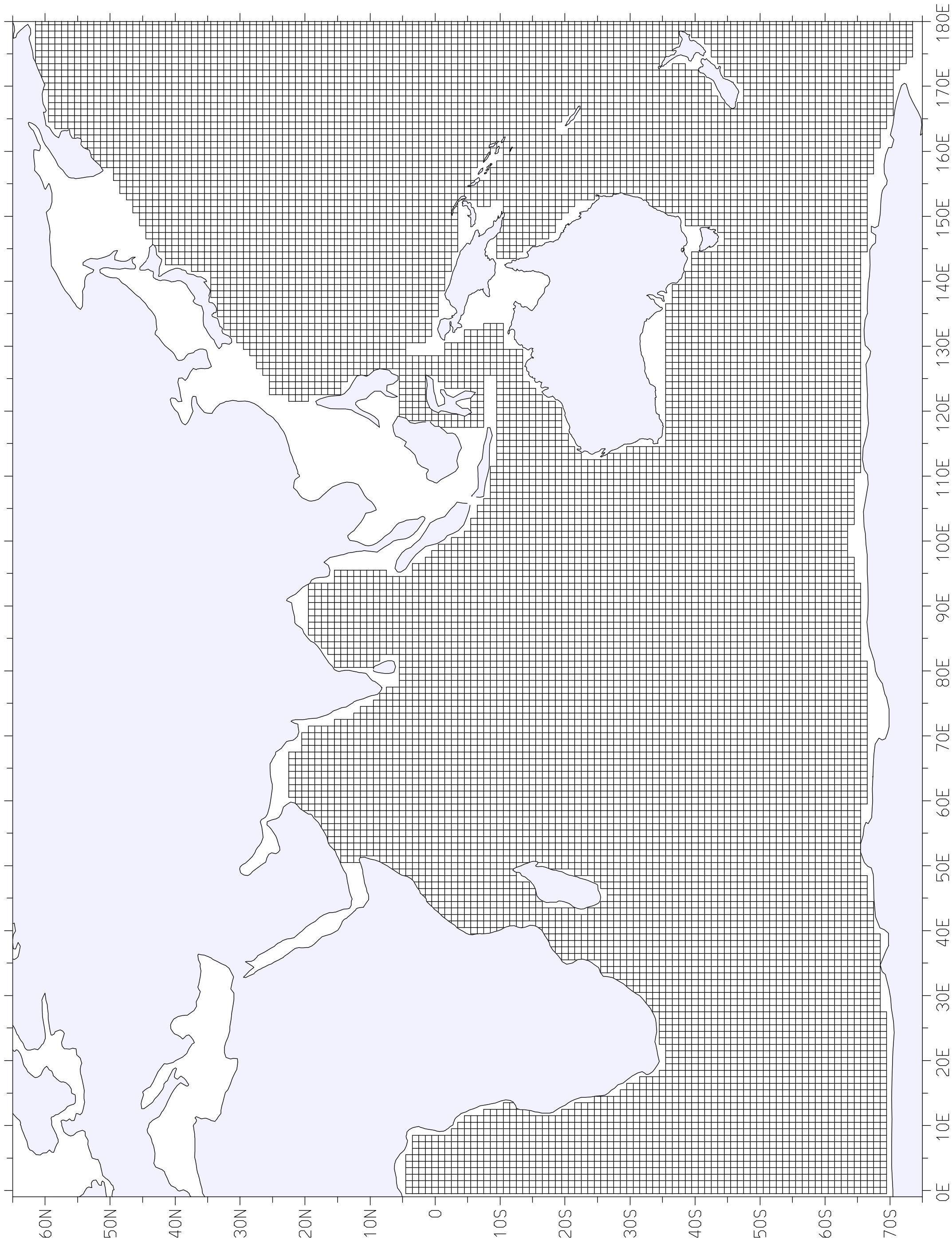

Figure 1.3: **a:** [rotated] Outline of the world model grid over the eastern hemisphere. The horizontal grid resolution is 1°. The first row (J=1) is at 74.5°S and the top row (J=140) is at 64.5°N. The first column (I=1) is at −0.5°E and the last column (I=362; next figure) is at 360.5°E. Column 1 is overlaid with 361, and 362 is overlaid with 2, to form cyclic boundaries. There are seven islands, including Antarctica.

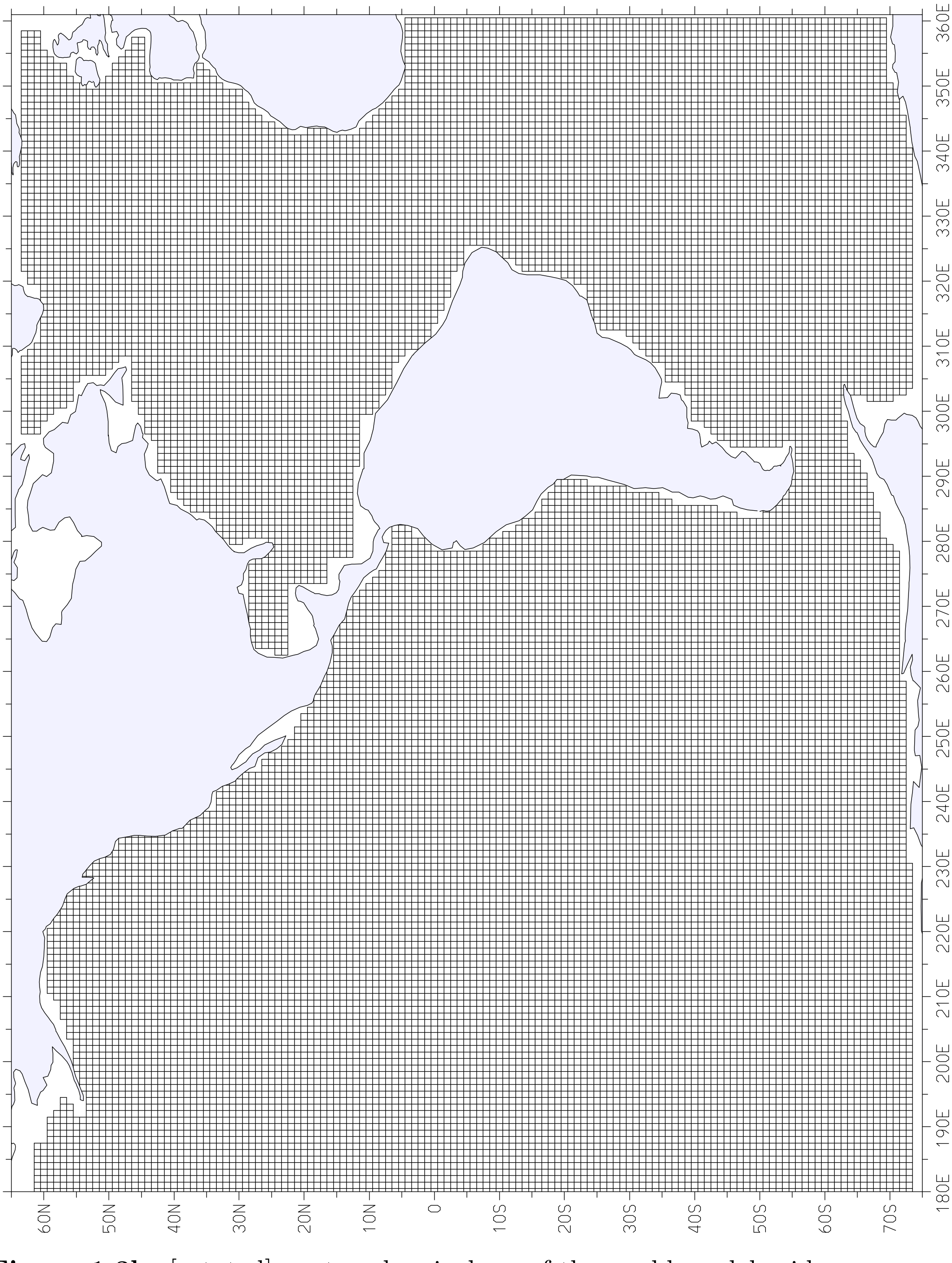

Figure 1.3b: [rotated] western hemisphere of the world model grid.

problems, but island chains in the western South Pacific may play some limited role in equatorial dynamics. The same spin–up methods are used, followed by the conversion to biharmonic viscosity and diffusion, and then finally to seasonal forcing. The world model requires substantial computational resources and all integrations were performed on one processor of a Cray YMP/2E.

While the modelling work was at the Pacific–Indian basin stage, data from two comprehensive surveys, by the *R.V. Franklin*, organized and led by Derek Burrage, became available for the Coral Sea. (Most of the transport analysis of hydrographic data was performed by myself, and is presented for the first time in this thesis.) The July–90 cruise (Fr0690) offered probably the first relatively good set of ADCP data for this area, and the second cruise in September–91 (Fr0791) offered even more data with better accuracy. It quickly became apparent from the Coral Sea data that a significant western boundary current exists in this area. The current begins near 15°S on the Australian coast and flows northwards towards PNG. It circulates cyclonically (clockwise) around the Gulf of Papua and then eastwards along the southern coast of PNG. These two surveys covered only areas to the west of PNG's eastern tip (Rossel I.) and so could not provide any information as to the boundary current's fate once it reaches Rossel Island. Data from the July–85 *R.V. Franklin* cruise was obtained, as well as hydrographic data from the *R.V. Oceanographer*, which had made two transects of the Coral and Solomon Seas in July–87 (TEW2/387). These two data sets clearly show that the boundary current turns northwards at Rossel I., and is presumably the source of the Vityaz St. throughflow. The volume flux of the current is estimated to be about $25\,Sv$ between $1500\,m$ and the surface. The Pacific–Indian basin model had shown a fairly strong western boundary current along the PNG coast, with the same direction as that observed and with about the same strength. In the present study, the current was, in fact, first noticed in the model and then specifically looked for in the data, so it is fair to say that it was originally a model prediction. (While most of the data were collected before the final model results, systematic analysis was performed with the aid of the model results.) The current was also predicted by the Semtner and Chervin model, and by a number of others. Godfrey's (1989) global Sverdrup model shows this boundary current beginning near 18°S at the Australian coast, and attains a strength exceeding $20\,Sv$.

Fr0791 ADCP data show a very complex and unexpected pattern of circulation seawards of the EAC, in the vicinity of 24°S. As expected, the EAC was found be flowing southwards near the shelf, with near surface velocities over $1\,m\,s^{-1}$. However, further seawards ADCP measurements show currents of similar magnitude to be flowing in many different directions, most surprisingly northwards and eastwards. The length scales were generally too large for these currents to be generated by mesoscale eddies, and the world model gave no indication of this behaviour at all. Its flow at 24°S at the Australian coast was mostly southwards and fairly coherent; a strong boundary current recirculation was not apparent immediately offshore. It was considered that the observed flows were unlikely to be generated in a model using biharmonic viscosity and so a little used viscosity, Smagorinsky mixing, scheme was tried. This scheme is occasionally used by atmospheric modellers, but to the best of the author's knowledge, has been used only once before in a large–scale primitive equation ocean model, that of Rosati & Miyakoda (1988). Haney & Wright (1975) used it in a rectangular domain quasigeostrophic model, and this will be discussed in Chapter 4. A strong recirculation of the EAC developed off the coast; this had very intense gyres that were elongated in the meridional direction. These gyres were sufficiently strong and spread far enough offshore to be remarkably consistent with the ADCP data. A little more experimentation showed that these gyres only develop along western boundaries that are almost meridional. Otherwise, Smagorinsky mixing produces results not dissimilar to those of biharmonic mixing.

It was originally intended to produce a study involving only modelling work, but as the number of useful results from the field data grew steadily, it was decided to incorporate this work into the present thesis. Thus, this report contains about equal amounts of modelling and empirical results. Each has reinforced and prompted a deeper investigation of the other, finally resulting in a project which has three main findings. The first is the existence of a substantial western boundary current along the coast of PNG; the *Hiri Current* (Chapter 3). The second finding is the development of intense recirculation gyres along meridional western boundaries (Chapter 4). The third finding is the sensitivity of the IT to modifications of the ACC, and somewhat less sensitivity on the Pacific wind stress than has previously been assumed (Chapter 5).

The findings detailed in Chapters 3 and 5 are under consideration by *Deep–*

Sea Research, while the contents of Chapter 4 are under consideration by the *Journal of Physical Oceanography* (see References). This report presents only the major findings of the project and is not representative of the amount of work and experimentation that was involved. Hopefully, the brevity will allow this report to be quickly read and easily comprehended.

Chapter 2

Numerical Model Details

The model code chosen for the project is MOM–1.0 (Pacanowski *et al.*, 1991), developed at GFDL–Princeton, and is based on the 1984 Cox–Bryan code. Quite a number of options have been included in MOM–1.0, although a good deal of re–coding is still necessary for relaxation methods, seasonal forcing and open boundaries. Two high–latitude filters are optionally available, but filtering has not been used in any of the present runs because of its detrimental effects. This chapter outlines the basic equations of motion, the grid geometry, various techniques for time integration, and reconstruction of the surface pressure from other dynamical fields.

2.1 Dynamical Equations

The basic equations of motion were set out by Bryan (1969), and are shown below. The lengthy derivations of the finite difference forms used in the code are given by Cox (1984). The primitive equations (PE) of motion using the Boussinesq and hydrostatic approximations, in spherical coordinates are:

$$\frac{\partial u}{\partial t} + \Gamma(u) - fv = -\frac{1}{\rho_0 a \cos\phi}\frac{\partial p}{\partial \lambda} + F^u \tag{2.1}$$

$$\frac{\partial v}{\partial t} + \Gamma(v) + fu = -\frac{1}{\rho_0 a}\frac{\partial p}{\partial \phi} + F^v \tag{2.2}$$

$$\frac{\partial p}{\partial z} = -\rho g \qquad \text{or} \qquad p(z) = p_s + g\int_z^0 \rho(z')\, dz' \tag{2.3}$$

$$\Gamma(1) = 0 \qquad \text{or} \qquad \frac{\partial w}{\partial z} + \frac{1}{a\cos\phi}\left[\frac{\partial u}{\partial \lambda} + \frac{\partial\,(v\cos\phi)}{\partial\,\phi}\right] = 0 \tag{2.4}$$

$$\rho = \rho(\theta, S, z) \tag{2.5}$$

$$\frac{\partial T}{\partial t} + \Gamma(T) = F^T \tag{2.6}$$

where, for any scalar quantity σ

$$\Gamma(\sigma) = \frac{1}{a\cos\phi}\frac{\partial(u\sigma)}{\partial\lambda} + \frac{1}{a\cos\phi}\frac{\partial}{\partial\phi}(v\sigma\cos\phi) + \frac{\partial}{\partial z}(w\sigma) \tag{2.7}$$

$$F^u = K_m\frac{\partial^2 u}{\partial z^2} + A_m\left(\nabla^2 u + \frac{(1-\tan^2\phi)u}{a^2} - \frac{2\sin\phi}{a^2\cos^2\phi}\frac{\partial v}{\partial\lambda}\right) \tag{2.8}$$

$$F^v = K_m\frac{\partial^2 v}{\partial z^2} + A_m\left(\nabla^2 v + \frac{(1-\tan^2\phi)v}{a^2} - \frac{2\sin\phi}{a^2\cos^2\phi}\frac{\partial u}{\partial\lambda}\right) \tag{2.9}$$

$$F^T = K_h\frac{\partial^2 T}{\partial z^2} + A_h\nabla^2 T \tag{2.10}$$

$$\nabla^2(\sigma) = \frac{1}{a^2\cos^2\phi}\frac{\partial^2\sigma}{\partial\lambda^2} + \frac{1}{a^2\cos\phi}\frac{\partial}{\partial\phi}\left(\frac{\partial\sigma}{\partial\phi}\cos\phi\right) \tag{2.11}$$

Here, $u, v, w, z, \phi, \lambda, p, p_s, \rho$ are zonal velocity (east), meridional velocity (north), vertical velocity (upwards), latitude, longitude, pressure, surface pressure and density, respectively; g is gravitational acceleration, a is the Earth's radius, ρ_0 is a nominal constant density (Boussinesq approximation) and $f = 2\Omega\sin\phi$ is the Coriolis parameter for the Earth's angular velocity Ω. After u and v are found, w may be calculated from the continuity equation, (2.4), and thus it is not a prognostic variable in the model. T represents the scalar value of any passive or active tracer that is advected and diffused with the fluid motion. Two active tracers are used in the model, potential temperature Θ and salinity S, to determine density and subsequently the pressure. Time updates of Θ and S are performed via (2.6). Γ is the nonlinear advection operator and its terms are generally small for large–scale motions, except near the equator and western boundary currents, where it can play a significant role. The Fs are the diffusion operators for momentum and tracers. Their magnitudes are usually small, but are essential for stability in numerical computations, and they play a significant role in long–term climatological behaviour. Equation (2.6) implies the conservation of any tracer quantity. A_m and A_h are the horizontal mixing coefficients for momentum and tracers; K_m and K_h are the respective vertical coefficients.

In eliminating the surface pressure variable from the equations, it is convenient to split the flow field into barotropic and baroclinic components (below). The rigid–lid condition, $w(0) = 0$, is imposed at the surface to eliminate high speed external gravity waves. As a result, the CFL condition (Courant *et al.*, 1928) on the numerical time step can be increased by a factor approaching 100. Recent models which utilize a free–surface (Killworth *et al.*, 1991; Dukowicz & Smith, 1992) carry the surface elevation as a prognostic variable, while the baroclinic and barotropic splitting is retained. The external component may be integrated explicitly in time (Killworth *et al.*), with subcycles for each baroclinic time step, or implicitly (Dukowicz & Smith). The principal motivation for the free–surface is to allow comparisons with altimetric data, and assimilations. Islands do not cause accuracy problems, as in rigid–lid models, and their numbers can be greatly increased without compromising execution efficiency. Another advantage of the free–surface formulation is the elimination of the Killworth (1987) barotropic instability problem, so steeper bathymetric gradients may then be included.

The surface boundary conditions, namely the wind stress $\boldsymbol{\tau}$ and surface restoring of tracers, provide the primary forcing mechanism for the model ocean. Except for the vertical velocity, the conditions are of the Neumann type. For $z = 0$:

$$
\begin{aligned}
\rho_0 K_m \left(\frac{\partial u}{\partial z}, \frac{\partial v}{\partial z} \right) &= \left(\tau^\lambda, \tau^\phi \right) \\
K_h \frac{\partial T}{\partial z} &= \eta \\
w &= 0 \qquad \text{(i.e., rigid–lid).} \qquad (2.12)
\end{aligned}
$$

Here, τ^λ, τ^ϕ are the zonal and meridional components of the surface wind stress, respectively, and η is a prescribed flux of the tracer T through the surface of the fluid. Thus, insolation, rainfall, etc., can be taken into account. This is normally done by *relaxation* (discussed later) where the values of salinity and temperature in the top layer are slowly coaxed towards known values. Models that include polar ice usually have separate dynamics for this. At lateral walls the boundary conditions are (n is the local normal direction):

$$u, v, \frac{\partial T}{\partial n} \;=\; 0\,. \tag{2.13}$$

This is known as the *no-slip* boundary condition for velocities, and there is no loss or gain of tracers through the walls. The bottom conditions are similar except for the vertical velocity, which is not necessarily zero. The vertical velocity w is computed in different ways for tracers and velocities, respectively. When used in tracer calculations, i.e., w_t, it is simply set to zero at the bottom. For velocity calculations, w_v is computed from (u, v) and ∇H, and will normally be nonzero where there are nonzero bathymetric gradients.

$$\begin{aligned} \rho_0 K_m \left(\frac{\partial u}{\partial z}, \frac{\partial v}{\partial z} \right) &= \left(\tau_B^\lambda, \tau_B^\phi \right) \\ \frac{\partial T}{\partial z} &= 0 \\ w_v &= -\frac{u}{a\cos\phi}\frac{\partial H}{\partial \lambda} - \frac{v}{a}\frac{\partial H}{\partial \phi} \\ &\qquad\qquad \text{for} \qquad z = -H \end{aligned} \tag{2.14}$$

$H(\lambda, \phi)$ is the total depth of the fluid and $\tau_B^\lambda, \tau_B^\phi$ are the bottom frictional stresses. Bottom stress, if desired, can be implemented in a number of ways; e.g., by a quadratic friction law $\rho C_d\,|(u, v)|(u, v)$ or by simple Rayleigh damping $\partial_t(u, v) + (u, v)/R$. All boundary conditions must ensure that mass cannot be lost or gained via external exchanges, excluding, of course, the tracer relaxation terms.

With the rigid–lid condition in place and time variations permitted, the depth–averaged (barotropic) velocity can be represented as the gradient of a scalar, the volume transport stream function ψ:

$$\bar{u} = -\frac{1}{aH}\frac{\partial \psi}{\partial \phi} = \frac{1}{H}\int_{-H}^{0} u\,dz \qquad\qquad \bar{v} = \frac{1}{aH\cos\phi}\frac{\partial \psi}{\partial \lambda} = \frac{1}{H}\int_{-H}^{0} v\,dz \tag{2.15}$$

The overbar operator denotes depth averaging. Since the barotropic velocity is represented this way the conservation of volume is automatically assured down to the numerical accuracy of the machine being used, without any extra effort.

The pressure variable is eliminated from equations (2.1) and (2.2) by depth integration, which then gives a relation for the barotropic velocities. Depth integrating the continuity equation (2.4) gives

$$w(0) - w(-H) \;=\; \frac{-1}{a\cos\phi}\left[\frac{\partial}{\partial \lambda}\left(\int_{-H}^{0} u\,dz \right) + \frac{\partial}{\partial \phi}\left(\int_{-H}^{0} v\cos\phi\,dz \right) \right]$$

$$-H\frac{u}{a\cos\phi}\frac{\partial H}{\partial\lambda} - H\frac{v}{a}\frac{\partial H}{\partial\phi} \tag{2.16}$$

Thus, the depth integral of w can be represented in terms of $(\bar{u}, \bar{v})$ and the bathymetric gradient. At the surface $w(0) = 0$, and $w(-H)$ is given by (2.14). After integrating (2.1) and (2.2) with respect to z, they are then multiplied by $a\rho_0\cos\phi/H$ and $a\rho_0/H$ respectively, to give

$$-\frac{\cos\phi}{H}\frac{\partial^2\psi}{\partial t\partial\phi} = -\frac{\partial p_s}{\partial\lambda} + \frac{f}{H}\frac{\partial\psi}{\partial\lambda} + \mathcal{F}^u\cos\phi \tag{2.17}$$

$$\frac{\sec\phi}{H}\frac{\partial^2\phi}{\partial t\partial\lambda} = -\frac{\partial p_s}{\partial\phi} + \frac{f}{H}\frac{\partial\psi}{\partial\phi} + \mathcal{F}^v \tag{2.18}$$

where

$$\mathcal{F}^u = \frac{-a\rho_0}{H}\int_{-H}^{0}\left[\Gamma(u) - \frac{uv\tan\phi}{a} - F^\lambda + \frac{g\ \sec\phi}{a\,\rho_0}\int_z^0\frac{\partial\rho(z')}{\partial\lambda}\,dz'\right]\,dz$$

$$\mathcal{F}^v = \frac{-a\rho_0}{H}\int_{-H}^{0}\left[\Gamma(v) + \frac{u^2\tan\phi}{a} - F^\phi + \frac{g}{a\,\rho_0}\int_z^0\frac{\partial\rho(z')}{\partial\phi}\,dz'\right]\,dz \tag{2.19}$$

The surface pressure is now eliminated by taking the vertical component of the *curl* (cross differentiating) of equations (2.17) and (2.18), which gives a time evolution relation for ψ

$$\nabla_z\times(\bar{u}_t, \bar{v}_t) = \frac{\sec\phi}{a}\left[\bar{v}_{t\lambda} - \frac{\partial^2\,\bar{u}\ \sec\phi}{\partial t\,\partial\phi}\right] \qquad \text{which gives}$$

$$\left[\frac{\partial}{\partial\lambda}\left(\frac{\sec\phi}{H}\frac{\partial^2\psi}{\partial\lambda\partial t}\right) + \frac{\partial}{\partial\phi}\left(\frac{\cos\phi}{H}\frac{\partial^2\psi}{\partial\phi\partial t}\right)\right] - \frac{\partial}{\partial\lambda}\left(\frac{f}{H}\frac{\partial\psi}{\partial\phi}\right) - \frac{\partial}{\partial\phi}\left(\frac{f}{H}\frac{\partial\psi}{\partial\lambda}\right)$$

$$= -\left[\frac{\partial}{\partial\lambda}\left(\frac{g}{\rho_0 H}\int_{-H}^{0}\int_z^0\frac{\partial\rho(z')}{\partial\phi}\,dz'\,dz\right) - \frac{\partial}{\partial\phi}\left(\frac{g}{\rho_0 H}\int_{-H}^{0}\int_z^0\frac{\partial\rho(z')}{\partial\lambda}\,dz'\,dz\right)\right]$$

$$+\left[\frac{\partial}{\partial\lambda}\left(\frac{a}{H}\int_{-H}^{0}F^v - \Gamma(v)\,dz\right) - \frac{\partial}{\partial\phi}\left(\frac{a\cos\phi}{H}\int_{-H}^{0}F^u - \Gamma(u)\,dz\right)\right] \tag{2.20}$$

The baroclinic component of (u, v) is denoted by a caret:

$$(u, v) = (\bar{u}, \bar{v}) + (\hat{u}, \hat{v}) \tag{2.21}$$

The $\bar{u}, \bar{v}$ components can be updated in time via (2.20). To update $\hat{u}, \hat{v}$ in time, equations (2.1), (2.2), and (2.3) are combined to give, temporarily setting p_s to zero:

$$\frac{\partial u'}{\partial t} - \Gamma(u) - fv = -\frac{g \sec\phi}{\rho_0\, a}\frac{\partial}{\partial \lambda}\left(\int_z^0 \rho\, dz'\right) + F^u \tag{2.22}$$

$$\frac{\partial v'}{\partial t} - \Gamma(v) + fu = -\frac{g}{\rho_0\, a}\frac{\partial}{\partial \phi}\left(\int_z^0 \rho\, dz'\right) + F^v \tag{2.23}$$

u' and v' are only slightly different from u and v, due to the neglect of the component of pressure force that depends on p_s. The baroclinic component of horizontal velocity is then found from

$$(\hat{u}, \hat{v}) = (u' - \bar{u}', v' - \bar{v}') \tag{2.24}$$

The error incurred by assuming $p_s = 0$ is essentially eliminated since that error is independent of z and is therefore removed by subtracting out the barotropic components of velocity, $\bar{u}'$ and $\bar{v}'$.

For a completely closed domain with no islands, the boundary conditions are reasonably straightforward to implement; that for the stream function is the easiest. Since there can be no barotropic or baroclinic flows into, or out of, any simply connected land boundary, the stream function may be set to any arbitrary constant value on the single boundary. The RHS of (2.20) reduces to an elliptic PDE, with Dirichlet boundary conditions, which is solved implicitly to obtain the time update of ψ. This problem can be solved by the Successive Over Relaxation method (SOR) or by various conjugate gradient methods. For many years the five–point finite difference molecule has been used in the numerical solution. However, it has become evident (Pacanowski, private communication) that the nine–point molecule gives better accuracy when reconstructing the surface pressure from Eqns. (2.17) and (2.18). Unfortunately, this increases errors in the stream function estimates, particularly when many islands are included. All operational modelling during the project used only the five–point molecule and conjugate gradient solutions for the elliptic PDE. Solving the stream function update problem is the most time consuming operation since it does not lend itself readily to vectorization; SOR is not vectorizable and classical conjugate gradient methods can suffer from slow convergence. More modern conjugate gradient methods, which use matrix preconditioning, are now appearing in the free–surface implementations. The newly emerging parallel architectures may greatly change the solution methods; PE formulations are amenable to parallelization after a good deal of rearrangement of Bryan's original equations (e.g., Dukowicz & Smith, 1992).

The inclusion of islands complicates the solution somewhat. The updating method is based on that proposed by Kamenkovich (1962), and modified by Takano (1974). It is referred to as "hole relaxation" and involves taking the closed line integral of ∇p_s around each island, on the set of grid points next to its coast. This integral must vanish since the pressure field is conservative. Although the stream function is constant along all connected perimeter points, the external and internal pressures will, in general, not be constant. Each island's stream function value is adjusted so that the residual of the integral tends to zero, and the computations are done simultaneously with the SOR, or conjugate gradient iterations, for the entire model domain. The line integrals are converted to area integrals (Cox, 1984) via Stokes' theorem to allow for more compact coding, although only the perimeter points are actually used. Depth averaging (2.22) and (2.23), and changing to an area integral, yields the time evolution relation for ψ around each island,

$$\frac{1}{a}\int_A \left[\left(\frac{\psi_{t\lambda}}{H\cos\phi}\right)_\lambda + \left(\frac{\psi_{t\phi}\cos\phi}{H}\right)_\phi\right] dA \;=\; \int_A \left[\left(\overline{v'_t}\right)_\lambda - \left(\overline{u'_t\cos\phi}\right)_\phi\right] dA \tag{2.25}$$

where t, λ, ϕ subscripts denote partial differentials. Thus, after the velocity fields are updated, the stream function may also be updated. Eqn. (2.25) is merely an area integral of (2.20).

2.2 Viscosity and Diffusivity

The representation of subgrid scale Reynolds stresses is regarded as one of the most serious limitations to the numerical formulation of the PEs. The diffusion of momentum and tracers, in (2.8) to (2.11), invariably needs to be made larger than that present in nature so that purely computational modes are suppressed (i.e., used as a numerical filter). A_m is made only large enough so that obvious grid noise is suppressed. A_h is usually a little less sensitive but it is still too large to be realistic. The most commonly used horizontal mixing regimes are itemized below.

- *Constant Laplacian mixing*: $A_m \nabla^2(u, v, T)$. A_m is a constant value for the entire grid. This originates from the relationships for a Newtonian fluid.
- *Constant biharmonic mixing*: $A_m \nabla^4(u, v, T)$. A_m is a constant value for the entire grid. This operator has no real basis in fluid theory although, in models, its effect is similar to the Laplacian operator.
- *Nonlinear mixing*: after Smagorinsky (Rosati & Miyakoda, 1988). A_m is proportional to the grid scale and to the local instantaneous velocity shears.
- *Isopycnal mixing*: (Cox, 1987) performs tracer mixing along isopycnal surfaces, since that is thought to be more realistic. A tensor is calculated from the slope of the surface, so that there are horizontal and vertical components. This method is expensive to run and is still the subject of much experimentation.

Biharmonic and nonlinear mixing (§2.2.1) represent an attempt to reduce the effects of excessive damping on the modelled flow encountered with Laplacian mixing, while still maintaining sufficient noise suppression. The biharmonic operator acts over smaller length scales and is less dissipative for structures larger than the two grid point wavelength. For the same grid resolution, biharmonic mixing is less dissipative for eddies. A von Neumann analysis of the one–dimensional diffusion problem, using ∇^2 and ∇^4, gives the amplification factors as

$$\begin{aligned} \text{Laplacian :} \qquad & \frac{2A\Delta t}{\Delta x^2}[\cos(k\Delta x) - 1] + 1 & \simeq & \; 1 - Ak^2\Delta t \\ \text{Biharmonic :} \qquad & 1 - \frac{2A\Delta t}{\Delta x^4}[\cos(k\Delta x) - 1]^2 & \simeq & \; 1 - Ak^4\Delta t \end{aligned} \tag{2.26}$$

A (positive) is the diffusivity, k is the wave number, Δt and Δx are the time step and grid spacing, respectively. Effects of biharmonic mixing on much larger scales of motion and long–term integrations are not known, but are probably not greatly different to Laplacian mixing. It is probable that baroclinic eddies, at mid and high latitudes, will not be generated for grid spacings of greater than $20\,km$, nor will true mesoscale instabilities.

Values of A_m and A_h, for the Laplacian mixing phases of the present model, are set to $6 \times 10^7\,cm^2s^{-1}$ and $10^7\,cm^2s^{-1}$, respectively. Corresponding values of A_m and A_h, for the biharmonic mixing phases, are $-7 \times 10^{20}\, cm^4 s^{-1}$ and $-5 \times 10^{20}\, cm^4 s^{-1}$, respectively.

Vertical diffusion of momentum and tracers can be accomplished by several methods. In nature these mechanisms are rather complex and poorly understood. This remains an area of theoretical and practical research for general circulation models. Commonly used vertical mixing schemes are itemized below.

- *Constant vertical mixing*: $K_m \partial_z^2 (u, v)$. For tracer quantities it is, $\partial_z \left(K_h / \delta\, \partial_z T \right)$, where δ is 0 or 1. The 0 case is used to stabilize density inversions (convective adjustment). This is the simplest type of mixing, and it is the analytic solution for a uniformly stratified fluid. This is perceived to be a little too simplistic for z-coordinate models, although it is consistent with the equations of motion, in the limit of zero grid spacing.

- *Implicit vertical mixing*: the same as the previous type, but the vertical structure equation is solved implicitly for the entire water column, at each horizontal grid node. This allows for large K_m and K_h without the need to reduce the time step, e.g., when dealing with density inversions.

- *Pacanowski & Philander (1980) mixing*: a Richardson scheme developed for very fine vertical grid resolutions. Originally used for studying equatorial undercurrents, but has gained widespread acceptance in general circulation models.

The vertical eddy diffusity scheme chosen for the model was constant mixing, solved implicitly at each time step. The vertical eddy diffusivity, K_m, is fixed at $10\, cm^2 s^{-1}$. The vertical tracer diffusivity uses the same scheme but K_h varies only with depth, and the values are displayed in Table 2.1 (§2.3). Cummins *et al.* (1990) examine the merits of making K_h proportional to the local Brunt–Väisälä frequency, i.e., variable with depth, horizontal position and time. The effects of such nonlinear vertical mixing are not well known, and it is yet to be proven effective, so K_h is fixed in time and horizontal position for the present model. For the present model, the depth profile of K_h is made proportional to the global annually–averaged Brunt–Väisälä frequency, at each depth layer. Values range from 0.21 in the mixed layer to 1.8 at the ocean floor (Table 2.1).

The real ocean has density inversions in specific areas at mid and high latitudes. The two most significant areas are the North Atlantic and the southern reaches of the Southern Ocean. Subduction from these surface waters is quite large, being about 10–20 Sv in the North Atlantic and 15–40 Sv in the Southern Ocean, near Antarctica. Such vigorous vertical motions are poorly represented by the simple Fickian parameterizations and so some other method is required to simulate these subductions in the model. The Cox–Bryan code has always utilized an 'infinite' mixing regime for density inversions. For explicit vertical mixing, if two layers are found to be unstable then temperature and salinity values are repeatedly averaged between the two layers until stability is reached, or some other limit set in the code. This method is fairly crude but is the easiest way to include subduction. Thermohaline processes are critical in the real ocean's long–term behaviour, and hence in long–term model behaviour. Since it was not intended for the present model to be used over long time scales, the simplest vertical mixing scheme is used. Vertical diffusion is of the implicit type for all the model runs, and the vertical averaging for density inversions is effected by using very large values of K_h ($10^6\, cm^2\, s^{-1}$).

2.2.1 Smagorinsky Mixing

Smagorinsky mixing is used in the major finding of Chapter 4, and so it will be given some attention here. This scheme, after J. Smagorinsky (1963), is similar in formulation to Laplacian mixing but the viscosity and diffusivity coefficients are proportional to gradients in the velocity and tracer fields, and is therefore inherently nonlinear. The mixing terms (the Fs) in Eqns. (2.8) to (2.10) are recast as stress tensors (Rosati & Miyakoda, 1988; Deardorff, 1973):

$$F^{\lambda} = ma^{-1}\left[\frac{\partial \tau^{\lambda\lambda}}{\partial \lambda} + m\frac{\partial \tau^{\lambda\phi}\cos^2\phi}{\partial \phi}\right] \tag{2.27}$$

$$F^{\phi} = ma^{-1}\left[\frac{\partial \tau^{\phi\lambda}}{\partial \lambda} + \frac{\partial \tau^{\phi\phi}\cos\phi}{\partial \phi} + \tau^{\lambda\lambda}\sin\phi\right] \tag{2.28}$$

where $m = \sec\phi$ is the map factor. F^{λ} and F^{ϕ} represent the meridional and zonal components of the Fs in Eqns. (2.8) to (2.9). $\tau^{\lambda\lambda}$, $\tau^{\lambda\phi}$, $\tau^{\phi\lambda}$ and $\tau^{\phi\phi}$ are the stress tensor components, given by:

$$\tau^{\lambda\lambda} = A_m^{\lambda}\, D_t \qquad\qquad \tau^{\lambda\phi} = A_m^{\phi}\, D_s \tag{2.29}$$

$$\tau^{\phi\lambda} = A_m^{\lambda} D_s \qquad \tau^{\phi\phi} = -A_m^{\phi} D_t \tag{2.30}$$

The tension and shearing strains, D_t and D_s, are given by:

$$D_t = \frac{m}{a}\frac{\partial u}{\partial \lambda} - \frac{1}{ma}\frac{\partial mv}{\partial \phi} \tag{2.31}$$

$$D_s = \frac{m}{a}\frac{\partial v}{\partial \lambda} + \frac{1}{ma}\frac{\partial mu}{\partial \phi} \tag{2.32}$$

The effective eddy diffusivity coefficients are functions of the strains and zonal and meridional wave numbers:

$$A_m{}^{\lambda} = c^{\lambda}\,|D| \tag{2.33}$$

$$A_m{}^{\phi} = c^{\phi}\,|D| \tag{2.34}$$

where $$D^2 = 2(D_t^2 + D_s^2) \tag{2.35}$$

In a numerical implementation c^{ϕ} and c^{λ} are made proportional to the horizontal grid spacing and to a dimensionless constant c :

$$c^{\lambda} = (cma\,\Delta\lambda)^2/\sqrt{2} \tag{2.36}$$

$$c^{\phi} = (ca\,\Delta\phi)^2/\sqrt{2} \tag{2.37}$$

Smagorinsky (1993) provides an historical review of the use of nonlinear mixing, and an informal derivation of the above equations, but the details are too lengthy to reproduce here. The stress–strain tensor relations of classical continuum mechanics are modified so that Reynolds stresses are assumed proportional to the rate of strain, $\nabla\mathbf{v}$. This yields a fourth–order tensor with eighty–one components, for isotropic three–dimensional flows. This is simplified by invoking axial symmetry about the vertical axis, and the hydrostatic approximation, which requires some terms to be ignored so that the resulting mixing operator always yields dissipation. The remaining terms above are the simple velocity shears, u_{ϕ} and v_{λ}, and tensions or compressions, u_{λ} and v_{ϕ}. Qualitatively, when flow gradients are small, then the resulting turbulent diffusion is small — several orders of magnitude smaller than for Laplacian mixing. The dependence of dissipation on wave number, equations (2.33) through (2.37), is derived from Kolmogorov's similarity theory where energy dissipation is assumed proportional to the modulus of the wave number.

For the Smagorinsky runs the wave number coefficient, c, was chosen to be 0.3 (Chapter 4), which is somewhat larger than the 0.15 chosen by Rosati &

Miyakoda. The world model domain has a relatively large number of islands and the larger value of c was simply chosen to control the resulting stream functions errors. This value lies at the high end of empirically and theoretically determined values listed by Smagorinsky (1993, Table 1). A smaller value of c may well suffice if fewer islands are included, or in a free–surface model, which does not use the stream function formulation.

2.3 Grid Geometry

The grid spacing is one degree in latitude and longitude, and there are seventeen layers in the vertical. The horizontal and vertical arrangements of the mesh are Arakawa's "B" grid (1977), shown in Fig. 2.1. T points represent active tracers such as potential temperature and salinity, or passive tracers such as O_2. The stream function ψ points correspond to T points. The velocity points UV are at the northeast corner of the T box, so each T point is surrounded by four UV points, and vice versa. Thus, second order accurate finite difference operators for velocity can easily be found, centred at T points, and correspondingly for tracer derivatives centred at UV points. Vertical velocity points W lie between the T and UV layers to again give second order accuracy, although W is not a prognostic variable. W_t points lie directly below and above T points, and correspondingly W_v points lie above and below UV points. The pressure grid points P are defined at either T points or W_t points. Internal pressures, calculated prognostically during model execution, lie at T points, while those related to surface pressure calculations (§2.6) lie at W_t points. The grid of the Cox–Bryan code is normally aligned with latitude and longitudes, for simplicity.

The world model has its T grid at half–degree latitudes and longitudes, i.e., -0.5,0.5,1.5 ... . The horizontal grid domain is displayed in Fig. 1.3. There are seventeen layers in the vertical ($k = 1$ to 17), and the T point depths and layer thicknesses are displayed in Table 2.1: the last number is the bottom depth, $4900\,m$. Layers are to set to a thickness of $645\,m$ near the bottom to resolve bottom pressure torques, although success has been marginal; $400\,m$ or less is needed.

The horizontal and vertical grid spacings do not truly resolve some important aspects of real ocean flows, such as western boundary currents, equatorial under-

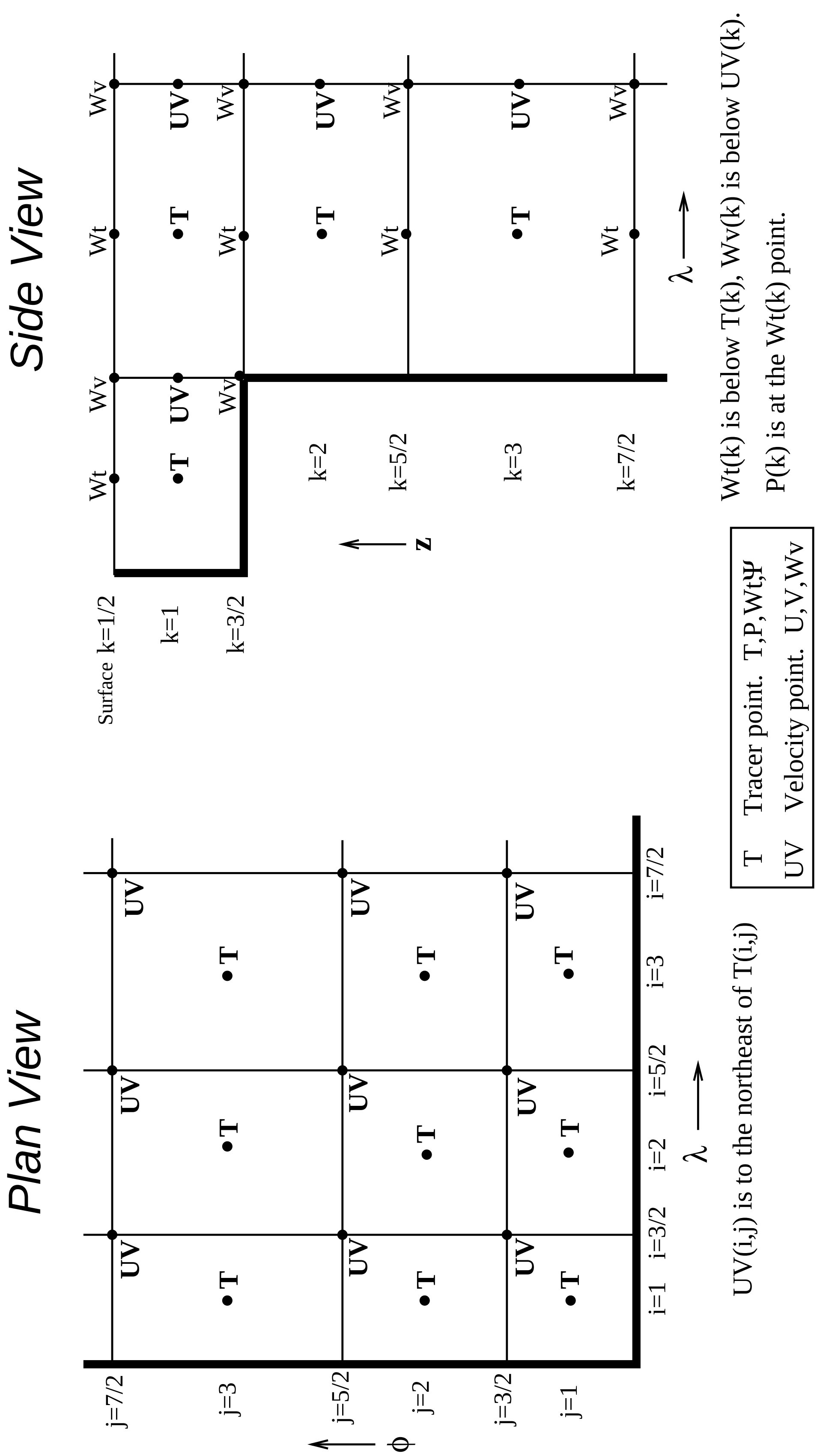

Figure 2.1: **:** [rotated] Horizontal and vertical arrangements of the Arakawa "B" grid. ϕ is longitude (positive eastwards) and λ is latitude (positive northwards). The depth z is positive upwards from the bottom at $-H$, but the vertical index k is usually taken as positive downwards.

k	Z_t (m)	ΔZ_t (m)	K_h $(cm^2 s^{-1})$
1	13.5	27.0	0.21
2	40.5	27.0	0.21
3	67.5	27.0	0.21
4	98.0	34.0	0.21
5	142.0	54.0	0.21
6	210.5	83.0	0.25
7	308.5	113.0	0.29
8	448.0	166.0	0.33
9	641.0	220.0	0.37
10	896.5	291.0	0.43
11	1227.0	370.0	0.54
12	1636.0	448.0	0.70
13	2120.0	520.0	0.95
14	2672.5	585.0	1.16
15	3287.5	645.0	1.36
16	3932.5	645.0	1.75
17	4577.5	645.0	1.80
18	4900.0	—	—

Table 2.1: **:** Tracer layers are numbered 1 to 17, and 18 is the seafloor. The second column is the depth of the centre of a layer, and the third column is the layer thickness. The fourth column is the depth dependent vertical tracer diffusivity (§2.2).

currents and mesoscale eddies. Real western boundary currents are typically 40 to 80 km wide, which is smaller than the model's grid spacing of 31.5 to 111 km. Model western boundary current velocities are smaller than those found in nature, typically about half. However, these reduced velocities are distributed over the width of a grid box, and so the resulting fluxes are in reasonable agreement with those found in reality. Similar arguments apply to the vertical grid spacing. The internal temperature and salinity fields are smoothed to the grid resolution, thereby smoothing thermal wind shears. However, the depth integrated shear, i.e., the volume flux, remains the same. Resolution of the Pacific Equatorial Undercurrent is somewhat better. Its peak and average model velocities are $85\,cm\,s^{-1}$ and $45\,cm\,s^{-1}$, respectively, being realistic figures.

Earlier model configurations (Pacific–Indian basin) had twelve layers with the bottom layer being over 1000 m thick. High latitude bathymetric features, such as the Pacific–Antarctic Ridge, had no effect on the barotropic field but this situation has improved considerably with the seventeen layer configuration. Bottom buoyancy interactions and bathymetric steering intensified in the path of the Antarctic Circumpolar Current. Even more layers would be preferable, but suitable computational resources were not available. The Ekman layer (real and modelled) is generally not in tight geostrophic balance since the horizontal pressure applied by the wind stress is comparable with the Coriolis force. Layer one, 0–27 m, has large deviations from geostrophy while layer two, 27–54 m, deviates by no more than a few percent in some open areas. The Ekman spiral is generally not observable in the model since the Ekman dynamics are entirely averaged within the first layer, but surface layer velocities are observed to be directed at 60–90° to the applied wind stress, to the left (right) in the southern (northern) hemisphere. However, this does not obviate the need for high resolution in the surface layers.

The vertical grid spacing gives acceptable resolution of the thermocline[1], although other factors in the model cause problems over this depth range. It is well known that PE models tend to deepen and diffuse the base of the thermocline with time, therefore affecting internal wave propagation, heat and salt fluxes, and other important characteristics. PE models used to study equatorial

[1]In this thesis, the thermocline is defined to be the depth range of large temperature gradients, as opposed to the depth of the base of the mixed layer.

phenomena often use vertical resolutions of $5\,m$ near the surface but quite thick layers at depth, to keep the computational workload down. The layer thicknesses chosen for the present study are intended for low to midlatitudes, and to give approximately equal resolution for all depths. There is less need for mixed layer resolution at high latitudes since the stratification is much weaker, but there is a greater need for bottom resolution because of the greatly increased effects of bathymetric steering.

Bathymetry data are from ETOPO5 (1978) and the Scripps 1° data sets. The area bounded by New Zealand, Australia and the equator has been given more attention, as have the Indonesian passages. The bathymetry was manually edited to make it as realistic as possible and also to incorporate features which were certain to have significant effects on flow patterns. As a simple example, the Solomon Islands ridge completely disappears with smoothing since it is long and narrow, but it effectively forms a solid wall to the westward zonal flows and was therefore included as a regular island in the model. The Queensland Trough was included in an attempt to understand the sources of the Great Barrier Reef Undercurrent (Church & Boland, 1983), despite the fact that it is narrower than the grid spacing. Vityaz Strait has not been included since it is quite narrow, $37\,km$ across the $200\,m$ isobaths[2], and an extra island would have again increased stream function errors. Areas around the Sulu Sea (near the Philippines) had their bottom depths reduced to $1200\,m$, to remove the radical temperature values in the Levitus (1982) climatology data base. The Sulu Sea is closed to the open Pacific below $420\,m$ and so has quite high temperatures at abyssal depths, as do several other nearby basins. Sulu Sea temperatures decreases with depth to about 10° at $990\,m$ (Wyrtki, 1961a), and are then nearly constant down to the bottom. The Levitus data has these values smoothed into the nearby open North Pacific.

The Indonesian passages are far too complex and narrow to be sensibly represented by a 1° grid, but the inclusion of a passage connecting the Pacific and Indian Oceans is essential. The sill depth is set realistically to $1412\,m$. The island chains of Flores and Java were combined into a single peninsula connected to mainland Asia, and only Sulawesi (Celebes) is kept as an island. This gives two

[2] Ref. Aust. Bureau of Mineral Resources bathymetric chart: *Western Solomon Sea, Papua New Guinea.*

connecting passages and two possible paths for the Mindanao Current. Malacca Strait is quite shallow and is known to carry insignificant volume fluxes (Wyrtki, 1961a), and so is not included in the model. Torres Strait is not included for the same reasons (Wolanski *et al.*, 1989). Early model configurations included Lombok Strait, which is thought to carry a sizable fraction of the Indonesian throughflow, but was later removed when experimentation showed it had no effect on the nett throughflow. The Kermadec ridge was edited to ensure its sill depth was realistic. Near Fiji, this ridge is only $500\,m$ deep and it blocks a great deal of the flow from the east.

The 1° grid is neither eddy resolving nor boundary current resolving. However, all the essential features of western boundary currents appear in the model; the modelled current widths are about twice their real widths. The essential dynamics of mesoscale eddies cannot be represented by such a coarse grid.

2.4 Relaxation and Acceleration Techniques

Ocean general circulation models usually have their temperature and salinity fields 'relaxed', or coaxed towards observed climatologies, such as the data base provided by Levitus (1982). The relaxation is normally performed during the early stages of time integration (diagnostic), at all depth layers, until the model's tracer fields are within some prescribed tolerance of the climatology data. After this, the relaxation is either greatly reduced or completely removed (prognostic), except for the surface layer. The surface layer relaxation is retained to parameterize the effects of evaporation and precipitation and heat fluxes. Other more sophisticated methods in coupled atmosphere–ocean models use virtual salinity fluxes. Relaxation is accomplished by a Newtonian damping method. The tracer time derivative operator in Eqn. (2.6) is modified to

$$\frac{\partial T}{\partial t} \quad\longrightarrow\quad \frac{\partial T}{\partial t} + \frac{1}{r}(T - T_0) \tag{2.38}$$

where r is a decay constant with units of time, and T_0 is the climatology data base value at the particular grid point. The solution to the differential equation $T_t = 1/r\,(T_0 - T)$ is an exponential decay of T to the value T_0. Thus, r is referred to as the decay time or e–folding constant. If the model dynamics are "loose" (close to degeneracy) then the relaxation will quickly bring T to within 2% of

T_0, in about four e–folding periods. The values of r used in the present work are 35 days for the surface layer increasing to five years at the ocean floor. These values are similar to those used in the Semtner & Chervin (1988, 1992) model. Haney (1971) discusses appropriate values of r for surface layers. It is well known that prognostic integration yields temperature and salinity distributions that individually diverge away from observed climatologies, but density distributions do not diverge by the same relative extent. The degree of divergence is generally thought to be dependent upon the type of model vertical diffusion employed and the corresponding diffusivity coefficients. Since the long–term climatological behaviour of the model is not the main focus of this project, relaxation below the thermocline has been retained, but is a little weaker than that used by Semtner & Chervin. Retaining deep–water relaxation helps prevent the thermocline from diffusing and deepening and the loss of deep–water stratification. Spin–up methods will be discussed in more detail in §2.7.

PE models of the ocean are substantially more expensive in computer time than their atmospheric counterparts. The time required for ocean models to reach a quasi–equilibrium is many centuries to several thousand years, compared with about 1 year for the atmosphere. The time steps used for oceanic models are of order 2 days to a few minutes, because of the large range of internal wave speeds. A technique used for many years is that of climatological acceleration, which can greatly reduce the computational load. This is formalized by Bryan (1984). The method involves using different time steps for velocities and tracers, respectively. The equilibration of the tracer fields could be hastened by increasing their corresponding time step, but this would violate the CFL condition. Bryan shows how reducing the velocity/stream function time step, relative to the tracer time step, has an equivalent effect. The ratio between the two time steps is termed the acceleration factor α. The drawback of this technique is that all wave activities are greatly distorted: frequencies are reduced by α, celerities are reduced by $\sqrt{\alpha}$ and the rate of energy release from baroclinic instability is similarly reduced. Midlatitude Rossby waves with wavelengths in the 50–400 km range have their group velocities reduced (Bryan's Fig. 1), and these are the most dynamically important of the midlatitude planetary waves to consider. There is little distortion of group velocities outside of this wavenumber range. Another consideration is the geostrophic adjustment time, which is increased by a factor of α. As α is increased, the density fields can be changed relatively quickly by relaxation, but the velocity field may not be able to respond quickly. Thus, it may be possible to "unlock" geostrophy in near surface layers, if α is very large (say 200) and the climatology is rapidly varied.

Multiple equilibria behaviour has been observed in ocean models (F. Bryan, 1987) although it is not known exactly what bearing acceleration has on this. Acceleration is therefore appropriate for models with constant annually–averaged forcing, and its effects on seasonally forced models is not very well known. The methods of Semtner & Chervin are used here. The diagnostic spin–up phase, using annually–averaged forcing, is performed with an acceleration of 12:1, and after this the seasonally forced phase is synchronous, i.e., $\alpha = 1$ and surface forcing is synchronous with the model's calendar. All depth layers are relaxed during the first four years of model integration. For all times after this, layers two to nine are free of relaxation, i.e., a free thermocline, and more details are give in §2.7.

2.5 Stability Conditions.

The most basic requirement for the successful numerical solution of an initial value problem is that of long–term stability. Crucial to long–term stability is the requirement of the conservation, in finite difference form, of certain mean and mean squared quantities (e.g., kinetic energy) which are conserved in the continuous differential equations. Particular finite difference formulations of the nonlinear advective terms are required in order to ensure these constraints, as first demonstrated by Arakawa (1966) for the two–dimensional nondivergent velocity fields (see also Arakawa & Lamb, 1977). Bryan (1969) demonstrates, with an elegant and compact derivation, how these constraints can be enforced for the present set of primitive equations.

The best known stability criterion is the Courant–Friedrichs–Lewy (CFL; 1928) condition on the time step. For a two dimensional hyperbolic problem it is: $c\,\Delta t/\Delta x < 1/2$, where Δt is the time step, Δx is the grid spacing and c is the magnitude of the largest phase velocity, group velocity or material speed possible in the solution. The 1/2 becomes 1/4 for uncentered differencing. The smallest horizontal grid spacing in the world model is $31.5\,km$ at 73.5°S, and the fastest possible motions are about $4\,m\,s^{-1}$, giving an upper limit of $3937\,s$ for the time step. This is for synchronous integration, where internal waves travel at (nearly) realistic speeds. The $4\,m\,s^{-1}$ motions are near–surface internal gravity waves ($2.7\,m\,s^{-1}$), propagating along the coastline of Antarctica, that are embedded in an ambient flow of about $1.3\,m\,s^{-1}$. The actual time step used for the seasonally forced phase is $3600\,s$, and instabilities are apparent for time steps larger than $3900\,s$. When α is larger than 1, wave motions are retarded proportionally and the (tracer) time step may be increased. Material velocities then determine c since they are not greatly affected by acceleration, and the time step can be increased typically by a factor of four. The world model time step was $15900\,s$ during the spin–up phase ($\alpha = 12$) with Laplacian viscosity.

The velocity CFL condition is usually the most stringent condition on the time step, with the exception of conditions necessary for biharmonic mixing to remain stable. Consider the simple biharmonic diffusion relation, where A is A_m or A_h:

$$\frac{\partial \theta}{\partial t} = A\frac{\partial^4 \theta}{\partial x^4} \tag{2.39}$$

With explicit time stepping, this is discretized as (A is negative):

$$\theta_j^{n+1} - \theta_j^n = B[\,(\theta_{j+2}^n + \theta_{j-2}^n) - 4(\theta_{j+1}^n + \theta_{j+1}^n) + 6\,\theta_j^n\,] \tag{2.40}$$

where $B = A(\Delta x)^4/\Delta t$, $n \Leftrightarrow t$ and $j \Leftrightarrow x$. The general solution is:

$$\theta_j^n = \gamma^n \exp ik_j \Delta x \tag{2.41}$$

Solving the eigenvalue problem for (2.40) and (2.41), and setting $\beta = k\Delta x$, gives:

$$\gamma = 1 + 4B[1 - \cos(\beta)]^2 \tag{2.42}$$

$|\gamma| < 1$ is necessary for stability, and since $B < 0$, we have

$$\Delta t < \frac{(\Delta x)^4}{16\,A} \tag{2.43}$$

Another constraint is readily shown to be

$$\frac{c\,(\Delta x)^3}{16\,A} < 8 \tag{2.44}$$

The corresponding restrictions for horizontal Laplacian diffusion, and vertical diffusion are:

$$\frac{c\,\Delta x}{2A} < 2 \qquad\qquad \frac{w\,\Delta z}{2K} < 2 \tag{2.45}$$

$$\Delta t < \frac{(\Delta x)^2}{2A} \qquad\qquad \Delta t < \frac{(\Delta z)^2}{2K} \tag{2.46}$$

were K is K_m or K_h, z is the vertical coordinate and w is the maximum magnitude of the vertical velocity. Conditions relating to velocities ensure that the grid Reynolds (2.45) number is less than 2, and similarly for the Peclét number (2.46) of tracer diffusion. These restrictions can be considered as diffusive CFL conditions, and are normally easily met, except for certain configurations of biharmonic mixing. During the accelerated spin–up (§2.7) the time step was $15900\,s$ using Laplacian mixing, but this had to be reduced to $12000\,s$ during the biharmonic phase. All diffusive conditions were easily satisfied by the $3600\,s$ time step during synchronous integration. Weaver & Sarachik (1990) and Bryan (1984) discuss more detailed aspects of these types of restrictions.

The model time discretization is the centred leapfrog scheme. To prevent two separate solutions developing for odd and even time steps, an Euler backward time step is performed regularly. This involves averaging two consecutive stream function fields, and swapping all other fields. Simple hyperbolic problems normally only require a backward step for every ~100 steps, but experimentation shows that this needs to be 10 to 20:1 for PE models. The backward time step ratio is 17:1 during phases that have fixed forcing and 13:1 for seasonally varying forcing. If the ratio is too large, a weak instability develops and errors are first noticeable in the stream function.

2.6 Reconstructing the Surface Pressure

The surface pressure is calculated at regular intervals while the model is running, and then dumped to disk for examination and storage. The spatial derivatives of p_s can be found from (2.17) and (2.18), once the time derivative of ψ is known. A little work is still required, though, to actually find p_s from $\partial_x p_s$ and $\partial_y p_s$. A number of schemes are available for accomplishing this. For example, $\nabla^2 p_s$ could be found and easily solved, but this requires differentiation of the already noisy spatial derivatives above, and some type of Takano method to obtain boundary conditions. A simple method of integrating the derivatives was developed for this project. A closer examination of how $\partial_x p_s$ and $\partial_y p_s$ are distributed on the Arakawa B–grid gives a direct, but clumsy, way of performing the integration. Fig. 2.2 shows where p_s and its derivatives are defined on the B–grid. As mentioned previously, pressure nodes associated with p_s are defined to be coincident

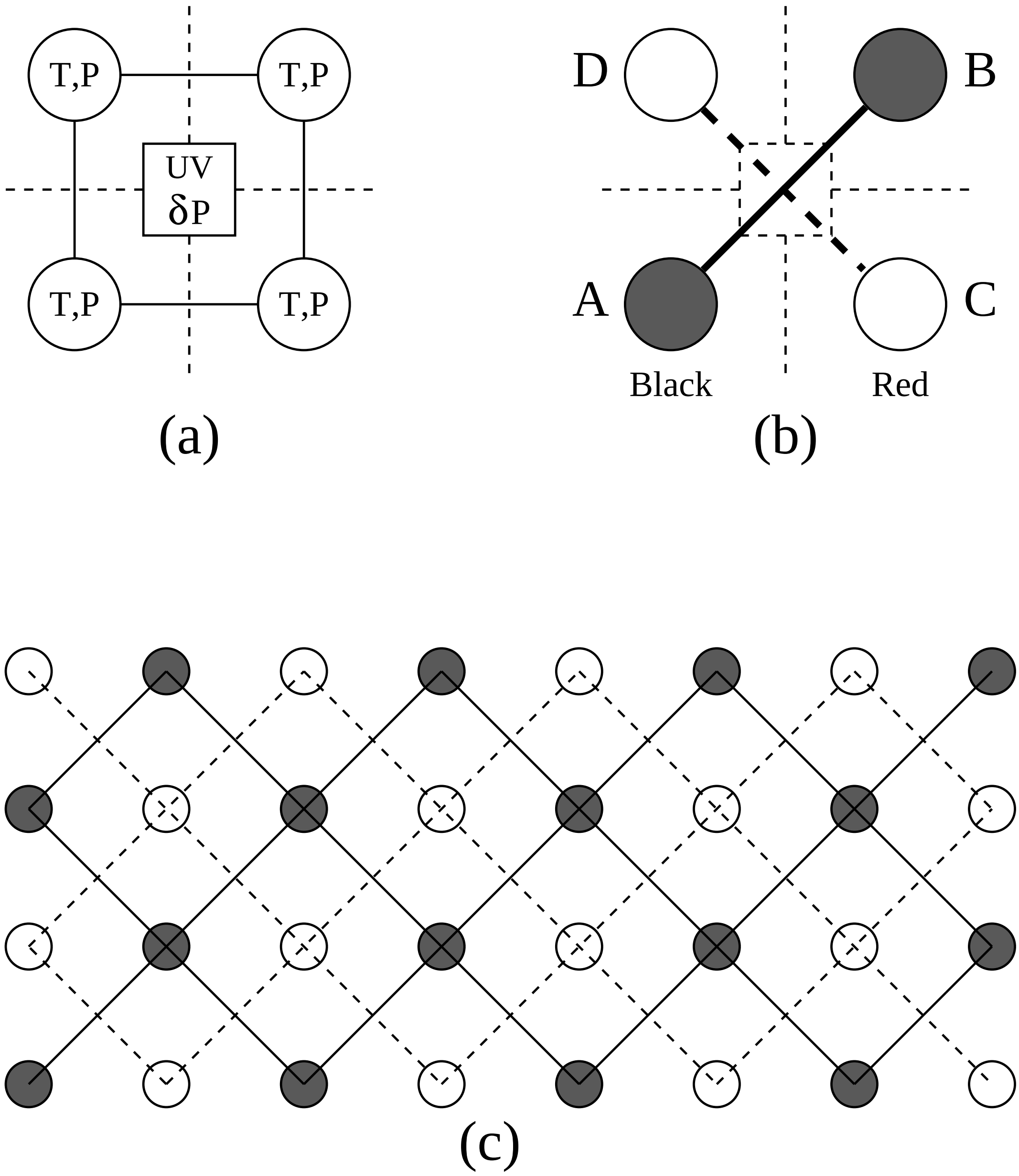

Figure 2.2: **:** Reconstructing P_s from $\partial_x \mathrm{P}_s$ and $\partial_y \mathrm{P}_s$. (a) P_s is defined at T points and its spatial derivatives are defined at UV points, on the B–grid. (b) The pressure field exists on two decoupled grids, i.e., 'Red' and 'Black'. Given P_A, P_B can be calculated directly, independently of P_C and P_D. Similarly, P_C and P_D can be found directly from each other. (c) The Red and Black grids can be integrated independently by starting with two arbitrarily set points, one on each grid, and scanning backwards and forwards, filling–in unknown values. The means of the two grids are then adjusted to zero to effectively couple them.

with w_t points (bottom of slab), and since second order accurate finite differences are be used, $\partial_x p_s$ and $\partial_y p_s$ are defined at UV points in the horizontal. (Internal pressure gradients are calculated during model execution, and these are defined at the mid–depth of a slab, i.e., at UV points.) The pressure derivatives are coincident with w_v points (Fig. 2.1), in the vertical.

It can be shown that the finite difference pressure field operators have a null space (Margolin, 1978), and the degree of decoupling is dependent on how the stream function elliptic PDE is solved, i.e., with a five–point or nine–point operator. The second order accurate formulæ for $\delta_x p_s$ and $\delta_x p_s$ are (Fig. 2.2):

$$\delta_x p_s = \{(P_B - P_D) + (P_C - P_A)\}/2 \tag{2.47}$$

$$\delta_y p_s = \{(P_D - P_A) + (P_B - P_C)\}/2 \tag{2.48}$$

where $\delta_x p_s$ and $\delta_y p_s$ represent zonal and meridional changes of p_s, respectively, and are found from (2.17) and (2.18). There are four unknowns and only two equations, but the equations decouple to

$$-P_A + P_B = \delta_x p_s + \delta_y p_s \tag{2.49}$$

$$P_C - P_D = \delta_x p_s - \delta_y p_s \tag{2.50}$$

Thus, if P_A is known, its diagonal counterpart P_C can immediately be given, and similarly for P_C and P_D (Fig. 2.2-b). Thus, using the above method, the set of pressure grid nodes is split into two independent subgroups; the Red and Black grids.

Two points are arbitrarily selected from both grids, and arbitrary values are then assigned to those points; zero for the present study. The grids are each scanned from left to right, bottom to top, and unknown points are assigned values from their corresponding diagonal partner, if it is known. For efficiency, the scanning order is reversed on alternate scans, i.e., right to left, top to bottom. For a simple rectangular grid with no islands, only one scan of each grid is required to set all points. If the domain has an arbitrary shape, or if islands are present, then more than one scan is required. The number of scans will depend on the number of islands and the level of "concavity" of all borders. This is closely tied to the polygon–crossing algorithm used in computer graphics. Generally, two or more scans of each of the Red and Black grids are required if islands are present. The scan number increases in proportion to the number of bays and to the complexity of bay shapes (i.e., bays within bays). Six scans where required to solve for all points of the world model grid. Once the two grids are evaluated they must be coupled in some way, since their two initial pressure values were arbitrary. This is achieved by independently setting the averages of the two grids to zero, and they then yield nearly equivalent pressure distributions. Small errors in $\delta_x p_s$ and $\delta_x p_s$ will cause the checker–boarding pattern commonly encountered in the stream function. The nine–point stream function operator yields much smaller errors in the pressure derivatives, but, unfortunately increases the noise level in stream function itself. Checker–boarding in p_s can be virtually eliminated by lightly smoothing the combined Red and Black grids with a five–point smoothing operator. Open ocean checker–board errors found in the world model are typically less than $1\,mb$ (*millibar*), before smoothing, and so are of no real concern. The errors can be larger along island coastlines, up to $10\,mb$ in some cases, but this does not affect the performance of the model (directly) since pressure is not a prognostic variable.

While this algorithm has been useful for the present study, it can hardly be regarded as a useful technique for solving the surface pressure problem, since it cannot be vectorized. It could possibly be parallelized by an adaptive method, using only nearest–neighbour communication, but convergence criteria have not been examined. The algorithm is, however, a direct method and a result is guaranteed after a fixed number of iterations.

Once p_s is known, the internal pressure field can easily be found from the hydrostatic relation (2.3). It is important to use the model's equation of state when doing this, since one is formulated for any particular vertical grid distribution. The JPOTS–82 (UNESCO, 1981) standard is used to construct the model equation of state, which is a simple third order polynomial fit at each depth layer. Only horizontal pressure gradients are calculated prognostically during the normal execution of the model, so that absolute errors in the vertical pressure distributions are of no great consequence (this is not true for σ–coordinate models).

2.7 Spin–up and Integration Methods

The integration method for the fixed and seasonally varying phases is the same as that used by Semtner & Chervin (1988, 1992), but with some minor differences. The relaxation time constants at the base of the pycnocline are the same as theirs, being 1100 days, but increase to 1900 days at abyssal depths. Bottom friction is used only during biharmonic mixing and has a coefficient of 10^{-3}. The first phase of the spin–up is nearly the same as that used for the FRAM model (Webb *et al.*, 1991), where the ocean is set to be cold (-2°C), saline ($36.69\,psu$) and motionless at $t = 0$. For the present model, the Standard Ocean is used: S=$35\,psu$ and T=0°C. Relaxation to the annually–averaged Levitus climatology is performed, using time constants of 35 days at the surface and 360 days at all other levels. Laplacian mixing is used for this phase, but not bottom friction. The annually–averaged wind stress (Hellerman & Rosenstein, 1983) is gradually switched on over a six month period, after the first year of integration.

To conserve machine time the climatological acceleration is 12:1 (α in §2.4) rather than Semtner & Chervin's 7:1, since several different bathymetries are concurrently tested. The deficiencies of using large accelerations, say 50:1, do not appear to be too much of a problem for the model. After four years of this heavy relaxation, i.e., four e–folding periods, the temperature and salinity fields are within about 1% of the Levitus data, and there is little point in continuing with it. The free–thermocline run is commenced at four years with relaxation present in the surface layer (35 days) and below $750\,m$ (1100 to 1900 days). The light relaxation phase of Semtner & Chervin (years 5 to 10) is bypassed and the free–thermocline phase is immediately commenced. The free–thermocline run is only seven years long but this is perhaps mitigated by the increased acceleration. In principle, the level of equilibrium achieved during this shorter period should not be too different from that achieved in Semtner & Chervin's runs, although both models are far from being equilibrated in the sense of abyssal thermohaline circulation. Only coarse resolution models are sufficiently inexpensive in machine time to allow runs of many centuries of model time, although this situation is likely to change in the near future with newer machine architectures. The thermocline tracer, velocity, pressure, and stream function fields are, however, in a quasi–equilibrium. The surface pressure equilibrates quite rapidly at the start of the free–thermocline run, or at least its rate of change quickly drops to a small value. The switch over to the biharmonic viscosity operator is performed in the last two years of the free–thermocline run. In hindsight, the entire run could have been performed with this viscosity formulation since it is only about 30% more expensive to use than the Laplacian operator, for a 1° grid.

After the free–thermocline run, the wind stress and surface tracers are seasonally varied, with updates being performed every 24 hours using smooth interpolations from the monthly climatology data. Snapshots of the dynamical fields are saved on the fifteenth day of each calendar month and more frequently for other information. Time stepping is now synchronous ($\alpha = 1$ and surface forcing synchronous with model's calendar), which is about seven times more expensive than the accelerated phases. Switching over to seasonally forced synchronous integration is as smooth as can be expected. The large Rossby wave activity generated in the North Pacific takes about 1.5 years to dissipate to realistic levels.

England's (1992) suggestions relating to winter surface salinities in the Southern Ocean have been implemented. The Levitus data tend to underestimate the winter increase of surface salinities, and the decrease of temperatures due to polynya formation, in the Ross and Weddell Seas. The winter increase of surface water density is thought to be responsible for large overturning and bottom water production. Pack ice formation increases salinity via salt rejection, while logistical difficulties mean that very few winter surveys have been made in these areas. England's model has winter salinities increased to 34.9 psu for Antarctic shelf waters and this leads to the development of an overturning cell which produces Antarctic Bottom Water. For the present model, Levitus surface salinities are increased in these two seas, during winter months, and the change is then imparted to the prognostic fields only by relaxation. Salinities are slowly increased to 34.9 psu during late April and early May, and are then slowly reduced to normal levels during September–October. The surface temperature is reduced by 1.5°C, in a similar fashion. The model's success has been marginal with respect to this; its Antarctic Bottom Water production rate is only 1.7 Sv (§5.4), but real production rates are estimated to be up to 41 Sv (Stuiver & Quay, 1983). A more heavy–handed method will be required to increase the bottom water production rate. The shelf areas of the Ross and Weddell Seas are excluded by the wall at 75°S, a factor which may partially explain the low production rate.

At this stage, only eight model years of the seasonally forced phase have been completed but it is unlikely that the major circulation patterns will change greatly beyond this. However, the relatively short integration time has probably not allowed some of the slower moving planetary waves to fully cross the South Pacific. All wave activities are distorted in the free–thermocline run because of the acceleration, and the switch–over to seasonal forcing causes a perturbation, which then decays on time scales of the Sverdrup balance—about ten years for the South Pacific at 25°S, and thirty–five years at 44°S.

Relaxation below the thermocline is performed to prevent the base eroding over time, and losing its distinctness from deeper waters. This preserves the celerities and group velocities of internal waves, but prevents the model from being used to examine deep ocean fluxes. For the purposes of this study the former was considered to be much more important, hence the use of deep relaxation. The time constants chosen for the deep relaxation are hopefully not so small as to greatly distort abyssal currents, but are sufficiently small to preserve the thermocline.

Chapter 3

New Guinea Coastal Undercurrent

3.1 Historical Background of Coral Sea Studies

Fig. 3.1 depicts the basic bathymetric configuration of the Coral Sea region, although a detailed bathymetric chart should preferably be consulted as well, since some important features are too complex to clearly show here. Early investigators often found large volume fluxes entering and leaving the Coral Sea but the presence of western boundary currents, other than the East Australian Current (EAC), appears not to have been considered. In the northern Coral Sea, Thompson & Veronis (1980) find a clockwise flow of $40{\times}10^6\,m^3s^{-1}$ (or 40 *Sverdrups*) that enters the region from the east at 15°S, and intensifies along the southern coast of Papua New Guinea (PNG). The spatial coarseness of their sampling stations would not have permitted the identification of a western boundary current, nor do they refer to it as such.

Scully-Power (1973) finds fluxes of up to $28\,Sv$ flowing northwards into the Solomon Sea during the Austral winter, and up to $37\,Sv$ flowing into the Coral Sea from the east. He notes, with respect to seasonal variability, that the only permanent feature is the cyclonic character of the broader flow regime. Andrews & Clegg (1989), in the most recent study, use an inverse technique to determine the flow field above $1000\,m$, and also for the entire water column[1]. Above $1000\,m$, they find $14\,Sv$ flowing northwards into the Solomon Sea and a Coral Sea inflow of $24\,Sv$, between the Solomons and Vanuatu. A cyclonic flow of up to $6\,Sv$ is

[1]Their Figs. 7 and 8 are reversed.

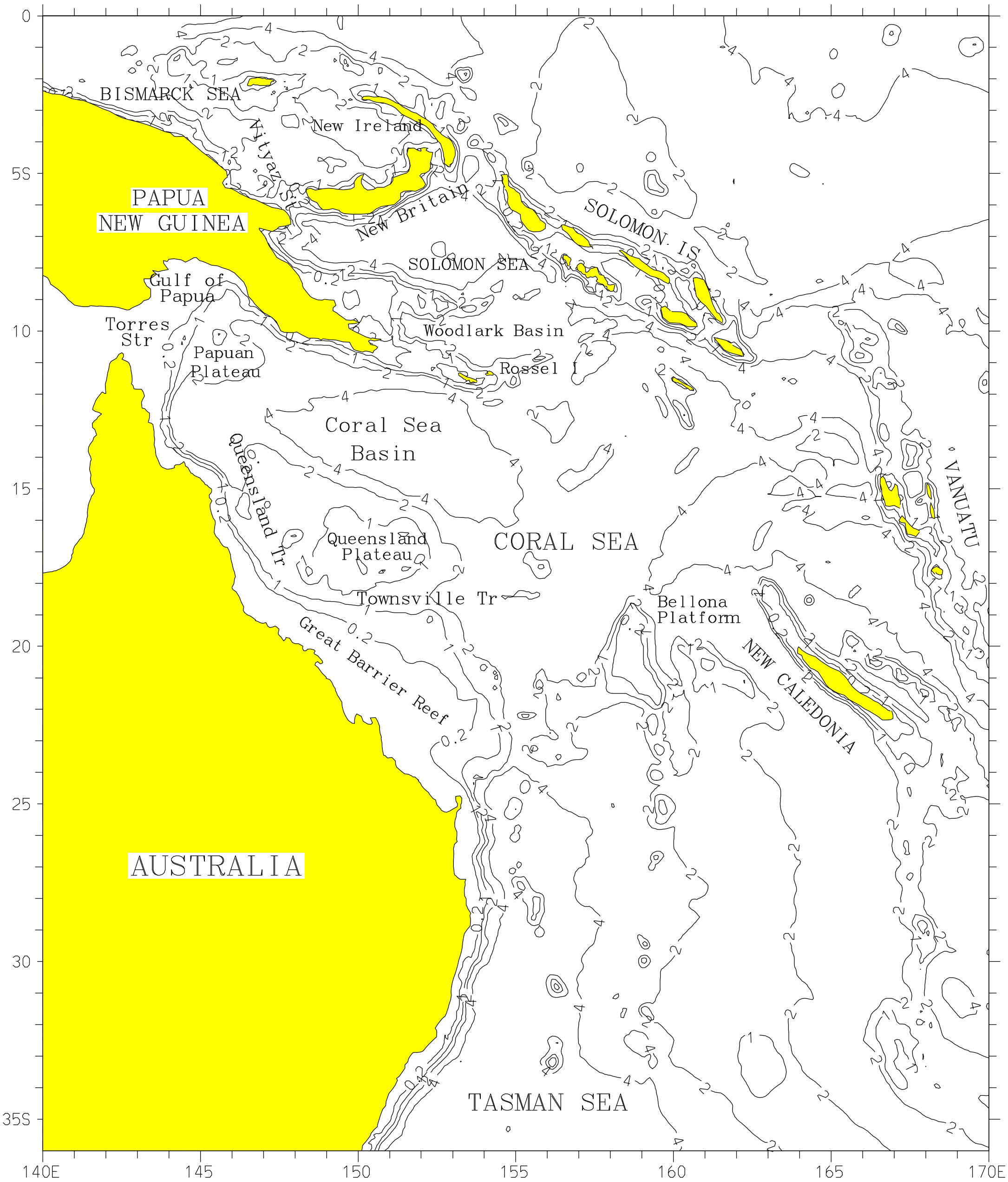

Figure 3.1: **:** Bathymetry (km) of the study area. A detailed bathymetric chart should also be consulted. Pocklington Reef lies 150 km ENE of Rossel Island. St. George's Channel lies between New Ireland and New Britain. Quoted sill depths have been obtained from SOPAC and GEBCO charts.

found in the northwestern Coral Sea. There is a substantial difference between their $0/1000\,m$ and total depth estimates, and the $1000\,m$ reference gives results more in accord with the results presented here. As noted by Thompson & Veronis (1980), inverse methods based on volume conservation can lead to very ill–posed problems; flux estimates for the entire water column can have errors larger than the estimates themselves.

The first comprehensive studies of this area were made by Rochford (1959, 1960a,b) and by Wyrtki (1960, 1961b, 1962a,b), although their analyses deal more with water properties and steric heights than specifically fluxes. Takahashi (1960) was the first to show direct evidence of a cyclonic (clockwise) flow in the northern Coral Sea. Donguy *et al.* (1970) give additional results for areas to the north and east of the Coral Sea. Pickard *et al.* (1977) review, in great detail, the findings of all investigations prior to 1977. Combining the three most influential studies of the area (Scully-Power, Thompson & Veronis and Andrews & Clegg) gives an overall consensus of a clockwise circulation in the northern Coral Sea, that is fed by an inflow between New Caledonia and the Solomons, and outflows into the Solomon Sea. A link between the Coral Sea and the Equatorial Undercurrent was clearly demonstrated by Tsuchiya (1968, 1981), by examining subsurface salinities. More recent investigations (Tsuchiya *et al.*, 1989; Lindstrom *et al.*, 1990; Godfrey *et al.*, 1993) reconfirm this, indicating that the Coral Sea gyre is part of a much wider flow regime. The exact route that the Coral Sea outflow takes through the islands that comprise Papua New Guinea and the Solomons is still unclear, as is the flow regime further to the north.

Ridgway & Godfrey (in preparation) analyse long–term historical data for the EAC and estimate its annually–averaged flux to be less than $10\,Sv$; this is the Sverdrup component (wind–driven) which they define to be the nett southwards flow across the 30°S parallel, between the Australian coast and 170°E. This is the only other known outlet for large fluxes impinging on the Australian east coast, and so it is reasonable to assume that the bulk of the Coral Sea's outflow is to the north. Scully-Power finds very little southward flux across 20°S except for the EAC. Fluxes ranging up to $40\,Sv$ are observed in the Coral Sea, so it is tempting to postulate the formation of western boundary currents, north of 20°S, using the classical ideas of open ocean gyres being closed by such currents. The WEPOCS expedition (Lindstrom *et al.*, 1987) found an intense westwards flow, about $8\,Sv$, through the narrow Vityaz Strait which they postulate to be a western boundary current. Recently analysed current meter observations suggest that the fairly steady throughflow is between $14\,Sv$, and $20\,Sv$, westwards (E. Lindstrom, private communication). Several other investigations have already demonstrated that strong flows exist along the southeast coast of New Britain (Godfrey *et al.*, 1989) and westwards through St. George's Channel (Butt & Lindstrom, 1993; Lindstrom *et al.*, 1990), between New Britain and New Ireland. The WEPOCS investigators named the Vityaz throughflow the New Guinea Coastal Undercurrent (NGCU) and that convention will be retained in this work for the strong cyclonic current found in the Coral Sea, under the presumption that it is closely related to the Vityaz throughflow. Further recent reports also consider flows in the Solomon and Bismarck Seas in terms of western boundary current dynamics (Godfrey *et al.*, 1989; Godfrey *et al.*, 1993; Lindstrom *et al.*, 1990), although these studies have focused on areas immediately to the north of the study area.

The modest data set of the Coral Sea that has accumulated over the last three decades is still inadequate to resolve many features of the Coral Sea, notably the seasonal variations. Numerical models of ocean circulation may provide an alternative means of bridging gaps in this knowledge and could allow costly field measurements to be planned in order to maximize information recovery. Modelling has definite advantages for areas close to the equator where thermal wind analysis becomes progressively more error prone. Conductivity-Temperature-Depth (CTD) instruments are sufficiently accurate, in principle, to give fair geostrophic flux estimates only 1° away from the equator. However, here the inertial period is $\sim$10 days and the general circulation can respond very rapidly to changes in the wind stress. Therefore, the ageostrophic component may form a substantial part of the total flow for some of the time. For example, an equatorial Rossby wave with a local circulation of $10\,Sv$ could travel up to $1000\,km$ in 10 days. This is even more problematic when the Rossby wave interacts with the Solomon Islands or the north coast of PNG to possibly yield hybrid Rossby-Kelvin modes. Thus, substantial nonlinearities are possible in the northern waters of PNG and the Solomons. These fast moving internal equatorial waves also make it difficult to obtain truly synoptic density data over large areas. There exists an opportunity for numerical models to move ahead of empirical knowledge, in contrast to the northern hemisphere oceans, where much was known about the general circulation features before numerical models achieved widespread use.

Fine–scale world domain ocean general circulation models often show westward intensification around the coast of Papua New Guinea, with strong western boundary currents moving westwards towards Indonesia. The source waters are the westwards flowing South Equatorial Current (SEC). For example, the global model of Semtner & Chervin (1992) shows a western boundary current of about $45\,Sv$ near the Louisiade Archipelago (Rossel I. in Fig. 3.1) although some of this is due to inertial recirculation. The present general circulation model shows the annually–averaged northwards flow between Rossel I. and the Solomons to be $19.9\,Sv$. This study provides observational confirmation of westwards intensification around the PNG area, that is commonly found in ocean general circulation models.

The analysis presented in this chapter uses data gathered from four surveys over a period of five years; from the Australian *R.V. Franklin* during July 1988, July 1990, and September 1991 (Fr0588, Fr0690 and Fr0791, respectively), and from the U.S. *R.V. Oceanographer* over July 1987 (TEW287 and TEW387: Mangum *et al.*, 1991). Cruises TEW2/387 and Fr0791 were made during ENSO years, and Fr0791 is the only one not in the midst of winter; the data are thus seasonally biased. In this chapter, it is confirmed that the cyclonic flow along the north coast of Australia and south coast of PNG is indeed a western boundary current, with dynamics that characterize such flows. It is shown that the scaling width is typically $70\,km$ and that the current axis undergoes substantial inertial meanders away from the shelf break, to distances of at least $160\,km$, and then re-attaches. The present measurements of the NGCU's volume flux, in the 0 to $1500\,m$ range, around the Gulf of Papua and Rossel I., vary from $17\,Sv$ to $33Sv$. Using a subset of very deep casts it is anticipated that flux estimates will not be greatly altered by including the deeper flows, at least not in the Solomon Sea.

3.2 Analysis Methods and Assumptions

The most important parameter needed for deducing volume fluxes from thermal wind analysis is the estimate of the correct offset velocity for the vertical profile. Since fluxes will be examined down to $1500\,m$ (§3.3), a nominal accuracy of $\pm 1\,cm\,s^{-1}$ is desired for the offset velocity. Fr0791 provides the most accurate and complete ADCP set of the cruises, but the calibration uncertainty is not less than $\pm 4\,cm\,s^{-1}$ and so these data cannot be used for determining offsets, as is usual. If ADCP measurements were sufficiently accurate they could be used for this purpose, averaged across station pairs, although only data below the Ekman layer or even the mixed layer should be used. An examination of the ADCP velocities in Fig. 3.24, compiled mainly from Fr0791 around 24°S:156°E, shows that the relative vorticity at a depth of $150\,m$ is up to 20% of the local planetary vorticity in an area extending up to $500\,km$ seawards from the Australian coast. Here, sharp thermal fronts that correspond to changes in direction of ADCP velocities are evident, so that the ADCP data are unlikely to be spurious. Total variations in temperature are only about 1.5°C but occur over $\sim 30\,km$, giving large density gradients. This intriguing, if not alarming observation, clearly demonstrates that thermal wind analysis should be used with caution in the northern limits of the Tasman Sea. In the analysis, ADCP data have merely been compared with thermal wind profiles. Some 1000 *decibar* (*db*) casts were made several hundred kilometres offshore in the southern region (not shown) and there is barely agreement in normal directions, and magnitudes between ADCP and thermal wind estimates.

The synoptic wind stress during the four cruises was predominantly from the southeast and thus the surface Ekman flux was presumably directed towards the southwest, causing a divergence along the southern coast of PNG and a convergence along the Australian coast. From simple theory the total Ekman flux southwest across the Coral Sea would have been approximately 2 to $4\,Sv$. The ageostrophic flux in the model's surface layer ($27\,m$ thick) is $1.7\,Sv$ (annual mean) towards the southwest. Whilst the Ekman flux is not insignificant it is considerably smaller than the total fluxes measured.

$CTDO_2$ units for all cruises were Neil Brown Instruments–Mark 3 types. The calibration errors for *R.V. Franklin* salinities are $0.0026\,psu$. O_2 measurement errors are $\pm 0.06\,ml\,l^{-1}$ in the 0 to $750\,db$ range and $\pm 0.04\,ml\,l^{-1}$ below that depth. The O_2 uncertainties for Fr0791 are about $\pm 0.1\,ml\,l^{-1}$ due to sensor degradation.

Assuming that errors in temperature and salinity measurements are coherent in such a way so as to maximize the resulting flux error for station pairs, the flux error is $\pm 0.3\,Sv$ in the 0 to $700 db$ range and $\pm 0.2\,Sv$ in the 700 to $1500 db$ range, at 15°S. Thus, the purely instrumental error between 0 and $1500\,db$ is $\pm 0.5\,Sv$, but the errors are unlikely to be coherent in this way and actual errors will be somewhat smaller. The *R.V. Oceanographer* data errors (similar to Fr0791) are given by Mangum *et al.* (1991) and Taft *et al.* (1991).

The instrumental error is independent of the transect length provided that the Coriolis parameter (f) is constant, but otherwise it is inversely proportional to f. In principle, total flux estimates are more accurate if only the two end CTD casts of a transect are used but this assumes that f does not vary significantly and that there is no intervening bathymetry. However, the flux estimate will be quite wrong if one or both of the end stations are spurious, so that various combinations of station pairs should be experimented with, utilizing all the data. If the reference velocities/offsets are known for each adjacent pair, they can be averaged over the various combinations. Many of the transects presented here have too large a variation in f for accurate end–point estimates, using the end–points shown in the figures, so subsets are used in the analysis. The flux differences between the sum of pairwise estimates and other combinations are found to be of no consequence, well away from shallow water and shelf breaks. None of the stations involved more than one CTD cast, so repeatability and short–term dynamic height variability are not known.

A through–hull intake of water, $4\,m$ below the surface, is continuously monitored by the thermosalinograph instrument. Its temperature and salinity accuracies are no better than $\pm 0.02°$C and $\pm 0.02\,psu$, respectively. While this is rather crude, its big advantage is that the measurements are continuous. Sharp thermal and salinity fronts are easily recorded, as will be seen later, whereas such fronts will normally be missed by CTD methods.

Bindoff & Wunsch (1992) provide long–term averaged T, S, O_2 and nutrient data on a regular grid for the South Pacific (SPAC data) and this will be used to determine the open ocean sources of water masses within the study area. The grid consists of 3° squares in the horizontal and thirty–eight depth layers. Although the horizontal resolution is inferior to the Levitus data (1982), for T and S, the vertical resolution is better and error estimates are provided. Any such data set, compiled at fixed depths, must be used with caution in the vicinity of western boundary currents. Their horizontal smoothing of data coupled with the large and variable deflections of isopycnal surfaces, in these regions, can be problematic. SPAC errors for nutrient data are too large to be used to successfully identify

Coral Sea source waters, i.e., to identify the latitude of origin with sufficient accuracy. All of the nutrient data fit within the SPAC error bounds so there are no serious discrepancies. Figs. 3.2 and 3.3 show the Fr0791 property distributions of PO_4 and SiO_2, respectively, against O_2. SPAC data along 175°E are overlaid as lines. All Fr0791 data shown are from the area bounded by 20°S, 158°E and the Australian and PNG coasts. The depth range is 0 to 2000 , and the two nutrients are plotted against O_2 since it has the largest meridional gradient of any tracer, in this region. These two nutrient property plots are given for completeness only, and are not considered further.

SPAC O_2 data are sufficiently good to identify the open Pacific origin latitude of a single Coral Sea cast to within 5°. In fact, O_2 is perhaps the most useful tracer since its meridional gradient is large ($0.6\,ml\,l^{-1}$ per 10°) in the western South Pacific thermocline. PO_4 could be useful if the SPAC errors were smaller, but SPAC's local SiO_2 distribution does not appear to form an ordered pattern.

3.3 Determining a Significant Reference Pressure

Leaving aside intraseasonal variations (if one considers this to be a source of error), the largest source of error in estimating volume flux arises from assumptions about the velocity at the reference pressure. In the absence of any other information, it is customary to choose a sufficiently deep pressure and then to assume that the velocity is zero there (i.e., a level of no–motion). If transects form closed polygons with each other or with flow barriers (i.e., land) the nett influx should be much smaller than the individual flows across the borders, but in principle it need not be zero because of Ekman pumping and other ageostrophic effects. The residual is useful for gaining an idea of the flux errors generally caused by incorrect assumptions about the reference velocity and, to a lesser extent, ageostrophic effects and instrumental errors. While this is not 'fool–proof' it is perhaps the only way of estimating the flux errors for the data of a single expedition, unless reference velocities can be measured via an independent method (e.g., Fieux *et al.*, 1993).

Some information about flow directions can be obtained from contours of

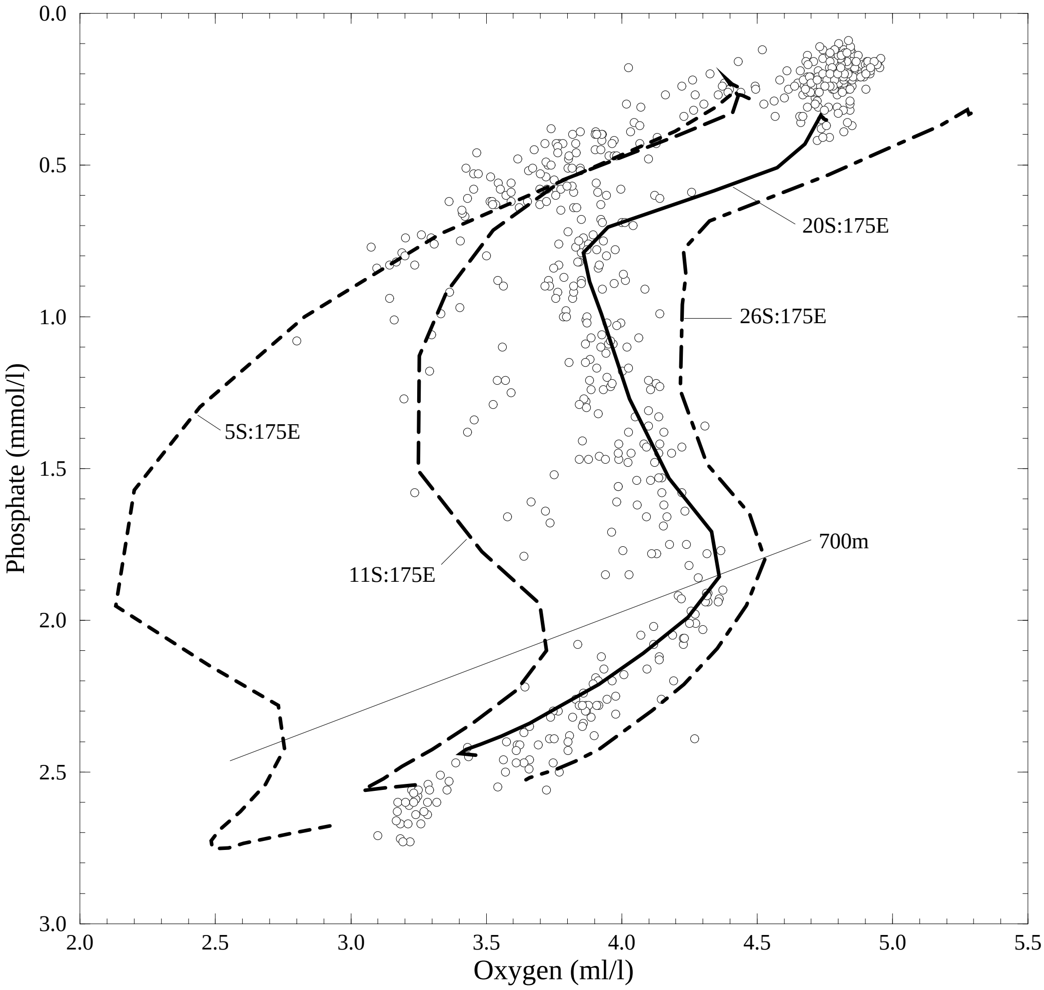

Figure 3.2: : PO_4 vs O_2 for Fr0791. Data are from the area bounded by 20°S, 158°E and the Australian and PNG coasts. The depth range is 0–2000 m; the indicated 700 m depth is approximate. Lines are SPAC data along 175°E. SPAC PO_4 errors are $\pm 0.7 \mu\, mol\, l^{-1}$ above 700 m.

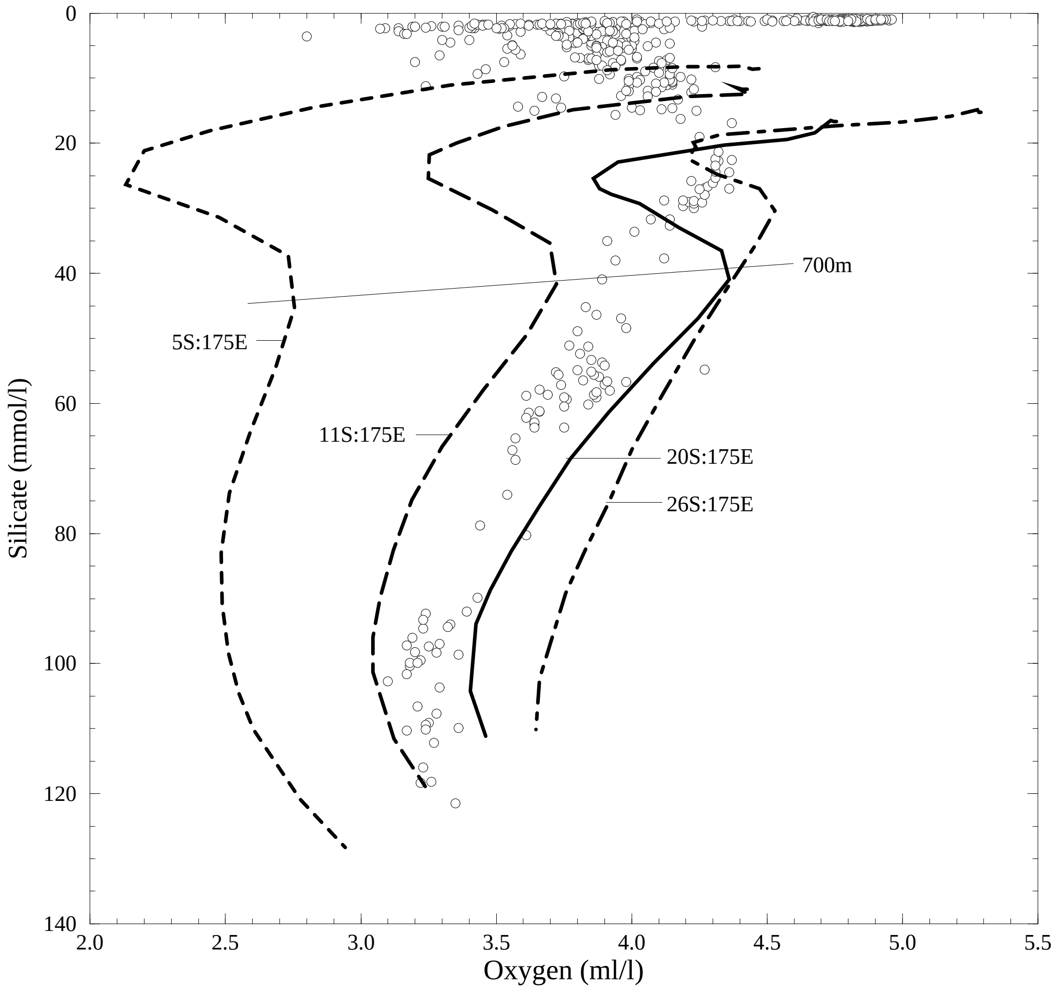

Figure 3.3: **:** SiO_2 vs O_2 for Fr0791. Data are from the area bounded by 20°S, 158°E and the Australian and PNG coasts. The depth range is 0–2000 m; the indicated 700 m depth is approximate. Lines are SPAC data along 175°E. SPAC SiO_2 errors are $\pm 10 \mu\, mol\, l^{-1}$ above 700 m.

tracer distributions, in the vertical. Fig. 3.4 shows the distribution of O_2 from TEW287 across the Coral Sea Basin from Rossel I. to the Queensland Plateau; the transect and station positions are available in Fig. 3.13, and the view is from the southeast. The transects do not form a perfectly straight line but this is not a severe problem. The reversal of isopycnal gradients at about 1600 m is clearly evident at the walls of the basin with the implication that the upper flow is cyclonic and the deeper flow is anticyclonic. Contours of T, S, Θ and σ_θ are quite similar, as are plots for the other three cruises. Thus there is motivation for using 1600 m as a level of no–motion. Of course, these tracer distributions alone cannot determine a unique flow field but merely the vertical shear. The TEW surveys are particularly useful since they consist entirely of bottom casts and there is an opportunity to test the assertion that 1600 m is a true level of no–motion.

Fig. 3.5 shows isotachs of thermal wind velocities based on the paired stations of Fig. 3.4. Five pairs of CTD stations had cast depths well below the sill depth of the Coral Sea basin, and it was assumed velocities below these depths are small. The thermal wind shears are a good deal smaller below the sill. The two deepest pairs were assumed to have zero velocity at the bottom and the offsets for shallower pairs were successively extrapolated towards the walls of the basin. Performing this shelf correction did moderately reduce the flux residuals below the sill depth. There is no obvious separation of flow regimes in the vertical, as is seen in the tracer plots. A strong eastwards flow along the shelf, that extends down to 2000 m is evident near Rossel I (0 km position on the distance axis). A westwards flow, at the 150 km position is evident down to 3500 m. At 420 km there is a strong westwards flow that is confined above 1000 m and below is a strong eastwards flow with a central axis at 1800 m. Thus, flow below 1500 m has a nett anticyclonic character around the Coral Sea Basin. Fig. 3.6 shows isotachs derived from Fr0690 data across the basin, looking from the east; the transect is the eastern side of B_{90} in Fig. 3.17. Again, a strong cyclonic circulation is found above 1000 m, and the flow is anticyclonic below that depth. The depth of reversal is 1000 m at the northern wall and 1200 m at the southern wall. Between 1500 m and 3800 m the anticyclonic flux amounts to about 4 Sv. Thus, at least along the sides of the basin, the flow regimes are not inconsistent with the tracer distributions. Since the distances between major flow directions are typically not

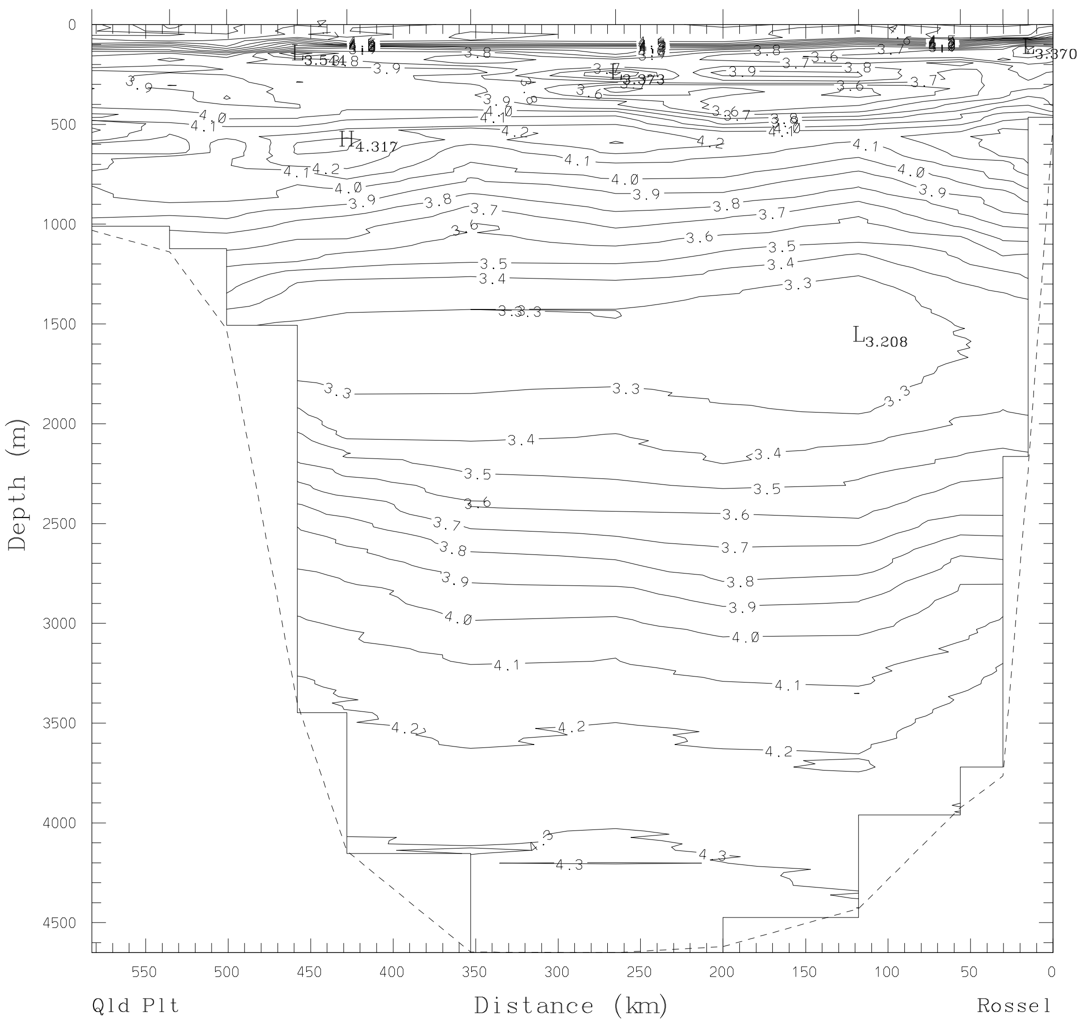

Figure 3.4: **:** O_2 distribution across the Coral Sea Basin for TEW287, looking from the southeast. The baseline (transect lines) is the northern transects of A_{87} in Fig. 3.13. Distance (km) is along the cruise track. $0\,km$ is at the Rossel I. shelf and $580\,km$ is at the Queensland Plateau. Contour interval is $0.1\,ml\,l^{-1}$. The dotted line is the bottom depth. Ticks across the top border denote CTD stations.

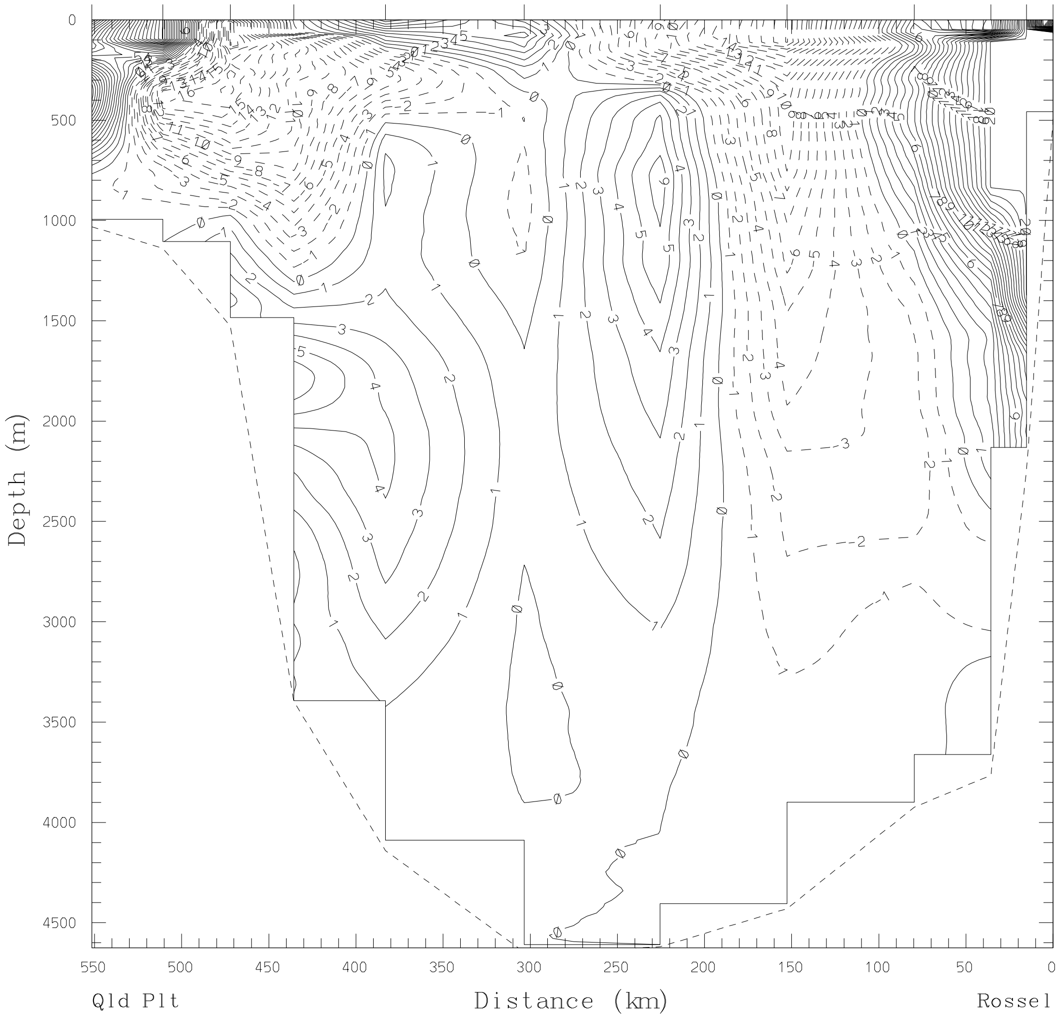

Figure 3.5: **:** Isotachs of thermal wind from TEW287 across the Coral Sea Basin looking from the southeast. Baseline is the northern transects of A_{87} in Fig. 3.13. Positive (solid) lines imply eastwards flow, i.e., out of the page. CI is $1\,cm\,s^{-1}$. Isotachs are clamped at $20\,cm\,s^{-1}$ for clarity. The depth of a contoured isotach column is the minimum depth across three consecutive stations. Ticks across the top border denote mid–points of station pairs. See Fig. 3.4 caption for other details.

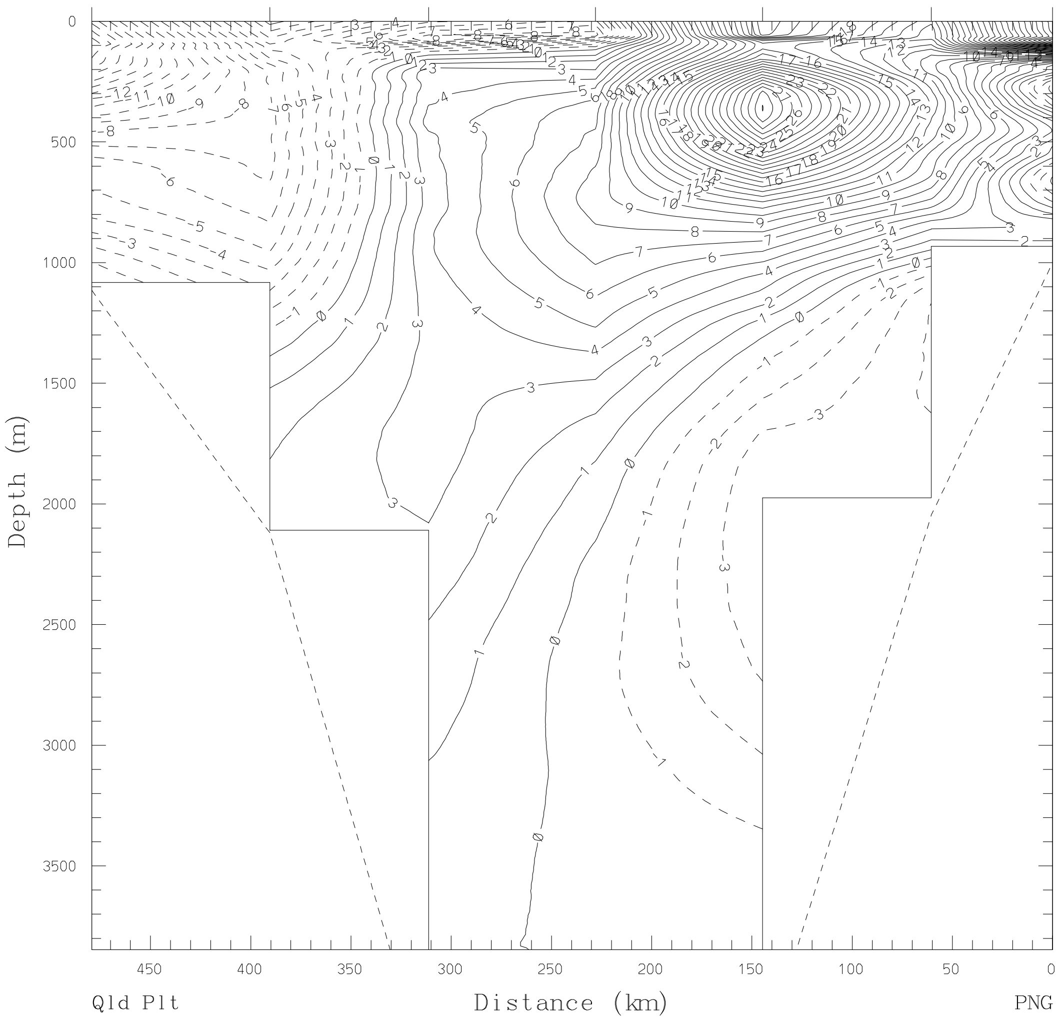

Figure 3.6: **:** Isotachs of thermal wind from Fr0690 across the Coral Sea Basin looking from the east. Baseline is the eastern side of B_{90} in Fig. 3.17. Positive (solid) lines imply eastwards flow, i.e., out of the page. Contour interval (CI) is $1\,cm\,s^{-1}$. The SEC is showning signs of western intensification along the northern edge of the Queensland Plateau. See Figs. 3.4 and 3.5 captions for other details.

much larger than 100 km, nonlinearities and inertial recirculations must be kept in mind. Setting all the bottom velocity offsets to zero does not greatly alter Fig. 3.5 but would certainly have a major impact on volume flux distributions.

Fig. 3.7 shows isotachs across the Solomon Sea derived from TEW387, and Fig. 3.13 shows the transect and station positions. There does not appear to be any depth which is useful as a level of no–motion and flows are correlated over the entire depth range. A very strong southwards flow is evident at the 180 km position with the central axis at 2200 m. Corresponding contours of tracer distributions do not show an obvious reversal of gradients at 1600 m as is seen in the Coral Sea. Isotach plots south of 22°S and close to the Australian coast show the EAC flowing southwards between the surface and 2000 m, while the deeper flow is northwards (see A_{91} in Fig. 3.23). This shows the same characteristic as the Coral Sea Basin, and is perhaps the reason why the basin's deeper flow is anticyclonic.

Since most of the field data are from the Coral Sea, rather than the Solomon Sea, 1500 db is chosen as the reference pressure and the flow regime above it is be analysed. Wherever possible the reference velocity is determined from casts deeper than 2800 db. However, extrapolations and interpolations of the reference velocity are not used over distances of more than 100 km or where there is intervening bathymetry. Casts over the Queensland Plateau and across the Queensland Trough are shallower than 1500 db and there is no other option but to assume that the bottom velocity is zero. Whilst the above analysis is a little more complicated than normal, it should provide better flux estimates than simply assuming 1500 m to be a true level of no–motion. Many of the available Fr0791 CTD casts are only to 1500 db, but are interspersed with much deeper casts so that reasonable estimates can be made for V_{1500}, i.e., the reference velocity at 1500 db.

3.4 Water Properties

As noted by Pickard *et al.* (1977) there is no significant local production of water types in the Coral and Solomon Seas (at least not between the base of the mixed layer and 1500 m). Wyrtki (1961b) finds the bottoms of the Coral and Solomon Sea basins to be occupied by water readily identifiable as originating from the

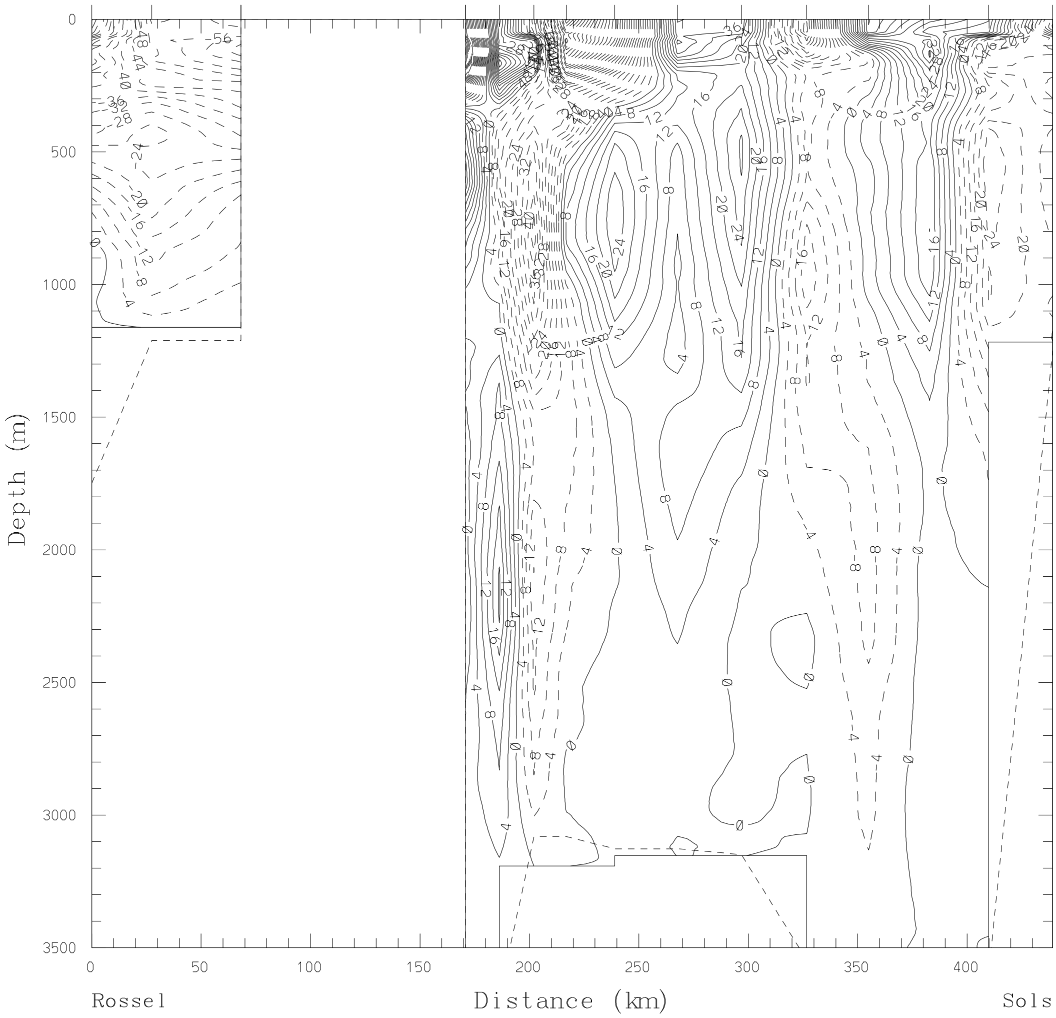

Figure 3.7: **:** Isotachs of thermal wind from TEW387 across the Solomon Sea looking from the south. Baseline is B–C_{87} in Fig. 3.13. $0\,km$ is at Rossel I. and $440\,km$ is at New Georgia, in the Solomons. The zero depth at $120\,km$ is Pocklington Reef. Positive (solid) lines imply southwards flow, i.e., out of the page. CI is $4\,cm\,s^{-1}$. See Figs. 3.4 and 3.5 captions for other details.

southern limits of the Tasman Sea, and the Θ–S properties of the present data lead to the same conclusion (Chapter 4). The Tasman Sea source water originates from depths between $2000\,m$ and $2700\,m$, and sinks to more than $4600\,m$ in the Coral Sea Basin. In ascending from the bottom of the basin, the properties change to those of the low latitude South Pacific at roughly $1700\,m$, with the interposed water a mixture of the two types. TEW387 data for the Solomon Sea Basin also show Tasman Sea influences, but these are slightly weaker. Since the present analysis is confined above $1500\,m$ there is no need to be concerned with localized production and only the open ocean sources need to be identified.

Fig. 3.8 shows a scattergram T–S distribution of the relevant TEW2/387 data between the surface and $2000\,db$. The domain is from 18°S to 11°S, between the Australian coast and the Solomons. Profiles from the SPAC data have been overlaid; these are taken at various latitudes along the 175°E meridian. The $700\,m$ depth of the SPAC data set is also shown, lying close to the Antarctic Intermediate Water (AAIW) core layer (S–min, O_2–max). The data show these two cores to have a typical vertical separation of 40 to $120\,m$ with the S–min being deeper. At about 600 to $800\,m$, some Solomon Sea salinities show a minor discrepancy with the SPAC data, by being a little higher, but corresponding salinities in the Coral Sea do not. Likewise, the peak value of the O_2–max core is a little lower in the Solomon Sea. Reductions in the strengths of these tracer cores may be due to turbulent mixing as the current abruptly changes direction near Rossel I. Another possibility is that the eroded cores are from a different, but not too distant, source. Examination of SPAC's salinity distribution shows that this particular source is likely situated within a few degrees of the equator, immediately to the northeast of the Solomons. Salinities at the upper salinity maximum (90 to $150\,m$) of Subtropical Lower Water (SLW) show a broader spread than the SPAC data and the mixed layer temperatures are a little lower. This is probably due to winter conditions and perhaps to the 1987 ENSO event, as noted by Bindoff & Wunsch (1992) in their analysis of the TEW data. Other than these two minor discrepancies the TEW data obviously fit within the latitude bounds of 23°S and 14°S, along the 175°E meridian. Other latitudes along 175°E show more distinctive differences from the TEW data.

Fig. 3.9 shows a scattergram of T–O_2 from 0 to $2000\,db$, using the same TEW casts of Fig. 3.8. For any given T, O_2 generally decreases, in proceeding from

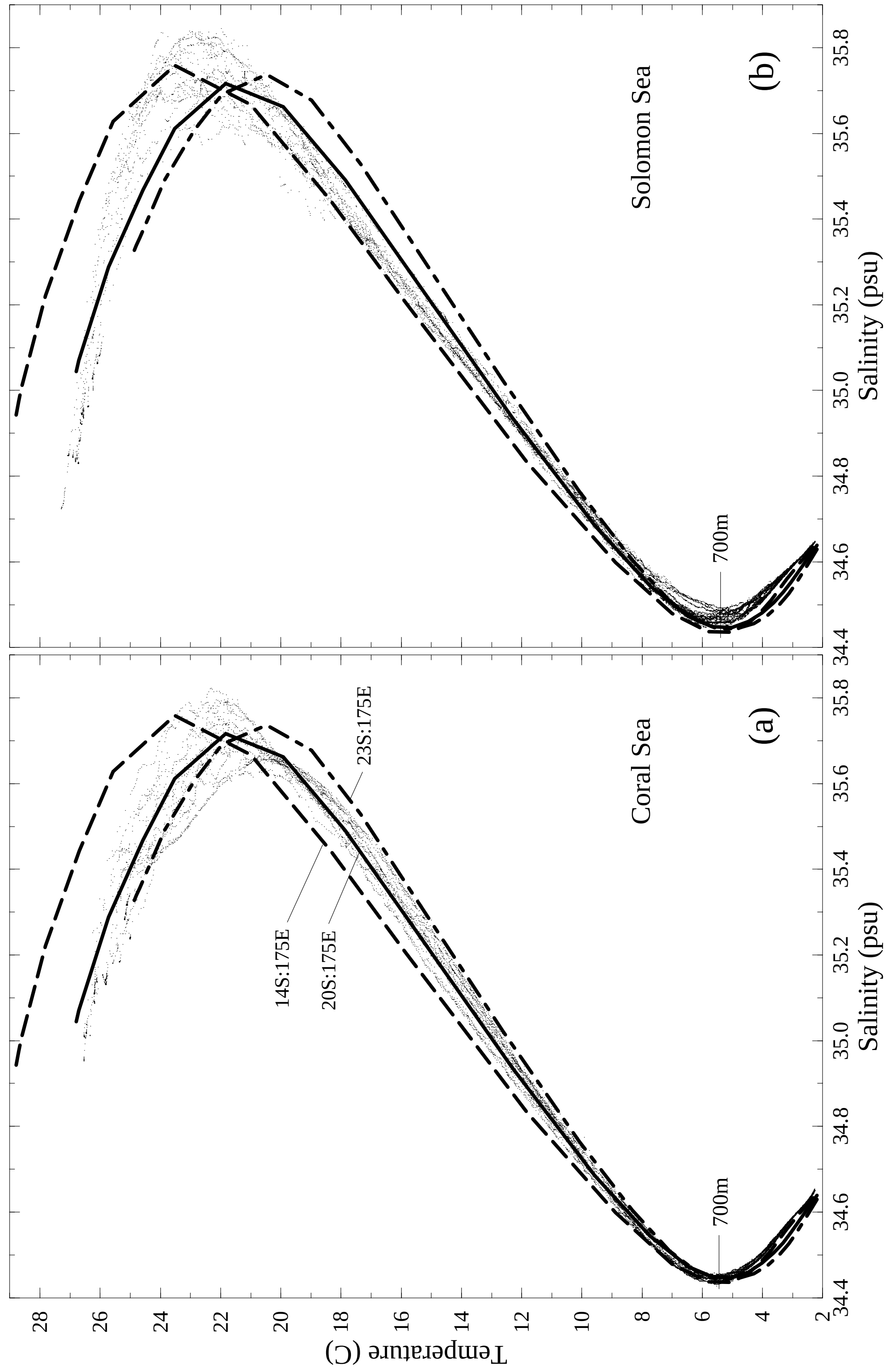

Figure 3.8: **:** [rotated] T–S scattergram of TEW2/387 data for (a) the Coral Sea, and (b) the Solomon Sea. Range is from the surface to a maximum of 2000 *db*. SPAC data for various latitudes along 175°E are overlaid.

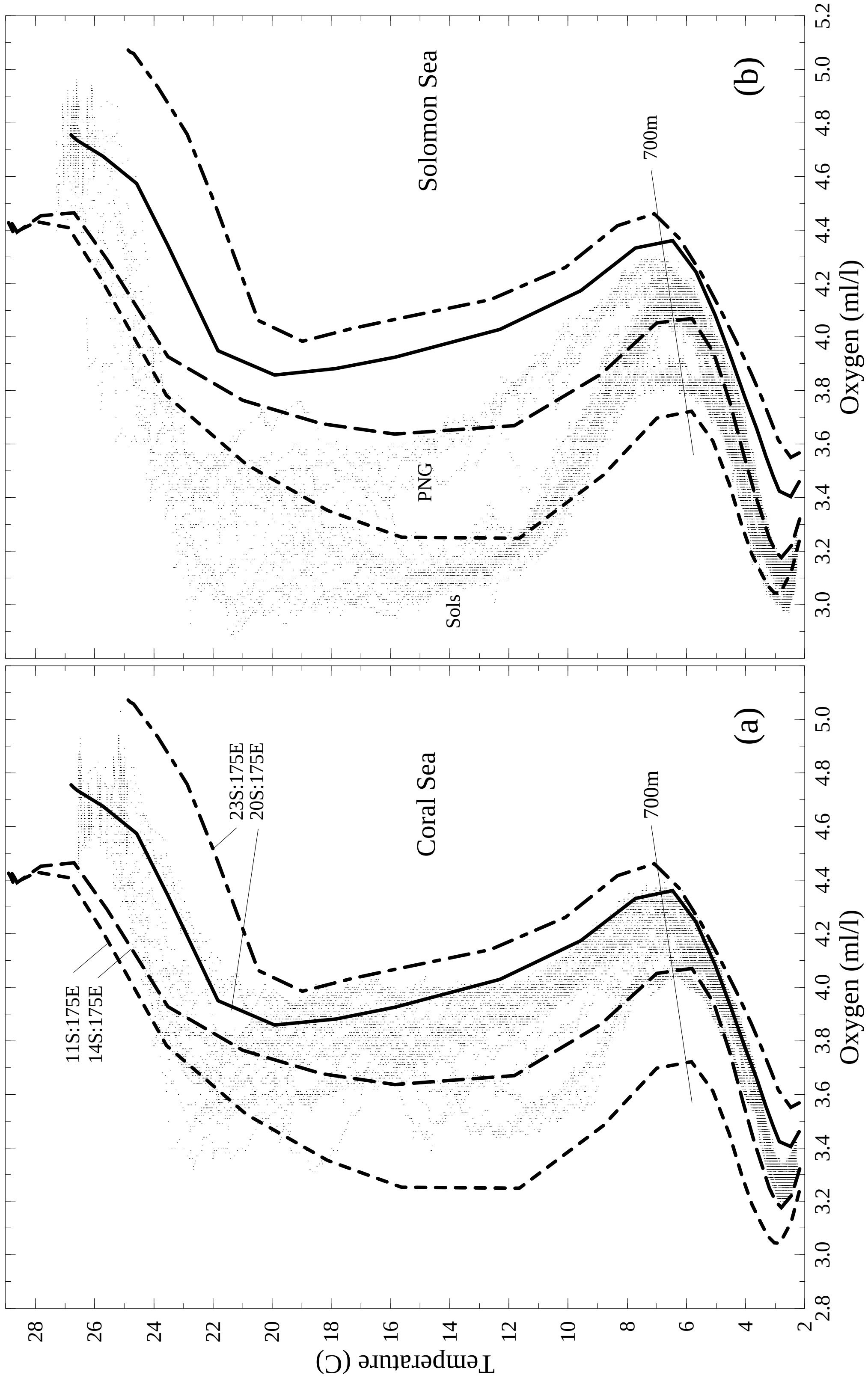

Figure 3.9: **:** [rotated] Same as Fig. 3.8 but shows corresponding T–O_2 relations.

the Australian coast to the Solomons, with the total variation being typically $0.8\,ml\,l^{-1}$. Along 175°E, SPAC O_2 has a large meridional gradient in the thermocline with higher values lying polewards; horizontal contours show that the isopleths are nearly zonal. The SPAC meridional gradient is comparable with the zonal gradients found across the Coral and Solomon Seas. Many of the O_2 values in the 12 to 24°C range are lower than the SPAC data at 11°S:175°E, possibly indicating a source within about 5° of the equator. These lower O_2 values are confined to the eastern side of the Solomon Sea (see graph annotation), and the salinities are not inconsistent with a near equatorial source. It must be kept in mind that these types of tracer relations give no indication of the volume fluxes involved.

Fig. 3.10 shows scattergrams of T–S and T–O_2, from 0 to $2000\,db$, of Fr0690 data. The domain is from 20°S to PNG, and from the Australian coast to 155°E. T–S values are consistent with an SEC source between 14°S and 23°S. Mixed layer salinities are lower than the SPAC data but within typically observed variances (Pickard *et al.*, 1977). T–O_2 profiles give an SEC source between 11°S and 20°S. Some lower than expected O_2 values are found within the SLW, as is seen in the TEW results for the Solomon Sea. Fig. 3.11 shows the same plots for Fr0791 data; there are no large differences with Fr0690.

The pattern that emerges from property–property analysis is that the meridional gradients which exist along 175°E are largely replicated as zonal gradients across the Coral and Solomon Seas. The clear implication of this is that much of the westwards flowing SEC, along ~17°S, turns northwards into the Solomon Sea when the land barrier of Australia–PNG is encountered. Some near equatorial source waters are also found in the study area and this will be discussed in the modelling section.

Fig. 3.12 shows the Thermosalinograph record of surface temperature and salinity along transect D_{91} (Fig. 3.23). There is a 1.5°C increase in temperature and a corresponding $0.35\,psu$ drop in salinity at 17.5°S. While this area is close to the EAC, the indicated latitude and the general westwards flow suggest a connection with New Caledonia. Much of the SEC must deviate around New Caledonia, presumably around the northern end of the island. New Caledonia has a large reefal complex at its northern tip, Récifs D'Entrecasteaux, so that the northern limit of the continental shelf is at 17.83°S. The southern limit of

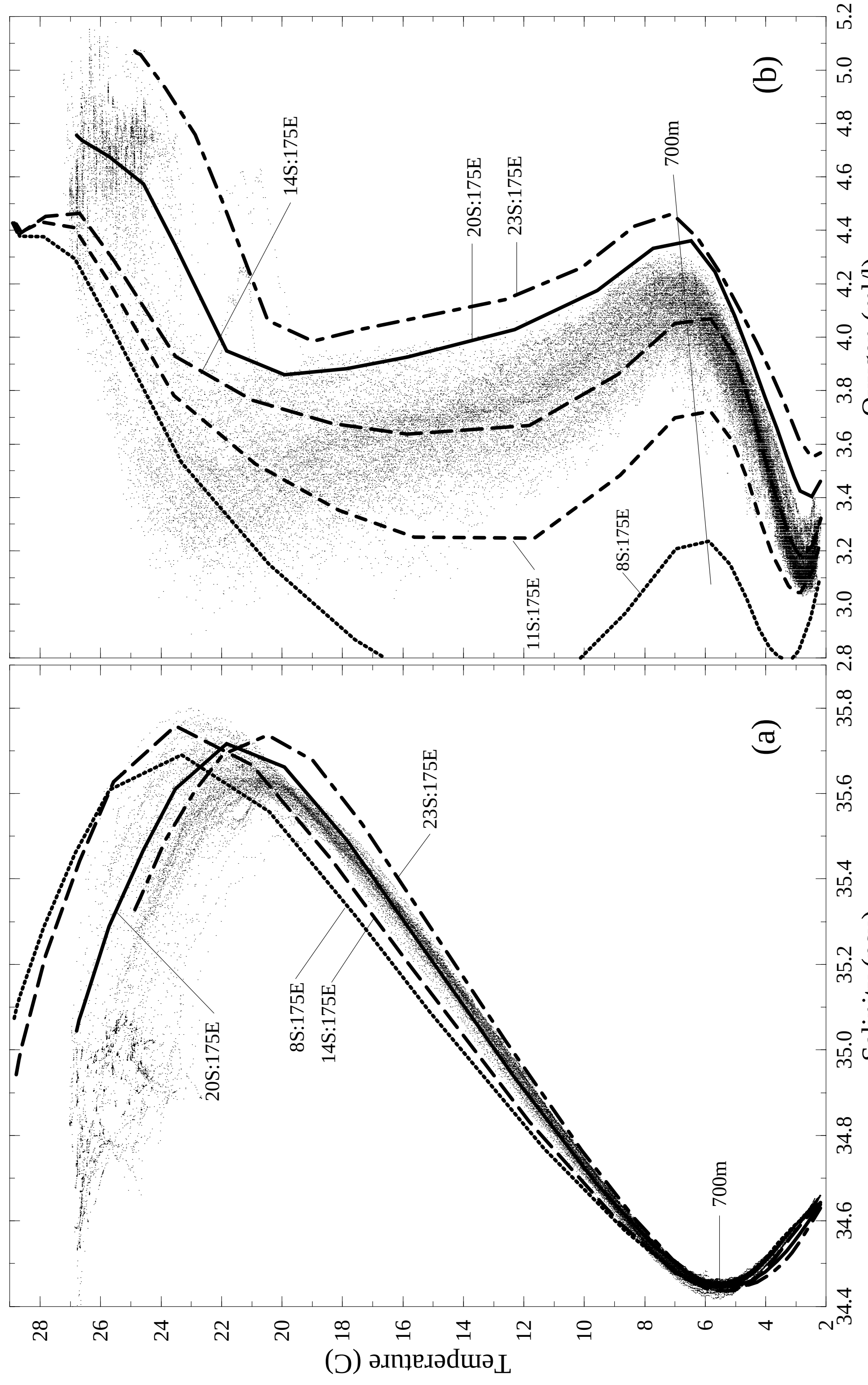

Figure 3.10: **:** [rotated] (a) T–S and (b) T–O_2 scattergrams of Fr0690 data north of 20°S in the Coral Sea. Range is from the surface to a maximum of 2000 *db*. SPAC data for various latitudes along 175°E are overlaid.

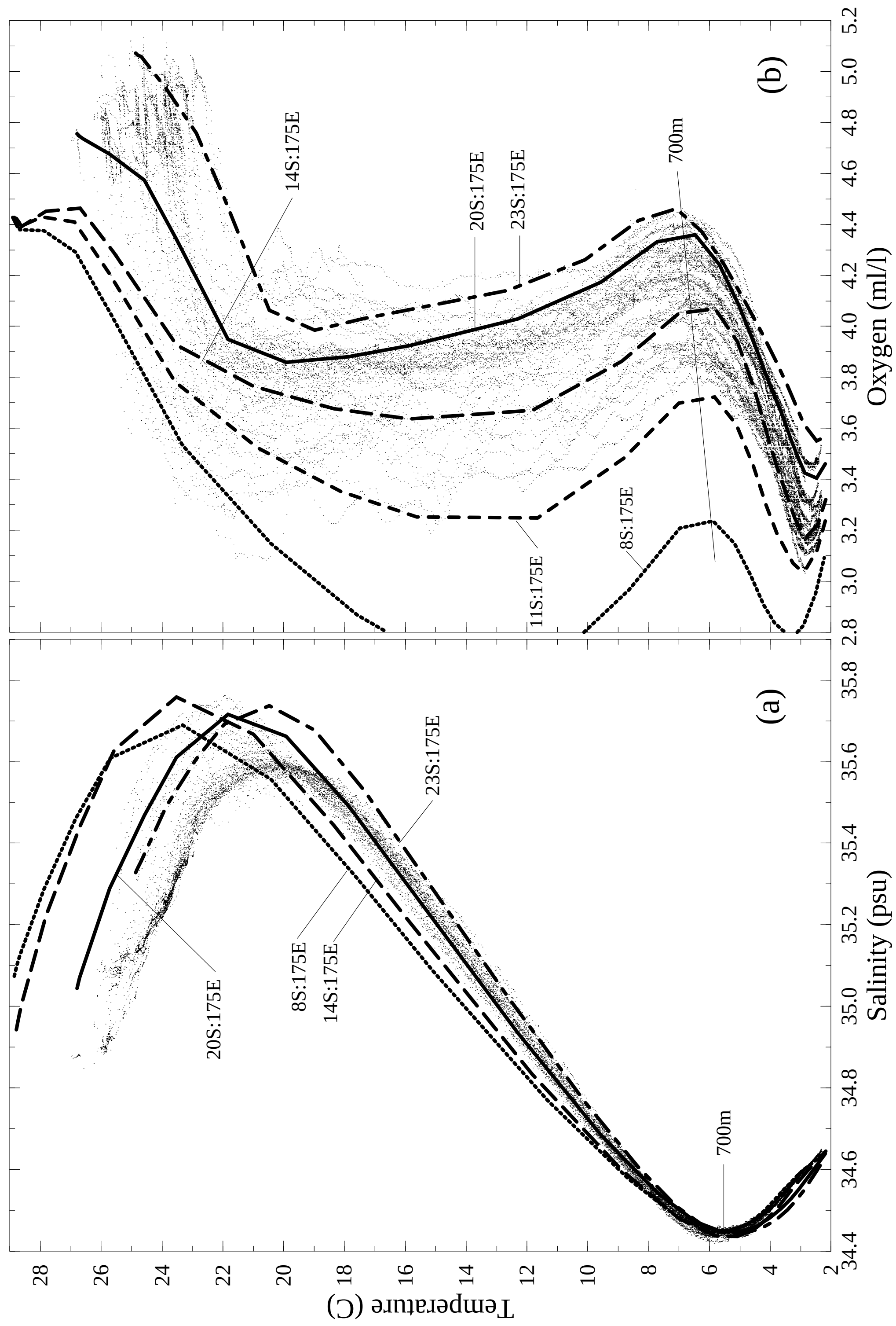

Figure 3.11: **:** [rotated] Same as Fig. 3.10 but for Fr0791.

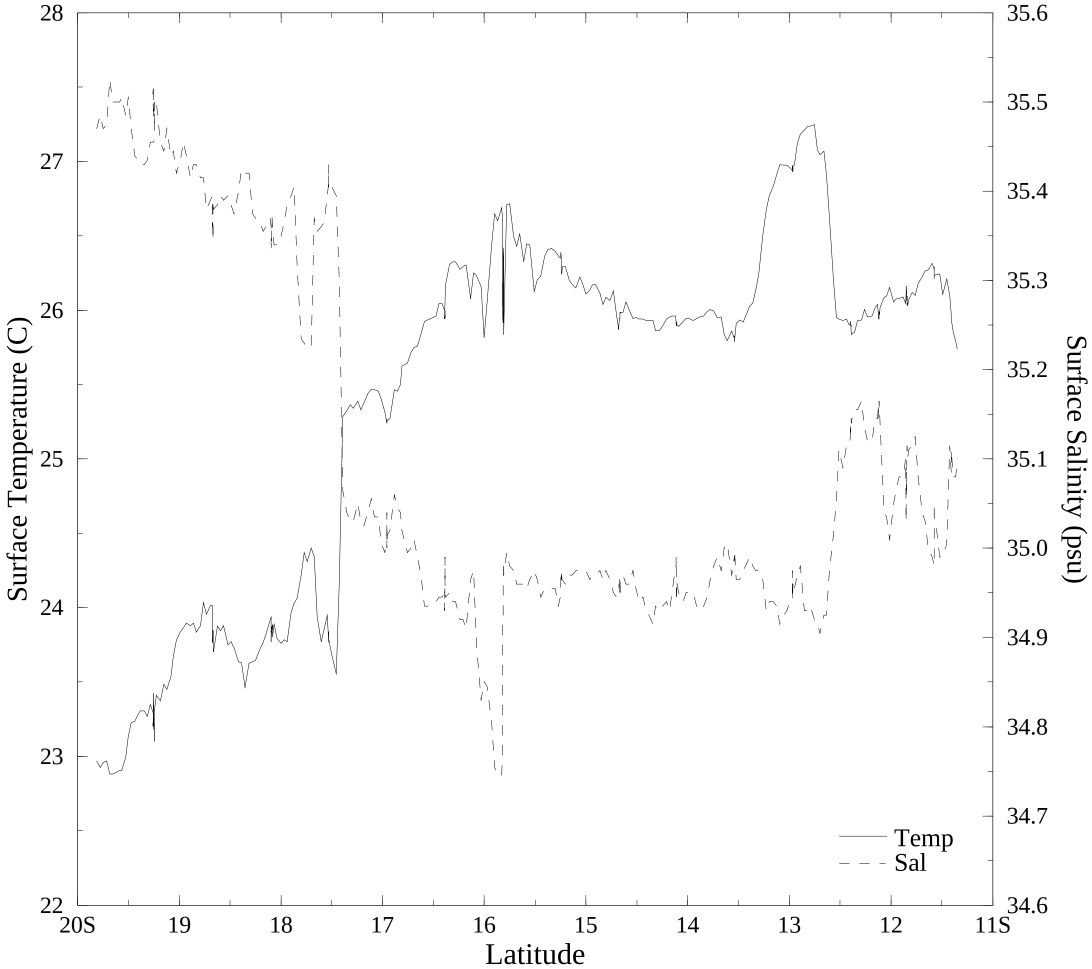

Figure 3.12: **:** Thermosalinograph record of surface temperature and salinity for D_{91} (Fig. 3.23). The baseline is along approximately 153.5°E. There is a 1.5°C increase in temperature and a corresponding $0.35\,psu$ drop in salinity at 17.5°S.

the continental shelf is at 23°S, and there will be significant differences in surface tracers between these two latitudes. The model predicts an eastward flow of cooler surface water at the southern end of New Caledonia, but no observations are presented here to confirm this. Regardless of direction of surface flow at the southern tip, there must be some noticeable irregularity in surface tracers at the northern tip, since the transit time from north to south (or vice–versa) is of order 1 month, or longer.

3.5 Geostrophic Transports, Vertical Profiles and ADCP Currents

The following conventions are used for transport analyses and diagrams in this section. End–points of sections have been arranged, where possible, so that they lie in stagnant areas between major flow directions. The given fluxes will therefore be reasonable estimates of the total flux contained within any major flow pattern, even though thermal wind analysis gives only the geostrophic normal component. ADCP data, if available, are useful in determining the major flow directions and stagnant areas. In this chapter, transport arrows in the figures are drawn in the direction of flow determined from ADCP data at 150 m. (In the next chapter, the deepest reliable ADCP data is used, 200–250 m.) All transport figures, except those of TEW, use this convention. While flow directions at 150 m are not necessarily representative of the entire water column, drawing the flux arrows this way gives useful information of, at the least, upper thermocline flow directions. All flux estimates (Sv) are between the surface and 1500 db. The end–points of individual sections are denoted by solid filled markers. Triangles denote CTD stations that are shallower than 2800 db and circles signify stations deeper than this, thus showing station pairs for which 1500 db reference velocities are estimated. The directions of flux arrows are derived from ADCP data averaged between the end–points.

3.5.1 TEW2/387

Fig. 3.13 shows the volume flux estimates for TEW across the Coral and Solomon Seas. Since ADCP data are not available for TEW387, and are too sparse for

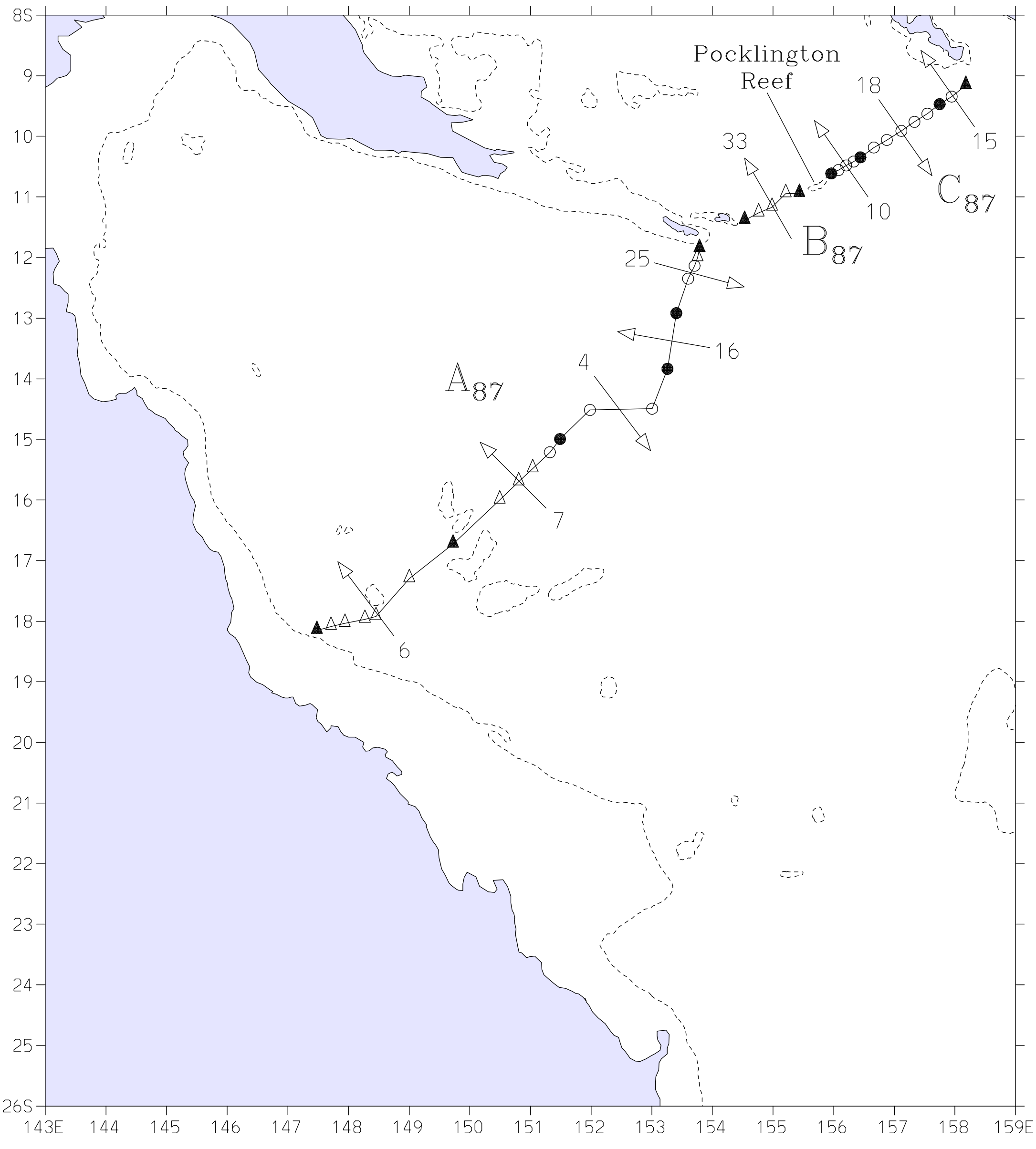

Figure 3.13: **:** Transects of the July-87 *R.V. Oceanographer* cruise; TEW287 stations are across the Coral Sea and TEW387 stations are across the Solomon Sea. Circles denote CTD stations deeper than 2800 db and triangles denote shallower stations. Solid filled markers denote end–point stations of transects. Fluxes are in *Sverdrups*. Dotted line is the 200 m isobath.

TEW287 the arrows in Fig. 3.13 have been drawn normal to the line joining transect end–points, in the usual fashion. Transects have been grouped into three main sections; A_{87}, B_{87} and C_{87}. A_{87}, from the Australian coast to the eastern tip of PNG, forms a closed section and the flux residual is less than $1\,Sv$, which is due perhaps more to luck than precise analysis. The 6 and $7\,Sv$ transects are in relatively shallow water, about $1000\,m$, and therefore these flux estimates are less reliable than the fluxes close to PNG, in deep water. An intense eastward flow of $25\,Sv$, confined to within $120\,km$ of the PNG coast, has a distinct subsurface character. This will be referred to as the NGCU, although it is yet to be proven unequivocally that it is the source of the Vityaz St. throughflow. The SEC inflow is split into three parts, one between the Australian coast and the Queensland Plateau, another along the northern shoulder of the Plateau and the last is immediately seawards of the NGCU.

Section B_{87} lies between Rossel I. and Pocklington Reef, and the average depth is only $1400\,m$ making it difficult to estimate reference velocities. Another consideration here is the small radius of curvature of the coastline which could give rise to strong nonlinearities and also perhaps permit the external mode to make a significant "invisible" contribution. The $33\,Sv$ estimate is made using the two end–points from $1415\,db$ with the reference velocity set to zero; Fig. 3.14 shows the corresponding thermal wind profile. Summing pairwise across the transect gives a lower estimate of about $25\,Sv$, because of errors due to the varying bathymetry. The thermal wind shear near $1400\,m$ is quite large and so the reference velocity is probably not sufficiently small to be ignored. If it is southwards, say by $5\,cm\,s^{-1}$, then the $33\,Sv$ estimate is reduced to $23\,Sv$. However, there is no evidence to suggest that the bottom flow is southwards and the water properties are much more akin to those found at $1400\,m$ on A_{87}, suggesting northwards flow instead. Extrapolating V_{1400} from the NGCU on A_{87} gives about $5\,cm\,s^{-1}$ to the north, which implies an increase of $8\,Sv$ for B_{87}. Thus, the flux estimate for B_{87} lies in the range[2] 25 to $41\,Sv$. With no acceptable evidence as to the direction and strength of V_{1415} for this transect it is simply set to zero and the flux estimate is given as $33\,Sv$. All casts along C_{87} are deep and so more reliable reference velocities are available for flux estimates; the nett flow is $7\,Sv$ to the north. This section is not entirely closed against the main chain of the Solomons since there

[2]Calculations rounded from two decimal places.

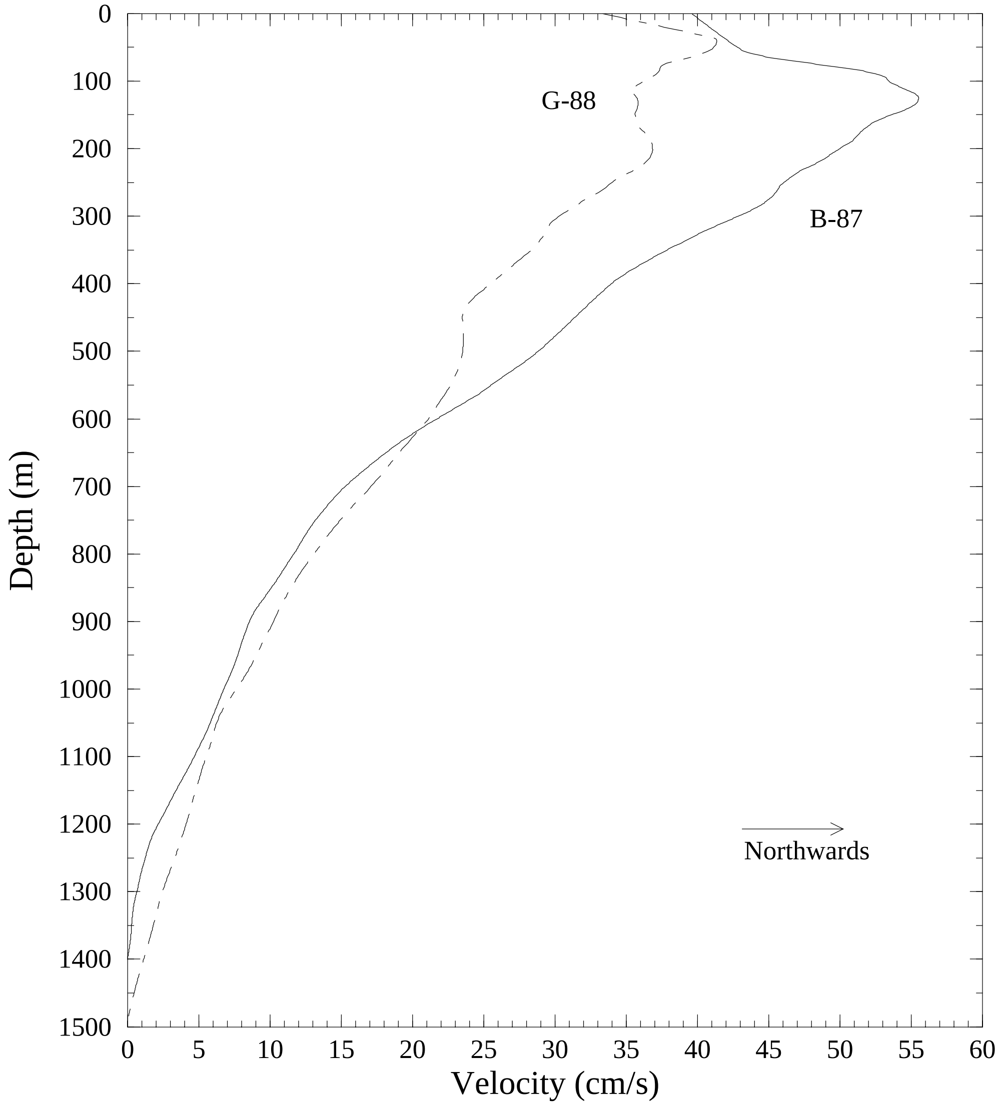

Figure 3.14: **:** Thermal wind profiles for G_{88} and B_{87}. Constructed from end–point stations only.

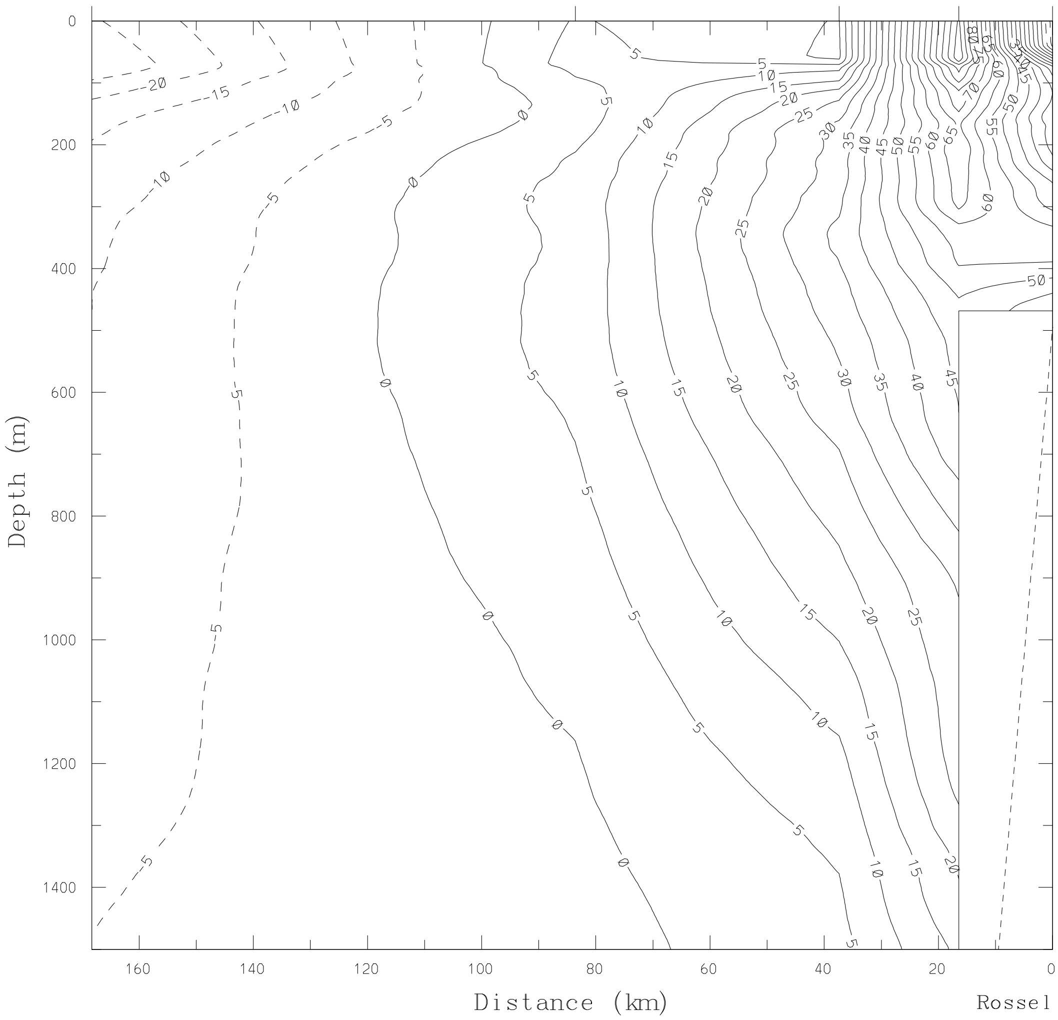

Figure 3.15: **:** Isotachs of thermal wind from TEW287 near Rossel I., looking from the east. Baseline is along the northern transect of A_{87}. $0\,km$ is at Rossel I. Positive (solid) lines imply eastwards flow, i.e., out of the page. CI is $5\,cm\,s^{-1}$. See Figs. 3.4 and 3.5 captions for other details.

is a narrow channel (New Georgia Sound) with a 600 m sill between the islands. Ignoring this, the PNG–Solomons throughflow, between 0 and 1500 db, is 40 Sv (i.e., 33+7) to the north and the uncertainty is about $\pm 10\,Sv$, which is due mainly to the uncertainty in B_{87}. There is some justification for erring towards the higher flux values. The PNG–Solomons throughflow between 1500 m and the bottom is only $\pm 1\,Sv$, and that correlates very well with the 1800 m (geometric) sill depth at the northern end of the Solomon Sea, between northernmost island of the Solomons (Buka I.) and New Ireland (SOPAC and GEBCO charts). Below 1500 m, the large abyssal currents observed crossing C_{87} (Fig. 3.7) largely cancel each other's contributions to the nett flux for C_{87}. The flux through B_{87} is a good deal larger than the 25 Sv flow along the southern coast of PNG which provides some evidence that part of the inflowing SEC goes directly north into the Solomon Sea rather than first circulating around the Coral Sea. The 16 and 25 Sv fluxes on A_{87} could be the manifestation of a localized recirculation but there is no way to determine this with the available data.

Fig. 3.15 shows zonal component isotachs of the NGCU, looking towards the 25 Sv transect of A_{87} from the east. Western boundary current characteristics are quite apparent and the scaling width (e–folding) across the shelf is about 50 km. The largest velocity present is $100\,cm\,s^{-1}$ eastwards in the mixed layer, at the 18 km position on the horizontal axis. A second maximum of $65\,cm\,s^{-1}$ is observed directly below this at 250 m, and going further offshore the depth of maximum velocity progressively increases. Unfortunately, ADCP data are not available for TEW387 so the actual peak velocities are not known. The depth of maximum velocity averaged across B_{87} is about 125 m (Fig. 3.14).

3.5.2 Fr0588

The July-88 cruise has seven shelf crossings along the coast of Papua, but nearly all casts are to depths of only 1500 db or less and so V_{1500} is set to zero in all cases, bar one (E_{88}). Fig. 3.16 shows the major transects for this cruise. The arrows show the approximate direction of flow, as determined from ADCP data, and their corresponding numbers show the estimated normal volume flux in *Sverdrups*. A single shelf crossing east of Rossel I. confirmed that the flow along the Gulf of Papua did indeed turn northwards, as it did for B_{87}, and there is good agreement

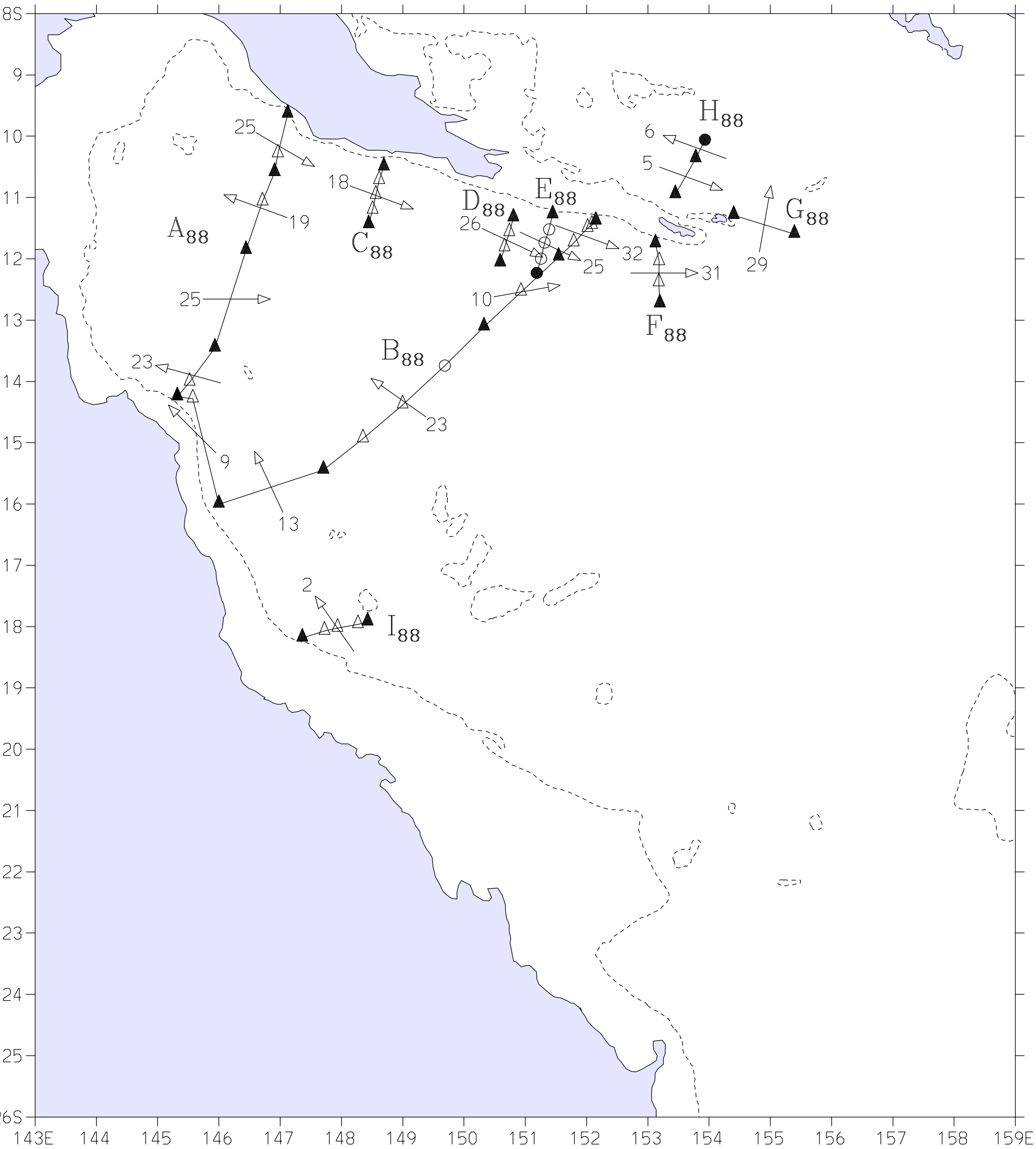

Figure 3.16: **:** Transects of the July-88 *R.V. Franklin* cruise, Fr0588. See Fig. 3.13 caption for other details.

with ADCP data (Fig. 3.24). The thermal wind profile for G_{88} is compared with that of B_{87} in Fig. 3.14 since the two transects are in similar positions. The 29 Sv estimate is quite similar to the 33 Sv figure of B_{87}. A series of deeper casts were performed about 35 km south of G_{88} and these suggest the velocity at 1400 m is between 0 and 1.7 $cm\,s^{-1}$ to the south. These casts have not been included in any of the analyses since their results for the thermocline are somewhat suspect in comparison with nearby transects. If 1.7 $cm\,s^{-1}$ southwards is also a fair estimate for July-87, then the 33 Sv estimate for B_{87} is only reduced by 3 Sv to about 30 Sv northwards, which is still well within the quoted error bounds.

The volume flux conservation for A_{88} is $-8\,Sv$, which is tolerable when compared with the magnitude of the flows. A positive residual implies excess inflow into the enclosed region. Torres Strait can be ignored as it is too shallow to support substantial throughflows (Wolanski *et al.*, 1988). The conservation for B_{88} is more acceptable at 3 Sv, but there is always the possibility that the errors caused by incorrect reference velocities have merely cancelled each other out.

A_{88} shows a meander in the NGCU between 13°S and 10°S; the current turns offshelf near the Australian coast and then re–attaches; along the PNG coast. The offshore meander distance is about 300 km. Unfortunately, not enough ADCP data are available here to get an overall confirmation, but there is reasonable confirmation for the 23 Sv and neighbouring 25 Sv transects. More concrete evidence of meandering behaviour will be presented in § 3.5.3. The 13 and 23 Sv inflow sections of B_{88} show the influx of the SEC, with the bulk of the inflow passing to the north of the Queensland Plateau, as in TEW287 (Fig. 3.5). This topographic structure contains large reef platforms, such as Tregrosse and Lihou, that block much of the otherwise westward (i.e., shoreward) flow. The strength of the NGCU near Rossel I. is 25–30 Sv.

The surface bifurcation of the SEC, which then forms the EAC and NGCU, occurs near 16°S at the Australian coast, as determined from ADCP data. When the two inner stations of I_{88} are analysed from the surface to 300 db the flux is 2.7 Sv southwards and ADCP data show that the EAC is partially developed across this transect. When analysed from bottom casts, the nett flux for the transect is 2.2 Sv northwards, so that a northwards flowing current of 5 Sv exists below the EAC and further seawards. This undercurrent was first reported by Church & Boland (1983), and in this work it is termed the Great Barrier Reef

Undercurrent (GBRU). The GBRU flows northwards along the Townsville and Queensland Troughs (1150 m sill depth) and rejoins the bulk of the SEC at the northern end of the Queensland Trough. Water properties show that its source is between 17 and 23°S in the inflowing SEC.

All casts along C_{88} were made only to 1000 db which accounts for the lower flux estimate for that transect. The flux through D_{88} is only 14 Sv when analysed with a reference pressure of 1000 db. It should be kept in mind that the total flux will have a nonlinear dependence on the reference pressure if this level is not sufficiently below the depths of strong flow. Only three casts in the Woodlark basin were sufficiently deep to analyse (H_{88}). They indicate that the NGCU does not enter this basin, but a moderate counterclockwise recirculation (5 Sv) is evident. The ADCP data also show this feature, with surface velocities of up to $1\,m\,s^{-1}$. The possibility of strong internal oscillations affecting this single observation cannot be ruled out; the dimensions of Woodlark basin are comparable with the local deformation radius.

3.5.3 Fr0690

This data set has the largest number of bottom casts of the three *R.V. Franklin* cruises and offers a more complete picture of the cyclonic circulation in the western Coral Sea. The depth of flow reversal for this cruise is about 990 to 1200 m (Fig. 3.6) in the Coral Sea basin, although fluxes are still calculated from 1500 m to be consistent with the other years.

The July-90 cruise (Fig. 3.17) demonstrated that the NGCU does not always follow the continental shelf in the Gulf of Papua. Unlike the July-88 findings, the bulk of the current heads directly towards Rossel I. along the 11°S parallel after turning eastwards at the Papuan Plateau. ADCP data indicate an abrupt southwards meander along the 30 Sv outflow section of B_{90} (see 12°S:150°E vectors in Fig. 3.24), and the two sections closest to Rossel I. show that the current then re-attached to the PNG coast. An isotach plot of the two eastern transects of B_{90} (7 Sv inflow and 30 Sv outflow) is shown in Fig. 3.18. The axis of the NGCU is 160 km offshore from the PNG coast, is 350 m deep and has a peak speed of $30\,cm\,s^{-1}$ (station pair average). The e–folding width is 75 km, which is within the bounds of being classed as a western boundary current. There is

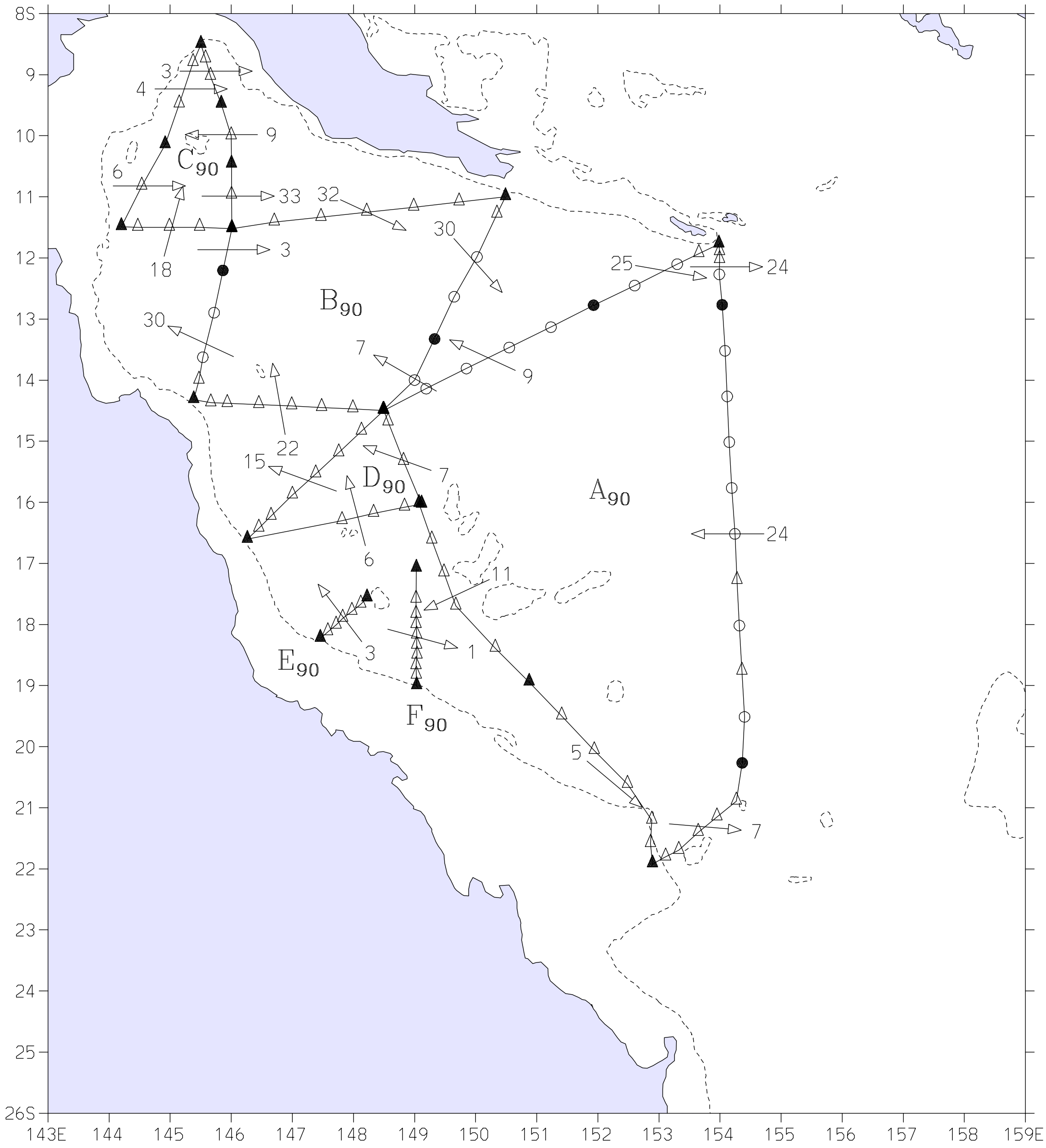

Figure 3.17: **:** Transects of the July-90 *R.V. Franklin* cruise, Fr0690. See Fig. 3.4 caption for other details.

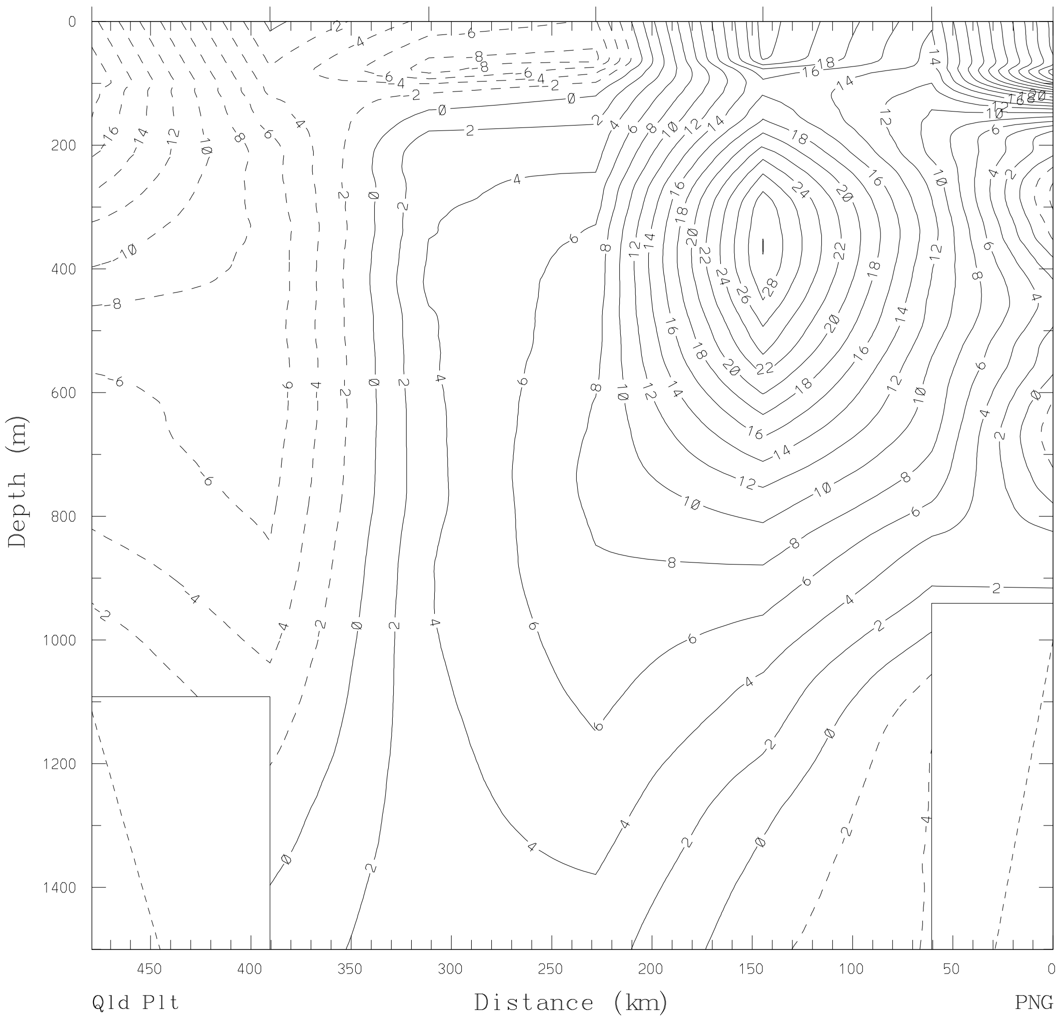

Figure 3.18: **:** Isotachs of thermal wind from Fr0690 across the Coral Sea Basin, looking from the east. Baseline is along the eastern transect of B_{90}. $0\,km$ is at the PNG coast. Positive (solid) lines imply eastwards flow, i.e., out of the page. CI is $2\,cm\,s^{-1}$. The NGCU is detached from the PNG coast by $160\,km$. The SEC is intensifying along the northern edge of the Queensland Plateau. See Figs. 3.4 and 3.5 captions for other details.

still an intense $36\,cm\,s^{-1}$ eastwards flow attached to the PNG coast, between the surface and $150\,m$, but the flux associated with it is less than $3\,Sv$. At 12°S the internal deformation radius is about $100\,km$, which is comparable with the offshore distance of this observed meander.

Fig. 3.19 shows zonal component isotachs of the inflowing SEC and outflowing NGCU for the two $24\,Sv$ transects on the eastern side of A_{90}. The view is from the west looking due east towards the open Pacific, and values greater than $30\,cm\,s^{-1}$ are clamped at that value, for clarity. The baseline (two transect lines) is along approximately 154°E. The NGCU has still not fully re–attached to the PNG coast and there is a narrow band of westward flow $40\,km$, south of the Louisiades. A comparable plot of model isotachs is shown in Fig. 3.45. The SEC has four distinct V–max cores at various depths. At the $230\,km$ position (13.8°S), a near surface core has speeds of over $26\,cm\,s^{-1}$ and another strong near surface core lies at the $720\,km$ position (18.5°S). Beneath it lies a secondary core, just distinct, at depth of $300\,m$. Two weaker deep cores are found; $6\,cm\,s^{-1}$ at $480\,km$ (16.1°S) and $10\,cm\,s^{-1}$ at $560\,km$ (16.8°S). The model yields very similar isotachs for the SEC (Fig. 3.45), except that there are only two distinct cores between 10 and 20°S, that increase in depth, proceeding southwards. The distinct model cores are caused by the SEC's bifurcation around New Caledonia and Vanuatu, which is represented by a shallow submarine ridge. These islands cast a 'shadow' of stagnant water to the west, that exists for several thousand kilometres.

Fig. 3.20 shows the thermal wind profile of the inflowing SEC, averaged from the $150\,km$ to $810\,km$ positions of Fig. 3.19. The depth of maximum velocity is $90\,m$ and the overall profile is similar to those of northward flows observed at the Louisiades (Fig. 3.14). It is not strictly true that the SEC's maximum velocities occur at depth, however, it does have a subsurface character and the average thermal wind profile does have a subsurface peak.

The three eastern transects of A_{90} (Fig. 3.17) form an enclosed area with PNG and Australia, and the flux residual is $-7\,Sv$. The $7\,Sv$ nett outflow at the southern end of A_{90} is the southwards flowing EAC. Other closed transects for Fr0690 generally have flux residuals of about 15% of the main flows associated with the enclosed area. The NGCU flux is $24\,Sv$ near Rossel I. and the SEC inflow is also $24\,Sv$. In the western Coral Sea the NGCU is approximately $30\,Sv$, a little larger than its strength at Rossel I., which may be indicative of some

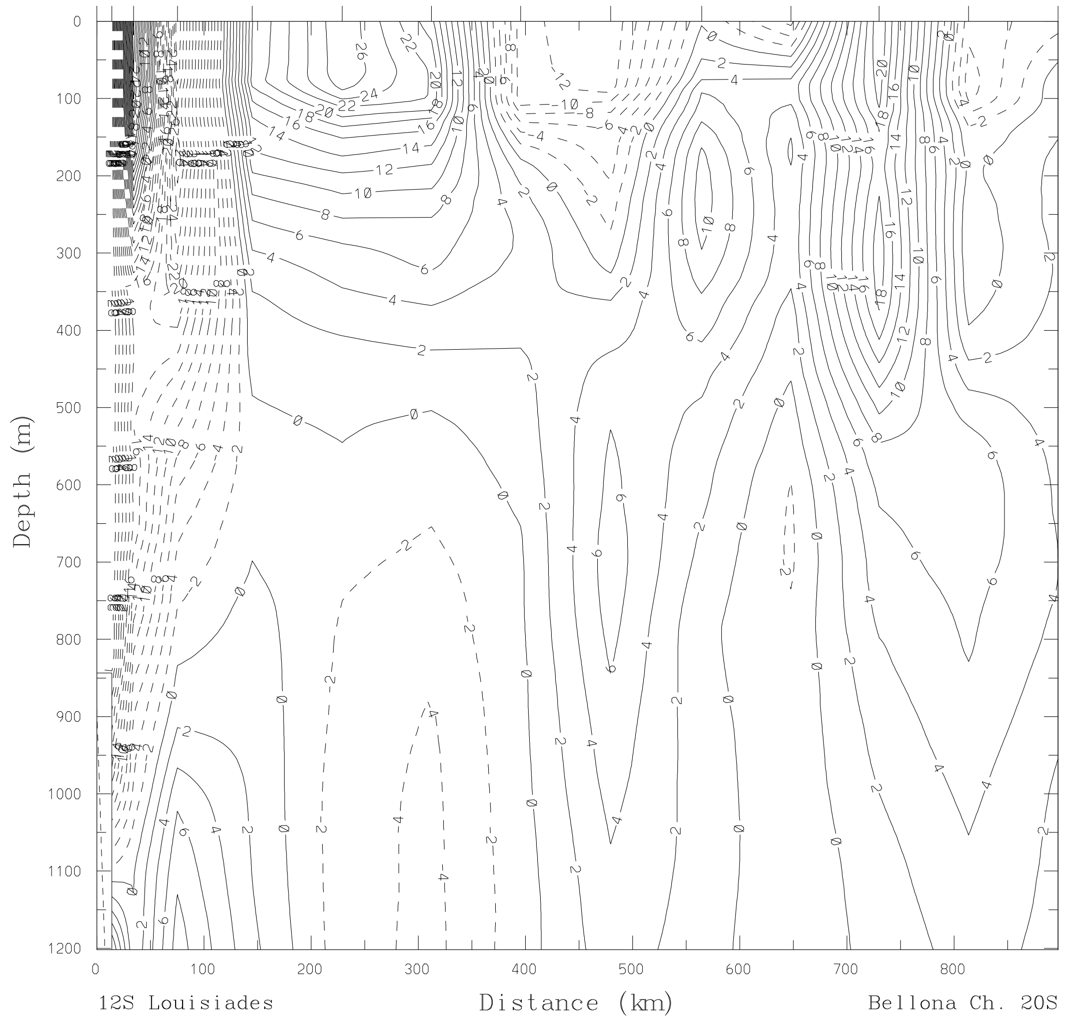

Figure 3.19: **:** Isotachs of thermal wind from Fr0690 along approximately 154°E, looking from the west. Baseline is along the two $24\,Sv$ transects of A_{90}. $0\,km$ is at the PNG coast. Positive (solid) lines imply westwards flow, i.e., out of the page. CI is $2\,cm\,s^{-1}$. The SEC has four V–max cores at various depths. See Figs. 3.4 and 3.5 captions for other details.

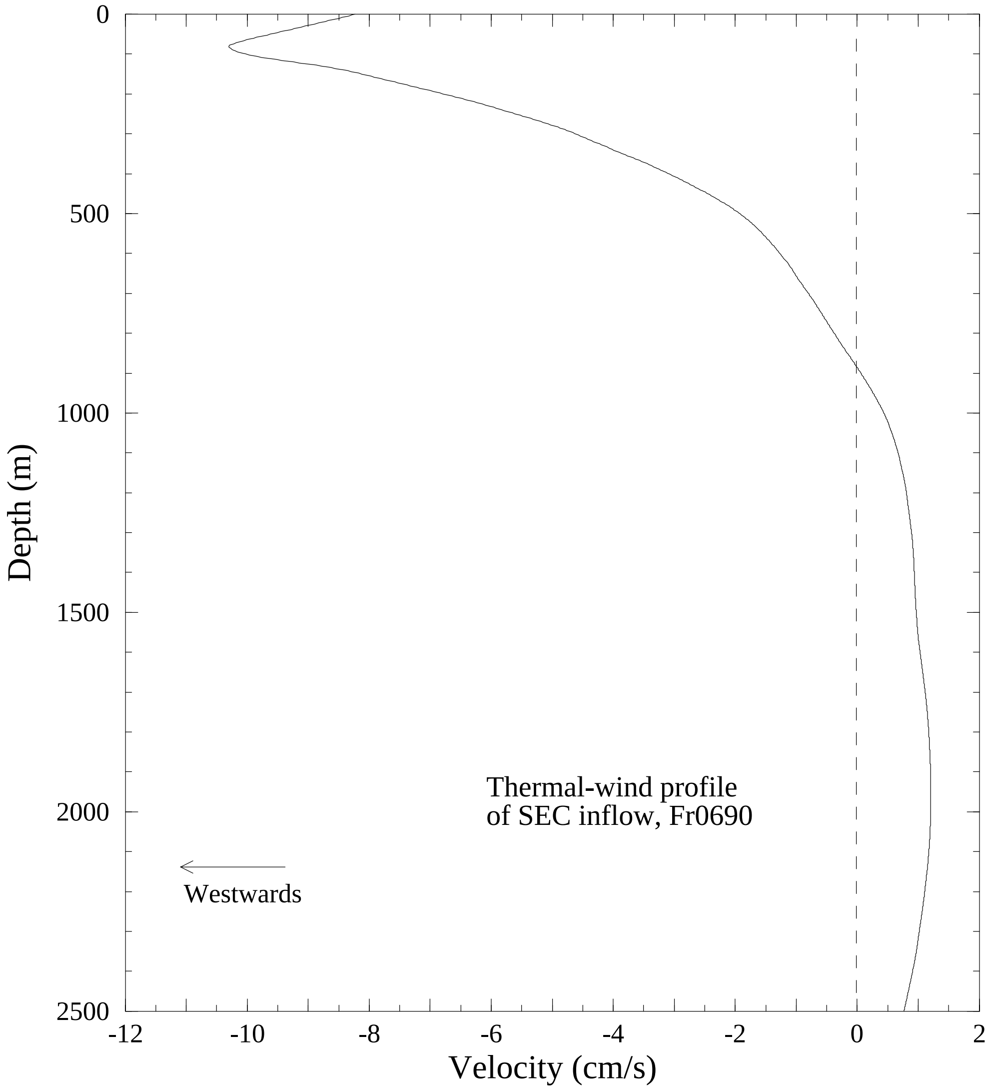

Figure 3.20: **:** Thermal wind profile for the SEC, averaged across the 24 Sv inflow transect of A_{90}. Integrated from a maximum of 3800 db. Negative values imply westwards flow.

clockwise recirculation. The bathymetry around the Papuan Plateau is generally less than 2000 m and the deep anticyclonic flow is possibly much weaker there, perhaps mitigating the crude assumption of setting V_{1500} to zero for C_{90}.

Transect E_{90} across the Queensland Trough is comprised of seven bottom casts. With the reference pressure at the bottom the nett flux is 2.6 Sv northwards. A reference pressure of 300 db yields 5 Sv southwards (the EAC) which therefore implies a northwards flux of 7.6 Sv below 300 db, for the GBRU. Figures 3.21 and 3.22 show isotachs of thermal wind velocities across transects E_{90} and F_{90}, respectively. Across E_{90} the EAC is confined to within 40 km of the Australian coast and is no more than about 300 m deep. At 400 m two large northward flows are evident, separated by some 50 km. The offshore core is only partially resolved by a single station pair and could be spurious because of the close proximity to Flinder's Reef. However, two separate cores are observed by Church & Boland (1983) who termed this a double cell structure. The isotach plot for F_{90} (Fig. 3.22) shows only a single undercurrent core even though this transect is in fairly close proximity to E_{90}, and actually spans a wider distance across the Queensland Trough (Fig. 3.17). Either the second core is created between E_{90} and F_{90} or else it moves in from the north between the two transects. A brief speculative explanation is offered here. The core further offshore may be generated by some of the SEC forming a jet between the large reefal structures of the Queensland Plateau and then joining the other core, which perhaps follows the main path of the Queensland Trough. Tracer properties show that the waters of the two cores originate from between 17 and 23°S, along the 175°E meridian and they are therefore closely linked with the SEC. An isotach plot of the high resolution transect of D_{90}, further to the north, shows no evidence of the double cell, so presumably the two velocity cores coalesce as they move northwards. Going further north along the Australian coast, the surface bifurcation of the SEC and EAC occurs at about 16°S, as determined from ADCP data (n.b. Fig. 3.24 ADCP data are 150 m deep).

Church & Boland note that the two V–max cores are associated with two O_2 maxima cores. Only one O_2 maximum core is found on E_{90}, but it is 200 m deeper and 20 km further offshore from the V–max core closest to the shelf. Also, the present V–max cores are a few hundred metres shallower than those depicted in Church & Boland's Fig. 3. There is no reason why the V–max cores

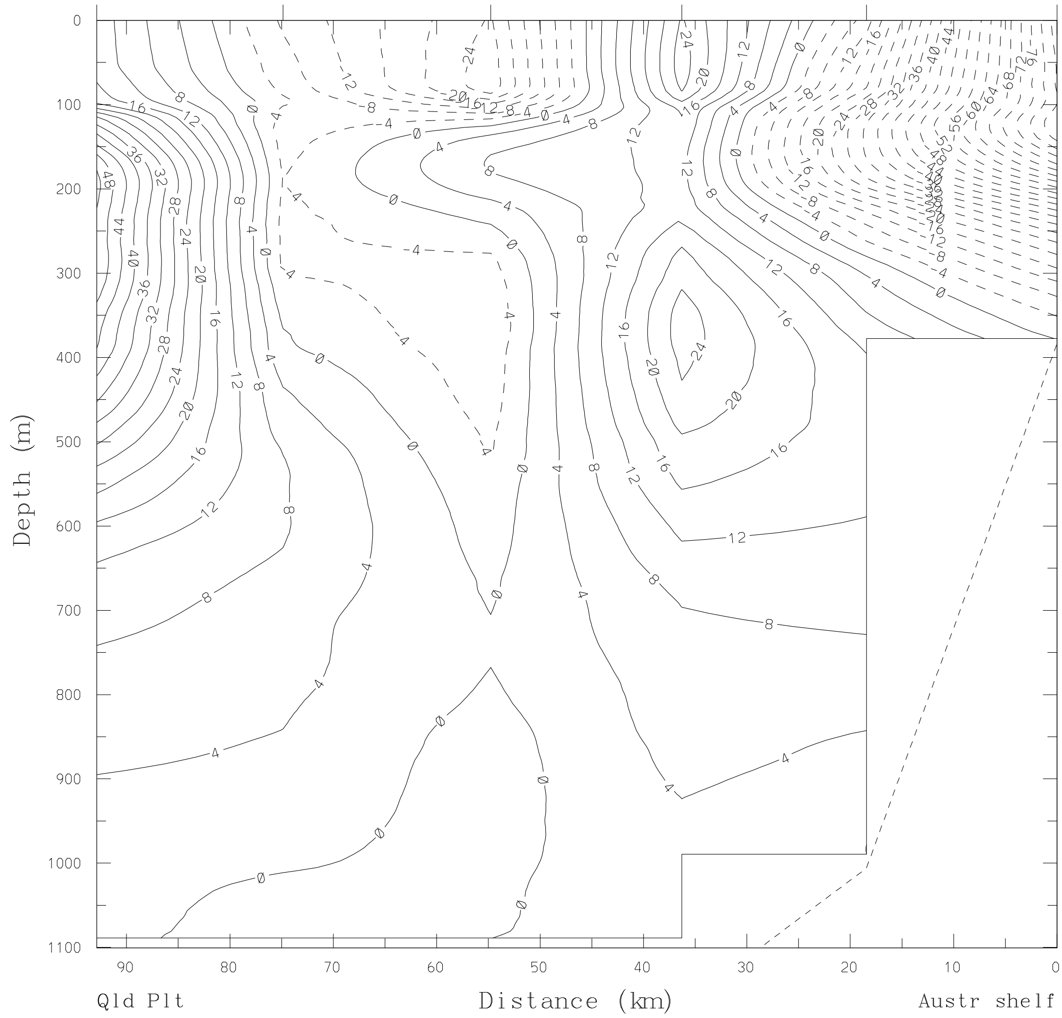

Figure 3.21: : Isotachs of thermal wind for E_{90}, looking from the northwest. Positive (solid) lines imply northwards flow, i.e., out of the page. CI is $4\,cm\,s^{-1}$. The EAC is evident flowing southwards along the shelf edge, and further offshore two cores are seen flowing northwards in the GBRU. See Figs. 3.4 and 3.5 captions for other details.

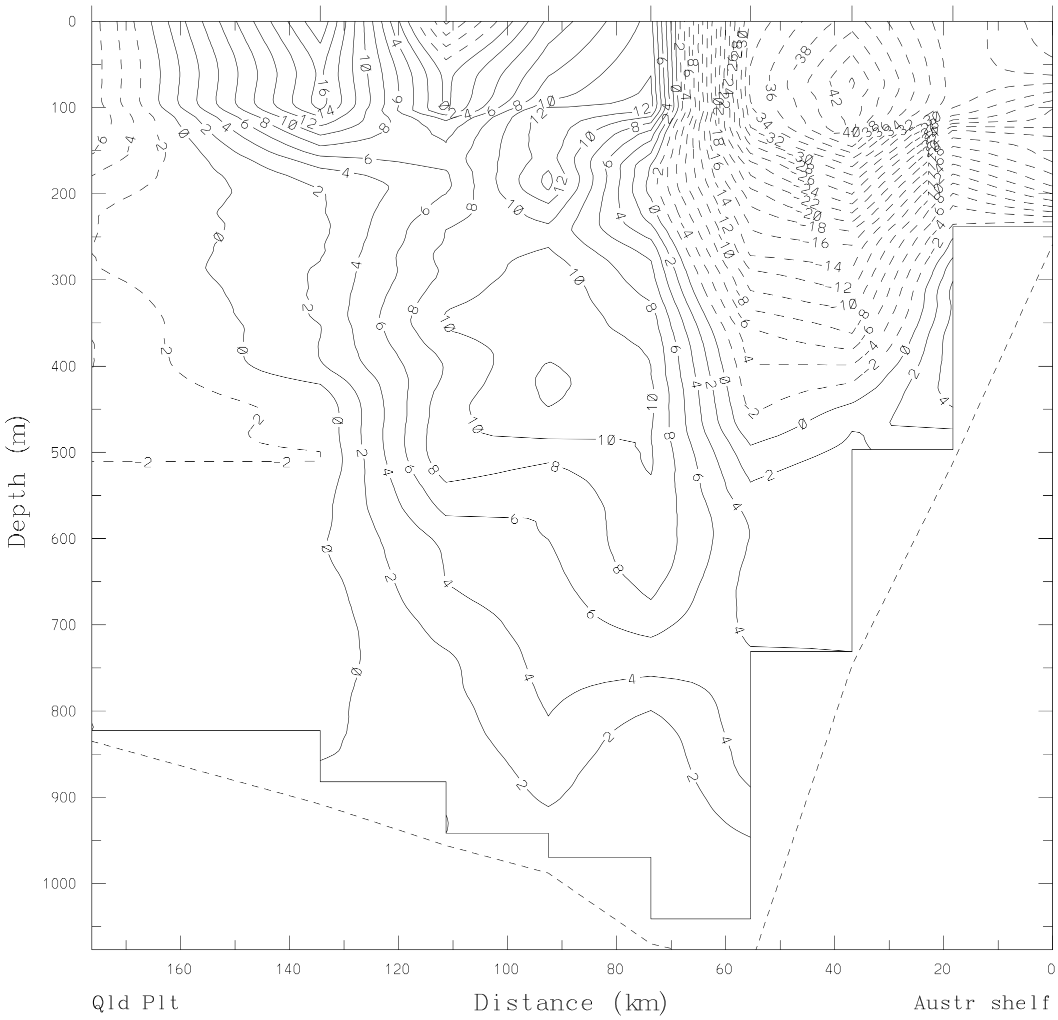

Figure 3.22: **:** Isotachs of thermal wind for F_{90}, looking from the west. Positive (solid) lines imply westwards flow, i.e., out of the page. CI is $2\,cm\,s^{-1}$. The EAC is evident flowing eastwards along the shelf edge, and further offshore only a single core is evident in the westwards flowing GBRU See Figs. 3.4 and 3.5 captions for other details.

should necessarily be associated with O_2 cores since the present data do not reveal any obvious strong O_2 cores (not shown) in the inflowing SEC. The V–max cores could develop apparent O_2 extrema if they rise or sink by several hundred metres, however, neither Church & Boland's nor the present data show extrema for other tracers. The only other possibility which explains the (minor) discrepancy between the data sets is that it is merely a manifestation of variability inherent in the SEC's open ocean flows. The O_2 extrema may be associated with particular events that have occurred at some previous time, in the open South Pacific. Information imprinted over localized areas of the SEC would be later observed in the GBRU.

3.5.4 Fr0791

The transects of interest for the September-91 cruise are shown in Fig. 3.23. The deep anticyclonic flow in the Coral Sea Basin is considerably stronger for this cruise, possibly up to $9\,Sv$, so making it even more imperative to accurately determine reference velocities. In fact, a number of deep station pairs show considerable thermal wind shear even at $2800\,m$, around the Coral Sea Basin, and so the assumption that V_{1500} is zero for shallow pairs is more dubious than for the previous surveys. Thus, many of the $1500\,db$ casts are excluded and deep ones are utilized wherever possible. Section A_{91} shows the EAC flowing southwards with a strength of $30\,Sv$, but immediately seawards there is a $19\,Sv$ northwards flow. The EAC is confined above $2000\,m$ while the northward $19\,Sv$ flow is highly barotropic; these two flows have nearly identical tracers. As mentioned previously, the ADCP data also show strong northwards flow here, with the relative vorticity being about 20% of f. A composite of the best ADCP data from the three *R.V. Franklin* cruises is shown in Fig. 3.24, and is compiled mainly from Fr0791. All vectors south of 17° are from Fr0791 and the northward flow near Pocklington Reef is from Fr0588.

Tracing along the transects of B_{91}, C_{91} and D_{91}, the northwards flow appears to reach at least 17°S, but T–O_2 characteristics do not show a single continuous water type. (O_2 measurements for A_{91} were from Niskin bottles because of a CTD winch failure.) The northward fluxes for A_{91} and B_{91} are perhaps mostly re–entrained into the southward flowing EAC above $1600\,m$, since the $19\,Sv$ and

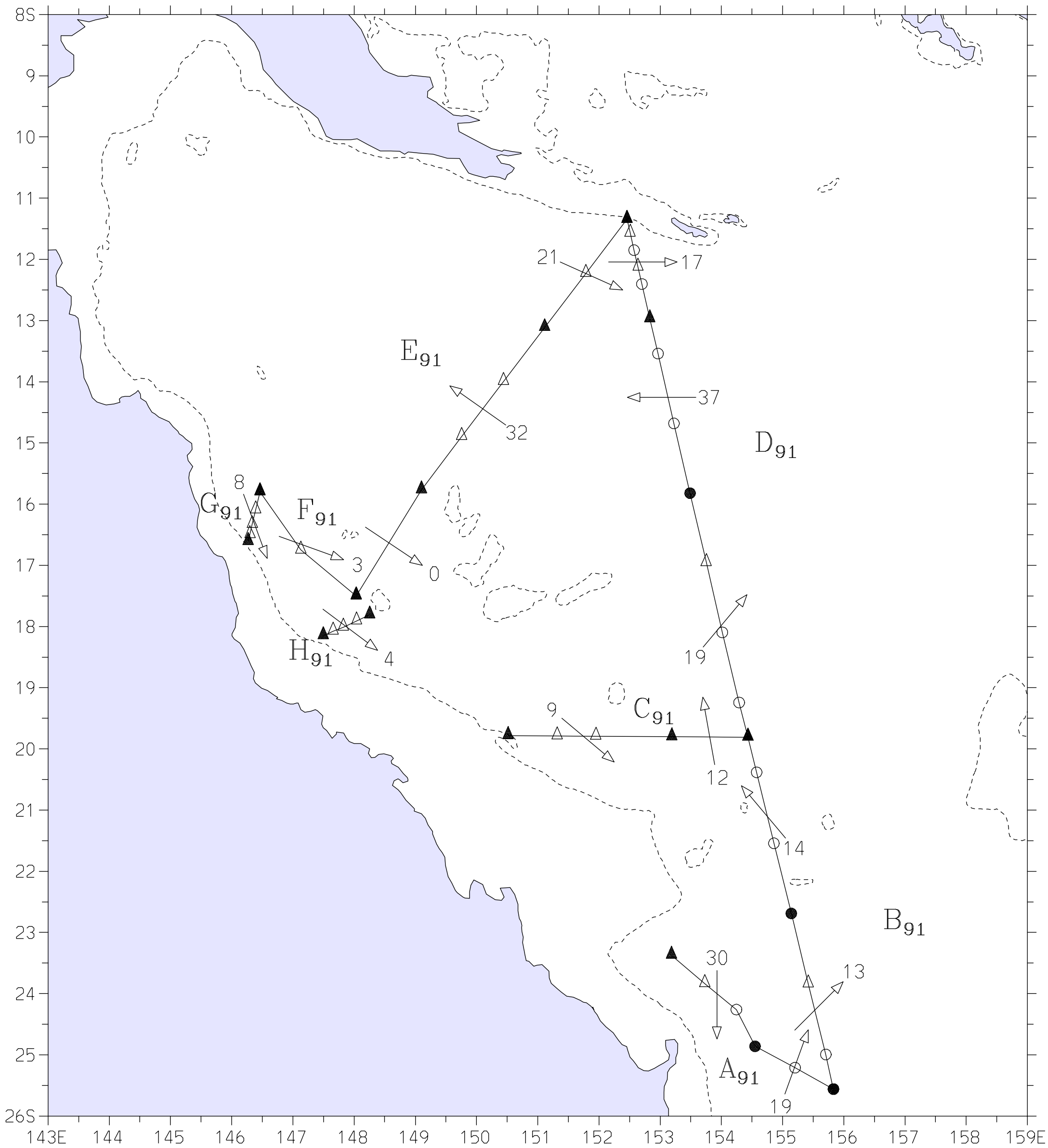

Figure 3.23: **:** Transects of the September-91 *R.V. Franklin* cruise, Fr0791. See Fig. 3.13 caption for other details.

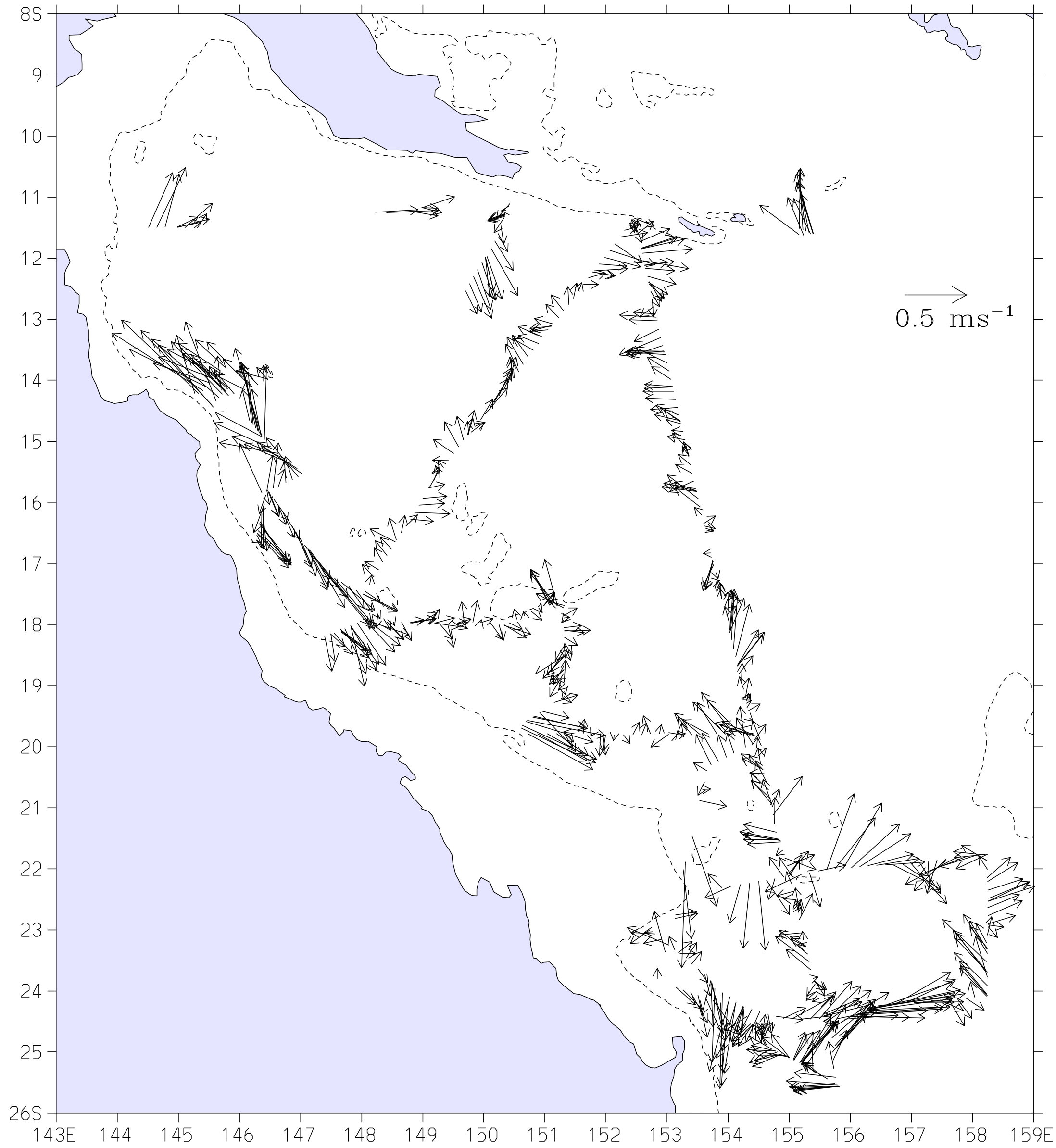

Figure 3.24: **:** A composite of the best ADCP data, at 150 m, from the three *R.V. Franklin* cruises. Compiled mainly from Fr0791. The northwards flow near Rossel I. is from Fr0588.

37 Sv flows across D_{91} are readily identifiable as SEC water. The only identifiable volumes of Tasman Sea water found on C_{91} and D_{91} are observed within roughly 600 m of the bottom of the channel lying between the Bellona Platform and the Australian coast (at 2200–2800 m), where the flow is northwards. Some qualification of "Tasman Sea water" is needed since the EAC in the Tasman Sea is actually supplied by the SEC, above about 1600 m. SPAC data show that below roughly 1600 m in the Tasman Sea, tracers are clearly akin to the various types found in the Southern Ocean (cf. Reid, 1986). This is due, no doubt, to the presence of the Kermadec Ridge which does not permit the deeper waters of the SEC to enter the Tasman Sea. Notably, there is an O–min at about 1700 m (Central Deep Water, CDW) and the S–max Antarctic Circumpolar Water (ACW) at about 2500 m. Thus, the deep Tasman Sea waters flowing into the Coral Sea Basin, observed in Fr0690 and Fr0791, are CDW and ACW, but with some mixing of SEC water. There is perhaps insufficient resolution in the southern sections of Fig. 3.23 to give a good idea of flow connectivities. ADCP data (Fig. 3.24) and SST images (not shown) indicate that some of the near surface water at the southern end of B_{91} moves eastwards to at least 158°E.

Only one high resolution shelf crossing was made near the Louisiades (D_{91} in Fig. 3.23) which gives an NGCU flux estimate of 17 Sv. The error estimate is fairly large at $\pm 5\,Sv$ due to uncertainties in the reference velocity. If V_{1500} is assumed to be zero, the flux estimate is 23 Sv, using simple corrections to the shallower stations of the shelf crossing. If V_{1500} is found from the deepest pair south of the shelf (3050 db) the nett 0/1500 flux for the NGCU drops to 12 Sv. The deep flow is strongly to the west but there is some doubt as to whether or not it is sufficiently close to the shelfbreak to reliably estimate V_{1500} there. A plot of zonal component isotachs of the NGCU, at the Louisiades shelfbreak is shown in Fig. 3.25. Some shallow casts not shown in Fig. 3.23 have been used in constructing the isotachs since the accuracy of reference velocities is less important for this. The main axis of the current is about 360 m deep, has a peak velocity of 46 $cm\,s^{-1}$ eastwards and an e–folding width of about 60 km. A separate eastwards flow of similar speed is seen closer inshore, but with the maximum speed at the surface and carrying only about 2 Sv. A single ADCP profile, reliable down to 320 m, was obtained directly above this deep core. This shows the sub–mixed layer velocities increasing with depth to 54 $cm\,s^{-1}$ eastwards

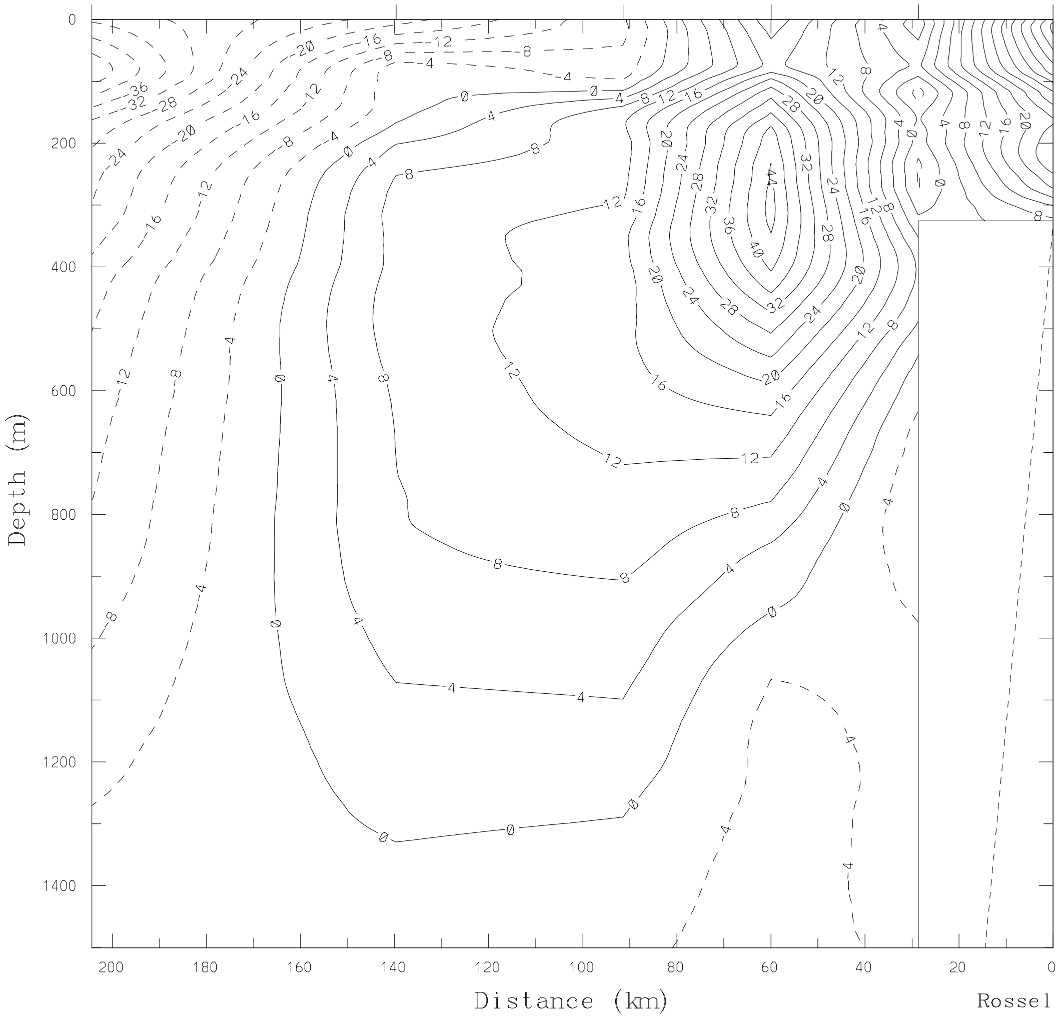

Figure 3.25: : Isotachs of thermal wind for the northernmost transect of D_{91}, looking from the east. $0\,km$ is at the Louisiades' shelf. Positive (solid) lines denote eastwards flow, i.e., out of the page. The NGCU's core is $46\,cm\,s^{-1}$ to the east, at a depth of $300\,m$. CI is $4\,cm\,s^{-1}$. See Figs. 3.4 and 3.5 captions for other details.

at 290 m. However, there are insufficient deep ADCP data across the station pair to give an average that can be compared with the thermal wind isotachs.

The 9 Sv transect of C_{91}, across the southwards flowing EAC, is at an acute angle to the shelf so making a shelf–edge correction to the flux estimate impossible. An offset for the thermal wind profile is found using ADCP data between 100 and 250 m (the only instance where this is done) and the uncertainty is about 4 Sv. The maximum residual found over closed sections is $-11\,Sv$, for A–B–C_{91}. Other residuals are about $\pm 6\,Sv$, which is a little higher than for the previous surveys.

Analyses for transects G_{91}, H_{91} and C_{91} along the Queensland Trough, unfortunately with many reference pressures being less than 1500 db, show that the EAC formed the dominant component of the flux through the Queensland Trough at the time of the survey. (This was during late winter 1991, and the Southeast Trade Winds were comparatively weak, but not reversed.) The EAC is well established on G_{91} with near-surface velocities up to $0.8\,m\,s^{-1}$, so that the surface bifurcation latitude of the SEC is well north of 16°S. This is a few hundred kilometres north of Church's (1987) observations of the winter bifurcation latitude. No firm conclusions can be made about the barotropic component along the trough but the trend in the data does suggest that the northward flowing GBRU is a little weaker for this cruise, and that the nett flux through the Queensland Trough is southwards. On transect H_{91} the EAC flux above 300 db is about 6 Sv southwards and the GBRU is carrying some 2 Sv northwards, leaving a nett of 4 Sv southwards. An isotach plot of H_{91} (not shown) shows no sign of the double cell structure and the single undercurrent core is $20\,cm\,s^{-1}$ northwards at 500 m, while the EAC reaches $104\,cm\,s^{-1}$ at the surface.

3.6 Model Results for Western South Pacific

The following sections cover the pressure, velocity and TS fields of the Coral and northern Tasman Seas, showing the entry and exit of the NGCU and its vertical structure. The global fields, including the Indonesian throughflow, are covered in Chapter 5, and the figures in that chapter may be perused in conjunction with the sections and figures below.

3.6.1 Seasonal Stream Function

Fig. 3.26 shows the IT and PNG–Solomons throughflow (PST) for years seven and eight of the seasonally forced phase; positive values imply flow towards the Indian Ocean and northwards between PNG and the Solomons, respectively. The eight year average values are $14.4\,Sv$ for the IT and $19.9\,Sv$ for the PST. The peak IT occurs typically in early to mid July and the PST peaks during August, but with a broad range. The most striking feature of the PST is the periodicity of order one month. Analysis of the model's pressure fields over a range of depths (not shown) shows that this is caused by wave activity along the equator, causing low latitude zonal flows to bifurcate around the Solomons. The period is suggestive of Legeckis waves (Legeckis, 1983) although observational evidence for these has been mainly from the eastern side of the Pacific. The model's near surface fields yield strong Legeckis wave activity only to the east of the Date Line, but the situation is quite different for deeper water. Zonal westwards currents near the equator regularly divert southwards along the east coast of the Solomons, rounding the southern tip of the islands and then flowing northwards into the Solomon Sea. There is also some indication of a monthly signal in the IT, as well. Fig. 3.27 shows two flux–depth histograms for the PNG–Solomons throughflow, that are instantaneous snapshots from 25-July-8 and 11-August-8, respectively (year eight of the seasonally forced phase). (Model data dumps were performed at 100 hour intervals during July-8 and August-8.) Of the $8.4\,Sv$ total PST variation, a little over half, $4.3\,Sv$, occurs between $751\,m$ and the sill depth. The variations have the same sign at all depths between the surface and the Solomon Sea's northern sill ($1860\,m$), implying that the wave motion's barotropic mode is stronger than its first baroclinic mode. CPU time and disk storage constraints prevented the running of a ninth year for the seasonally forced phase, with snapshots every ~ 24 hours. This would have allowed a much closer examination of the apparent abyssal Legeckis wave activity, however, the 25-July-8 and 11-August-8 snapshots are sufficient to show the basic behaviour.

Fig. 3.28 shows the model predictions for the barotropic stream function for July-8 (i.e., July, year eight of the seasonally forced phase) over the Coral, Solomon and northern Tasman Seas. Following normal convention, an advected particle has the more negative stream function value on its left hand side. Each land mass has a constant value of stream function along its coastline due to

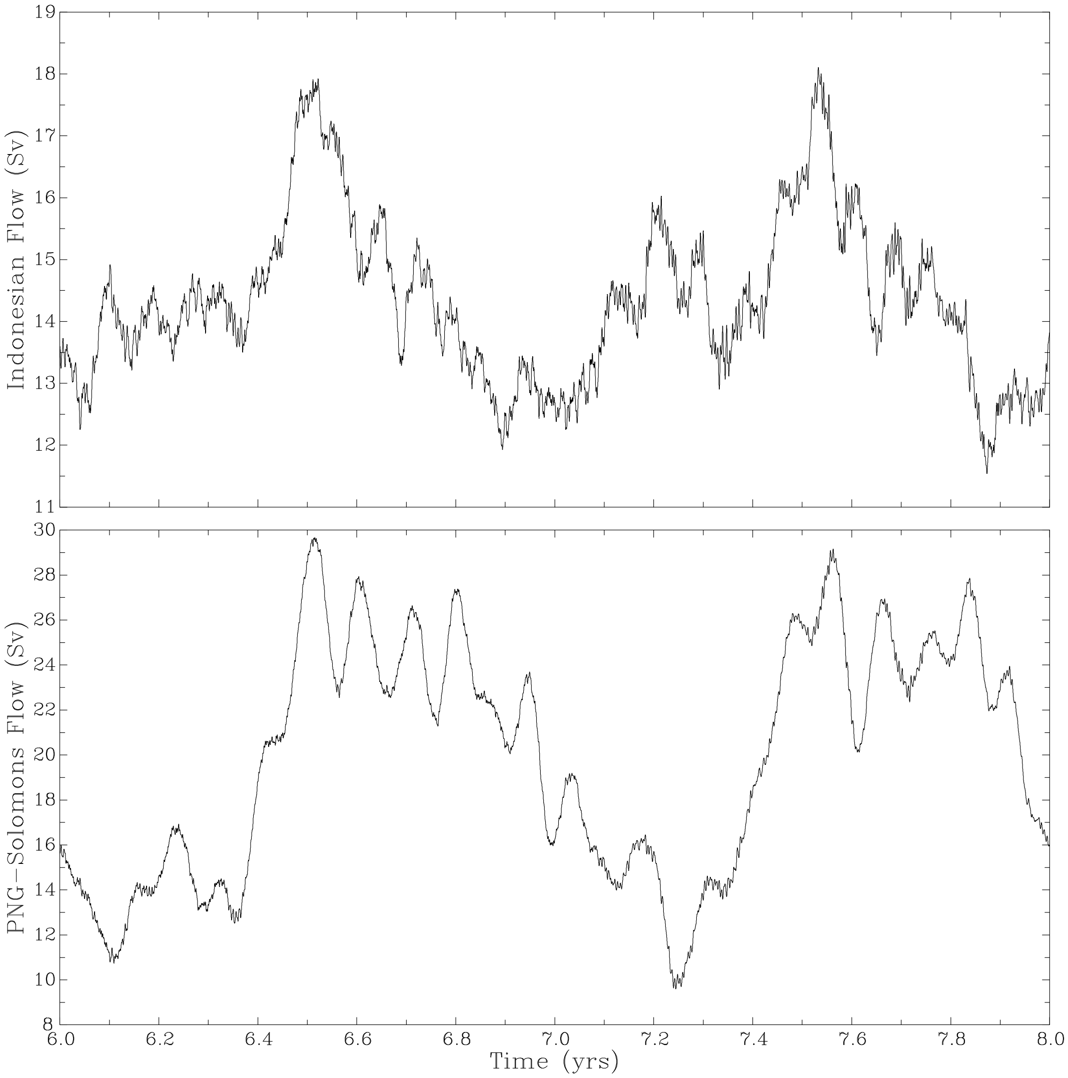

Figure 3.26: **:** Time series of throughflows (Sv) during year numbers seven and eight of the seasonally forced phase. Top panel is the southwards Indonesian throughflow, and the bottom panel is the northwards PNG–Solomons.

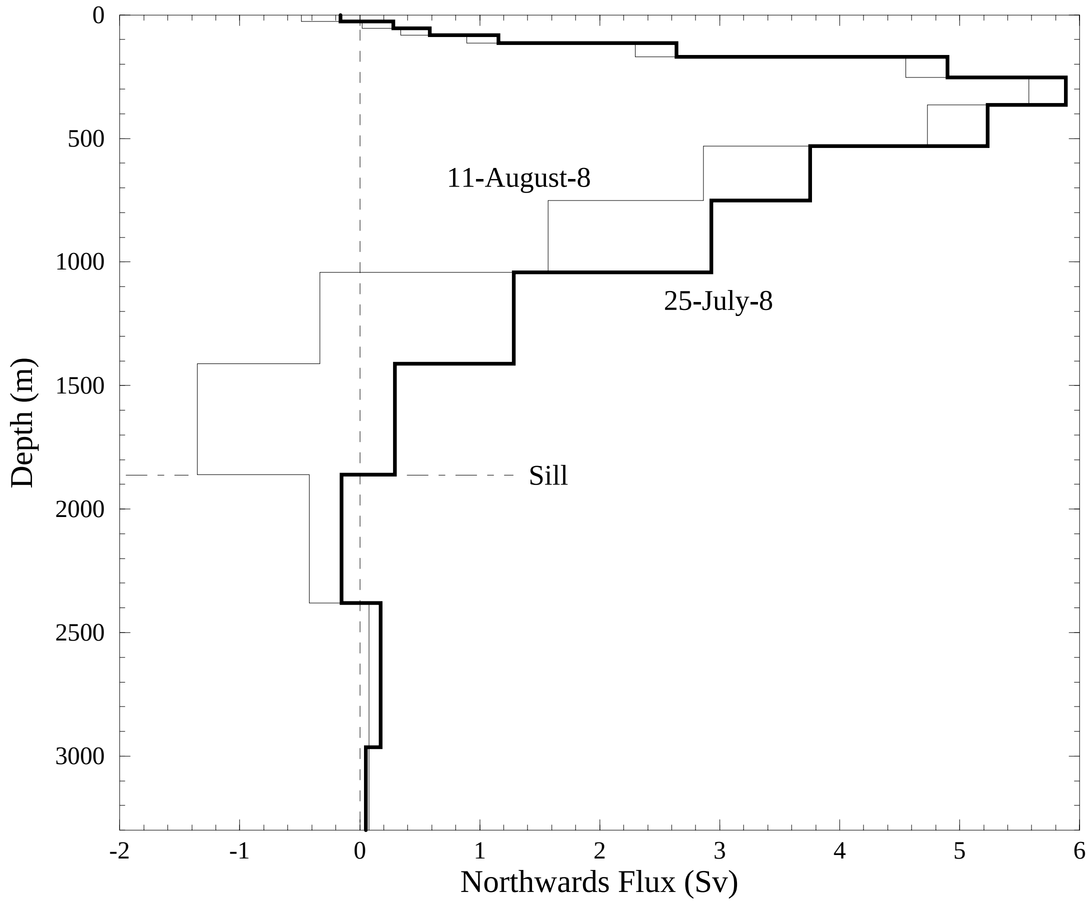

Figure 3.27: **:** PNG–Solomons throughflow (Sv) versus depth histograms, for 25-July-8 and 11-August-8, respectively. Flux is northwards through the 6°S parallel. The sill depth indicated is between New Ireland and the northern tip of the Solomons (Buka I). Total throughflows for July and August are $28.8\,Sv$ and $20.4\,Sv$, respectively.

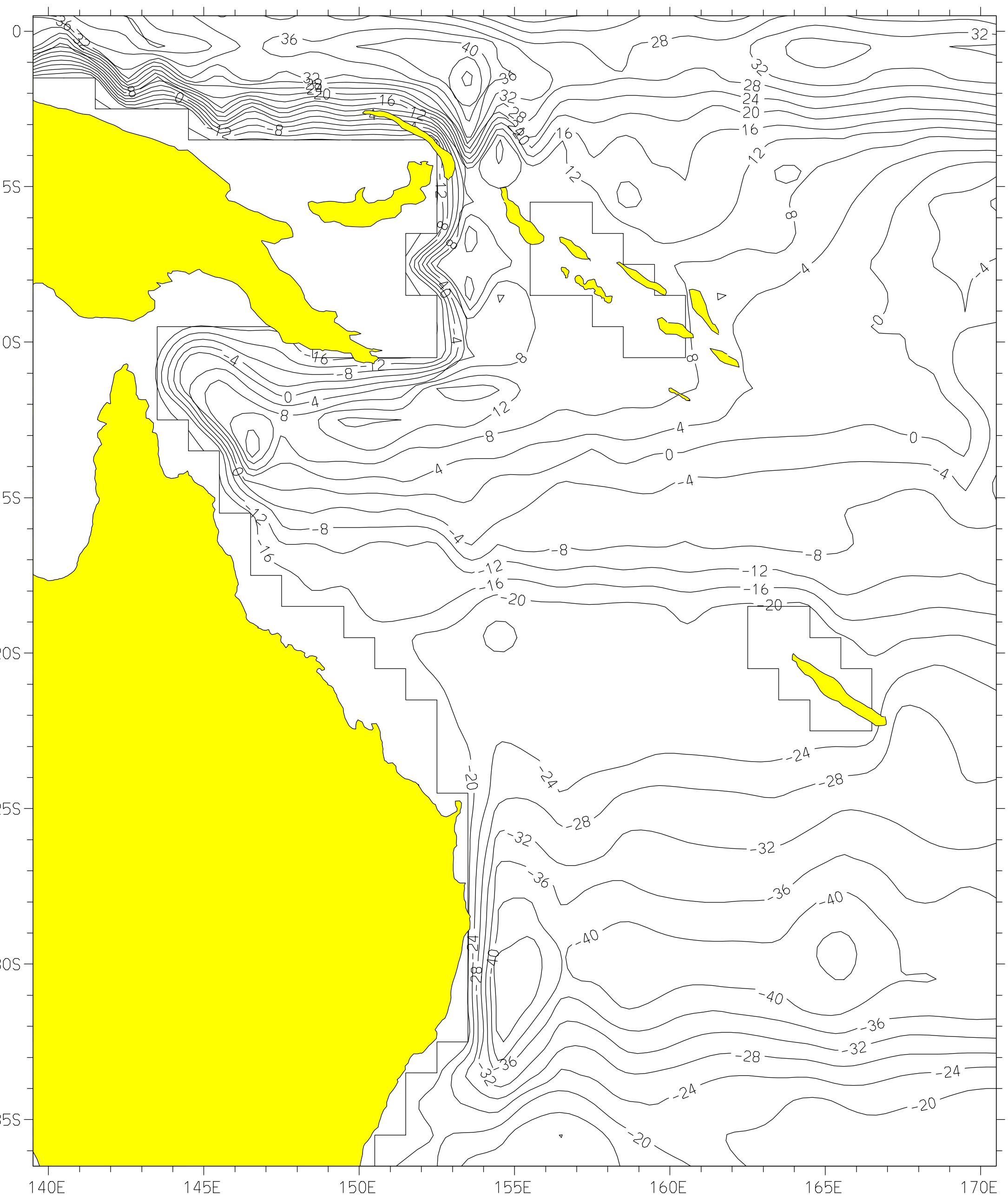

Figure 3.28: **:** Model's barotropic stream function for July-8. Contour increments are $4\,Sv$. The stream function value of Australia is $-18\,Sv$. PNG–Solomons throughflow is $27\,Sv$ and the EAC peak is $31\,Sv$.

the zero normal flux boundary condition. The stream function value for the Australia–PNG continent is $-18\,Sv$. This equates to the IT with opposite sign, where the value for mainland Africa–Europe–Asia–Americas is set to zero by convention. The JADE survey conducted in southern Indonesian waters, the most comprehensive and recent survey, estimates the IT at $21\,Sv$ (Fieux *et al.*, 1993) for August 1989. All of the observed southwards flow is confined above $300\,m$, and there is a weak reversal below the pycnocline.

Analyses of the present field data include only fluxes from $1500\,m$ to the surface. However including observed deep flows ($\sim 4\,Sv$), with the possible exception of Fr0791, would not greatly change those estimates and so comparisons with the model's barotropic stream function are not unreasonable. Abyssal currents in the model's Coral Sea basin also show anticyclonic flow but are weaker than those observed, generally being less that $1\,cm\,s^{-1}$.

The model NGCU near Rossel I. reaches a peak of over $35\,Sv$ but with some of that being due to a recirculating gyre. This is somewhat larger than the observations of 17 to $25\,Sv$, but the contribution from the external mode is, of course, unknown (hopefully small). If the model recirculation gyre is ignored then the NGCU flow is about $25\,Sv$, although the $\sim 25\,Sv$ observational estimates will also include any possible recirculation. The model velocity field shows the same subsurface characteristics as the observations. The model PST is $27\,Sv$, lower than the single observation of $40\,Sv$ from TEW387, but not far outside of the quoted error bounds ($40 \pm 10\,Sv$). The SEC inflow, between the Solomons and New Caledonia, is $30\,Sv$. The maximum flux of the EAC is $31\,Sv$, with about $9\,Sv$ of that being due to recirculation.

Vityaz St. has been closed in the model since the distance between two velocity grid-points is $110\,km$, which is much wider than the deep section of the strait ($37\,km$ between the $300\,m$ isobaths). If Vityaz St. were present in the model, and assuming it carried the observed flux of about $15\,Sv$ westwards (E. Lindstrom, private communication), then the remaining $12\,Sv$ of the model PST must presumably exit along the north coast of New Ireland, or via St. George's Channel. Thus, the modelling results imply that a strong westwards flow should exist, during winter, along the north coast of New Ireland, and that more than half of the volume flux should be below the pycnocline. Admittedly, the model is not representative of the true bathymetry around the northern waters of PNG and the flow paths actually taken may be quite different. However, if Sverdrup theory is a reasonable first order approximation of oceanic flows, then the nett volume fluxes carried by western boundary currents are very much determined by open ocean dynamics and not by the fine details of the bathymetry of a small area. (This may not be true of strong currents driven purely by equatorial dynamics.) In essence, the model's lack of bathymetric resolution around the PNG islands is not expected to alter the nett volume flux predictions. In reality, localized recirculations near western boundaries can greatly increase a boundary current's flux, but such dynamics are generally not apparent using a 1° grid. If the observed PST of $40\,Sv$ from TEW387 is accurate, and assuming the Vityaz throughflow was $15\,Sv$ at that time, then it is reasonable to assume that the remaining $25\,Sv$ would have been exiting northwards between the Solomons chain and New Ireland in July-87. Fig. 3.28 shows an additional large flux, flowing westwards to the north of the Solomons, that then joins the PST to flow westwards along the northern PNG coast. At 145°E this westwards flux is nearly $50\,Sv$ (i.e., $32-(-18)$) and flows westwards until reaching 'Halmahera I.' where it then retroflects eastwards a few degrees north of the equator (also Figs. 5.17 and 5.18). The flow is strongly westwards along PNG's north coast at all depths, for this particular snapshot. Below the pycnocline, the model flow in this area has a substantial seasonal reversal (see Figs. 5.23a and b).

A crude representation of the Queensland Trough is included in the model bathymetry, although it is excessively wide and shallow. Model predictions for July show that the barotropic component along the trough is about $2\,Sv$ to the north and the level of no motion is approximately $310\,m$. The GBRU reaches its maximum northwards velocity at about $450\,m$ and is driven by the bifurcation of the SEC around the Queensland Plateau. The surface bifurcation of the SEC at the Australian coast lies near 15.5°S (Fig. 3.30b). Analyses of data from a long–term current meter mooring (D.M. Burrage, private communication) at 14°21′S:145°21′E show predominantly southward flow at depths of 35 and $75\,m$ ($230\,m$ bottom depth), during all seasons. Therefore, the mean position of the real surface bifurcation is probably confined slightly northwards of 14°21′S.

The model's barotropic stream function for January-8 is shown in Fig. 3.29. The Australian stream function value has increased by $+5\,Sv$ to $-13\,Sv$. The EAC reaches a peak of $36\,Sv$, with about $12\,Sv$ of that being due to recirculation.

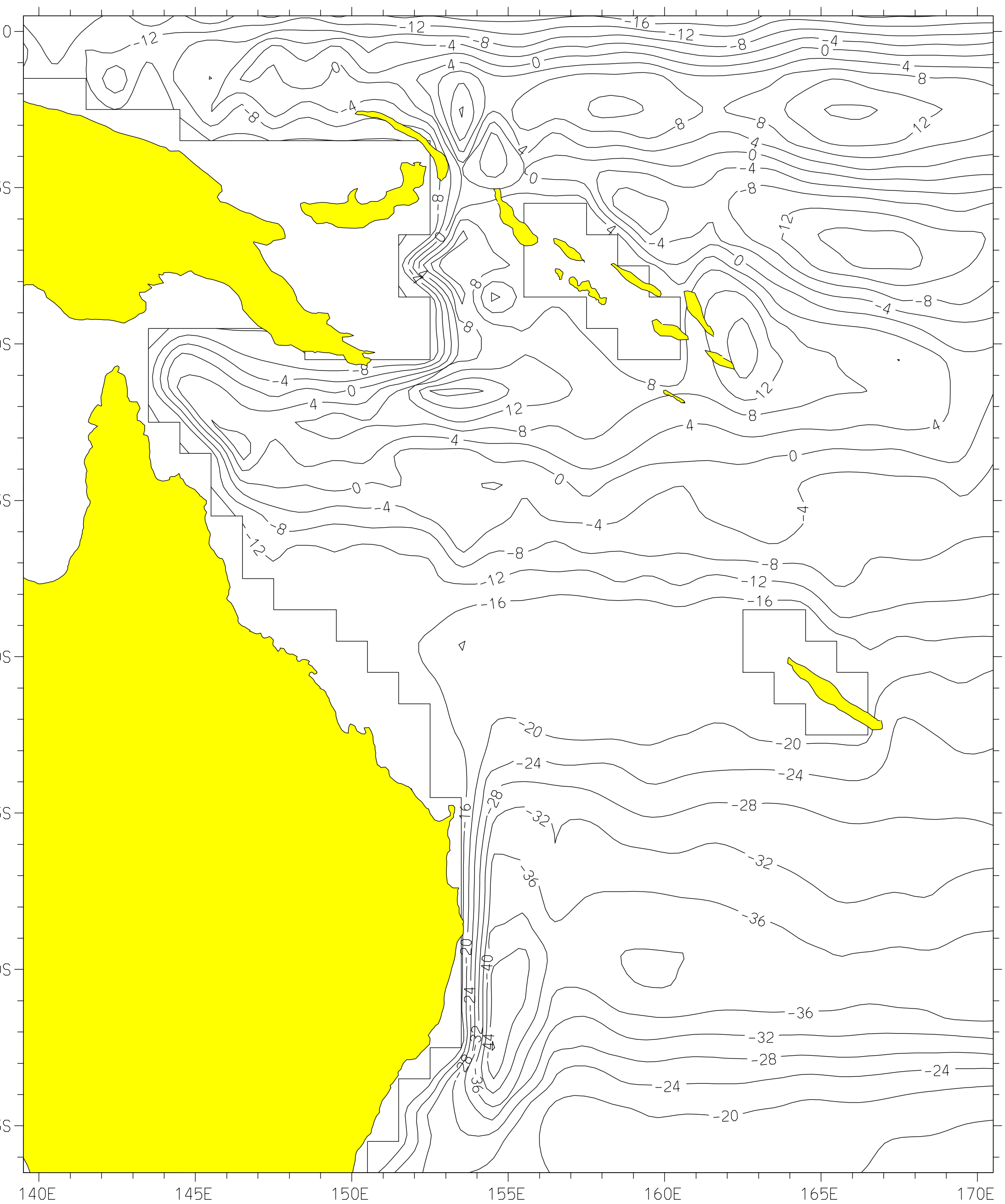

Figure 3.29: **:** Model's barotropic stream function for January-8. Contour increments are $4\,Sv$. The stream function value of Australia is $-13\,Sv$. PNG-Solomons throughflow is $19\,Sv$ and the EAC peak is $36\,Sv$.

The peak NGCU flux near Rossel I. still exceeds $30\,Sv$, and is partly due to a tight recirculating gyre. Neglecting the gyre yields about $20\,Sv$, showing that the nett flux of the NGCU is weaker over the austral summer. The gyre moves back and forth zonally by several hundred kilometres with the seasonal variation, and it is a permanent feature. Figs. 1 and 6 of Donguy *et al.* (1970) show clockwise recirculation, centered about $200\,km$ east of Rossel I., that is reminiscent of the model's gyre.

The westward flux along PNG's north coast is now only about $10\,Sv$, considerably smaller than the July estimate of $50\,Sv$, and entirely retroflects at 141°E. This flux figure is smaller than the observed fluxes through Vityaz St. so that a model with sufficient resolution to correctly include the strait will probably show different flow paths. An influx of northern hemisphere water, originating from the west–northwest and confined to the top layer, occurs in the Bismarck Sea (§3.6.3). Model currents along the northern coast of PNG and nearby islands shown substantial seasonal variability, over a large range of depths. The variability of near surface waters is mentioned above, and waters below the pycnocline show the same behaviour. At 145°E on PNG's north coast, alongshelf currents between the base of the pycnocline and the bottom reverse in direction over the summer–winter cycle. Velocities at $2000\,m$ can exceed $4\,cm\,s^{-1}$ westwards and these strong abyssal currents are responsible for the $50\,Sv$ flow in Fig. 3.28.

The January-8 PST is $19\,Sv$ but can be as low as $10\,Sv$ during summer. There is a small gyre feeding immediately back into the SEC from the east coast of the Solomons. The SEC inflow between New Caledonia and the Solomons has fallen slightly to $25\,Sv$. The nett flux through the Queensland Trough is to the south, but it is only about $1\,Sv$. The surface bifurcation of the SEC occurs at 14.5°S (Fig. 3.30a) on the Australian coast, being barely different from the July results. Analysis of the model's velocity and pressure fields (§3.6.2) clearly demonstrates a change in the bifurcation latitude of the SEC with depth, near the Australian coast. At $450\,m$ the bifurcation occurs close to 21°S for both July and January, just south of the entrance to the Queensland Trough.

3.6.2 Seasonal Pressure Distribution

Fig. 3.30 shows the surface pressure for January-8 and July-8. The contour interval is $2\,mb$, which approximates to $2\,cm$ of surface elevation. The global mean is arbitrarily set to $0\,mb$. The surface bifurcation the SEC is close to 14.5°S at the Australian coast, in January. Since the pressure field tends to be noisy along coastlines, the exact bifurcation latitude is a little difficult to judge from the figure alone. Examination of cross–shelf pressure gradients in the model data gives the latitude more accurately. The July bifurcation is barely changed, at 15.5°S, but the southwards flowing EAC is weaker in winter, while the NGCU is stronger. A closed gyre is evident near Rossel I., at all times of the year, and is similar to the tight cyclonic flow in Figs. 1 and 6 of Donguy *et al.* (1970). The South Equatorial Countercurrent (SECC; Kessler & Taft, 1987) is observed flowing to the east as a pressure ridge along 10°S. It forms along the eastern flank of the Solomons, and the source is from a westwards zonal flow along 4°S.

At about 25°S and further seawards of the EAC, the surface pressure reveals a northwards flow that turns eastwards towards New Caledonia. This flow originates from the anticyclonic loop near the departure latitude of the EAC (33°S). ADCP vectors from Fr0791 (Fig. 3.24) show northward and eastward flows in this area, and this feature will be discussed extensively in Chapter 4.

Fig. 3.31 shows the summer and winter pressure distributions at the model's depth level 2 ($210.5\,m$). Pressures are normally defined at w_t levels, but it is appropriate to average between two w_t layers to get the pressure at the interposed T–UV level. This permits the calculation of geostrophic velocities at the depth levels where horizontal velocities are defined for the B–grid. The surface pressure has not been averaged in this way. The globally averaged pressure at $210.5\,m$ is $216.01\,db$ for both summer and winter; the seasonal change is only of order $\pm 0.003\,db$. The seasonal bifurcation latitudes of the SEC are 16°S and 17.5°S for January and July, respectively. These are a little further south of the seasonal surface bifurcation latitudes. The flow through the Queensland Trough is to the east, but is weak. The pressure gradients of the NGCU are about the same as the corresponding surface pressure gradients, but the EAC is a little weaker. The SEC inflow is relatively constant throughout the year. It must be kept in mind that equivalent pressure gradients in the NGCU and EAC imply much stronger

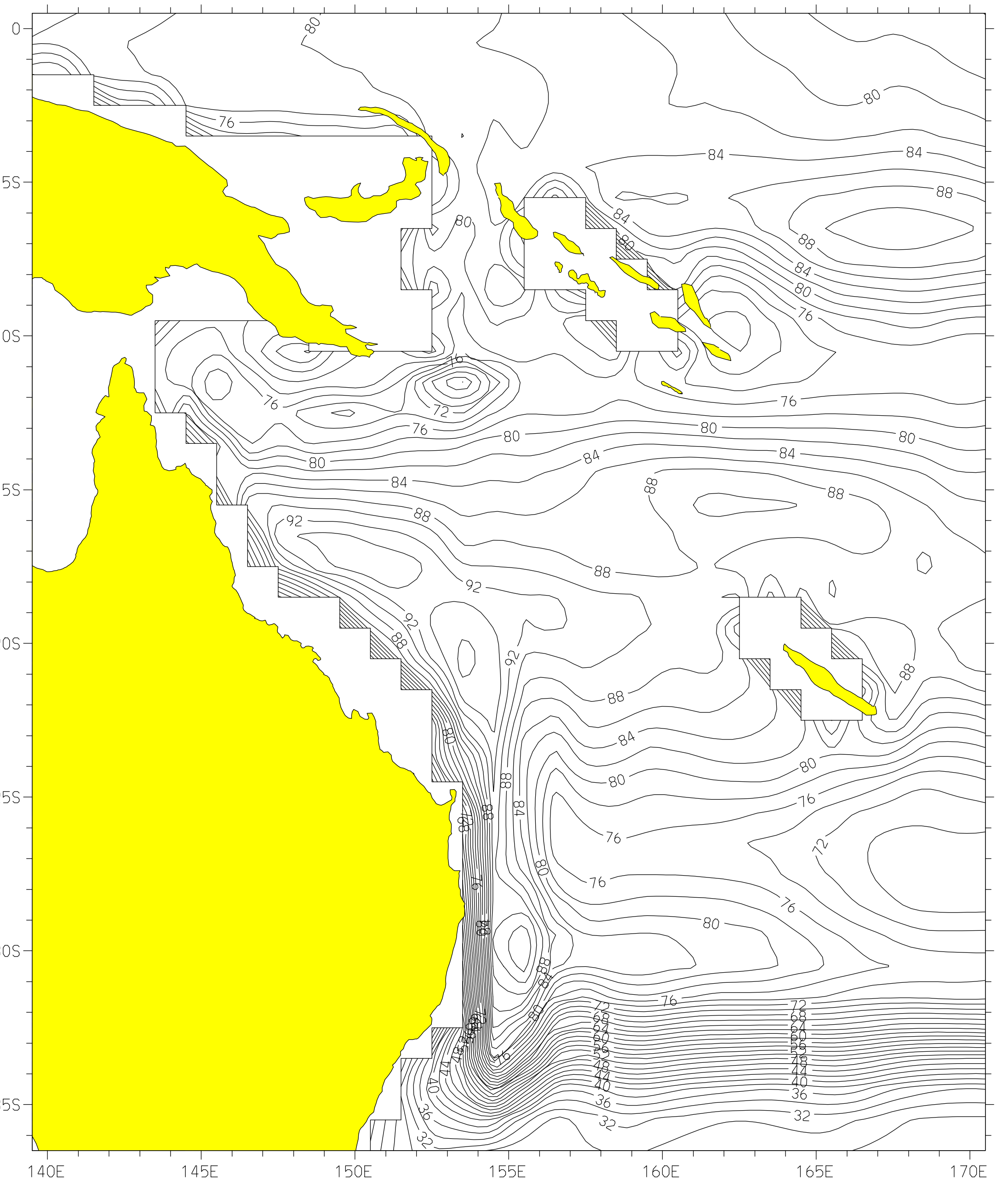

Figure 3.30: **a:** Surface pressure for January-8. Contour interval is $2\,millibars$. The surface bifurcation of the SEC is close to 14.5°S at the Australian coast. The NGCU has a closed gyre near Rossel I.

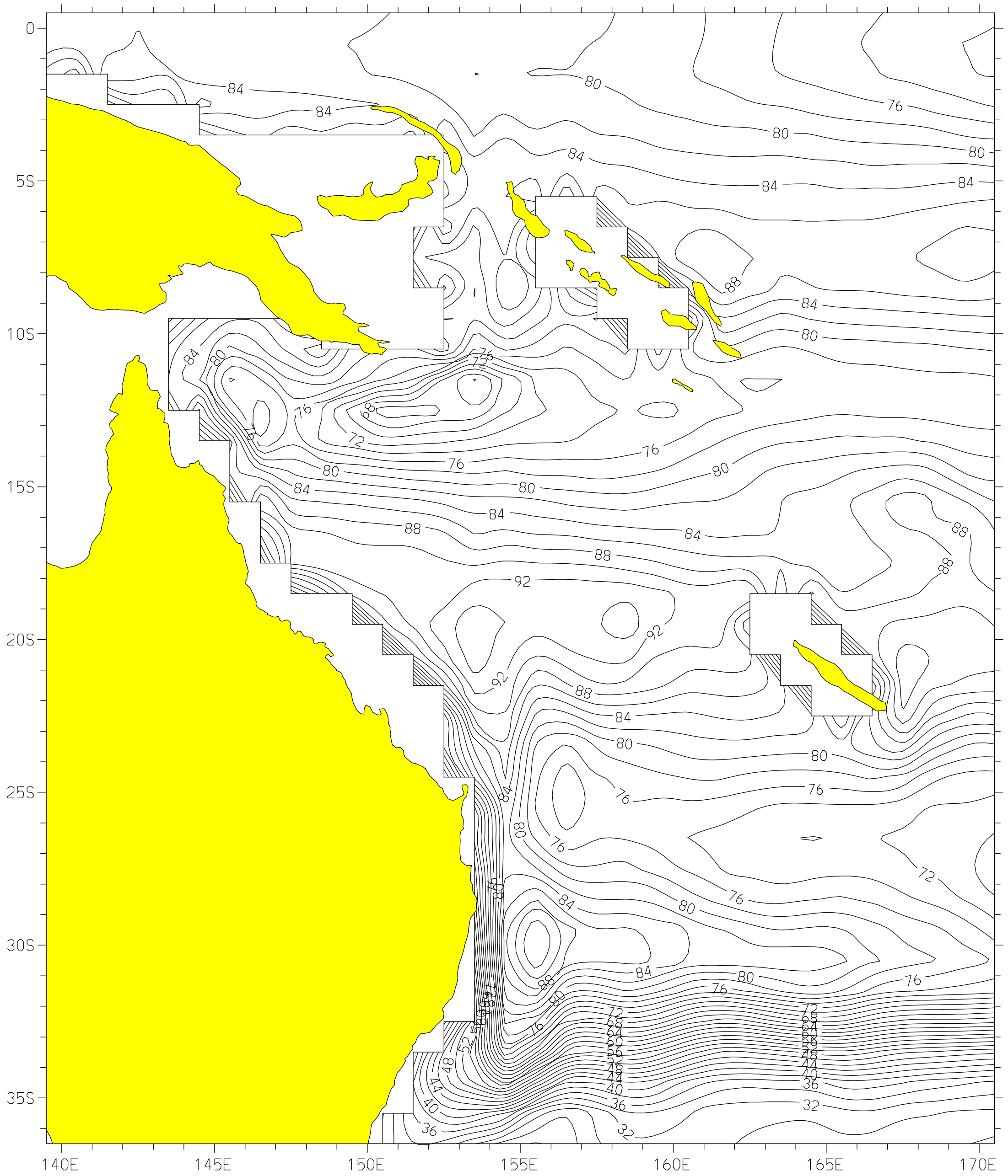

Figure 3.30b: Surface pressure for July-8. Contour increments are $2\,mb$. The surface bifurcation of the SEC is close to 15.5°S at the Australian coast. The NGCU has a closed gyre near Rossel I.

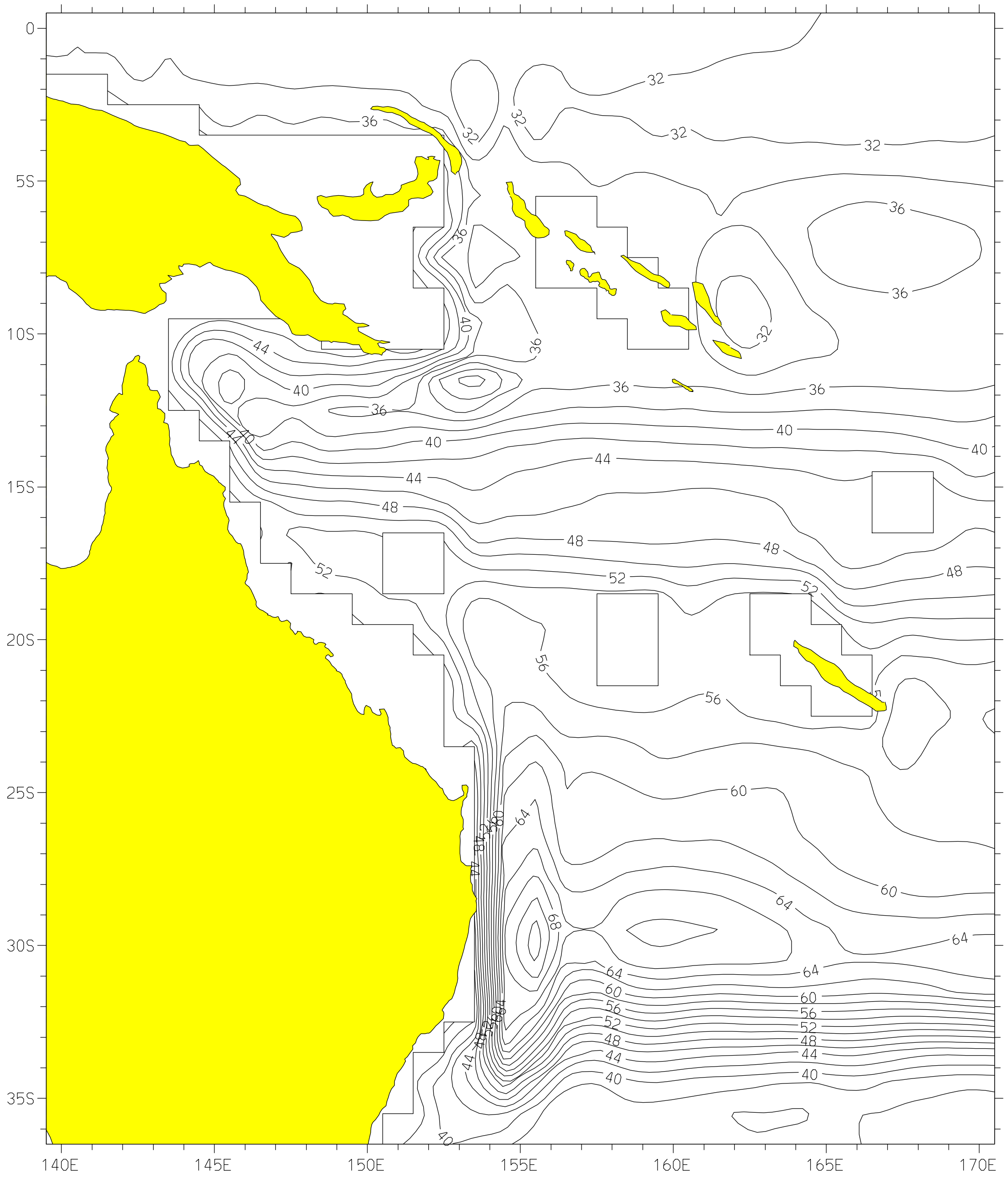

Figure 3.31: **a:** Pressure at 210.5 m (level 6) for January-8. Contour increments are $2mb$. The bifurcation of the SEC is 16°S at the Australian coast, and the flow through the Queensland Trough is eastwards (south–eastwards for the real bathymetry). The closed gyre near Rossel I. is still apparent.

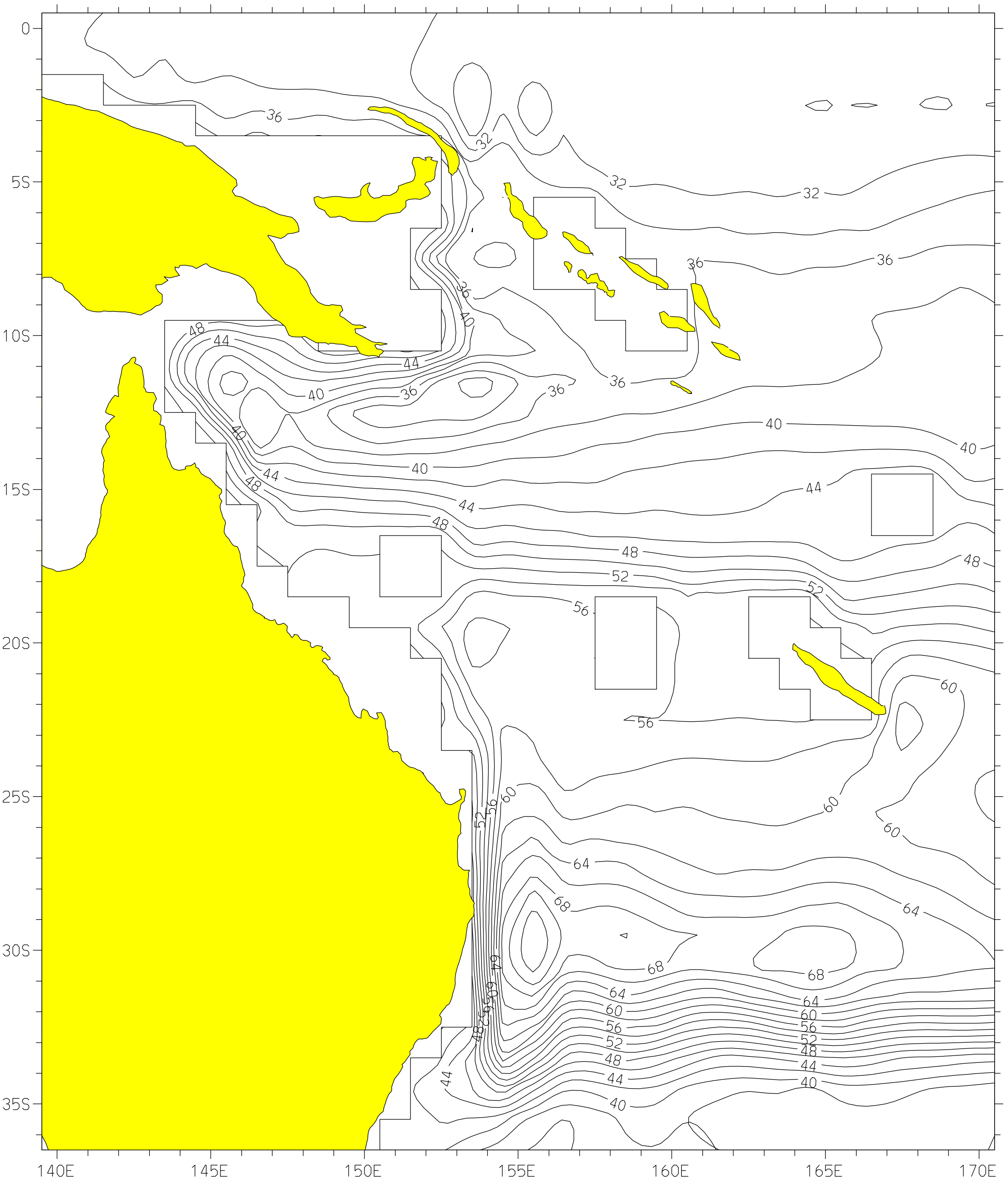

Figure 3.31b: Pressure at 210.5 m (level 6) for July-8. Contour increments are 2 mb. The bifurcation latitude of the SEC is 17.5°S at the Australian coast. The flow through the Queensland Trough is to the east, but is quite weak.

flows in the NGCU, since its local Coriolis parameter is less than half of that for the EAC area.

Fig. 3.32 shows the pressure distribution for January-8 and July-8, at 641.0 m (level 9). The globally averaged pressure at this depth is 658.798 db for January-8 and 658.793 db for July-8. The NGCU cross–shelf pressure gradients are stronger in winter (July), and taking its diminished Coriolis parameter into account, it has larger geostrophic velocities than the EAC, at this depth.

The seasonal bifurcation latitudes of the SEC are 23.5°S for both January and July. The flow though the Queensland Trough is strongly to the west (north–westwards for the real bathymetry) for all seasons. The NGCU cross–shore pressure gradient is quite weak on the northern side of PNG (f is also small). However, the velocities can be quite large: compare Figs. 3.40a and 3.40b. Below the pycnocline, model pressure fields can be somewhat noisy in certain areas, and so are not examined further.

The model surface pressure contours show a fall of about 15 mb between 20° and 13°, implying a strong surface inflow into the Coral Sea. Historical data do not show this feature; Wyrtki (1975) and Scully-Power (1983) both show the surface elevation to be fairly flat. Fig. 1 of Donguy *et al.* (1970) does show such a fall but the contour pattern is not connected with the South Pacific further eastwards. Fig. 3.20 does imply a strong surface inflow, although this merely one observation; the steric height fall implied is 29 cm. Thus, the models predicted height field is generally not in accord with the limited data of the area.

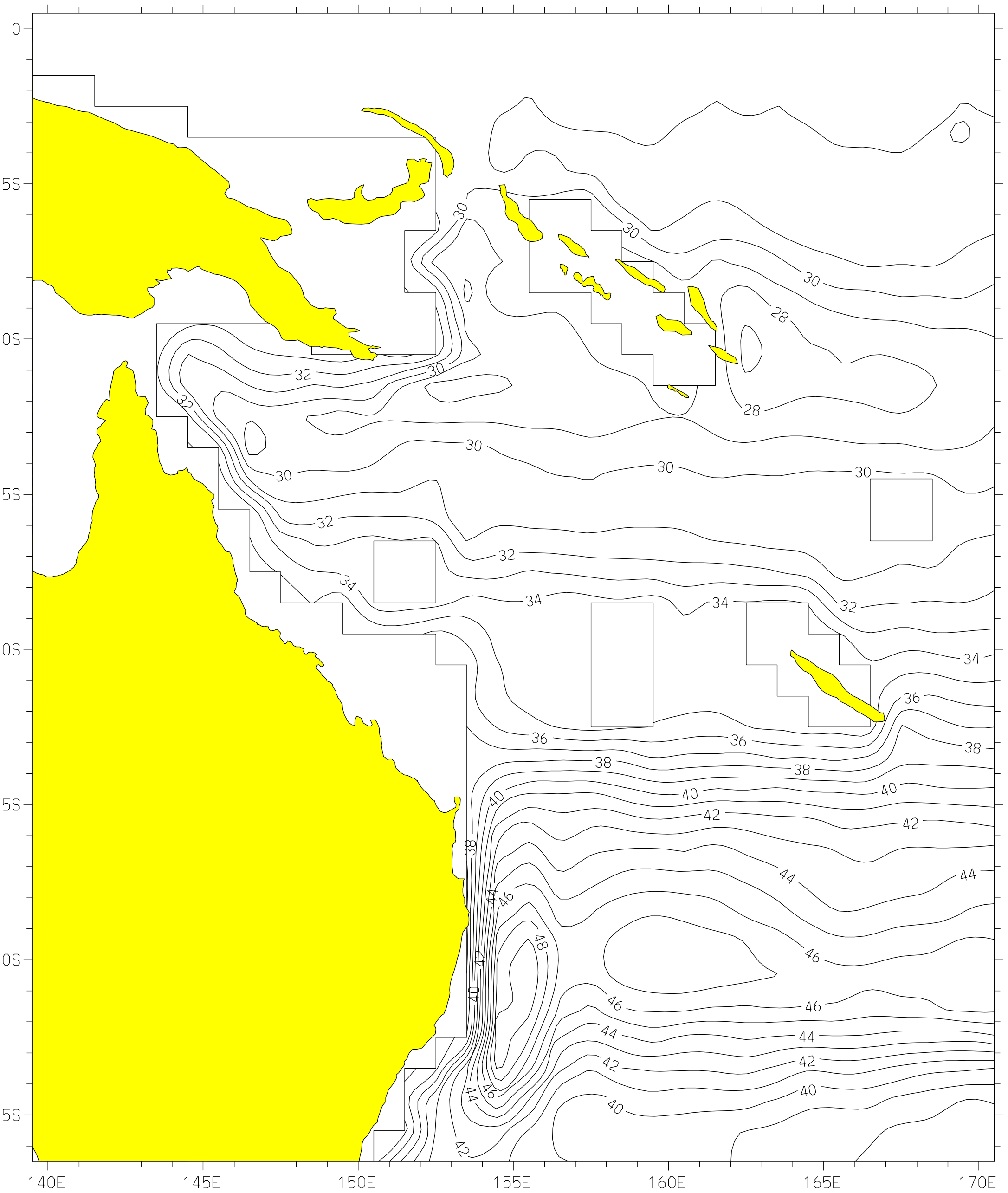

Figure 3.32: **a:** Pressure at 641.0 m (level 9) for January-8. Contour increments are 1mb. The bifurcation of the SEC is 23.5°S at the Australian coast, and the flow through the Queensland Trough is strongly to the west.

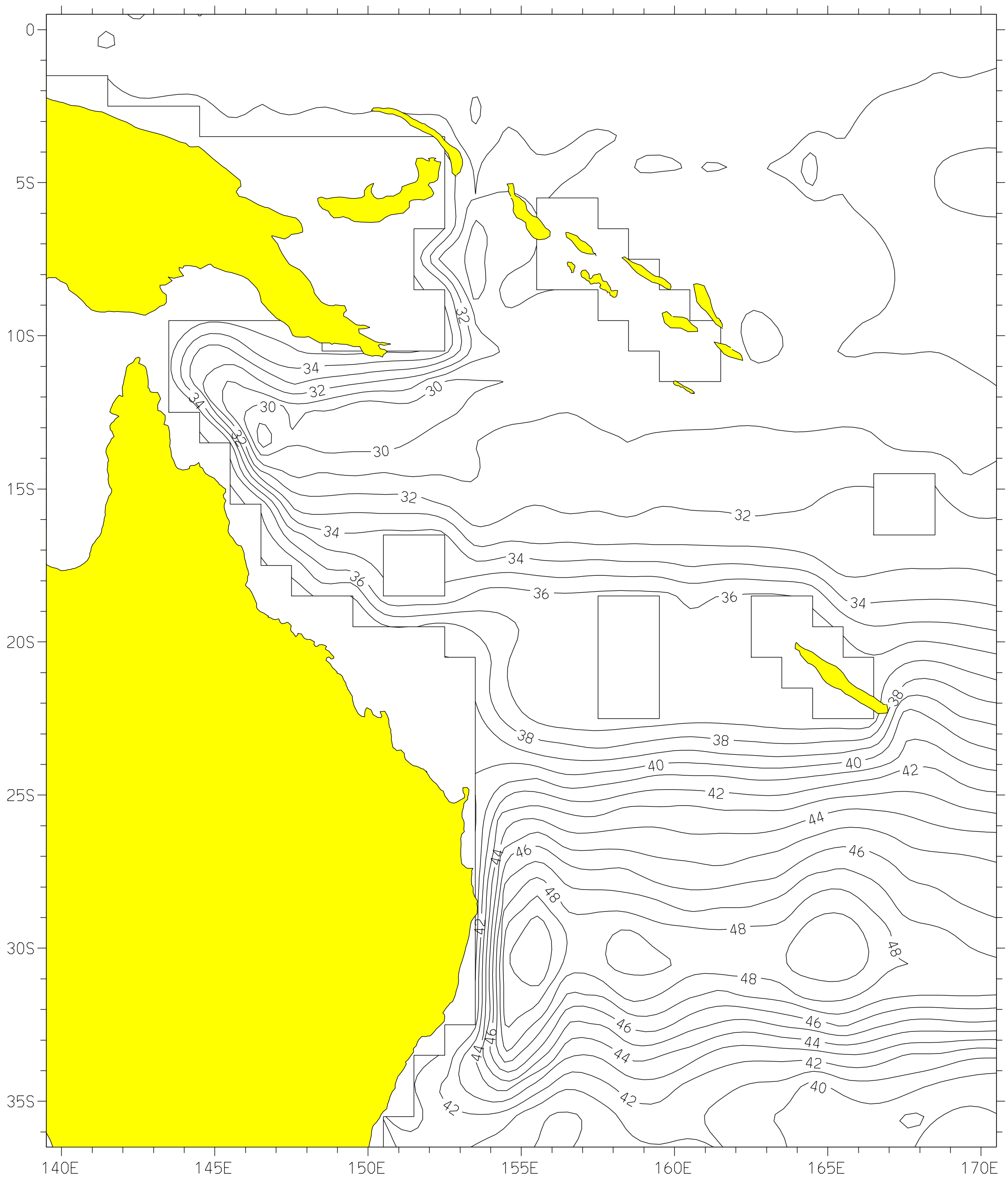

Figure 3.32b: Pressure at 641.0 m (level 9) for July-8. Contour increments are 1 mb. The bifurcation latitude of the SEC is 23.5°S at the Australian coast. The flow through the Queensland Trough is strongly to the west.

3.6.3 Seasonal Velocity Fields

Figs. 3.33 and 3.34 show velocities at $13.5\,m$ (level 1) for January-8 over the Coral Sea and areas further north, respectively. Level 1 effectively constitutes the Ekman layer, and although it is $27\,m$ thick, ageostrophic velocities clearly demonstrate the direct effects of the wind stress (see Fig. 3.37). NGCU velocities around the Gulf of Papua and Solomon Sea are comparable in magnitude with those of the EAC. However, the ADCP vectors of Fig. 3.24 show that near surface velocities are larger in the EAC; $100\,cm\,s^{-1}$ versus $60\,cm\,s^{-1}$. Either there are insufficient ADCP data, in time and in space, to give a good average, or else the model surface velocities have been distorted by the confined area of the Gulf of Papua. The eastward flow immediately to the south of New Caledonia, implied by the surface pressure, is not apparent in Fig. 3.33. It has been obscured by the south–westwards Ekman drift, but is observable in the deeper velocity fields. In general, the velocity field at level 1 is not in tight geostrophic balance unless the local wind stress is comparatively small. The SECC is evident near 8°S on the eastern side of the Solomons. It is present for the entire year and is stronger during December to April.

A strong eastward flow along the north coast of PNG–New Ireland (i.e., Bismarck Sea) is a regular occurrence in summer (Fig. 3.34), but only in the surface layer. Winter surface velocities are strongly to the west (Fig. 3.36). The central core of the NGCU, within the thermocline, does not reverse seasonally. The summer eastwards flow is sourced from north of the equator, at the western tip of Irian Jaya. Lindstrom *et al.* (1990) observe a surface salinity decrease of $1\,psu$ in Vityaz St. during summer. Donguy & Henin (1975a) observe similar low salinity surface water intruding southwards into the Solomon Sea, but they show that it is more likely due to local rainfall during the monsoon season than clearly identifiable northern hemisphere water. Since the model bathymetry does not include Vityaz St. it cannot be used to gauge the extent to which northern hemisphere surface water may actually intrude. In any event, since it is surface water, tracer information relating to its origins will be lost on a time scale of weeks. The local wind stress changes direction correspondingly over summer and is presumably the cause of the surface flow reversal. Close to the equator, the ocean can respond rapidly to changes in the wind stress, in a matter of weeks. The observed NGCU flow within the thermocline does not reverse seasonally in

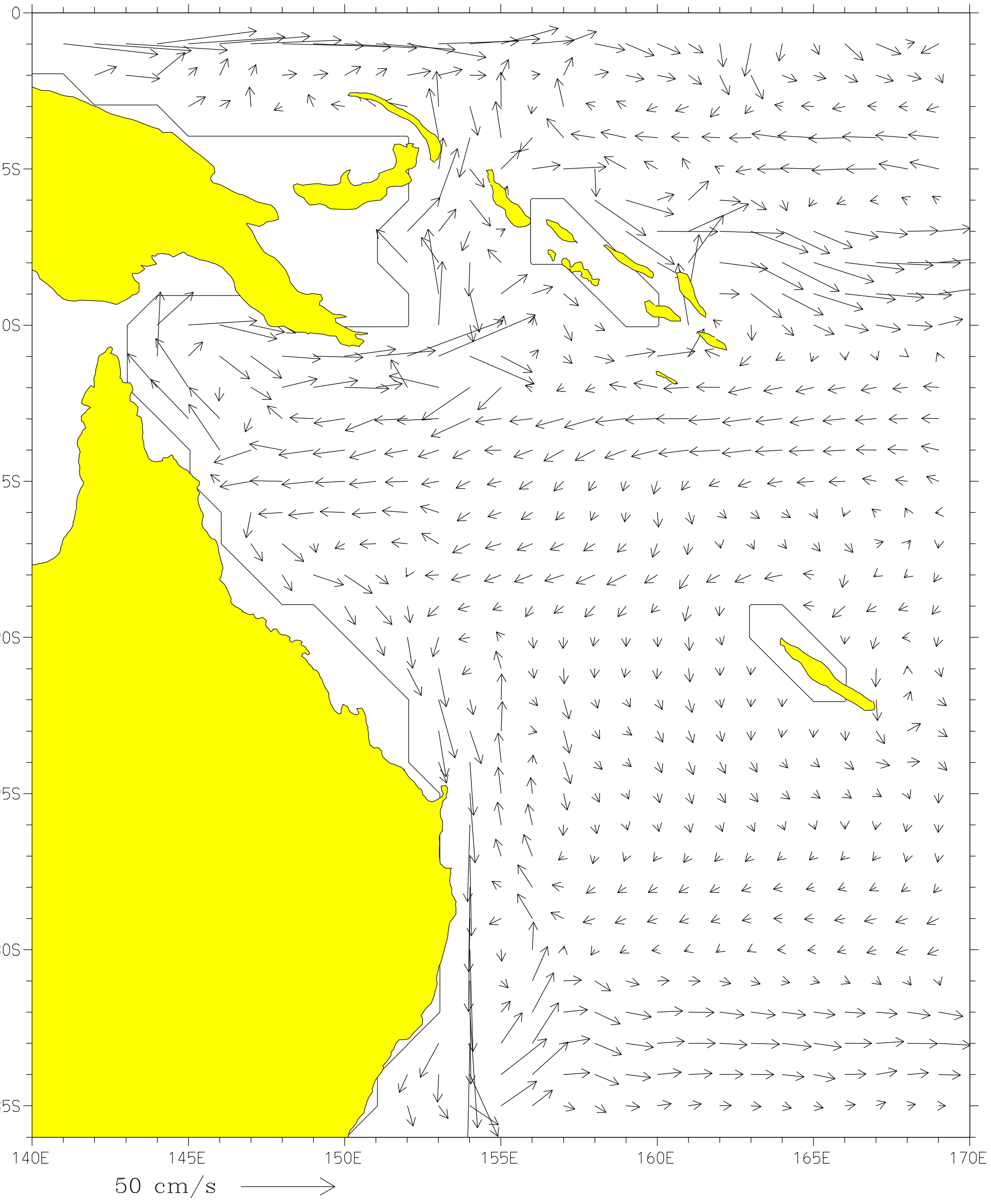

Figure 3.33: : Velocities for January-8 at 13.5 m (level 1).

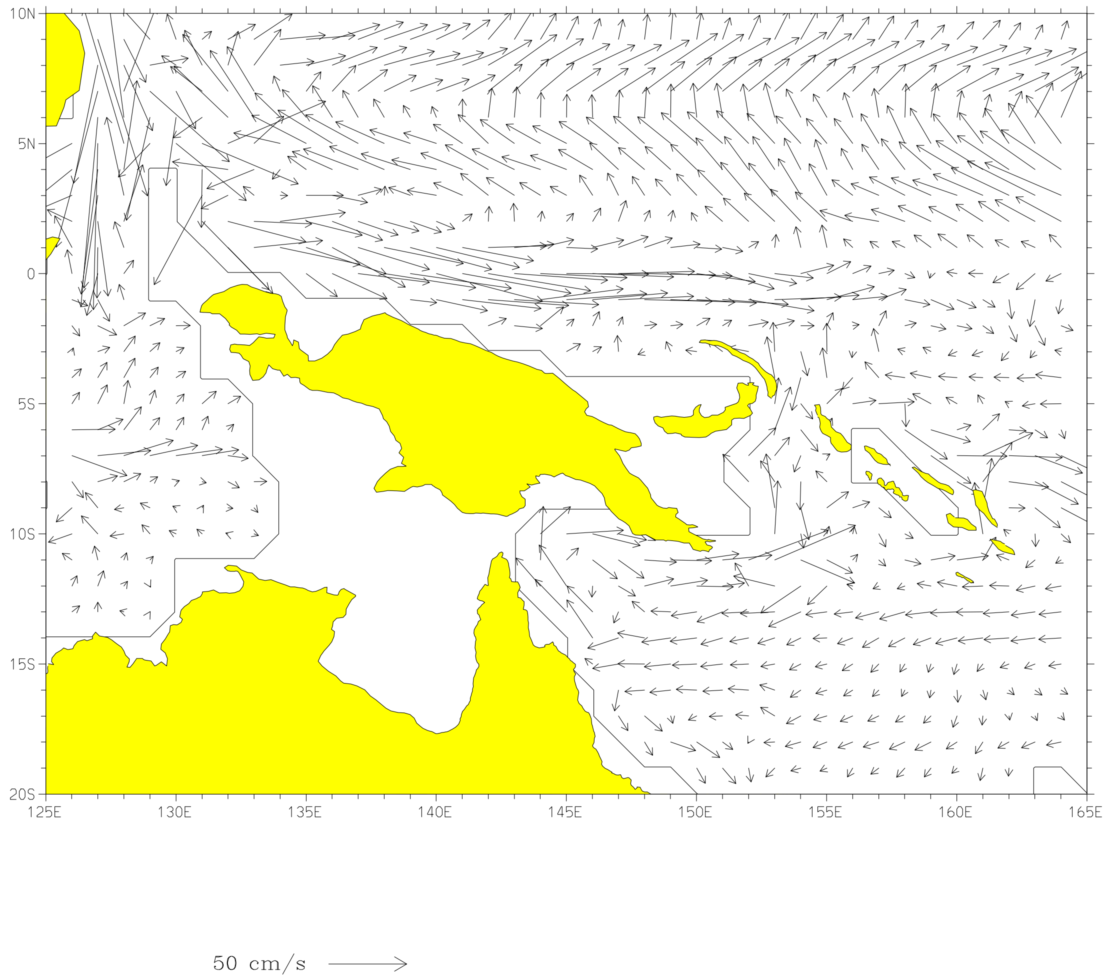

Figure 3.34: **:** Velocities for January-8 at 13.5 m (level 1), north of PNG.

Vityaz St. (E. Lindstrom, private communication). The model's NGCU exhibits a seasonal variation of its retroflection longitude (north coast of PNG and Irian Jaya), but it does not show a seasonal reversal in flow direction, whereas the corresponding subpycnocline waters do reverse.

Figs. 3.35 and 3.36 show velocities at 13.5 m, during July-8. Near 15°S, the Ekman drift from the strengthened Trade Winds is obvious, partially obscuring the NGCU in the Coral Sea. Fig. 3.37 shows the annually–averaged ageostrophic component at level 1 (13.5 m), and can essentially be regarded as the Ekman drift. The drift is quite large near 15°S, due to the winter Trades, but is weaker further to the south. Large ageostrophic velocities are evident near the equator. Along the north coast of PNG, the surface layer of the NGCU is enhanced by the increased Trades and the flow continues to Halmahera Island (the 'L'–shaped extension to Irian Jaya), before retroflecting.

Fig. 3.38 shows velocities at 40.5 m (level 2) during January-8 and July-8. The ageostrophic component (not shown) is much smaller than for the surface layer, and the NGCU flows in one direction only, for both seasons. It is a little stronger in winter, and the flow along the north coast of PNG is enhanced by a zonal current at 3°S, originating from east of the Solomons. This zonal flow is quite variable and is associated with the Legeckis waves mentioned in §3.6.1. A northwards flow is evident immediately seawards of the EAC, at 23°S, and is in modest agreement with Fr0791 ADCP data (Fig. 3.24).

Fig. 3.39 shows velocities at 210.5 m (level 6) during January-8 and July-8. The velocity field at this depth is similar to the 40.5 m field, but the EAC is weaker, and the flow through the Queensland Trough is nearly stagnant. The NGCU is stronger in winter, but is no longer intensified by the zonal flow north of the Solomons, for this particular winter snapshot. The bulk of the SEC's inflow occurs between New Caledonia and the Solomons. The SEC bifurcates on the eastern flank of the Queensland Plateau, at 17.5°S.

Fig. 3.40 shows velocities at 641.0 m (level 9), during January-8 and July-8. The NGCU is now noticeably stronger than the EAC, for both seasons, although the westwards flow along the north coast of PNG is not present in January-8. In January-8 the NGCU turns eastwards at the northern end of the Solomon Sea, flows along the eastern coast of the Solomons, and departs zonally to the east.

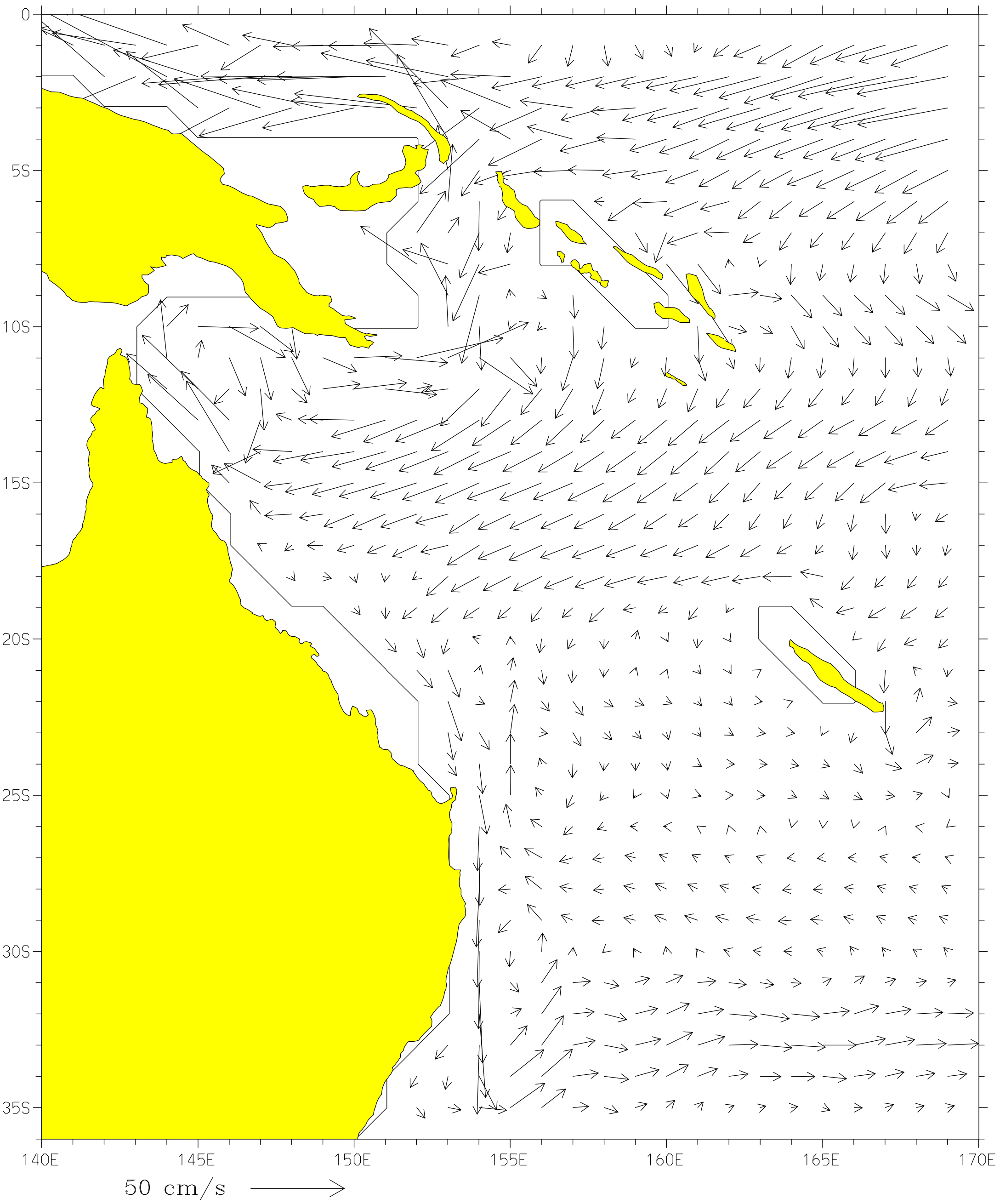

Figure 3.35: : Velocities for July-8 at 13.5 m (level 1).

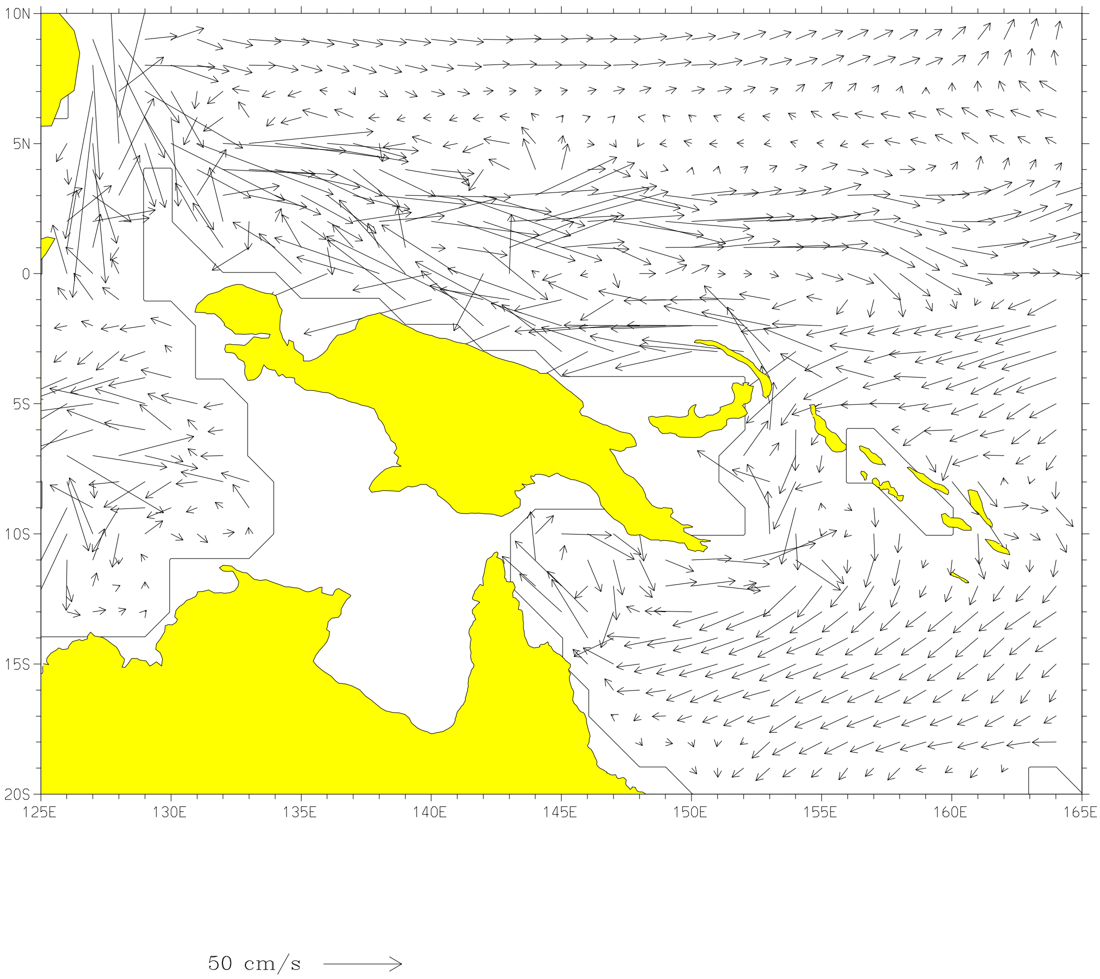

Figure 3.36: **:** Velocities for July-8 at 13.5 m (level 1), north of PNG.

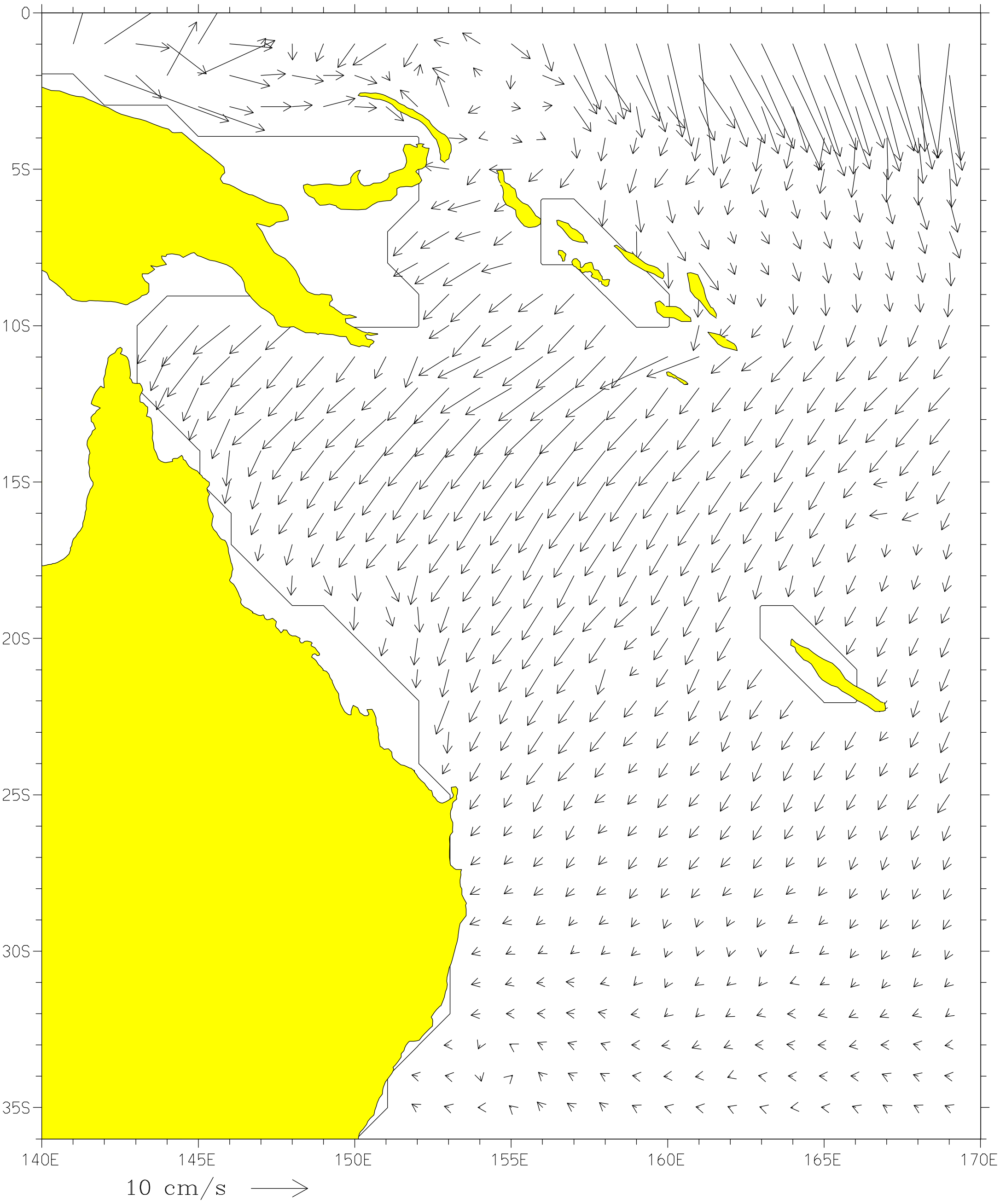

Figure 3.37: **:** Annually–averaged ageostrophic velocities at $13.5\,m$ (level 1).

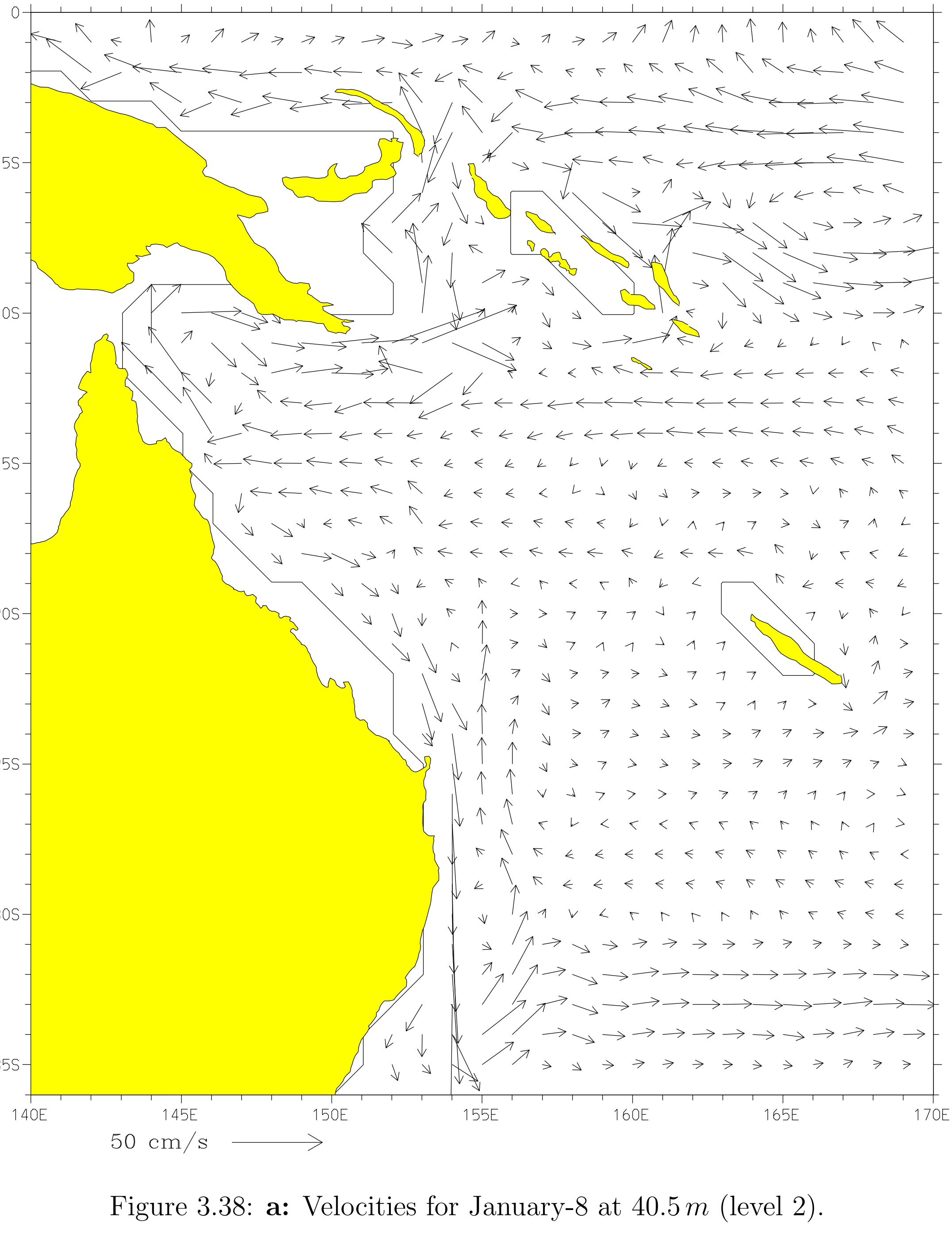

Figure 3.38: **a:** Velocities for January-8 at 40.5 m (level 2).

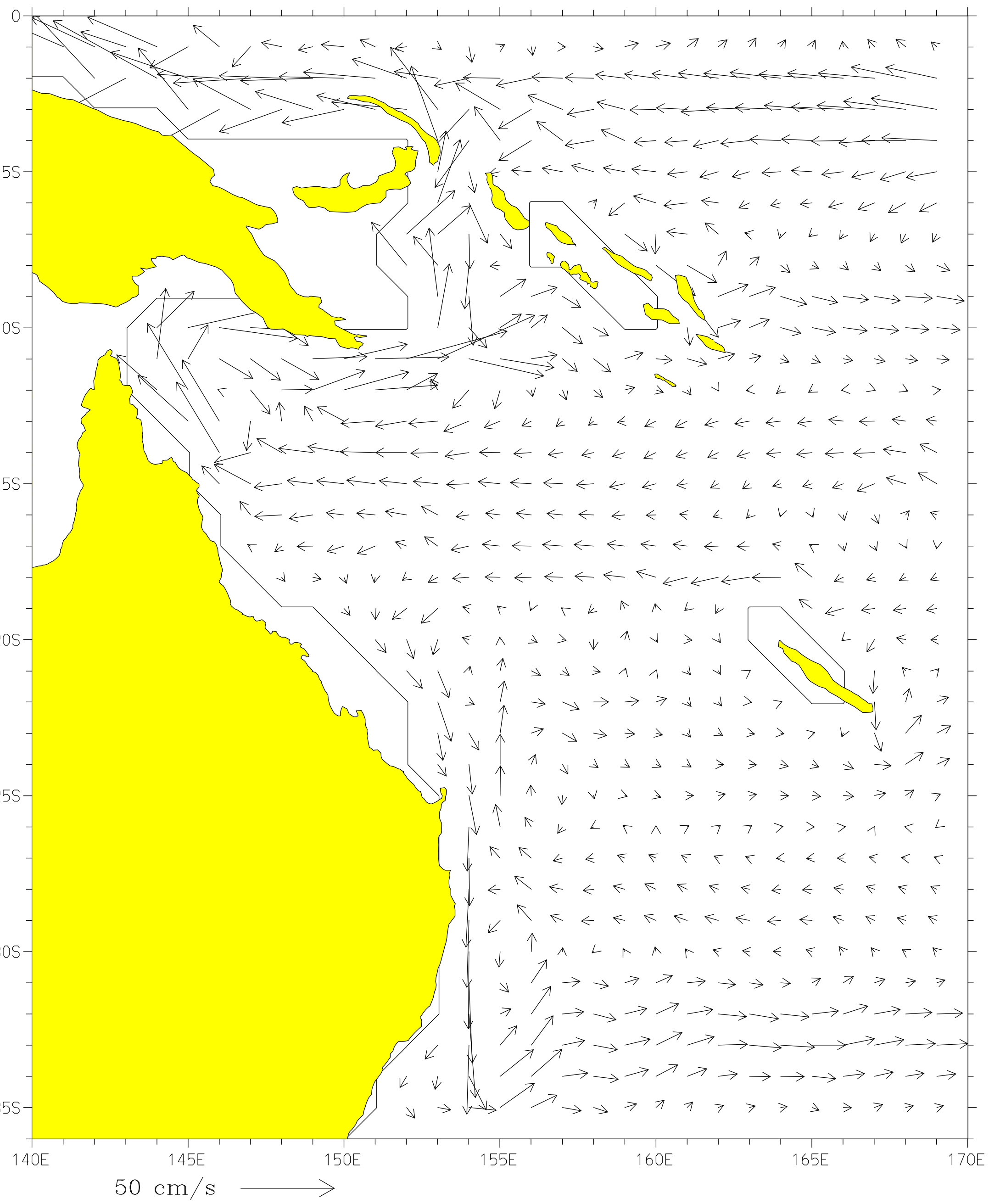

Figure 3.38b: Velocities for July-8 at 40.5 m (level 2).

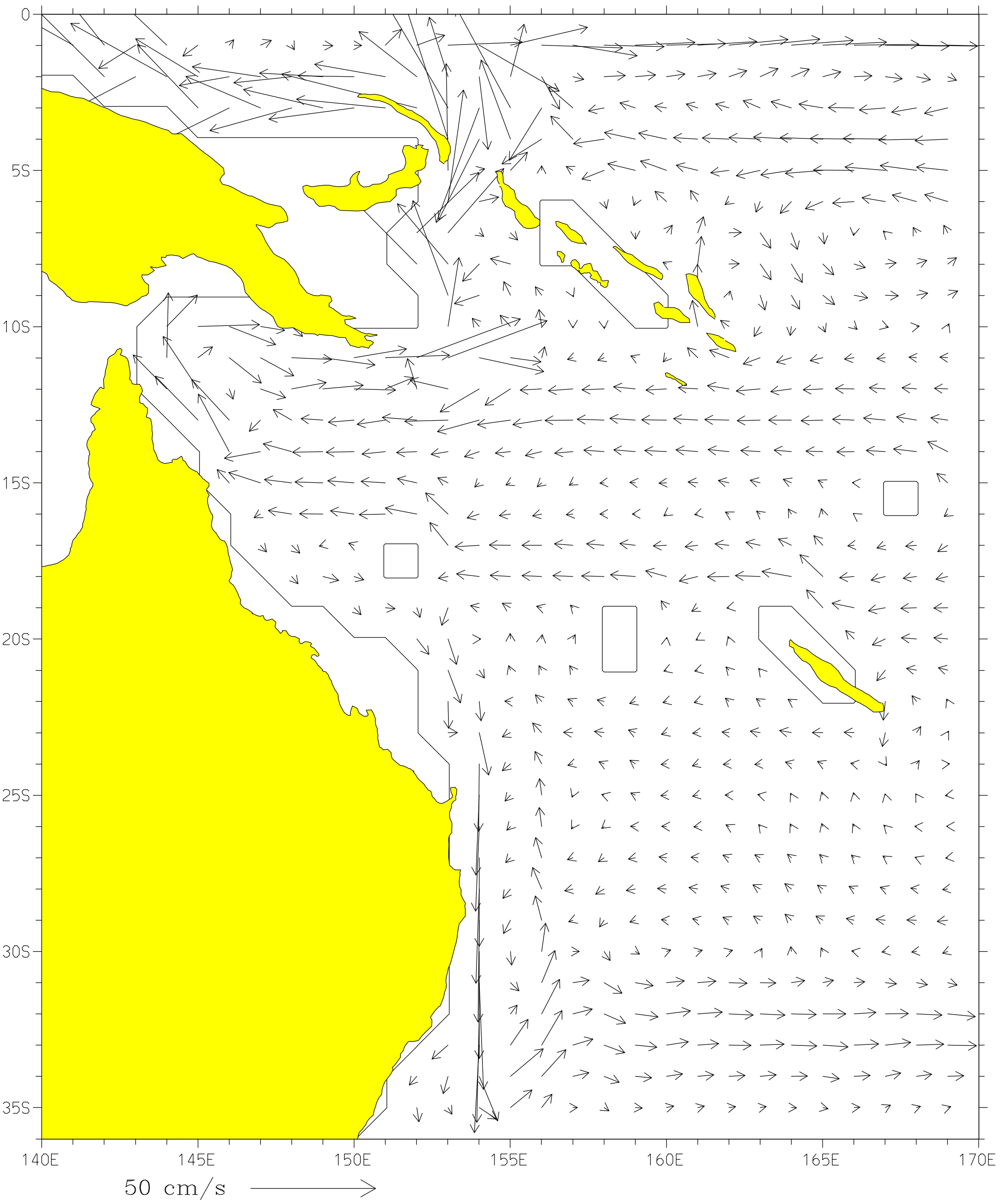

Figure 3.39: **a:** Velocities for January-8 at 210.5 m (level 6).

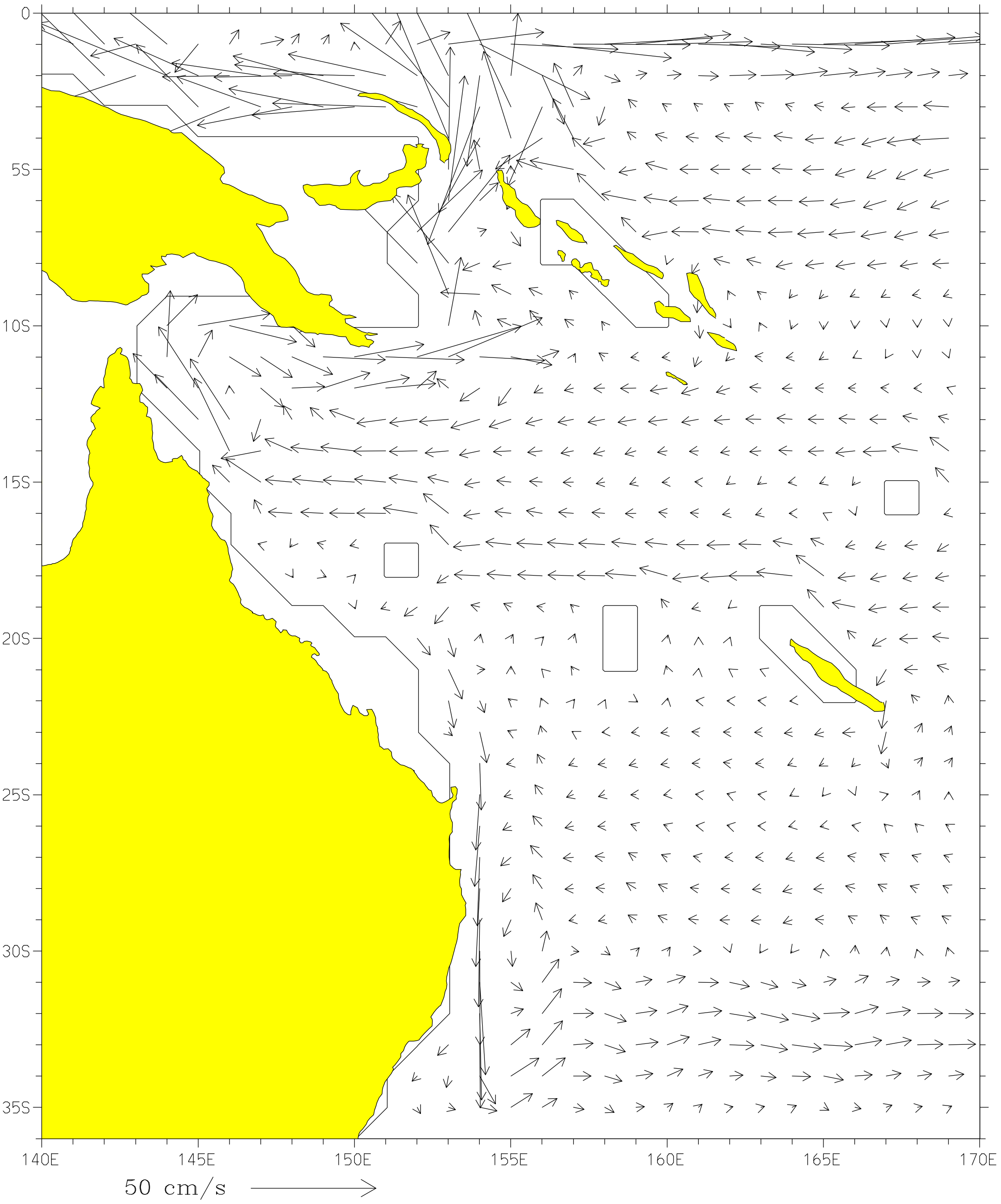

Figure 3.39b: Velocities for July-8 at 210.5 m (level 6).

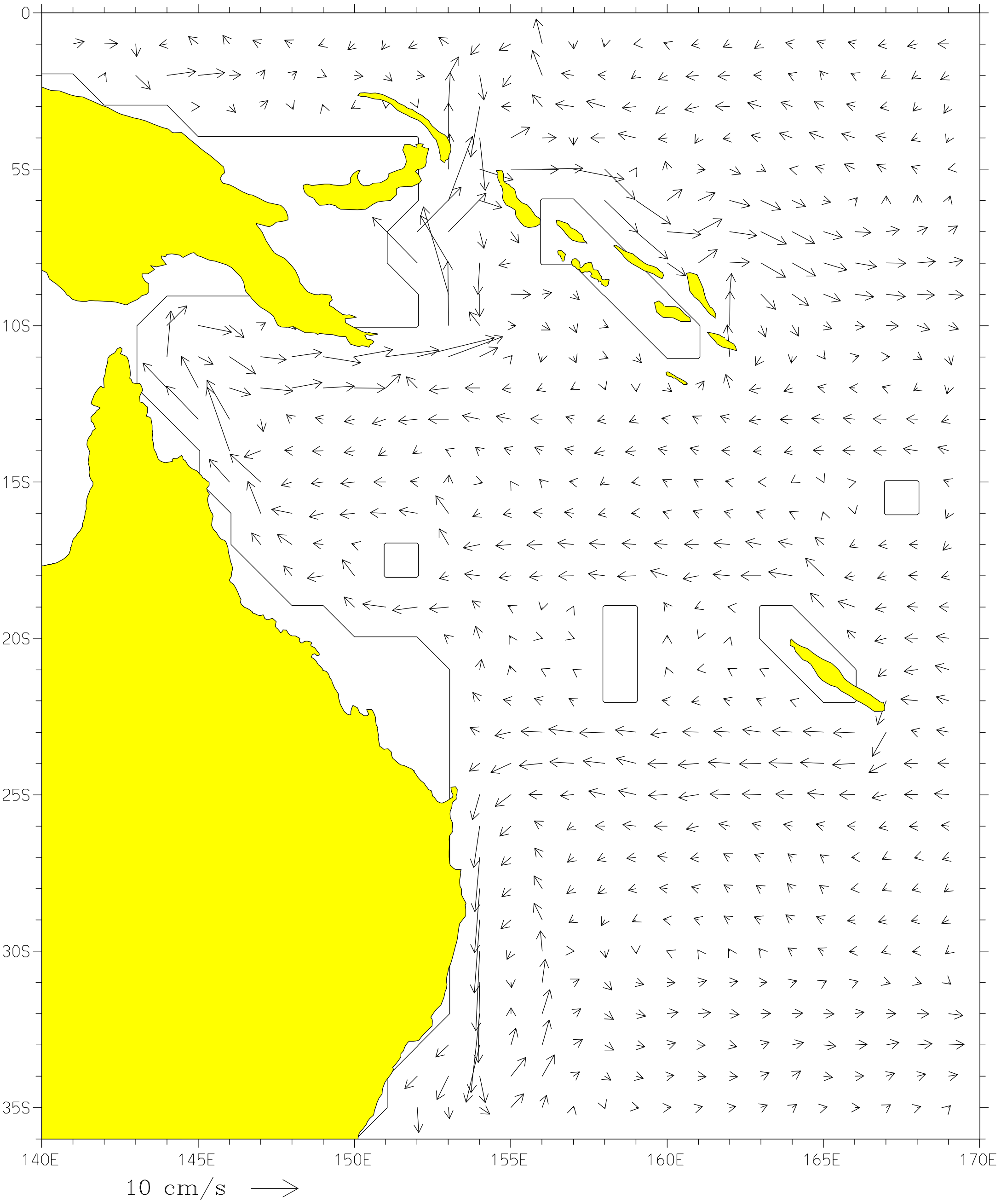

Figure 3.40: **a:** Velocities for January-8 at 641.0 m (level 9).

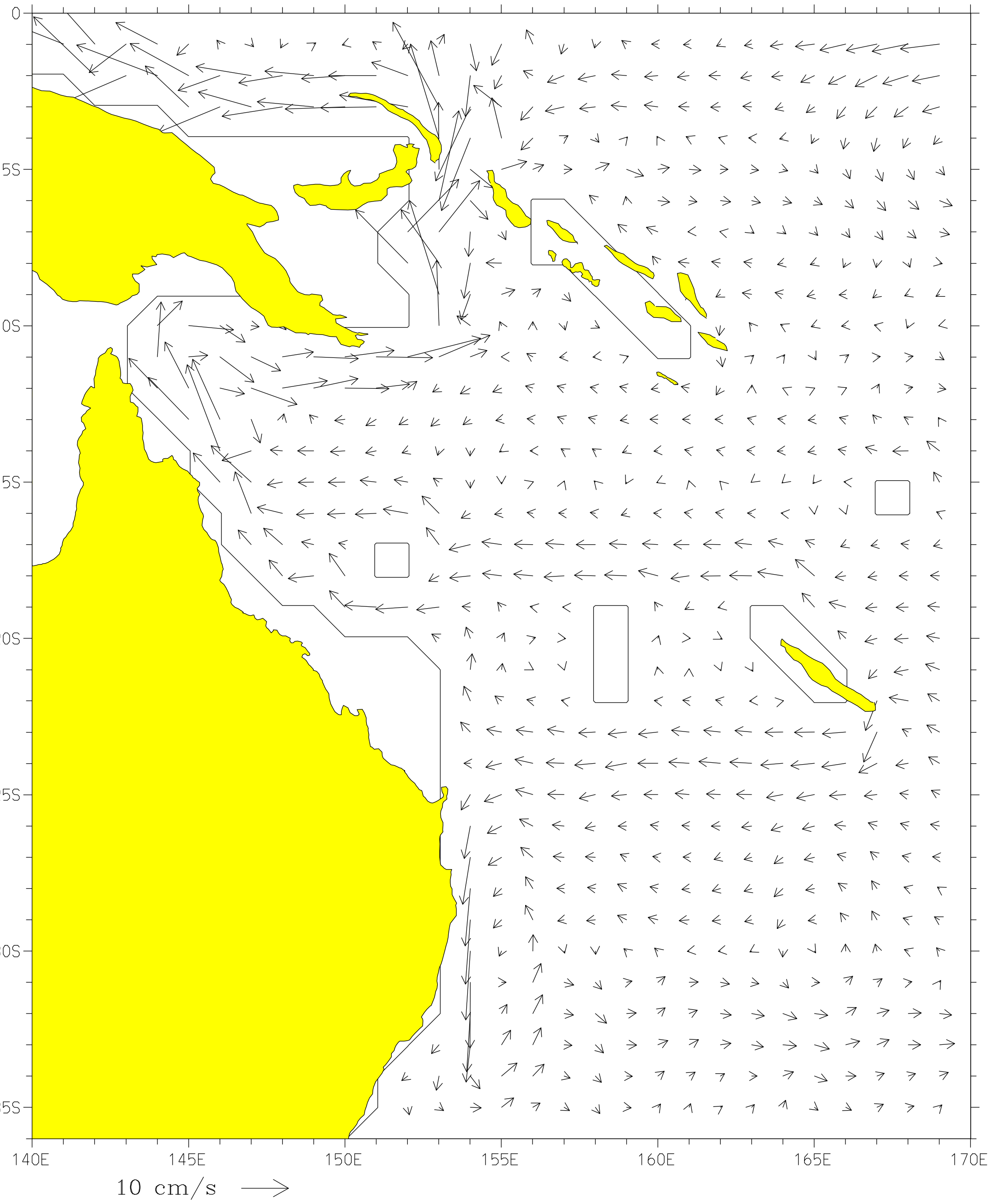

Figure 3.40b: Velocities for July-8 at 641.0 m (level 9).

However, in progressively deeper water, zonal flows at the equator determine the direction of flow along PNG's north coast, and the influence of the NGCU diminishes. The flow through the Queensland Trough is to the west (northwest for the real bathymetry) for all seasons. The zonal centreline of the SEC inflow is at about 20°S, and it bifurcates around New Caledonia. The bifurcation latitude at the Australian coast is 23.5°S.

Fig. 3.41 shows velocities at 1227.0 m (level 11), during January-8 and July-8. The NGCU is now only a recognizable feature during winter, and the flows along PNG's north coast are driven by zonal equatorial currents rather than the SEC. Part of an equatorial planetary wave is observed at 2°S:166°E (Fig. 3.41), having a clockwise circulation. The SEC's centreline is at 25°S, and most of it turns southwards at the Australian coast.

Fig. 3.42 shows velocities at 1636.0 m (level 12), during January-8 and July-8. The seasonal reversal of model equatorial flows is quite strong and the planetary wave is still observable at this depth (Fig. 3.42a, see also Fig. 5.23a). Whether or not such seasonal reversals occur in reality is unknown. There is a 2000 m deep plateau (Ontong Java) to the northeast of the Solomons and the planetary wave has just collided with it. The circulation in the Coral Sea Basin is roughly anticyclonic, in agreement with the field surveys. There are strong summer inflows into the Coral Sea, of low latitude water masses, which enter between PNG and the Solomons, and to the southeast of the Solomons. The flow between the Australian coast and the Bellona Platform (22°S) is entirely southwards for both seasons. It will be shown in Chapter 4 that this is not in accord with reality, and that a nonlinear viscosity scheme (Smagorinsky mixing) produces the correct northwards flow of Tasman Sea water.

Fig. 3.43 shows velocities at 2120.0 m (level 13), during January-8 and July-8, respectively. The planetary wave is abutted against the eastern flank of the Ontong Java Plateau. Some further analysis of the model's pressure and vector fields (not shown) reveals a steady stream of planetary waves arriving from the east, with zonal wavelengths of about 1000 km. As mentioned previously, these waves have periods of about one month, which is suggestive of Legeckis waves. The circulation in the Coral Sea Basin is more strongly anticyclonic in summer and is fed by an inflow southeast of the Solomons. The annually–averaged inflow of this low latitude water amounts to about 2 Sv over levels 12 and 13, and it

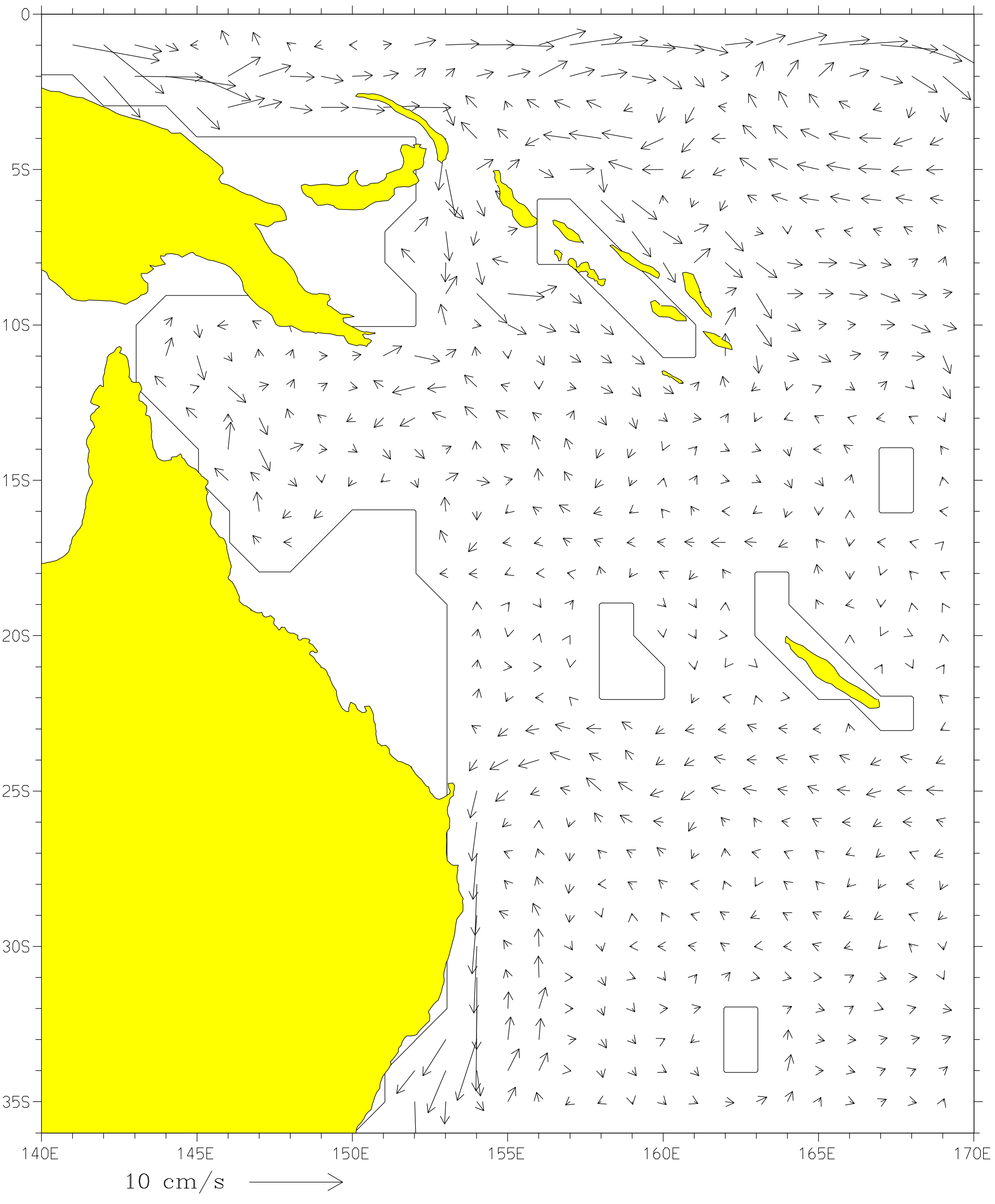

Figure 3.41: **a:** Velocities for January-8 at 1227.0 m (level 11).

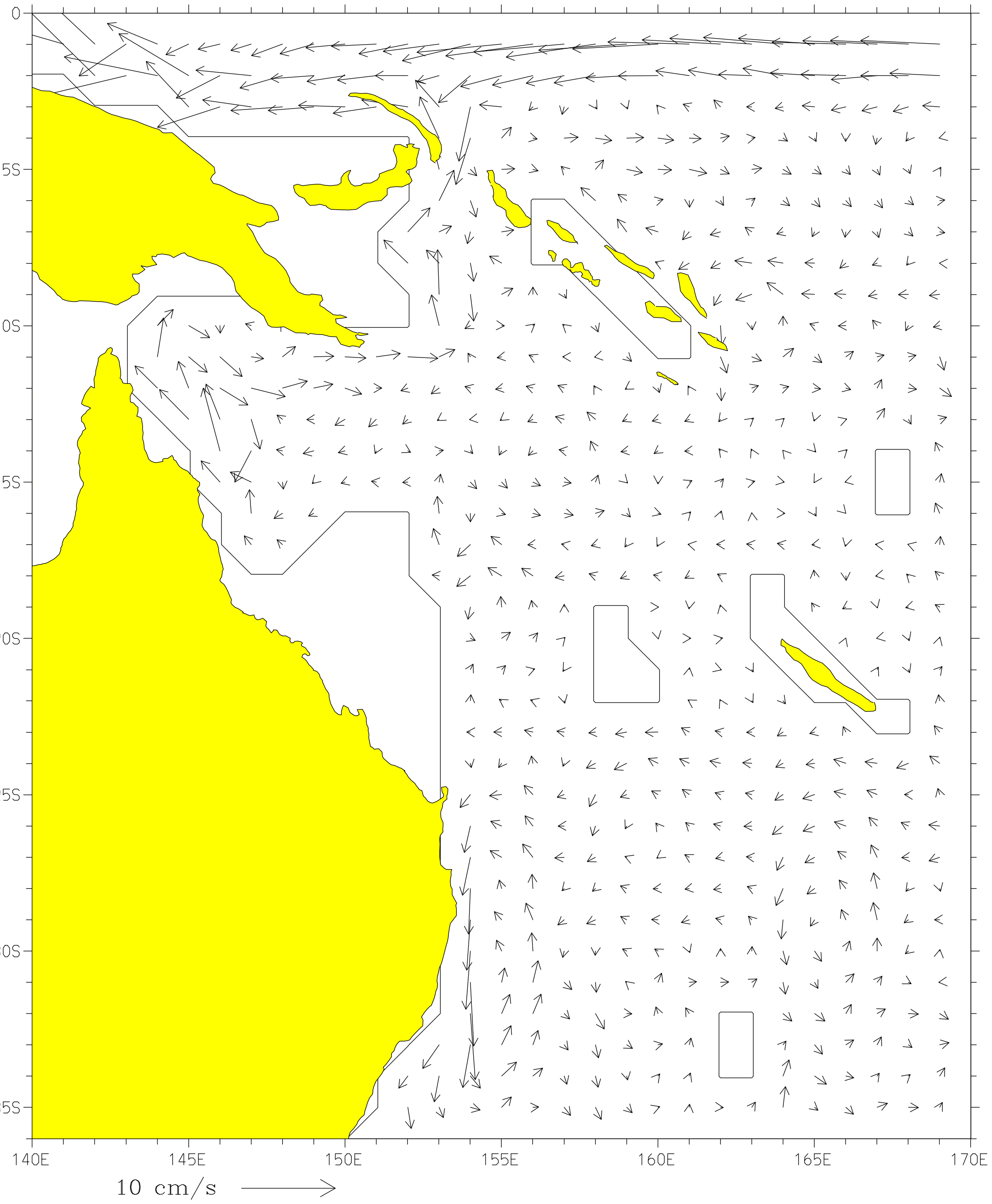

Figure 3.41b: Velocities for July-8 at 1227.0 m (level 11).

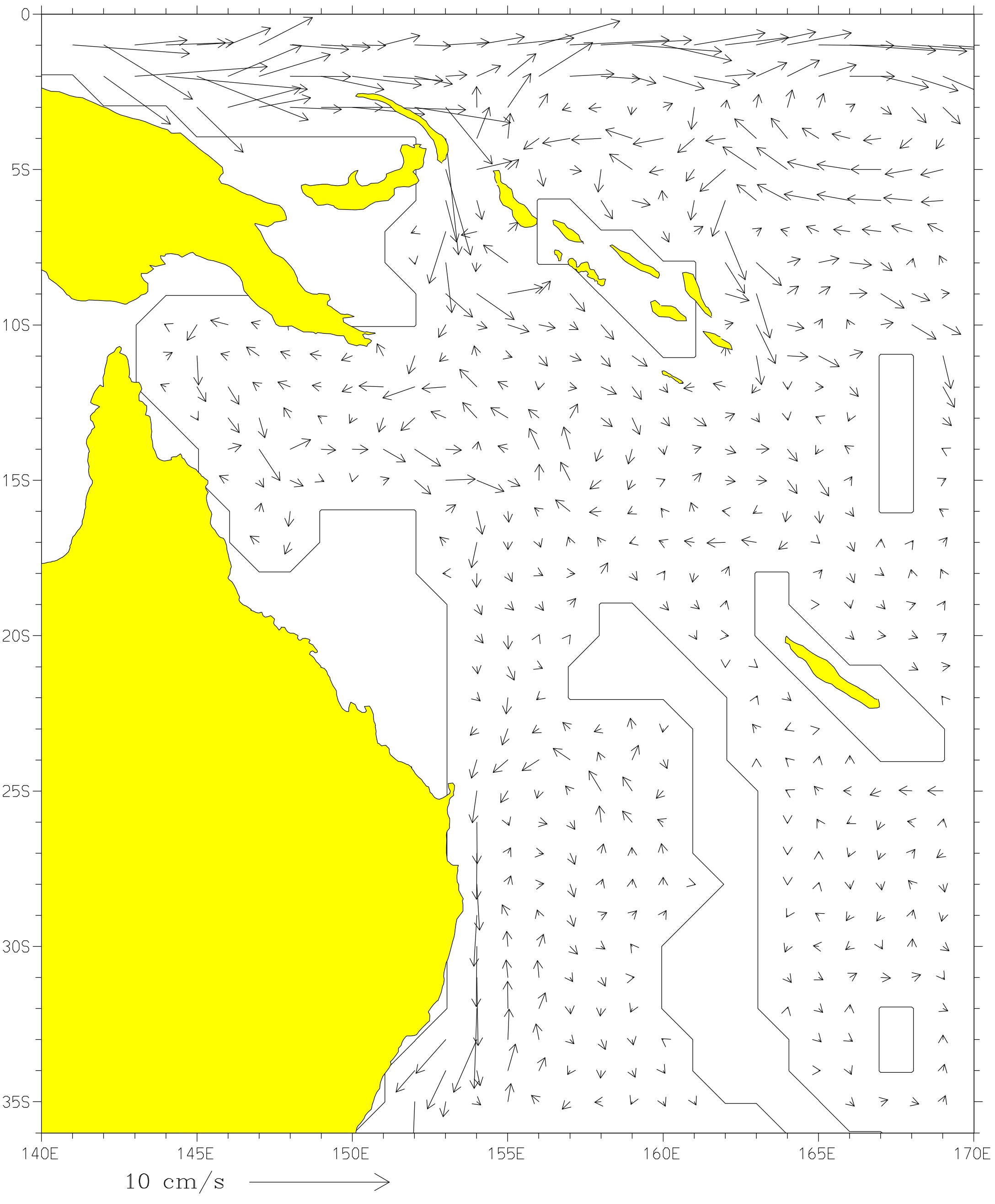

Figure 3.42: **a:** Velocities for January-8 at 1636.0 m (level 12).

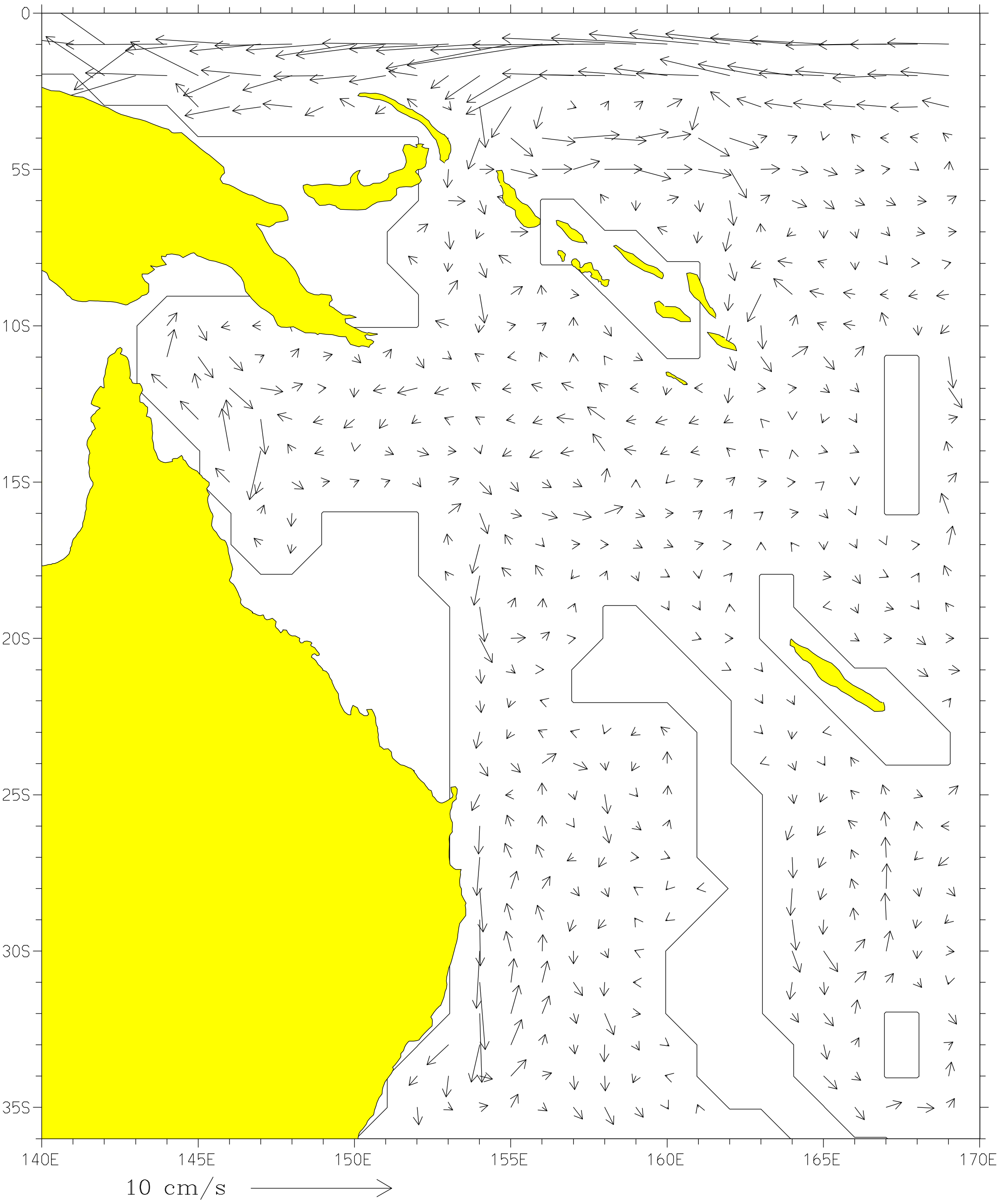

Figure 3.42b: Velocities for July-8 at 1636.0 m (level 12).

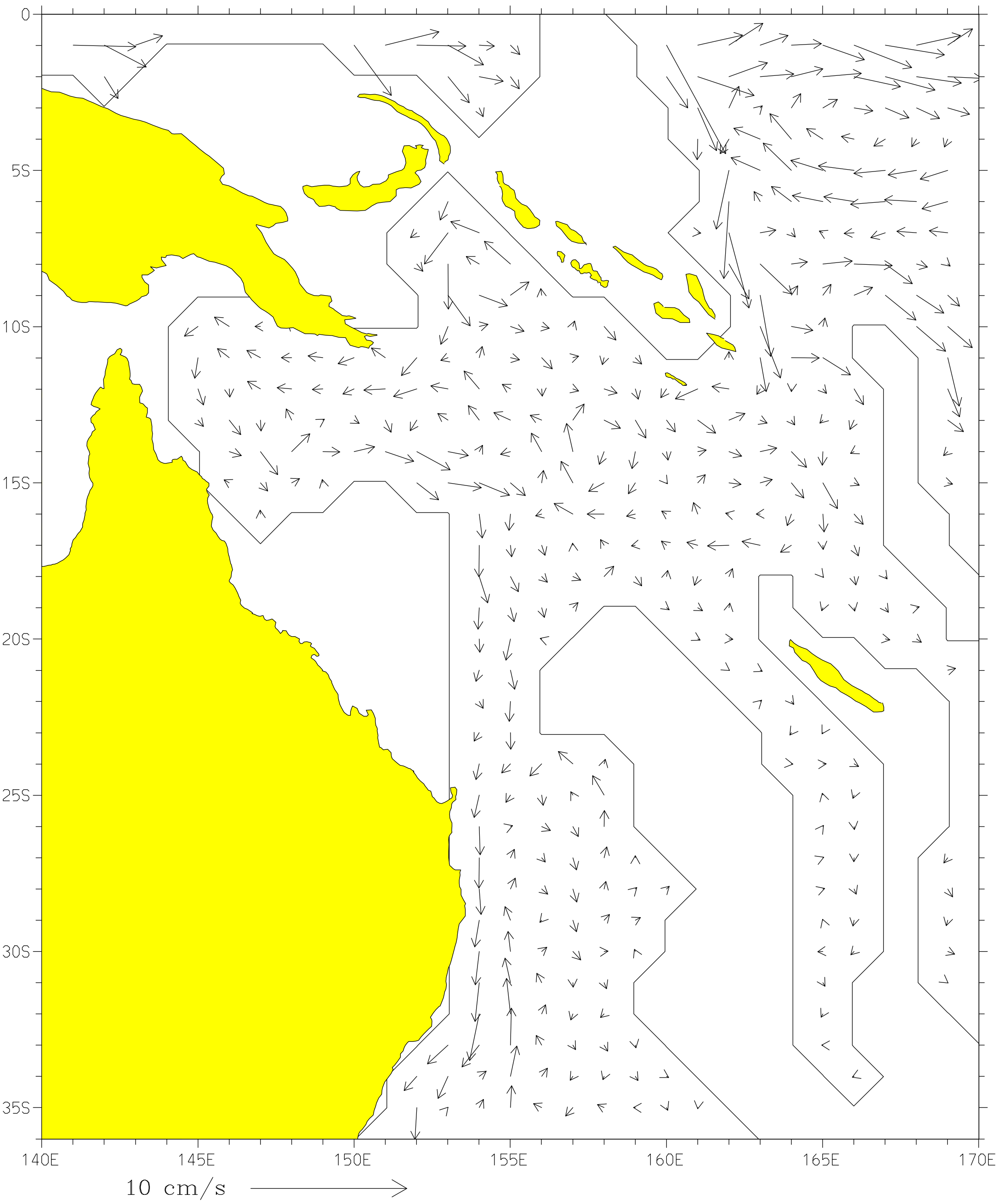

Figure 3.43: **a:** Velocities for January-8 at 2120.0 m (level 13).

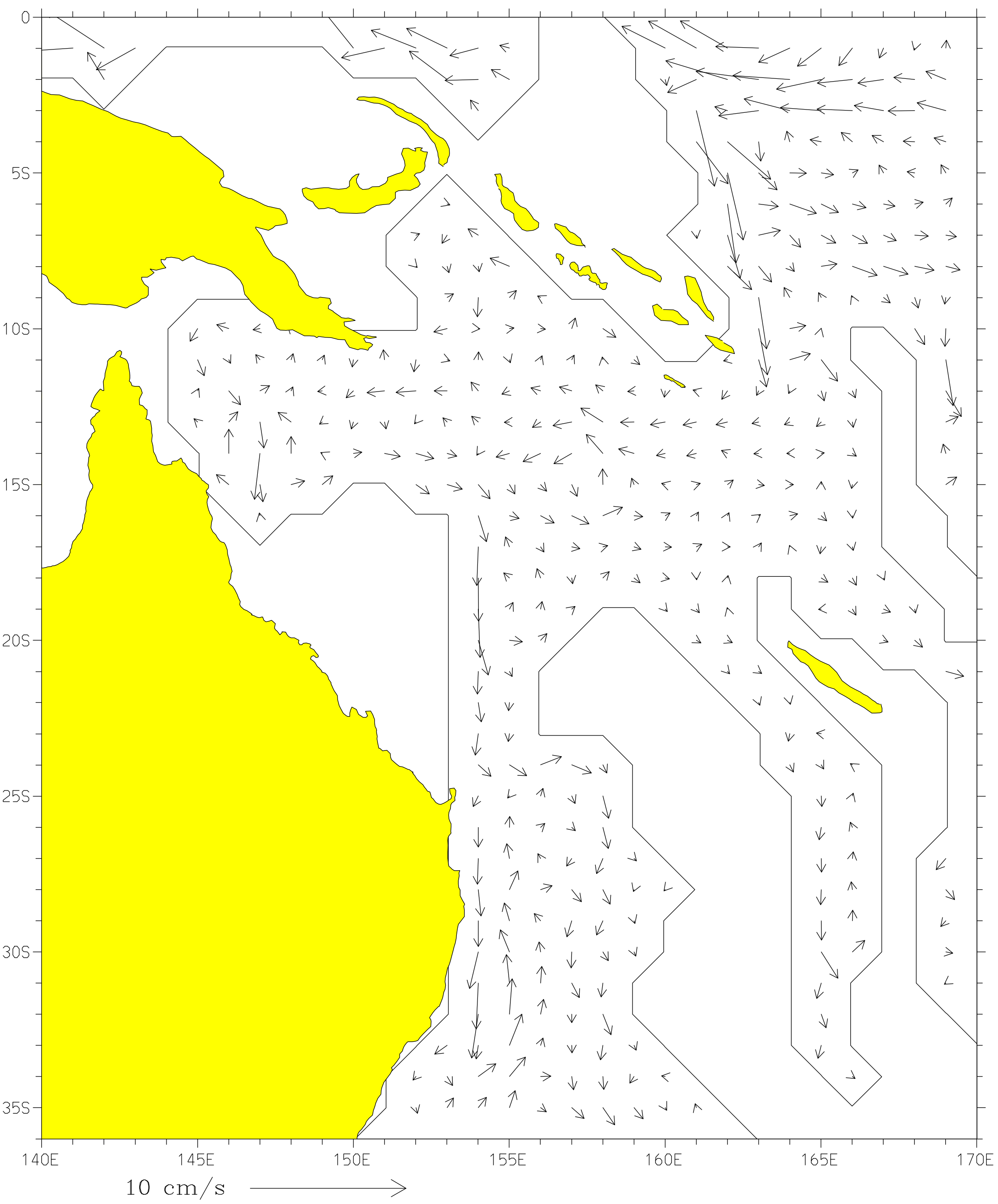

Figure 3.43b: Velocities for July-8 at 2120.0 m (level 13).

exits southwards from the Coral Sea via the Bellona Channel, to then join the deeper flows of the EAC. It will be shown in Chapter 4 that the abyssal waters of the Coral Sea and Solomon Sea Basins originate, in reality, from the Southern Ocean, via the Bellona Channel.

Fig. 3.44 shows isotachs of the PNG–Solomons throughflow, averaged over years seven and eight of the seasonally forced phase. The NGCU's subsurface character is clear in the Solomon Sea, with the V–max core being $220\,m$ deep at the PNG shelf (152°E). However, the V–max core around the Gulf of Papua is typically only $60\,m$ deep. Survey results around the gulf show peak velocities can occur close to the surface but the bulk of the volume flux is found in deeper water. The $60\,m$ core depth in the model could be due to the marginal grid resolution of the gulf area. The maximum model NGCU velocity in the Solomon Sea is only $24\,cm\,s^{-1}$ northwards (seasonal average), but when allowance is made for the grid resolution this figure becomes comparable with the observed maximum ADCP velocities of $\sim 60\,cm\,s^{-1}$. The model's peak NGCU velocity through the Solomon Sea is $28\,cm\,s^{-1}$, occurring over July to August. At 8°S the grid spacing in the zonal direction is $110.1\,km$, which equates to a V–max of $54\,cm\,s^{-1}$ using a western boundary current scaling width of $50\,km$. The model velocities adjust so that the volume flux is approximately correct. The abyssal Solomon Sea counter-currents observed during TEW3 are very weak in the model, generally smaller than $1\,cm\,s^{-1}$, and so will not be examined further.

Fig. 3.45 shows zonal component isotachs of the SEC. The baseline is along 154°E, close to the baseline of Fig. 3.19, but extends further southwards. The deep, but weaker core at 24°S is entrained mainly into the EAC, while the two northern cores form the NGCU. The three cores are the result of the SEC's bifurcation around New Caledonia and Vanuatu, as seen in Figs. 3.39a,b. The model SEC has subsurface velocity maxima over much of its domain in the mid South Pacific, and de Szoeke's (1987) ventilated thermocline model yields similar predictions. At 8°S in the present model, its maximum velocities occur close to the surface, but in proceeding southwards, the V–max core is found at progressively greater depths. At 22°S the core is $400\,m$ deep. de Szoeke uses a layered ventilated thermocline model of the South Pacific to determine the basin–wide baroclinic structure. He shows a basin inflow that is subsurface in character, due to the conservation requirement of potential vorticity and to the existence of the IT. He

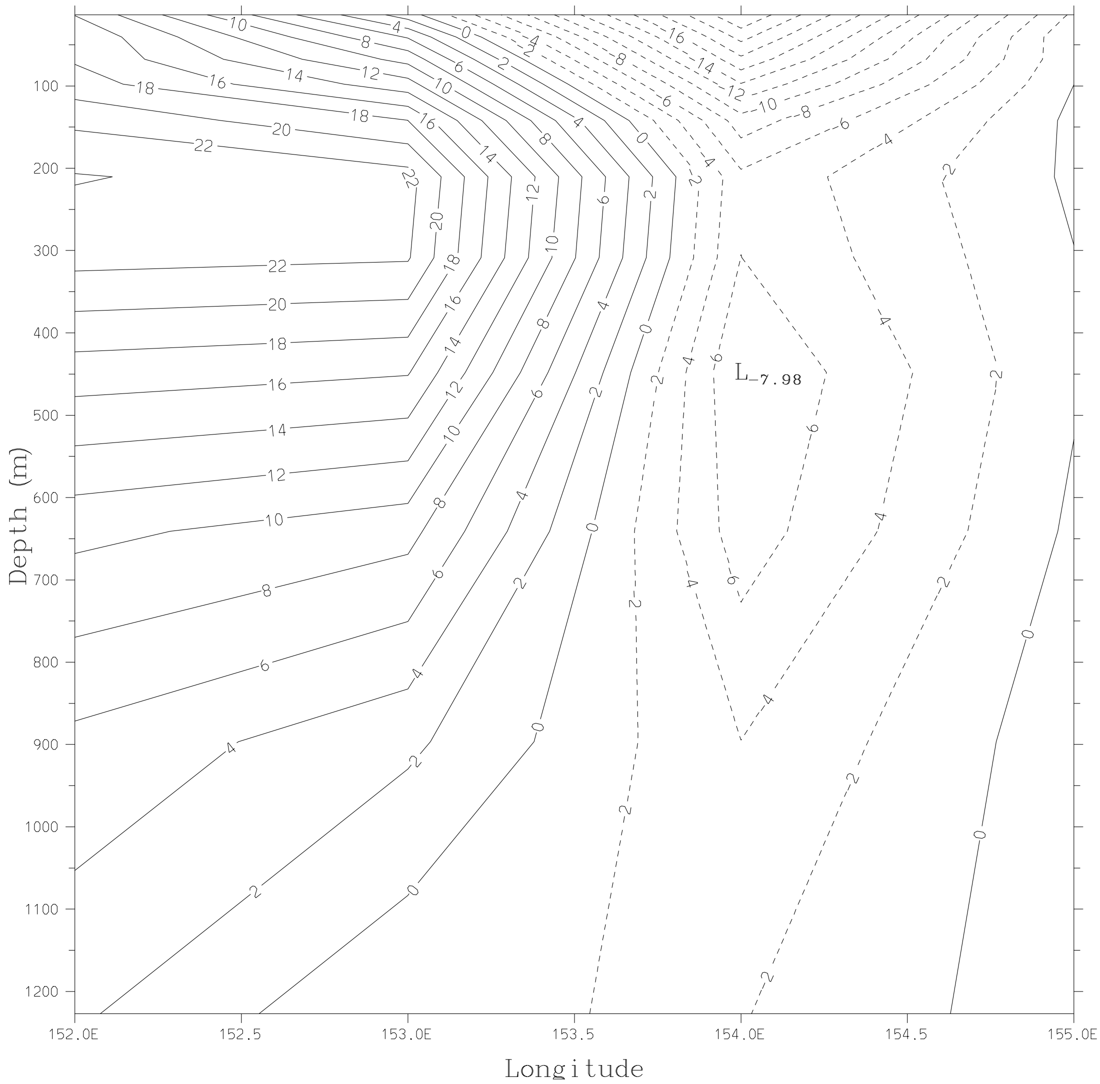

Figure 3.44: **:** Isotachs of the annually–averaged PNG-Solomons throughflow (v component), from $13.5\,m$ to $1227\,m$ (levels 1 to 11). The view is from the south and the baseline is along 8°S. CI is $2\,cm\,s^{-1}$ and negative (dashed) values imply southwards flow. The NGCU's core of maximum velocity is $24\,cm\,s^{-1}$, at a depth of $220\,m$.

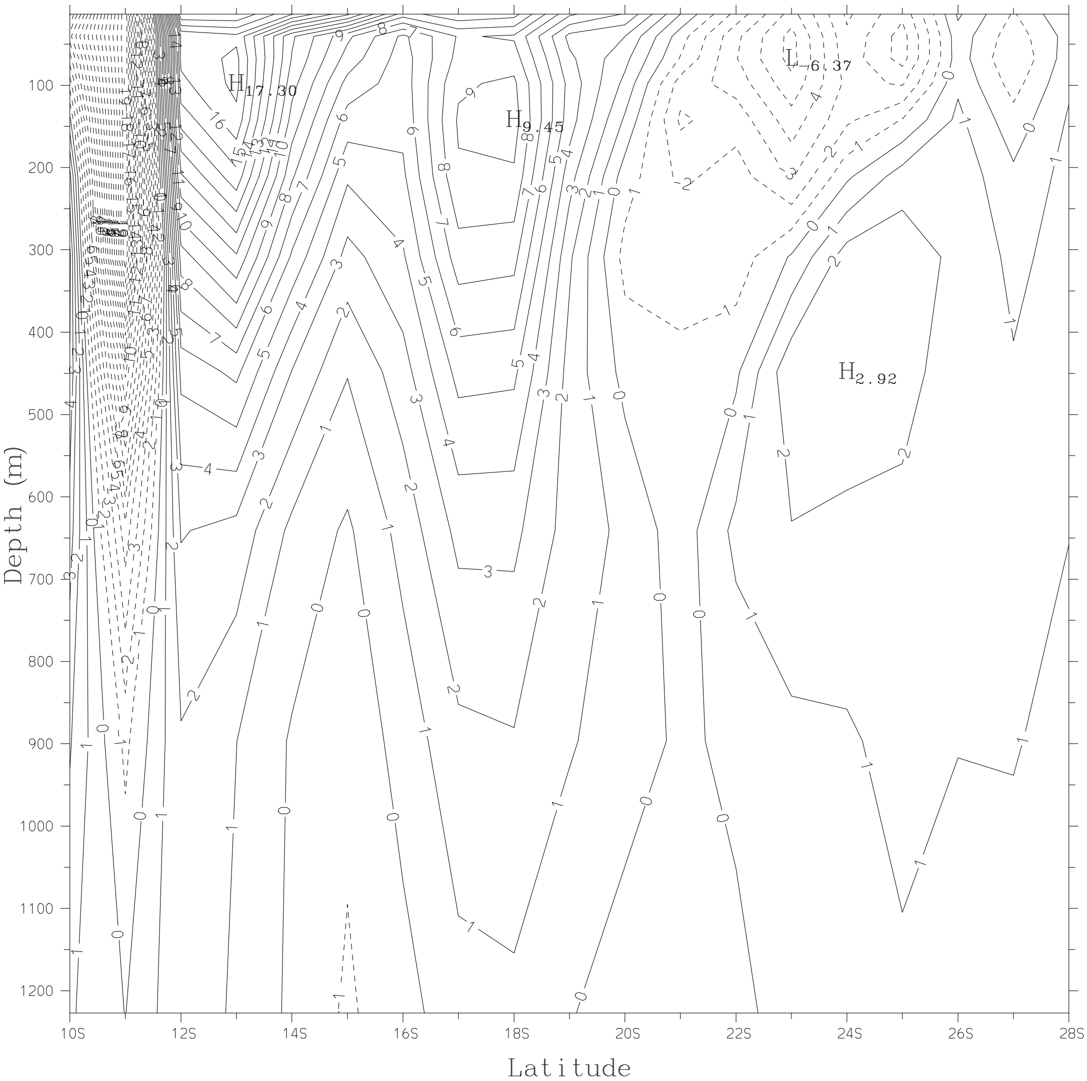

Figure 3.45: **:** Isotachs of the annually–averaged SEC inflow into the Coral and Solomon Seas (u component). CI is $1\,cm\,s^{-1}$ and positive (solid) values imply westwards flow, i.e., out of the page. The view is from the west and the baseline is along 154°E. Depth range is from $13.5\,m$ to $1227\,m$ (levels 1 to 11). The stagnant area at 20°S is due to the SEC's bifurcation around New Caledonia and the Bellona Platform. There are three V–max cores: $4.47\,cm\,s^{-1}$ at 24°S, $8.56\,cm\,s^{-1}$ at 17.5°S and $11.99\,cm\,s^{-1}$ at 13°S. The NGCU lies between 10°S and 12°S.

notes that isopycnals of the westwards flowing SEC must bank steeply to the left as they turn southwards at the Australian coast.

3.6.4 Western South Pacific TS Fields

Fig. 3.46 shows the surface potential temperature (13.5 m, level 1) for January-8 and July-8, over the western South Pacific. (Cox and MOM codes use *potential* temperature, as are all model temperatures reported in this thesis.) The surface layer is relaxed, using a 35 day time constant, towards the monthly varying Levitus data. However, the monthly varying wind stress and underlying water also have an appreciable direct effect. The largest variation of temperature, in this region, occurs around the EAC: 22°C in winter to 24°C in summer. Waters warmer than 29°C move zonally back and forth, northeast of PNG and the Solomons. The model seasonal variation in the Coral Sea is ∼1°C. Edwards (1979) provides surface temperature and salinity charts of the Coral and Tasman Seas, based on ten year averages for each month. Temperatures at 15°S:150°E range from 26°C in winter to over 29°C in summer. At the same location, the Levitus data range is 25.0°C in winter to 28.4°C in summer. The range for the seasonally forced phase of the model is 27°C in winter to 28°C in summer, which is at least within the correct limits. The relaxation time constant at the surface, 35 days, is therefore too large and could be reduced to 20–25 days for lower latitudes. However, this will probably not produce a sufficiently large seasonal variation, since the relaxation technique is merely a parameterization of complex processes in nature. The relaxation time constant would need to be reduced to zero, i.e., surface traces simply fixed to the Levitus data. To reach or exceed the seasonal variation, a surface flux needs to be included with the relaxation (Oberhuber, 1988). Flux conditions are more complex, notably for salinities, and can have unexpected behaviour.

Fig. 3.47 shows the model surface temperature anomalies (13.5 m, level 1) for January-8 and July-8. Anomalies are relative to the Levitus surface temperatures for the same two months, respectively. Anomalies are generally positive in winter (model too warm) and negative in summer (model too cold).

Cummins *et al.* (1990) find pervasive warming below the pycnocline, of about 0.8°C, in their idealized domain model, which is prognostically integrated to

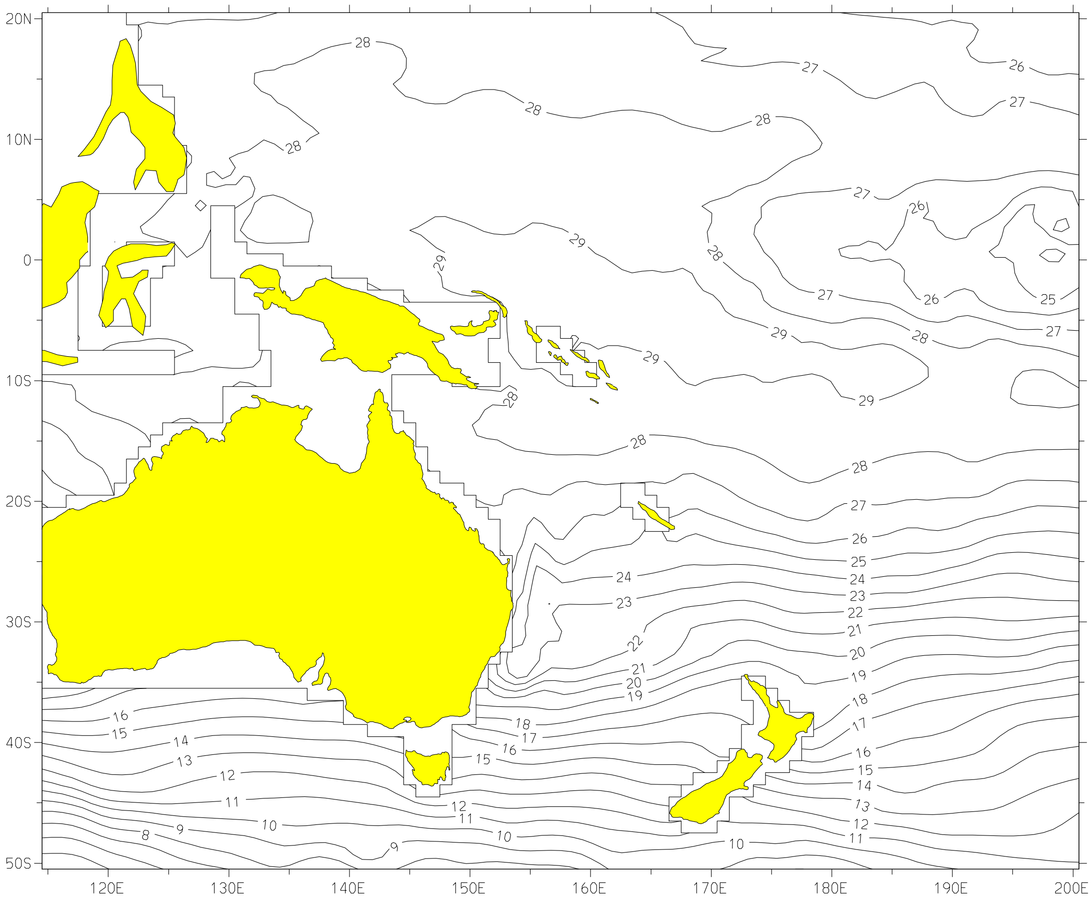

Figure 3.46: **a:** Western South Pacific surface temperatures (°C) for January-8 (13.5 m, level 1). CI is 1°C.

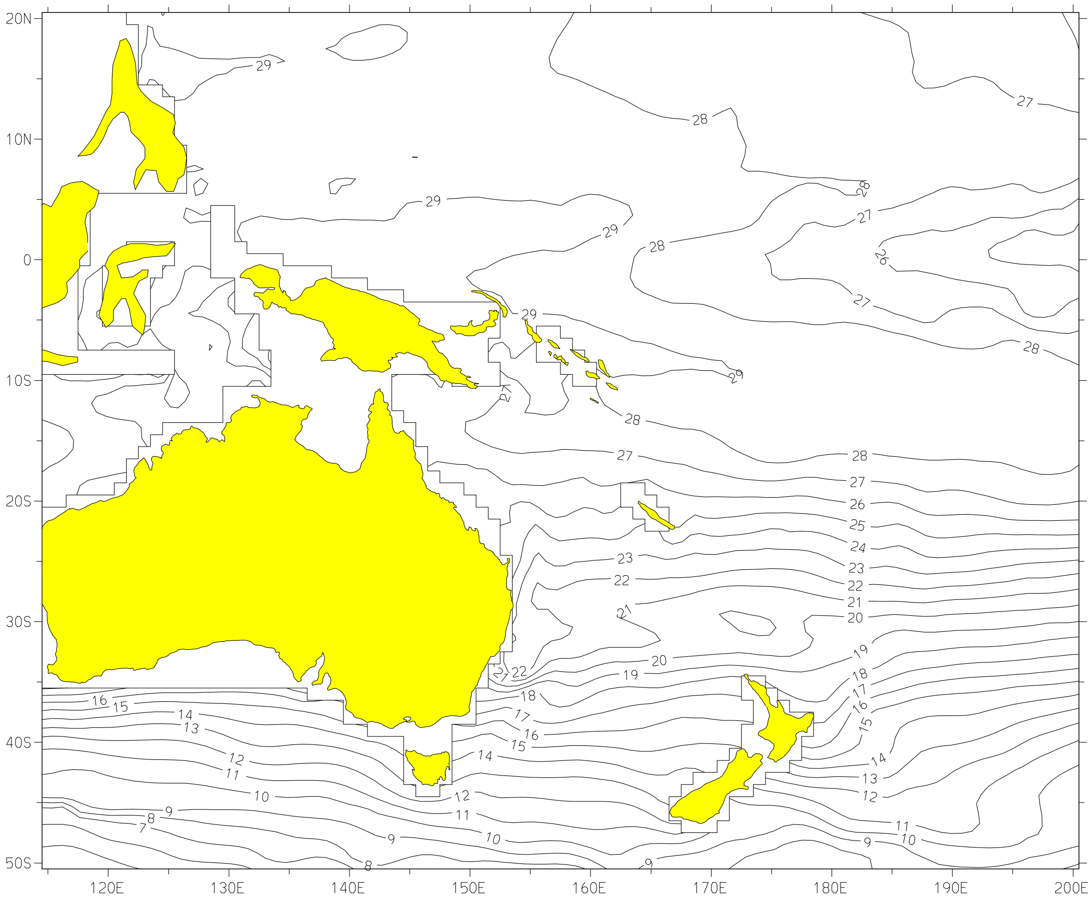

Figure 3.46b: Western South Pacific surface temperatures (°C) for July-8 (13.5 m, level 1). CI is 1°C.

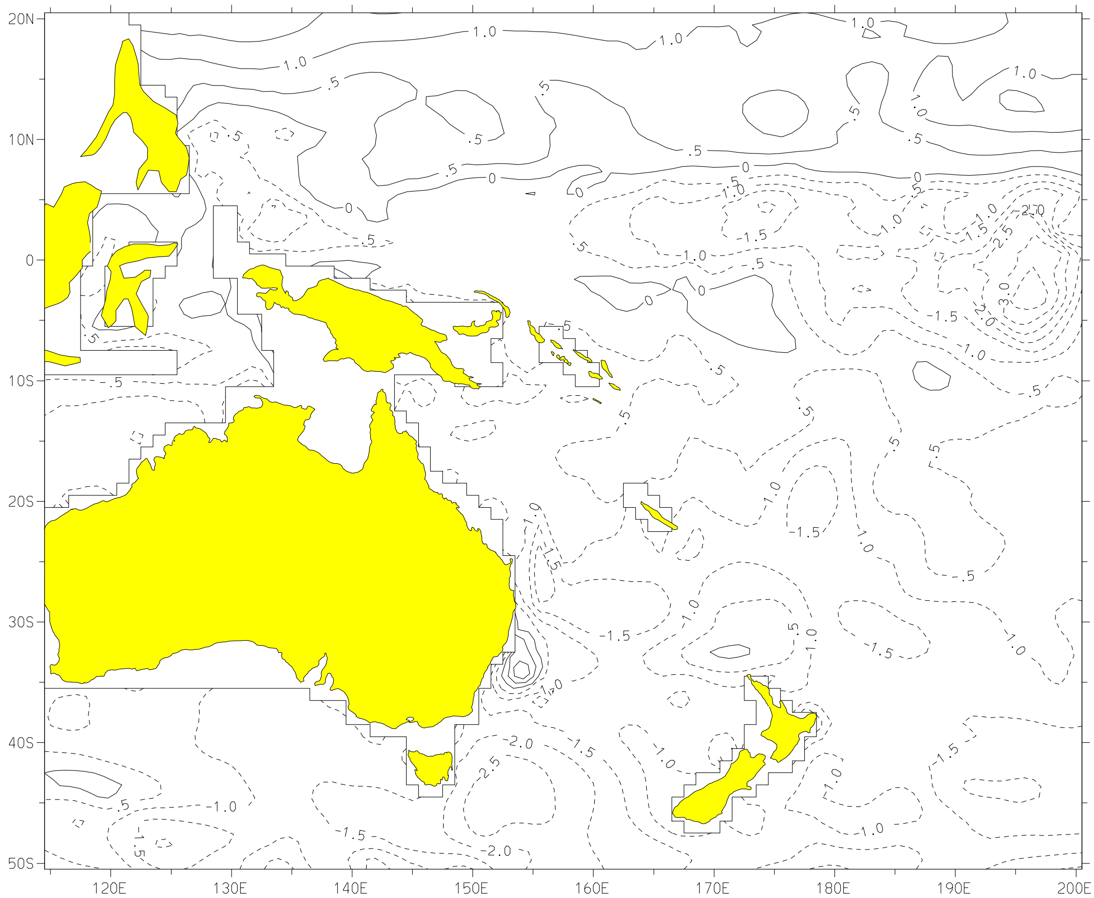

Figure 3.47: **a:** Western South Pacific surface temperature (°C) anomalies for January-8 (summer). Negative values are dashed. CI is 0.5°C. Anomalies are relative to the Levitus data for January. Coral and Tasman Sea temperatures are generally too low by about 1°C. Temperatures are up to ∼3°C too low in central and eastern equatorial regions.

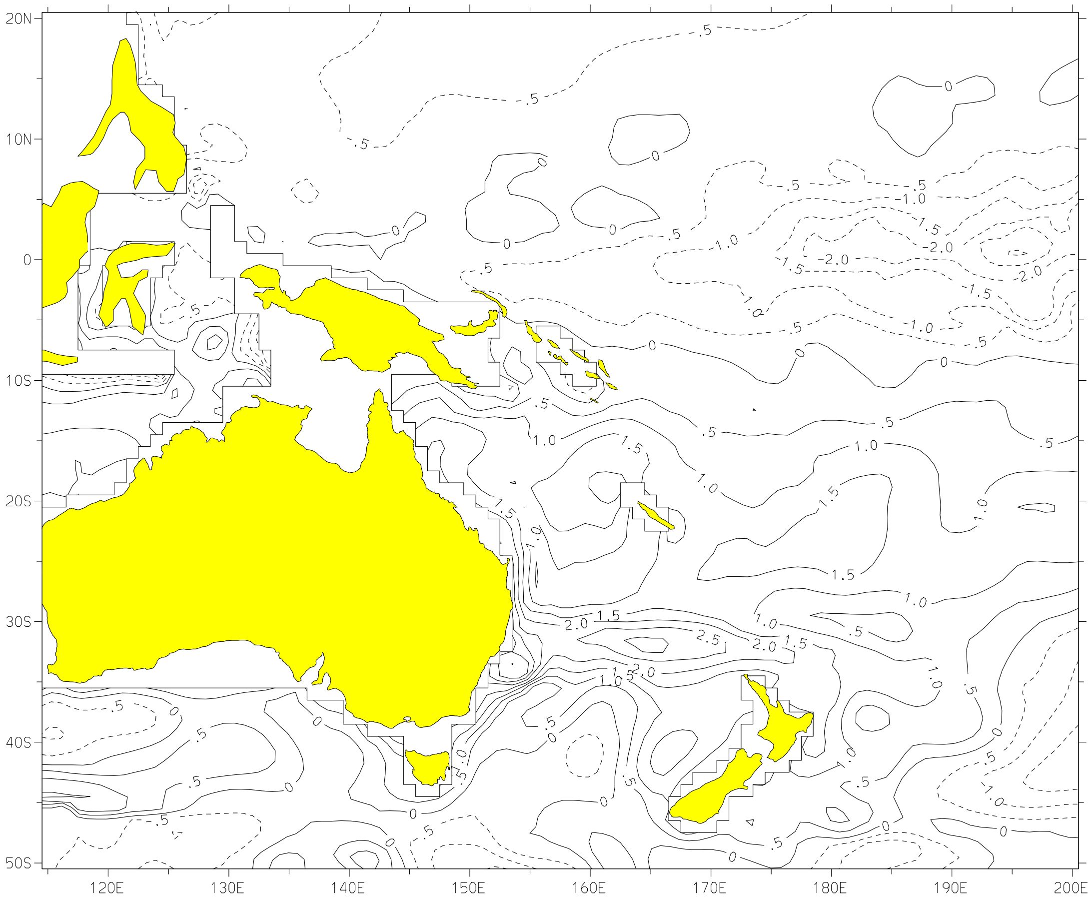

Figure 3.47b: Western South Pacific surface temperature (°C) anomalies for July-8 (winter). Negative values are dashed. CI is 0.5°C. Anomalies are relative to the Levitus data for July. Coral and Tasman Sea temperatures are generally too high by about 1.5°C, in direct contrast to the winter results. Thus, the model surface temperatures do not have sufficiently large seasonal variations about their mean values.

quasi–equilibrium. Such a warming trend is not found in the present model; temperatures at abyssal depths are within 0.1°C of the Levitus data except in certain localized areas. The deep water relaxation will, of course, attempt to prevent any possible warming, however, the integration time may not be sufficiently long enough to detect any trend. The deep vertical diffusivities generated in the model of Cummins *et al.* are about five times larger than those used (fixed) in this project, 1.8 versus $9\,cm^2s^{-1}$.

Fig. 3.48 shows the surface salinity ($13.5\,m$, level 1) during January-8 and July-8, for the western South Pacific. At 15°S:150°E salinity varies from $35.15\,psu$ in January-8 to $34.9\,psu$ in July-8. Edwards (1979) observes real salinities of $35.1\,psu$ in December, falling rapidly to $34.7\,psu$ in March and then rising slowly over winter. However, much larger seasonal variations are present in the Gulf of Papua and within a few hundred kilometres of Torres St. Gulf salinities can fall to $33.6\,psu$ in March. This is due to river run-off (e.g., Fly River and others nearby) and heavy precipitation during late summer months. Fresher water originating from Torres St. seems unlikely to cause this fall, given the $0.01\,Sv$ throughflow reported by Wolanski *et al.* (1987). Such extraneous variations cannot be accommodated in the model for such a small region, and so will not be considered further.

Figs. 3.49 and 3.50 show the annually–averaged temperatures and salinities at $210.5\,m$ (level 6), respectively. The average is calculated over years seven and eight of the seasonally forced phase. The Tasman Front (33°S:160°E) has an associated temperature variation of 4°C, while that for the North Equatorial Current (NEC) is 5°C. A zonal band of cooler water is evident at 5°N and is associated with the cyclonic circulation of the westwards flowing NEC and the eastwards flowing North Equatorial Countercurrent (NECC). This is a 'dome' of deeper cooler water in the model, that is elevated by isopycnal deflection in the stagnant area between the NEC and NECC. The NGCU retroflects near the western tip of Irian Jaya and forms the Equatorial Undercurrent; its associated temperatures are 17 to 19°C. Water flowing through the Indonesian passages is 16–17°C, a few degrees cooler than NGCU water at this depth.

A strong salinity gradient (Fig. 3.50) is evident along 2°N and is due to the NGCU forming the Equatorial Undercurrent. Tsuchiya (1968) and Tsuchiya *et al.* (1989) confirm this from observations. Indonesian throughflow waters are no

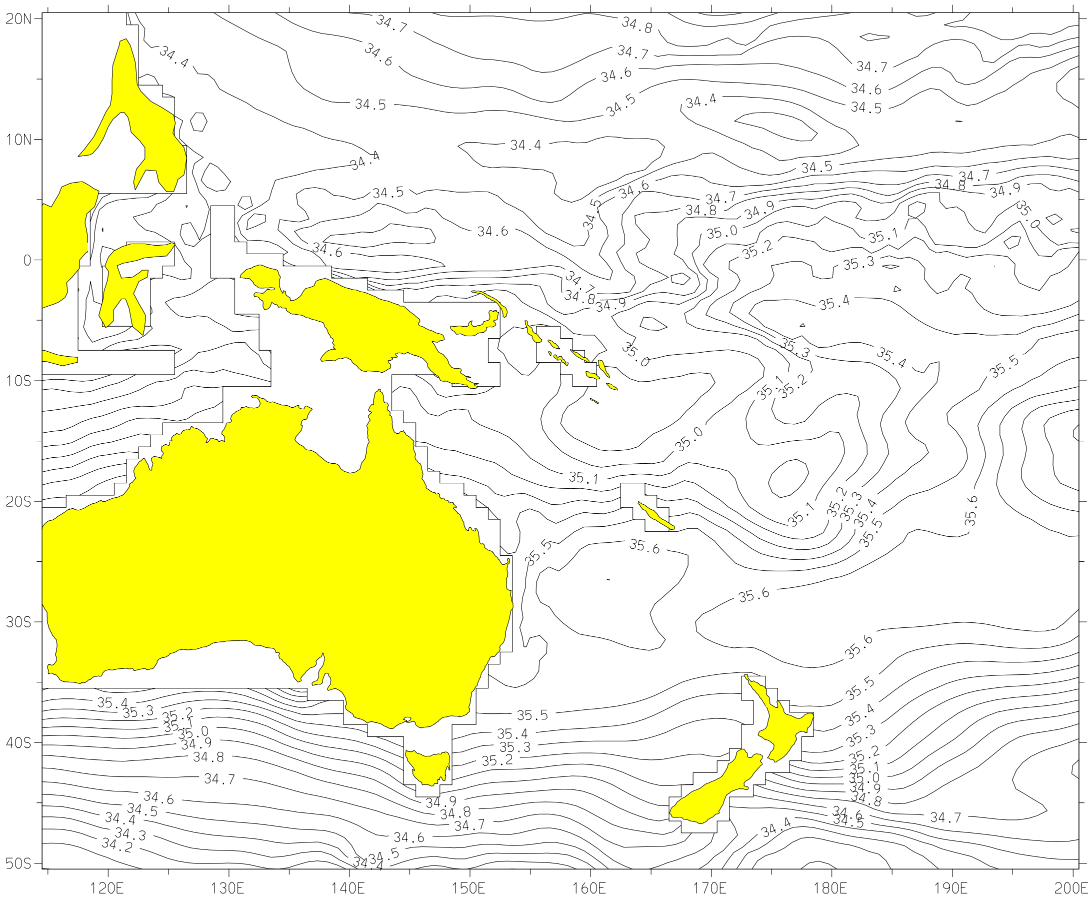

Figure 3.48: **a:** Western South Pacific surface salinities (psu) for January-8 (13.5 m, level 1). CI is 0.1 psu.

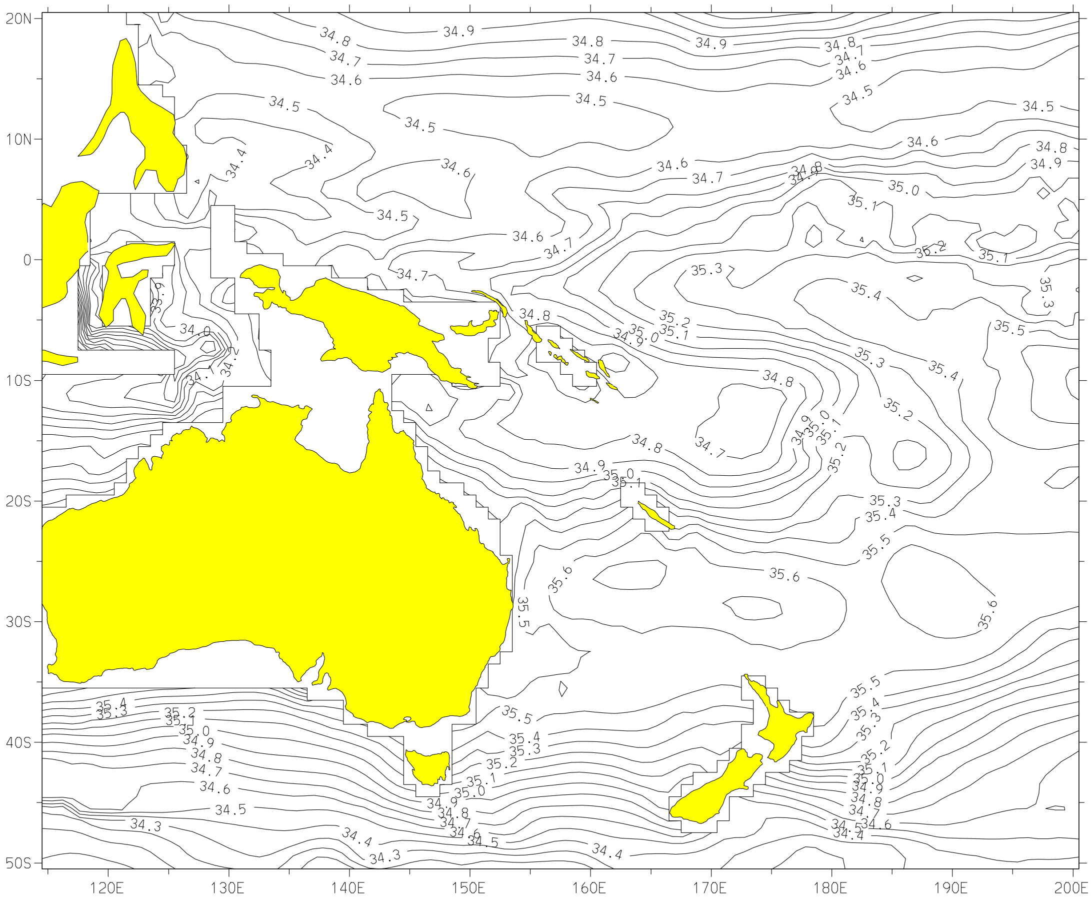

Figure 3.48b: Western South Pacific surface salinities (psu) for July-8 (13.5 m, level 1). CI is 0.1 psu.

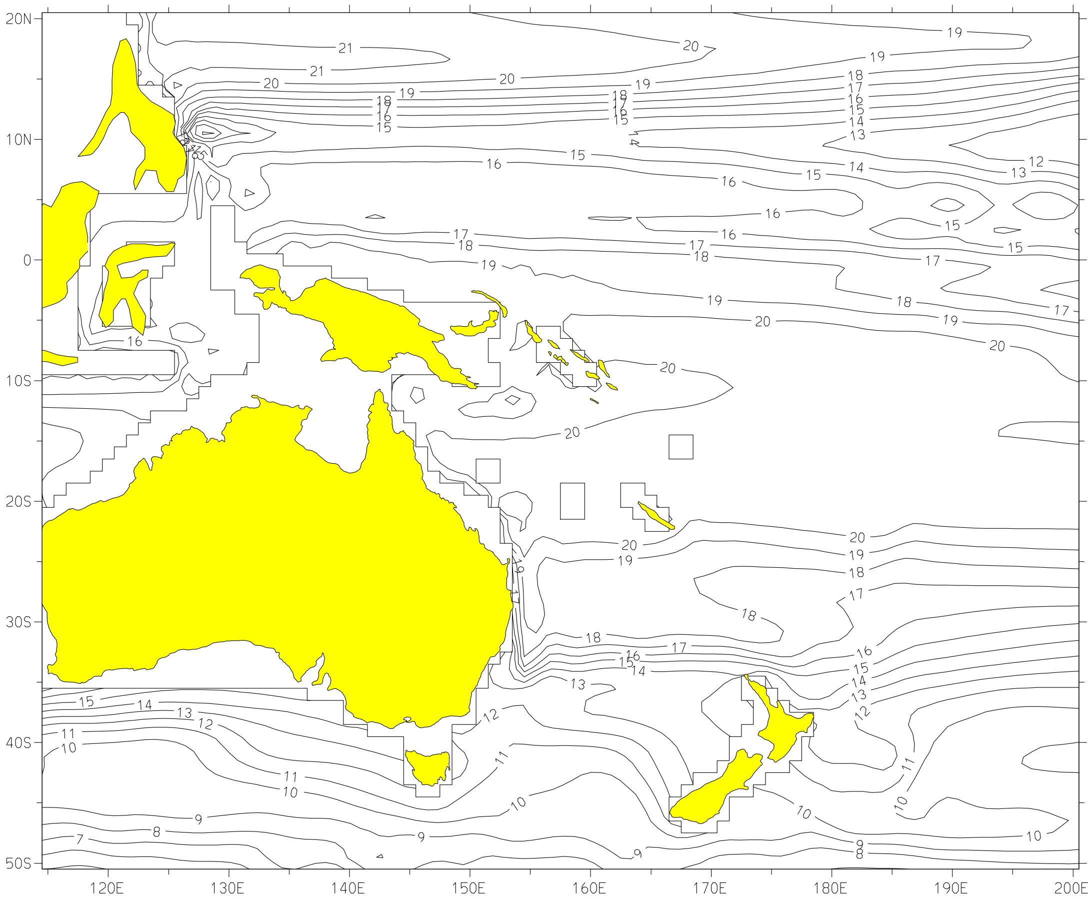

Figure 3.49: **:** Western South Pacific average temperatures (°C) at 210.5 m (level 6). CI is 1°C.

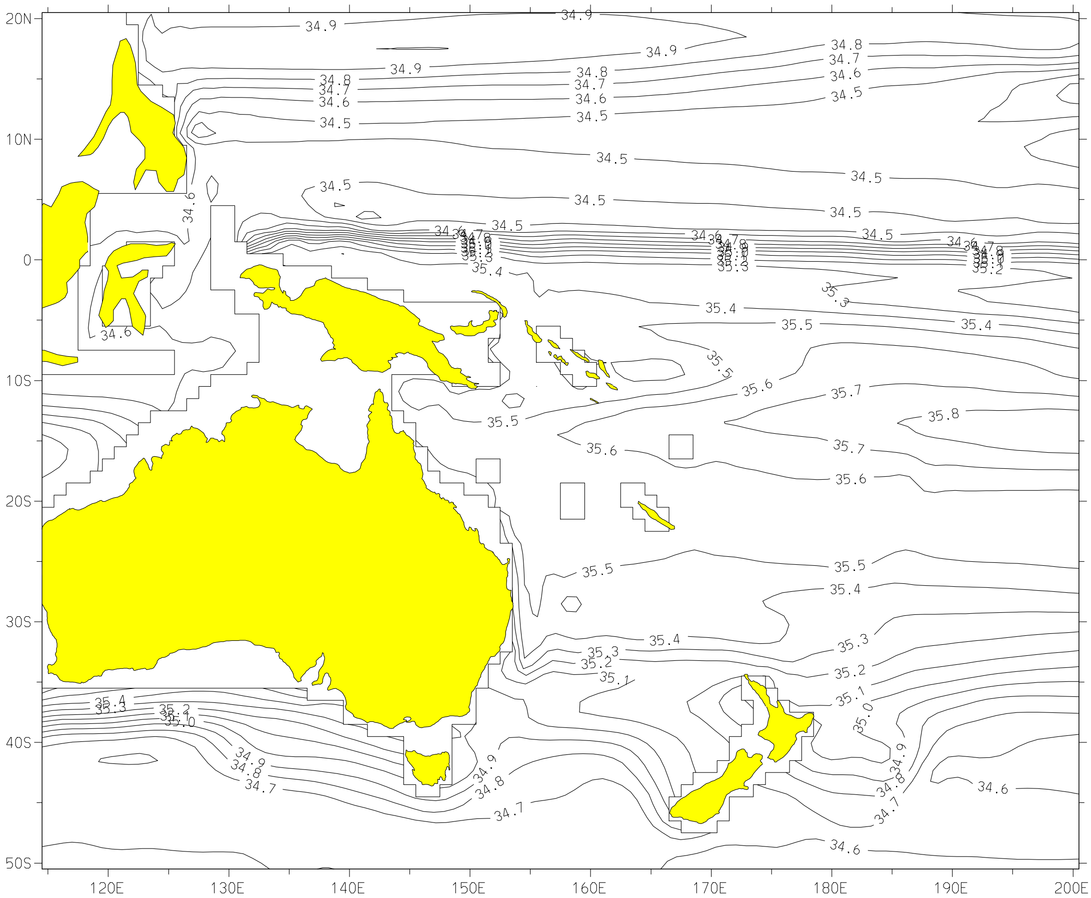

Figure 3.50: **:** Western South Pacific average salinities (psu) at $210.5\,m$ (level 6). CI is $0.1\,psu$.

saltier that 34.6 psu and clearly originate from the North Pacific. The maximum salinity of the model IT, over all depths, is less than 34.70 psu (Fig. 5.12). All observations of the main Indonesian throughflow have found that it is sourced from the North Pacific (e.g., Fieux *al.*, 1993). Godfrey *et al.* (1993) show some slightly higher salinity water along the southwestern coast of Irian Jaya (their Fig. 2) which indicates that a small amount of NGCU water may leak to the Indian Ocean, between Irian Jaya, Halmahera and Sulawesi. This could only occur during the austral winter when high salinity South Pacific water is observed near Halmahera I. (Wyrtki, 1961a). Any possible NGCU contribution to the Indonesian throughflow must be small, in comparison with the North Pacific's contribution, since upper thermocline waters in the northeastern Indian Ocean are too fresh to be (directly) sourced from the South Pacific. The model NGCU never participates in the throughflow at any time of the year. It is prevented from doing so by Halmahera I. at the western tip of Irian Jaya, and will be discussed further in Chapter 5. The Tasman Front salinity variation is 0.25 psu, contrasting the saltier waters of the SEC with the fresher waters of the Southern Ocean. Salinity has a relatively uniform spatial distribution in the Coral and Solomon Sea thermoclines, and is confirmed by the present surveys: Figs. 3.8, 3.10 and 3.11.

Figs. 3.51 and 3.52 show the annually–averaged temperatures and salinities at 641.0 m (level 9), respectively. The average is for years seven and eight of the seasonally forced phase. The SEC inflow is now more visible in the temperature distribution, as is its bifurcation around New Caledonia and at the Australian coast. This level is near the base of the thermocline, and isopycnal deflections, from geostrophy, give useful horizontal temperature contrasts. (In fact, at low latitudes, temperature and salinity fields often have more identifiable structure than pressure fields because of the reduced Coriolis parameter.) The strong meridional temperature gradient south of Australia is associated with the Antarctic Circumpolar Current. Local maxima in temperature and salinity occur along the equator, and are due to the presence of the north and south tropical gyres elevating cooler and fresher water, on both sides of the equator.

Figs. 3.53 and 3.54 show the annually–averaged temperatures and salinities at 1227.0 m (level 11), respectively. The average is calculated over years seven and eight of the seasonally forced phase. The SEC inflow is now confined

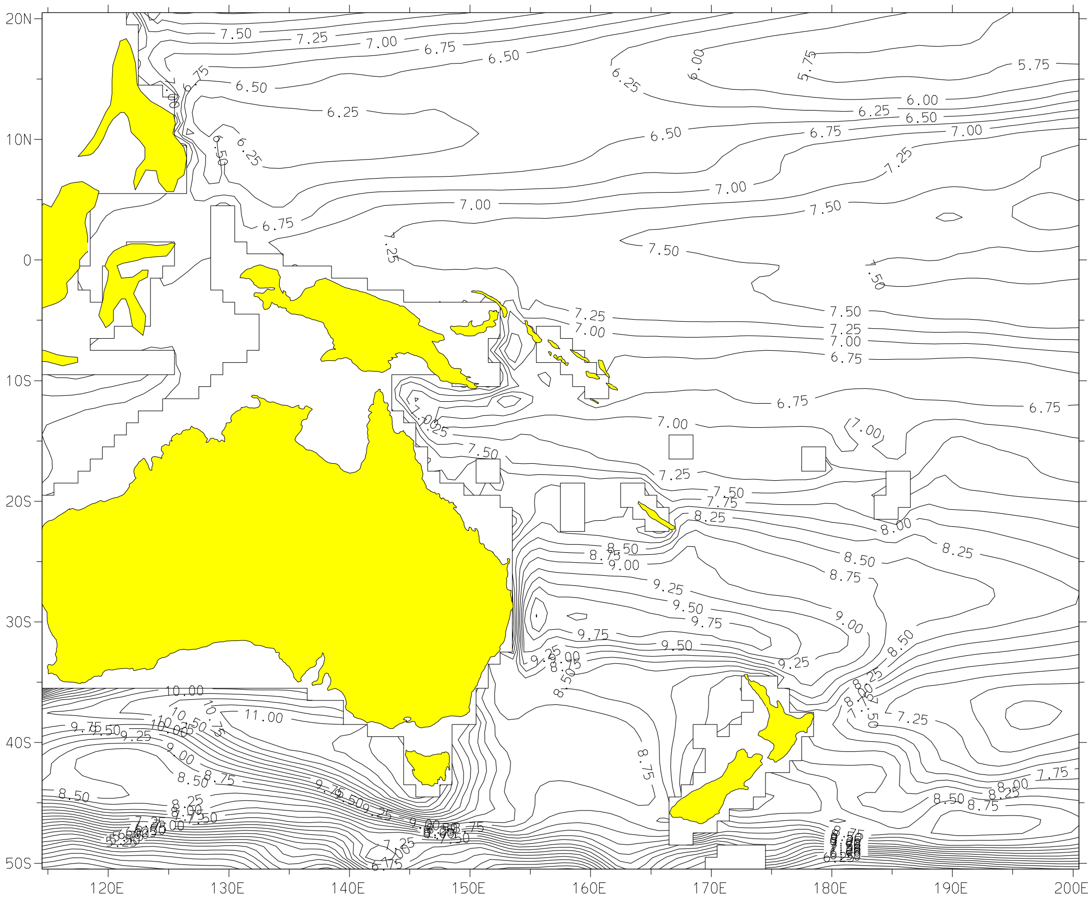

Figure 3.51: : Western South Pacific average temperatures (°C) at 641.0 m (level 9). CI is 0.25°C.

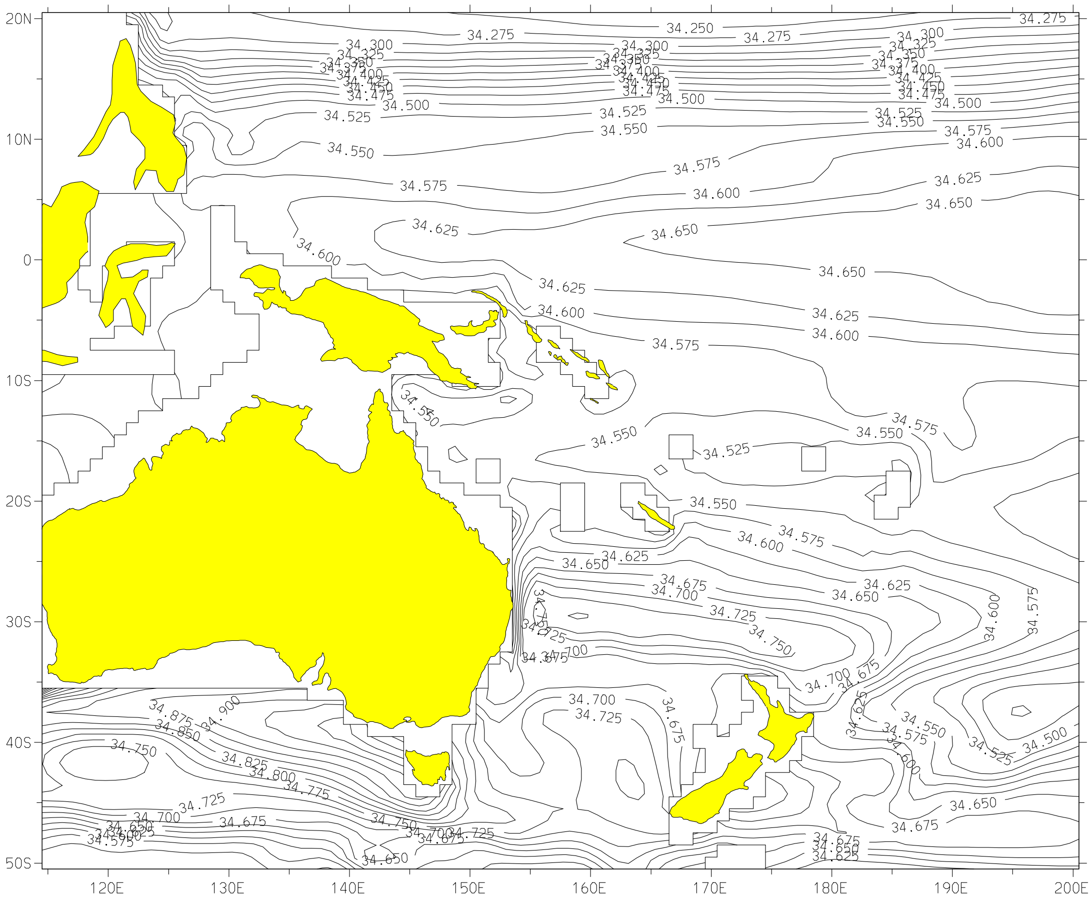

Figure 3.52: **:** Western South Pacific average salinities (psu) at $641.0\,m$ (level 9). CI is $0.025\,psu$.

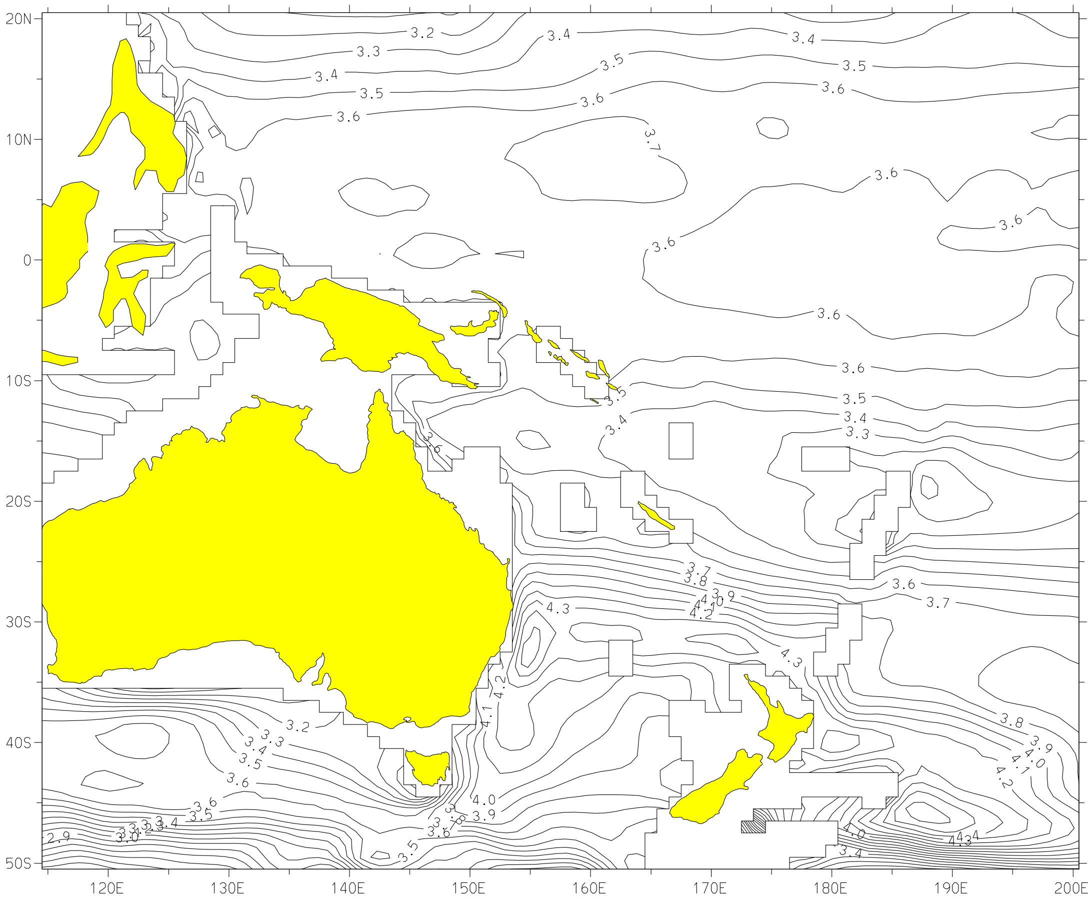

Figure 3.53: : Western South Pacific average temperatures (°C) at 1227.0 m (level 11). CI is 0.1°C.

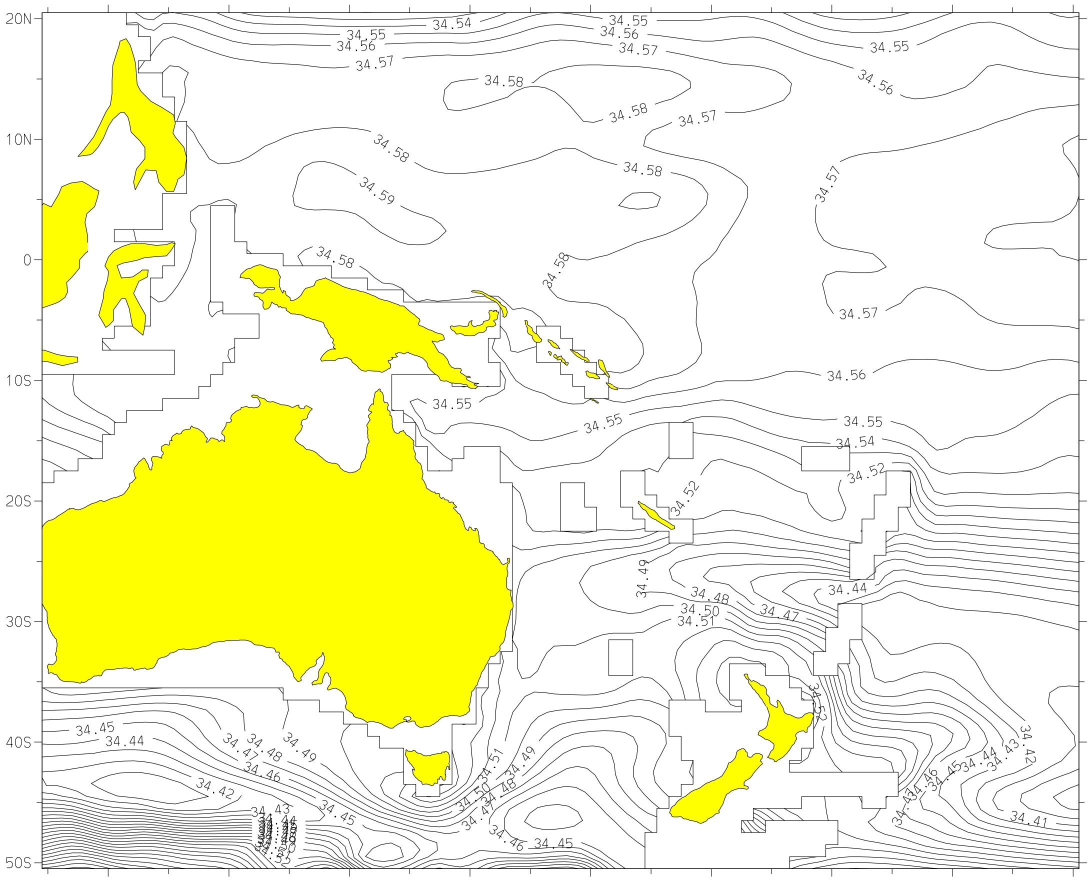

Figure 3.54: : Western South Pacific average salinities (psu) at 1227.0 m (level 11). CI is 0.01 psu.

almost entirely to the south of New Caledonia and it bifurcates near 25°S at the Australian coast. Waters along the north coast of PNG now have tracers sourced from north of the Equator (cf. Fig. 5.22a). Below 1227 m, model results for the Coral and Solomon Seas are at odds with observations, notably results of the seasonally forced phase of the model. Model and observational results for these deeper waters are examined in Chapter 4.

3.7 Summary and Conclusions for the NGCU

During all three *R. V. Franklin* cruises, the EAC north of 20°S was largely confined to the upper 300 m, whereas the NGCU exhibited a subsurface character with cores down to 360 m, and deeper still in the Queensland Trough. These two characteristics are almost certainly related. It is proposed that when the SEC bifurcates at ∼15°S on the Australian coast a larger amount of the near surface water turns southwards to form part of the EAC, and the lower levels of the SEC turn northwards to form the NGCU. At about 22°S there is no evidence of the NGCU/GBRU, and the SEC, now being the EAC, is flowing southwards between the surface and 2000 m. Thus the SEC bifurcation latitude moves southwards with increasing depth and this feature is well demonstrated in the model. There are insufficient data far offshore at 22°S to give a very clear idea of the SEC's behaviour there. Much of the vertical shearing occurs within the Queensland Trough, and over the Queensland Plateau, although the underlying reasons for the subsurface characteristics are probably related to dynamics on a much wider scale. A subsurface velocity maximum is observed in the inflowing SEC even before it has bifurcated into the two boundary currents. Thus, the present model and observations are in keeping with de Szoeke's (1987) predictions. Andrews & Clegg (1989) find subsurface characteristics in their normal modes, around the Gulf of Papua and the Louisiades, but not for the inflowing SEC. Their sections D–E–F may not extend sufficiently far southwards to show any possible subsurface V–max cores of the SEC.

The model's EUC, in the western Pacific, has a seasonal variation in the depth and strength of its V–max core. During November to January, the core is about 30 $cm\,s^{-1}$ at a depth of 200 m. During June and July, the EUC is over 80 $cm\,s^{-1}$, but at a shallower depth of 100 m (§5.3.1). While the local equatorial

Ekman divergence will cause some of the depth variability (cf. Kessler & Taft's observations) this feature is linked to the SEC's vertical shearing behaviour at the Australian coast (and partly to the SECC's variability). The strength and depth of the EUC is inversely correlated with the strength of the EAC; when the EUC is weak and deep, more SEC water is flowing southwards with the EAC. The EUC is stronger and shallower when a large amount of SEC water turns northwards at the Australian coast. The model's SECC has its origins on the eastern flank of the Solomons chain, and is quite distinct from the NGCU/EUC system. Its peak velocities are near the surface, along 8°S, and it is confined above $200\,m$. It exists throughout the year and is stronger during the second half of summer, January to March.

The existence of the GBRU is due to the presence of the Queensland Plateau, which forces the SEC to bifurcate around it, at depth. The surface bifurcation of the SEC along the Australian coast is observed to lie at approximately 15°S. Southwards from this latitude, the northwards flowing NGCU/GBRU is observed only at progressively greater depths.

The curl of the annually–averaged wind stress (Hellerman & Rosenstein, 1983) in the western South Pacific is zero along approximately 20°S, with positive curl polewards and negative curl equatorwards. However, the annually–averaged negative curl region only extends to about 210°E between 4°S and 20°S, and has a similar magnitude to the positive curl elsewhere. Sverdrupian theory therefore predicts that the NGCU should carry less closure flux than the EAC, which is not in accordance with observations. The implication is that the IT is responsible, directly or indirectly, for the stronger than expected NGCU. The directions of the modelled EAC and NGCU are consistent with the signs of their corresponding wind stress curls, but not their relative (to each other) volume fluxes; the actual EAC is too weak and the actual NGCU is too strong (cf. Fig. 10 of Hellerman & Rosenstein, 1983). The EAC flows polewards and the NGCU equatorwards, with the depth–averaged bifurcation probably occurring near 20°S at the Australian coast.

A limited number of observations along the north coast of New Ireland (Butt & Lindstrom, 1993) show only modest westwards fluxes, about $3\,Sv$, over the thermocline depth range. It should be noted that the modelled flow is highly variable with respect to the seasons, in keeping with equatorial dynamics, and the bulk of the wintertime $50\,Sv$ is confined below $800\,m$. If strong abyssal currents are actually present then extra care will be needed when performing thermal wind analysis. Butt & Lindstrom note severe discrepancies between their ADCP currents ($\sim 60 cm\,s^{-1}$) and thermal wind currents ($\sim 120 cm\,s^{-1}$), for areas within a few degrees of the equator. They attribute this to high frequency internal motions, but, as noted previously, low frequency fast moving equatorial planetary waves could also upset these measurements. ADCP versus thermal wind discrepancies are much smaller for the present data, around the Coral and Solomon Sea regions.

Estimating the volume flux of the NGCU along the southern coast of PNG is complicated by the possible presence of recirculation, which is of less interest than the open ocean flux closure. Observations give a mean NGCU strength of $24\,Sv$ eastwards, adjacent to the Louisiades, but a single observation across the Solomon Sea suggests that the PST is augmented by other flows not originating from the western Coral Sea. Seasonal variability cannot be inferred from the data but some intra–annual variability can be. Although not specifically a subject of this chapter, the deep anticyclonic flow was found to be possibly stronger during Fr0791, indicating some connection with the ENSO event of 1991–93.

The NGCU is observed to meander offshore along the south coast of Papua New Guinea, with the current diverting up to $300\,km$ seawards and then veering abruptly back to the coast. The frequency, direction and speed of propagation of these meanders remains unknown and, even more importantly, it is not known if they propagate to, or exist in, the northern waters of PNG. While the model shows some small scale variability of the NGCU around the Gulf of Papua, it does not reproduce the very abrupt meanders observed.

The WEPOCS investigators named the outflux from Vityaz Strait the New Guinea Coastal Undercurrent and that convention is used here, although it has not yet been rigorously proven that the boundary current along the southern coast of PNG is the same current that flows through the strait. Detailed O_2 data of Vityaz St. waters will allow an accurate determination of the origin latitude. The current that flows along the southern coast of PNG often has surface velocities exceeding $50\,cm\,s^{-1}$ and the term “undercurrent” is probably too restrictive. A suggested alternative name for the flow along the southern PNG coast is *Hiri* Current, which is perhaps a little more poetic and historically relevant. Papuan sea traders from ancient times sailed eastwards across the Gulf of Papua, home-bound from Torres Strait, during an annual event known as the Hiri.

Chapter 4

The East Australian Currents

4.1 Introduction

The general flow regime of the East Australian Current (EAC) has eluded researchers for many years and even estimating the total volume flux has proven to be notoriously difficult. This western boundary current begins at 14–20°S on the Australian coast, intensifies while flowing southwards and then departs to the open South Pacific near 33°S. The effects of EAC eddies have occasionally been observed as far south as 42°S. Fig. 4.1 shows the bathymetry of the Tasman and Coral Sea regions. Observational estimates of the EAC's volume flux vary greatly. The smallest estimate is $10 \times 10^6\, m^3 s^{-1}$ (or 10 *Sverdrups*) *northwards*, reported by Thompson & Veronis (1980), ranging up to $50\,Sv$ southwards, reported by Boland & Hamon (1970). Lilley *et al.* (1986) find the barotropic volume flux of a warm–cored EAC eddy to be $100\,Sv$, using horizontal electric field (HEF) methods in $4800\,m$ of water. Mulhearn *et al.* (1986) find intermittent jets of up to $35\,cm\,s^{-1}$, only $100\,m$ above the seafloor ($4800\,m$) of the Tasman Abyssal Plain, close to the Australian shelf. Temperatures of the jets are cooler by up to 0.16°C than the surrounding waters. Hamon (1965) gives a figure of $25\,Sv$ for the annually–averaged EAC flux, at about 30°S, adjacent to the Australian east coast. Meyers (1980) estimates that the open ocean volume flux for the South Pacific subtropical gyre, northwards across 28°S, is about $26\,Sv$, which implies a similar southwards closure flux for the EAC. Ridgway & Godfrey (in preparation) propose a much reduced EAC nett estimate of $9\,Sv$, flowing southwards between the Australian coast and 30°S:170°E.

The first comprehensive field surveys were undertaken by Hamon (1961) and

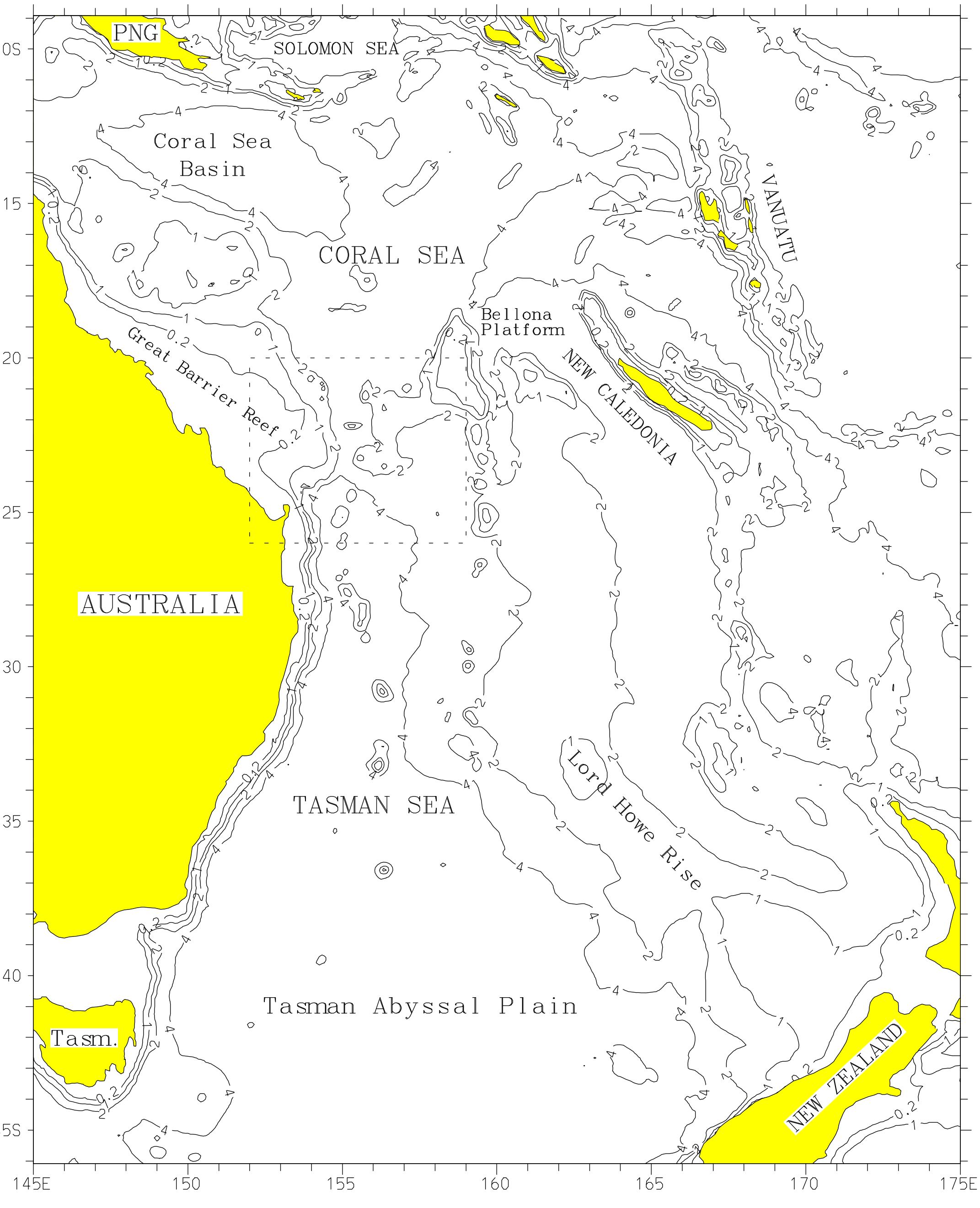

Figure 4.1: **:** Bathymetry (km) of the study area. The sill depth between the Coral Sea Basin and the Tasman Abyssal Plain is about 2700 m. The sill depth across Lord Howe Rise at 35°S is 1500 m. The Bellona Channel at 23°S:155°E is 3000 m deep, but shoals to about 2700 m further northwards. The most recent soundings give the sill depth connecting the Coral Sea Basin to the deep Pacific as 2500 to 3000 m at 11°S:163°E. The dashed rectangle refers to the area covered in Figs. 4.2 to 4.4. (Ref. SOPAC and GEBCO charts.)

by Wyrtki (1962b), who both suggest that the EAC is not strictly classifiable as a western boundary current. The absence of a large pool of comparatively warm water equatorwards of the departure latitude is not in keeping with other poleward boundary currents such as the Gulf Stream and Kuroshio. South of 33°S, Hamon observes intense anticyclonic warm–cored eddies, of about 250 km in diameter, that have rapid variability, while later surveys show a broad scale of temporal variability (Andrews & Scully-Power, 1976). The warm–cored eddies can have their largest horizontal temperature differences with the surrounding water at depths of more than 500 m, due principally to geostrophic isopycnal deflections, while warm–cored rings of the Gulf Stream and Kuroshio have their largest differences at the surface. Creswell & Legeckis (1986) find eddy life times of over one year, and in that time the eddies develop mixed layers similar to the surrounding water. This obscures their presence in surface measurements.

The EAC is often observed to flow around a tight poleward loop before it departs the Australian coast, and then flows zonally towards the north coast of New Zealand. This zonal flow creates the Tasman Front, although its total variation in temperature is only of order 2°C. Hamon postulates that the eddies are the result of pinch–offs of the anticyclonic loop, in a similar fashion to Gulf Stream ring formation, although cyclonic eddies of similar intensity have never been observed near the EAC. Creswell & Legeckis report on pinch–offs and re–incorporations of the eddies, in more detail. Hamon (1968) finds large variations in the monthly averaged sea level, up to 60 cm, at Lord Howe Island (31.5°S:159°E), which is rather uncharacteristic of midlatitude open ocean behaviour. Godfrey (1973) postulates that baroclinic instability plays a fundamental role in generating the eddies and is responsible for the observed substantial upwelling. A useful short review is given by Bennett (1983), who details other puzzling features of the EAC region.

Very little data were available around the formation area of the EAC, near 15°S, until the 1980s and the present amount is still far from satisfactory. Wyrtki (1961b) finds that water occupying the bottom of the Coral Sea Basin, up to 4600 m deep, is readily identifiable as originating from the Tasman Sea at depths a little shallower than 2700 m. Property profiles for the Solomon Sea Basin, between Papua New Guinea (PNG) and the Solomon Islands, show a very similar influence. Thus, he concludes that there is a northwards flow of Tasman Sea water, between the Australian coast and the Bellona Platform (sill $\sim$2700 m), that reaches the Coral and Solomon Seas.

Fr0791 (September-91) gathered a limited amount of conductivity temperature depth (CTD) data and acoustic Doppler current profiler (ADCP) data, in the vicinity of 25°S, from the shelf to several hundred kilometres seawards. As expected, the EAC was observed flowing southwards within $100\,km$ of the shelf, and confined above $2000\,m$, but another comparably large current was observed flowing to the northeast, immediately seawards of the EAC. The northwards flow was also about $100\,km$ in width but was much more barotropic. Intense deep–structured northward meanders of the EAC are regularly observed at the departure latitude, but no such countercurrents appear to have been reported as far north as 25°S. Fig. 9 of Boland & Hamon (1970) shows a northward flow in the surface pressure distribution, that reaches northwards to 29°S. The Great Barrier Reef Undercurrent (Church & Boland, 1983) cannot be considered as a recirculation since it originates from the SEC and continues northwards to join the NGCU.

The seasonally forced phase of the model gives no indication of any intense EAC recirculation. Using biharmonic eddy viscosity and diffusivity closure (i.e., ∇^4), it does reveal the southern inertial loop of the EAC but the flow over most of the water column is southwards, at 25°S near the Australian coast. Laplacian mixing (LM) does not show an inertial loop but only weak large–scale recirculation. Smagorinsky mixing (SM; Rosati & Miyakoda, 1988) gives quite different results for the model EAC, being in much better agreement with the field data and with historical observations. SM is a more realistic formulation of Reynolds stresses than the simple Fickian parameterizations of LM and biharmonic mixing (BM). Its spatial operator has an order equivalent to LM, i.e., ∇^2, but with the effective viscosity and diffusivity coefficients varying in space and time, by several orders of magnitude. The viscosity coefficient is based on the magnitude of local horizontal shear stresses. This closure scheme yields a quite unexpected result for nearly meridional western boundaries, such as the EAC's. Very intense gyres, elongated against the coast, are radiated eastwards and have zonal wavenumbers characteristic of short eastward propagating Rossby waves. The volume flux of an individual gyre can be much larger than the flux of the associated western boundary current. With no bathymetric obstacles and no seasonal perturbation, these gyres can propagate eastwards for many thousands of kilometres. If the western boundary is not meridional then the gyres do not form and the results are similar to those obtained with BM.

Haney & Wright (1975) noticed the formation of elongated gyres against a western boundary when using nonlinear mixing in a coarse resolution barotropic quasigeostrophic model. They assert that this behaviour is a false computational oscillation, due to certain coefficients being too small. To be precise, a computational mode is a solution to the discretized equations that is inconsistent with the original analytic relation. The present modelling work shows that the gyres only exist when the western wall is meridional and are easily disrupted by seasonal forcing and bathymetry. The gyres do not develop at all when the general circulation model is tested with no vertical density structure, and so there are clearly some fundamental differences from barotropic quasigeostrophic implementations.

The overall finding of this chapter is that the observed flows along the east coast of Australia bear an uncanny resemblance to the model gyres. Even if the model gyres are eventually proven to be computational artifacts, the real ocean still exhibits some dynamical behaviour which is not too different from the model results. The apparently conflicting historical observations of the EAC can be united to give good evidence for the actual existence of similar gyres. It is postulated that the gyre region spreads only to about 600 km east of Australia because of bathymetric constraints. SM yields much more intense abyssal currents, so another implication is that thermal wind derived estimates of the EAC's volume flux could be quite inaccurate. The HEF data of Lilley *et al.* (1986) give reasonable evidence that this is the case; the HEF method produces direct measurements of depth–averaged flows and is independent of arbitrary reference velocities.

4.2 Observations from Fr0791, TEW2/3 and Ga0260

4.2.1 Data Analysis Methods

Calibration details not covered below can be found in §3.2 The deepest reference pressure used in this chapter is 3740 db. Assuming that errors in temperature and salinity measurements are coherent in such a way as to maximize the flux error for station pairs, then the flux error is $\pm 0.2\,Sv$ from $0\,db$ to $700\,db$ and $\pm 0.5\,Sv$ from $700\,db$ to $3740 db$, at 24°S. Thus, the purely instrumental error between 0 and $3740\,db$ is $\pm 0.7\,Sv$, but such coherence is unlikely and the actual errors are likely to be somewhat smaller. These flux errors have been computed from the directly measured T and S variances over $2\,db$ intervals; any *invariant* systematic errors present in the calibration process will largely cancel in the thermal wind calculations. Thermal wind analysis is performed using reference pressures of $3740\,db$ and $2600\,db$. The reference/bottom velocities are assumed to be zero in both cases, except where shelf corrections are performed in shallower water. Fr0791 ADCP data have a calibration error of not less than $\pm 4\,cm\,s^{-1}$, and visual inspection shows random fluctuations between consecutive samples are about $\pm 6\,cm\,s^{-1}$, away from locations where there is a change in the ship's heading.

Thermal wind analysis is also performed using data collected from the March–60 cruise of the *H.M.A.S Gascoyne* (Ga0260). This is the 30°S zonal transect for which Thompson & Veronis (1980) find the EAC to be flowing northwards, using an inverse technique. More straightforward analysis is used here, but from much deeper reference pressures. Data were collected via Niskin bottles, so splines are constructed from the original coarsely spaced data to give interpolated values at $2\,db$ intervals. (Stations Ga0260-100 and Ga0260-103 have several spurious T and S values, which are adjusted here, but are well to the east of the area of interest.) Flux errors are difficult to judge for Ga0260 because of the interpolations, and will certainly be larger than those for CTD–derived estimates.

More than one hundred CTD casts were performed during Fr0791 over a large area of the Coral Sea, but with only eighteen casts to more than $3000\,db$. The main purpose of the survey was to observe flows above the base of the pycnocline and their biological significance, so that only a very limited number of casts are suitable for this analysis. Six of the deep casts were in the vicinity of 24°S close to the shelf, and they form the principal data set analysed in this chapter.

4.2.2 Fr0791 Currents and Transports

Fig. 4.2 shows ADCP vectors at $150\,m$ in the vicinity of the EAC at 24°S, and up to $500\,km$ offshore. Each vector represents a twenty minute average of profiles recorded at one second intervals. The southward flowing EAC is evident close to the 200 m isobath and has speeds of up to 90 $cm\,s^{-1}$; speeds exceed 120 $cm\,s^{-1}$ in the mixed layer. Velocities near 24.7°S:155.3°E show a flow of 60 $cm\,s^{-1}$ to the northeast, essentially in the opposite direction to the EAC. The southernmost transect has an included angle of about 40° with the central axis of the EAC. Assuming that the northerly flow immediately offshore is forced to flow parallel to the EAC at 25.0°S, then the relative vorticity exceeds 20% of the Coriolis factor f, i.e., the local planetary vorticity. The two current axes are separated by 165 km along the transect and would therefore be about 110 km apart at 25.0°S.

Over the entire eastern coverage area, currents with magnitudes similar to those of the EAC, and with comparable relative vorticities, are flowing in many directions. Velocities on the two zonal transects east of 155.5°E appear to have some meridional coherence with each other. Sharp thermal fronts corresponding to changes in directions of ADCP velocities are evident in the CTD data, Expendable Bathythermograph data (not shown) and in the continuously recorded sea surface TS. Thus, the apparently erratic changes in direction of ADCP velocities are most unlikely to be spurious. Total variations in temperature are only about 1.5°C but occur over distances of less than ∼30 km, so giving large density gradients.

Fig. 4.3 shows the positions of five deep CTD stations (up to 4600 db) in the vicinity of the EAC at 25°S. Station A is only 474 db and B is 1674 db. The arrows show the approximate direction of flow determined from the deepest reliable ADCP data, as described in §3.5. Numbers adjacent to arrow heads are flux estimates in *Sverdrups*. All thermal wind flux estimates are from the greatest common depth of 3740 db, except for pairs A–B and B–C which involve a shelf crossing extrapolation. The reference velocity for pair B–C (i.e., V_{1674}) is determined from 50% of V_{1674} using pair C–D. There is some doubt as to whether C–D is sufficiently close to B–C for the purpose of interpolating V_{1674} from C–D, so half of the C–D value is used, to be conservative. The two baselines are not quite collinear but this is of little consequence. A correction of 100% is performed in the same way for A–B using the newly computed B–C profile; the pressure is only 474 db so this correction is less critical. The flux residual for the enclosed area CDEFGC is 0.5 Sv outwards. The EAC is evident between A and D, and has a flux of 36 Sv. A northwards flow of 23 Sv (17+6) lies further offshore. The

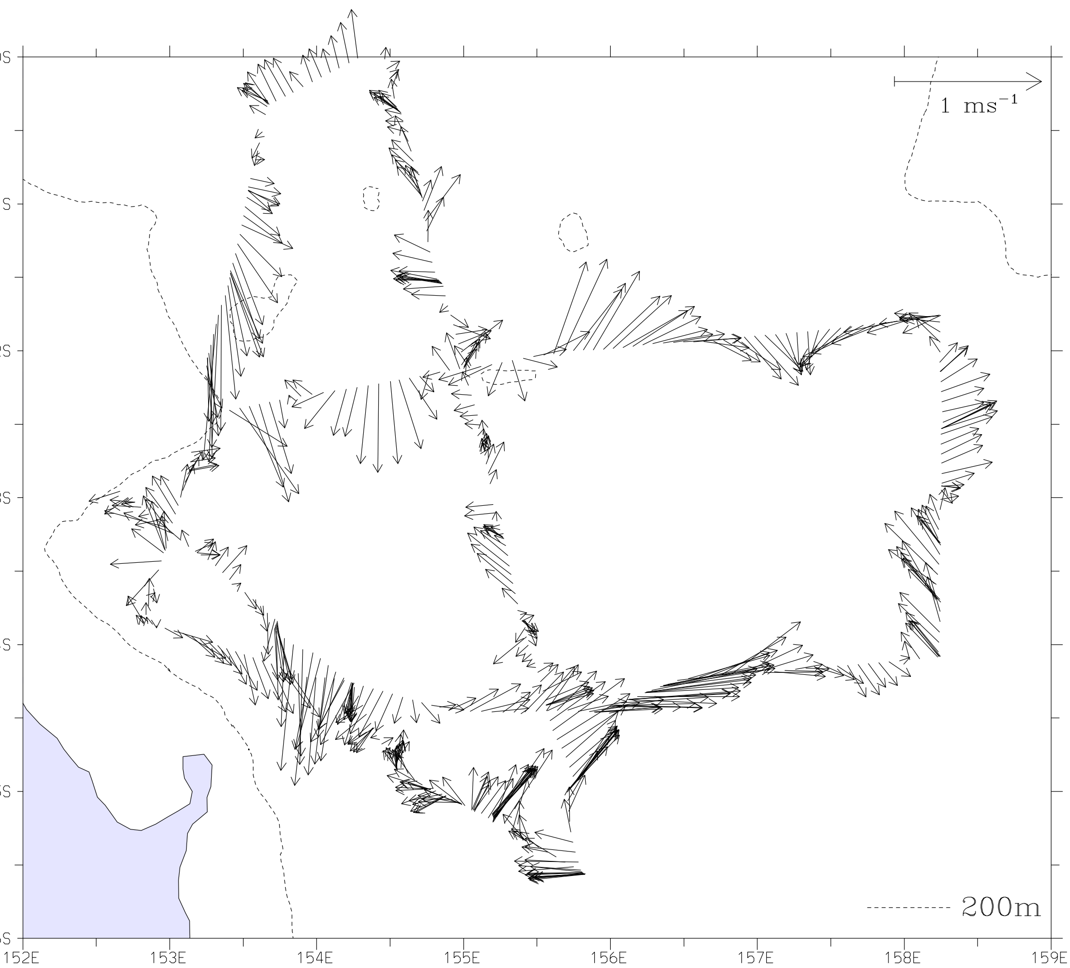

Figure 4.2: **:** Fr0791 ADCP velocities at a depth of $150\,m$. Each arrow represents a 20 minute average of samples recorded every 1 second.

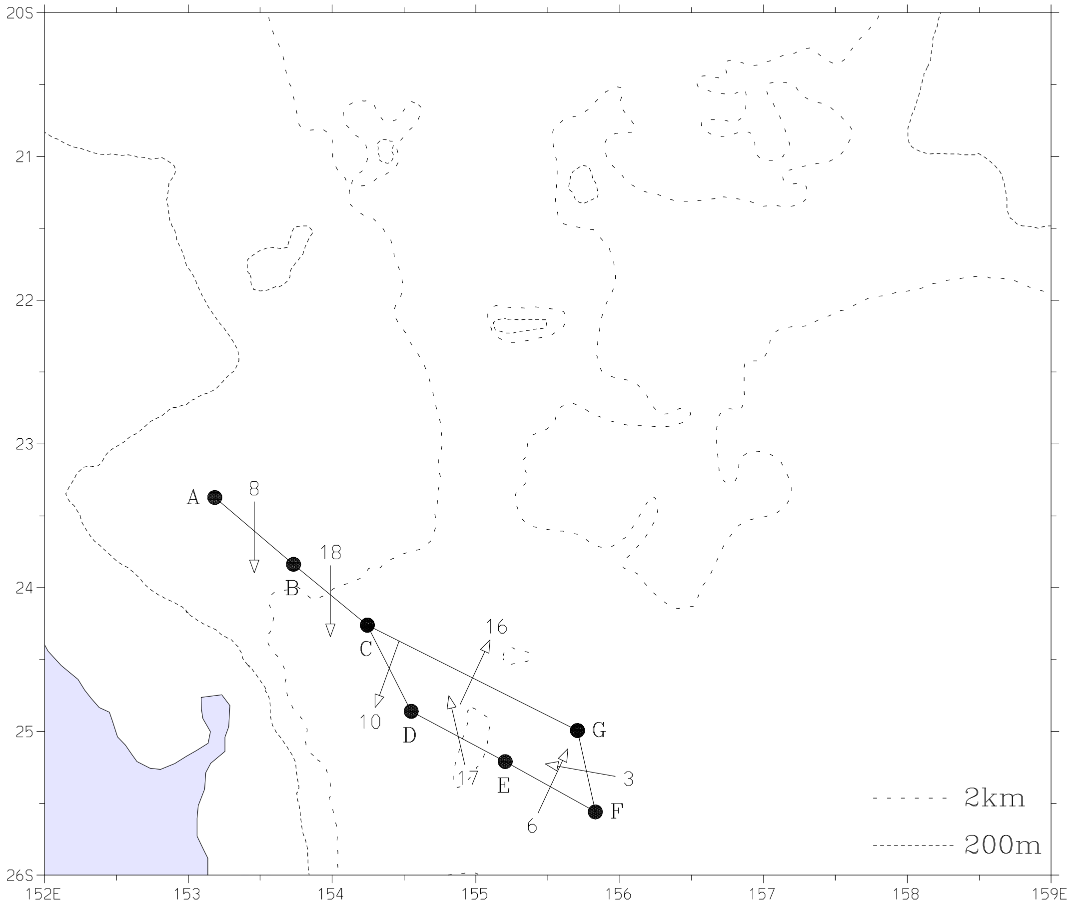

Figure 4.3: **:** Selected CTD stations from Fr0791. Arrows show the flow direction at about $200\,m$, determined from ADCP data. Volume fluxes are in *Sverdrups* ($10^6\,m^3 s^{-1}$), relative to $3740\,db$. Hydrographic stations are labeled A to G, in chronological order.

depth–averaged relative vorticity between B–D and D–E is 3.2% of f at 25°S.

Fig. 4.4 shows a larger set of CTD stations covering a wider area, but the greatest common reference available is now only 2600 db. Pair B–C is corrected in the same way as for the 3740 db analysis, but V_{1674} is simply set to zero for J–B. The EAC flux is now 41 Sv and the northwards flow further offshore is 18–23 Sv. Residuals of the two southern enclosed regions are less than 1 Sv but the northern one has a residual of 9 Sv outwards, indicating that V_{1674} for J–B is several centimetres per second rather than zero. The northeastward 23 Sv flow for G–H shows that most of the northern flow through D–F turns to the east. There is insufficient resolution to determine if this flow continues to the east or abruptly circulates in a counterclockwise direction (anticyclonically) to be entrained in the EAC. Virtually no information can be gleaned from tracer properties since they are nearly identical at all depths, except for the mixed layer (§4.2.3).

Fig. 4.5 shows isotachs of thermal wind velocities constructed from stations A to F in Fig. 4.3. The EAC is flowing southwards against the shelf and its e-folding width is about 70 km, normal to the coast. There is insufficient resolution to accurately determine its maximum depth, but these few stations suggest it is not much more than 2000 m. At 220 km on the baseline of Fig. 4.5, the strong northwards flow is visible and exists at all depths of the water column.

Fig. 4.6 shows the thermal wind profiles of pairs B–C, C–D and D–F down to a maximum of 3690 m (3740 db). The bottom correction of B–C is derived from C–D. The baseline of D–F is 165 km long, while the other two are about 75 km. Thus, to visually compare the relative fluxes of the three profiles (i.e., 'transports'), velocities for D–F should be increased by a factor of 2.2.

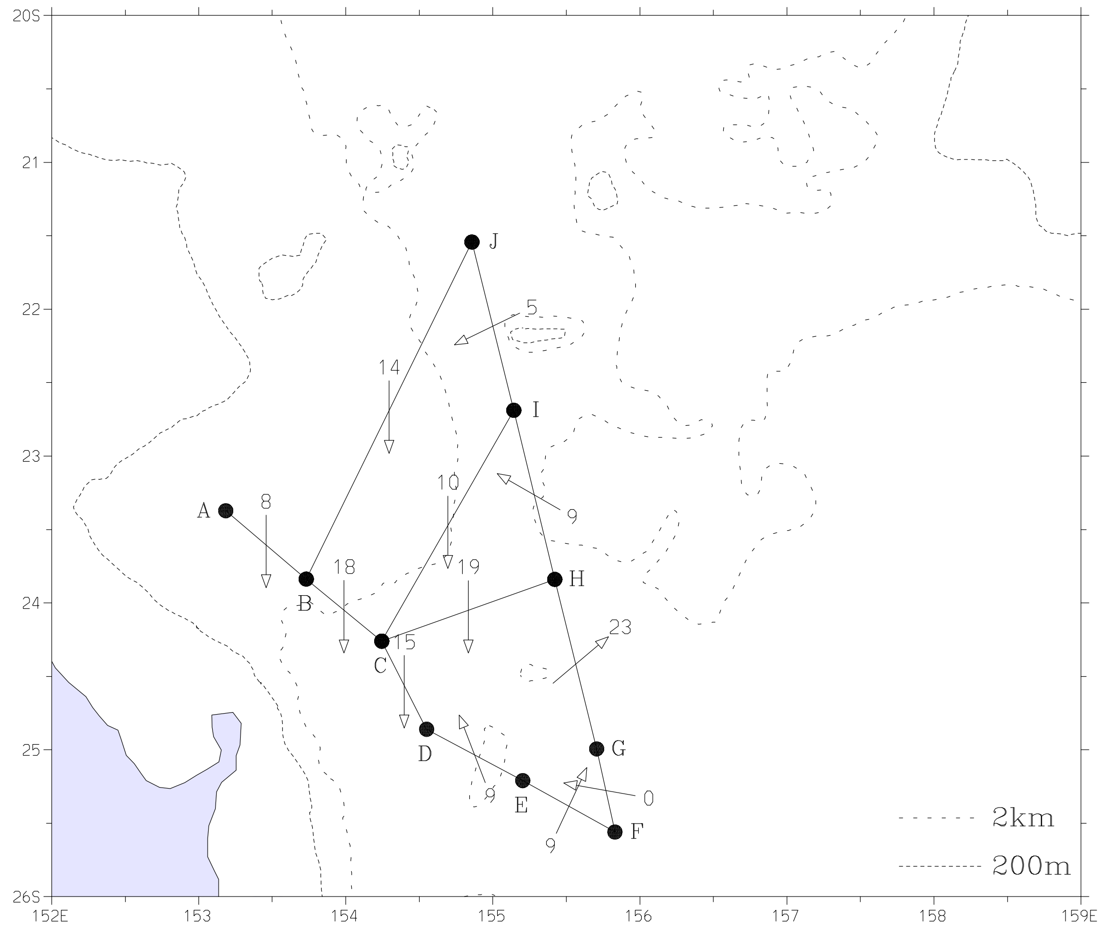

Figure 4.4: **:** Same as Fig. 4.3, but with a reference pressure of 2600 db. The northernmost enclosed region has the largest residual, being 9 Sv outwards. J–B flux is 0/1674 db. A–B flux is 0/474 db, corrected from B–C.

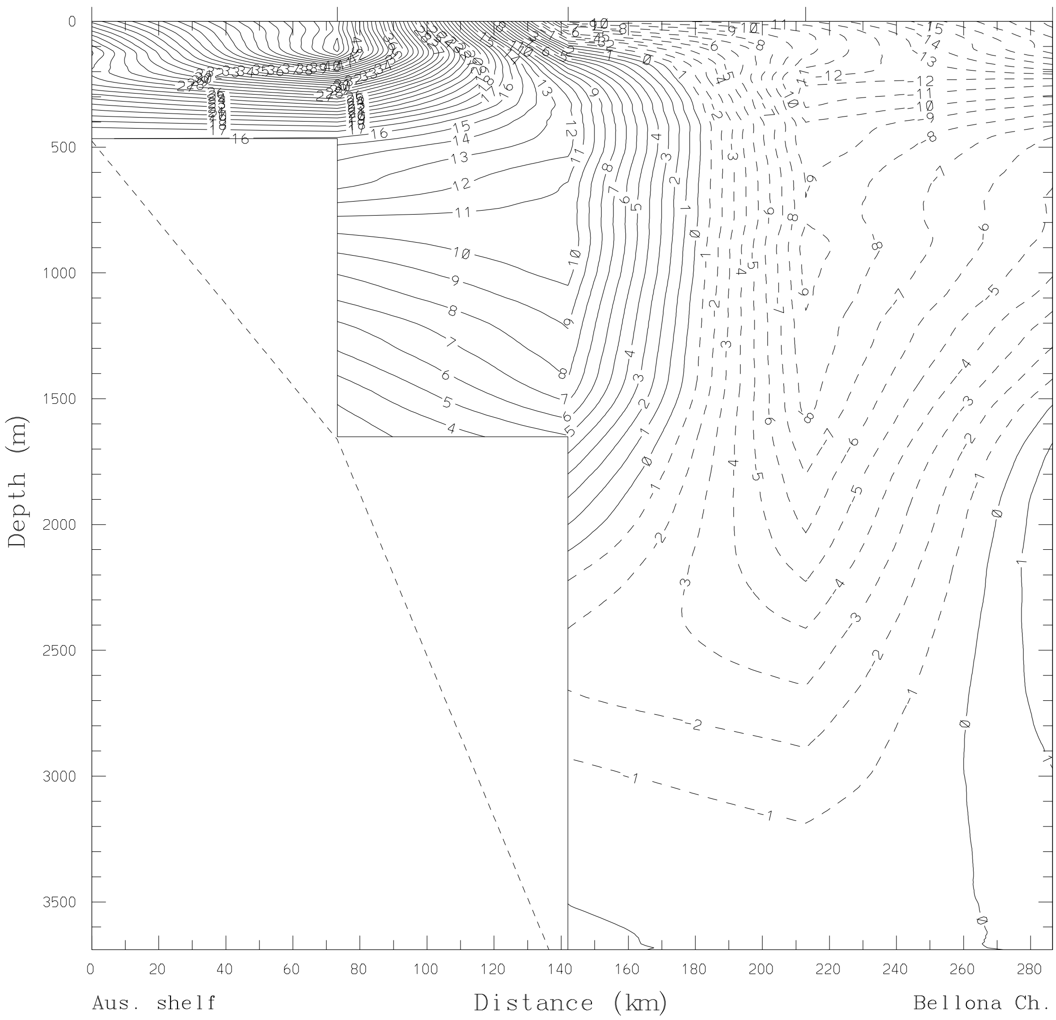

Figure 4.5: **:** Thermal wind isotachs derived from stations A to F. Positive (solid) lines imply southwards flow, i.e., out of the page. CI is $1\,cm\,s^{-1}$. Ticks across the top border denote mid–points of station pairs. The dotted line is the bottom depth. The central axis of the EAC is evident at $70\,km$ on the baseline. The strong northwards flow is evident at $220\,km$.

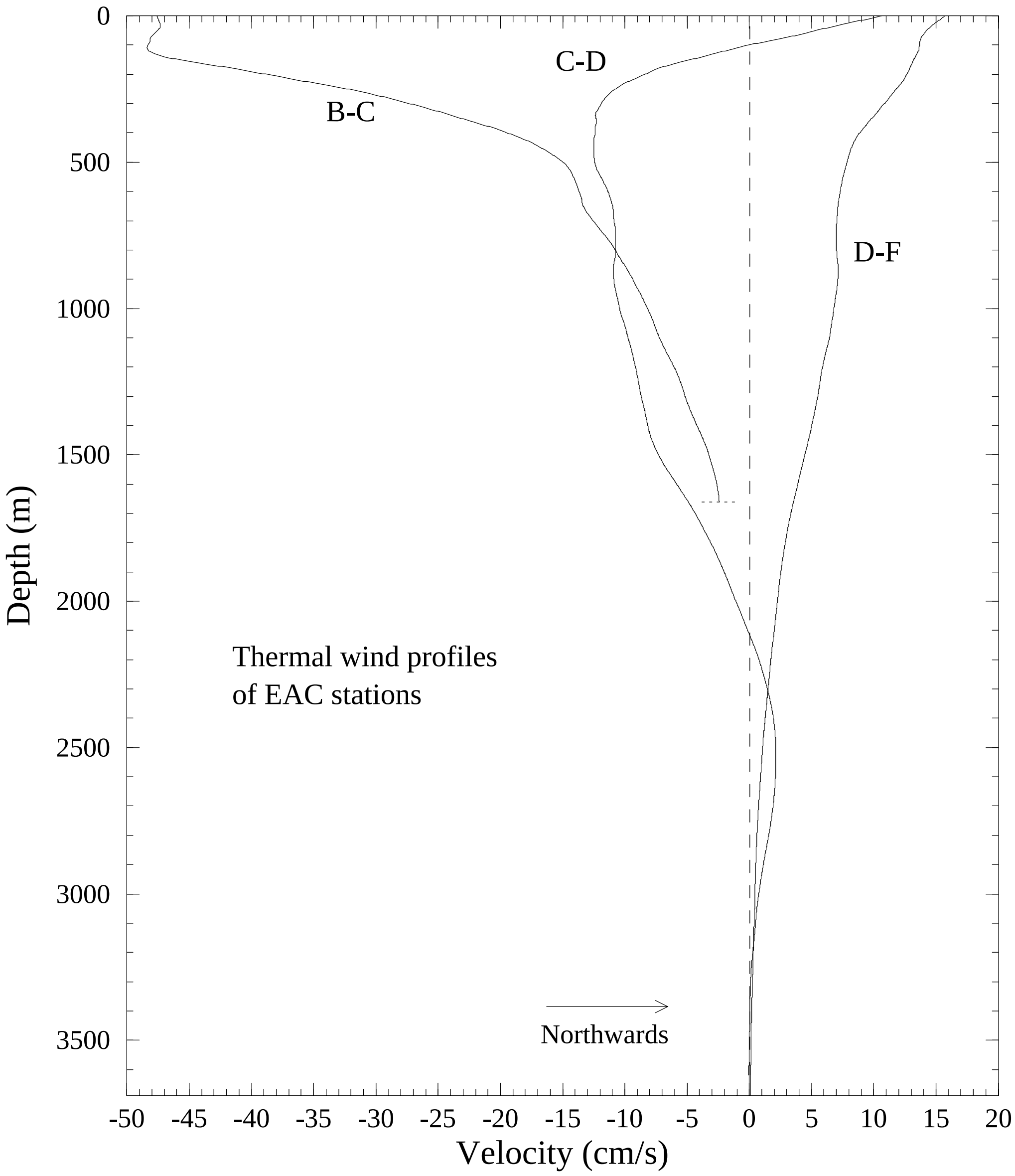

Figure 4.6: **:** Thermal wind profiles of station pairs B–C, C–D and D–F, from a reference of $3740\,db$ ($\sim 3690\,m$). B–C is relative to $1674\,db$, and is corrected (50%) from C–D. The peak value for the EAC is $48\,cm\,s^{-1}$ southwards. (Correcting for a shelf–transect included angle of $\sim 45^{\circ}$ gives $68\,cm\,s^{-1}$.)

4.2.3 Fr0791 and TEW2/387 Tracers

Fig. 4.7 is a Θ–S (potential temperature–salinity) property plot of the data for Fr0791 stations B to J, which cover the EAC and the associated northwards flow further offshore. Clearly, all eight casts have nearly identical Θ–S relationships, indicating that the EAC and the northward flow have a common source (or that very intense mixing is occurring at all depths in this location). Some salinity spiking is evident in the upper thermocline but otherwise differences between the casts are essentially negligible. The only significant differences are found in the mixed layer temperatures, which vary by about 2°C. Fig. 4.8 shows the corresponding Θ–O_2 relations for the stations of Fig. 4.7, but excludes A, B, E and F since they have no O_2 probe data, due to a CTD winch failure. Again, the properties are very similar except for the mixed layers and upper thermocline. Relative differences appear to be a little larger in comparison with Fig. 4.7, but there is a very large meridional gradient of O_2 in the South Pacific and O_2 calibrations for Fr0791 were only mediocre. SPAC (§3.2) property profiles have been overlain to gain an insight into the open ocean sources at various depths. Fr0791 data are nearly coincident with the 20°S:190°E SPAC profile, down to about 1700 m. Below this depth the relationship abruptly changes and becomes more akin to water from 44°S:156°E, i.e., the southern limits of the Tasman Sea. The O–min core at roughly 1700 m is Central Deep Water from the midlatitudes of the Southern Ocean.

Fig. 4.9 is a Θ–S property plot derived from stations B to I, two stations from TEW287 in the Coral Sea Basin, and two stations from TEW387 in the Solomon Sea Basin (10°S:157°E in Fig. 4.1). The depth range is from 900 m to a maximum of 4300 m, and the figure shows an expanded view of the deep water 'tail' in Fig. 4.7. SPAC Θ–S profiles from the same two locations used in Fig. 4.8 are overlain, but there is no obvious abrupt change at 1700 m, as is seen in Θ–O_2 profiles, perhaps because of the comparatively smaller meridional salinity gradient. However, Fr0791 and TEW data clearly follow the 44°S:156°E profile in deeper water. Profile end–points for both Fr0791 and TEW correspond to depths over 4000 m, while the depth of the S–max core of the 44°S SPAC profile is roughly 2600 m. The S–max core represents a weak presence of North Atlantic Deep Water, mixed with Antarctic waters, and is commonly referred to

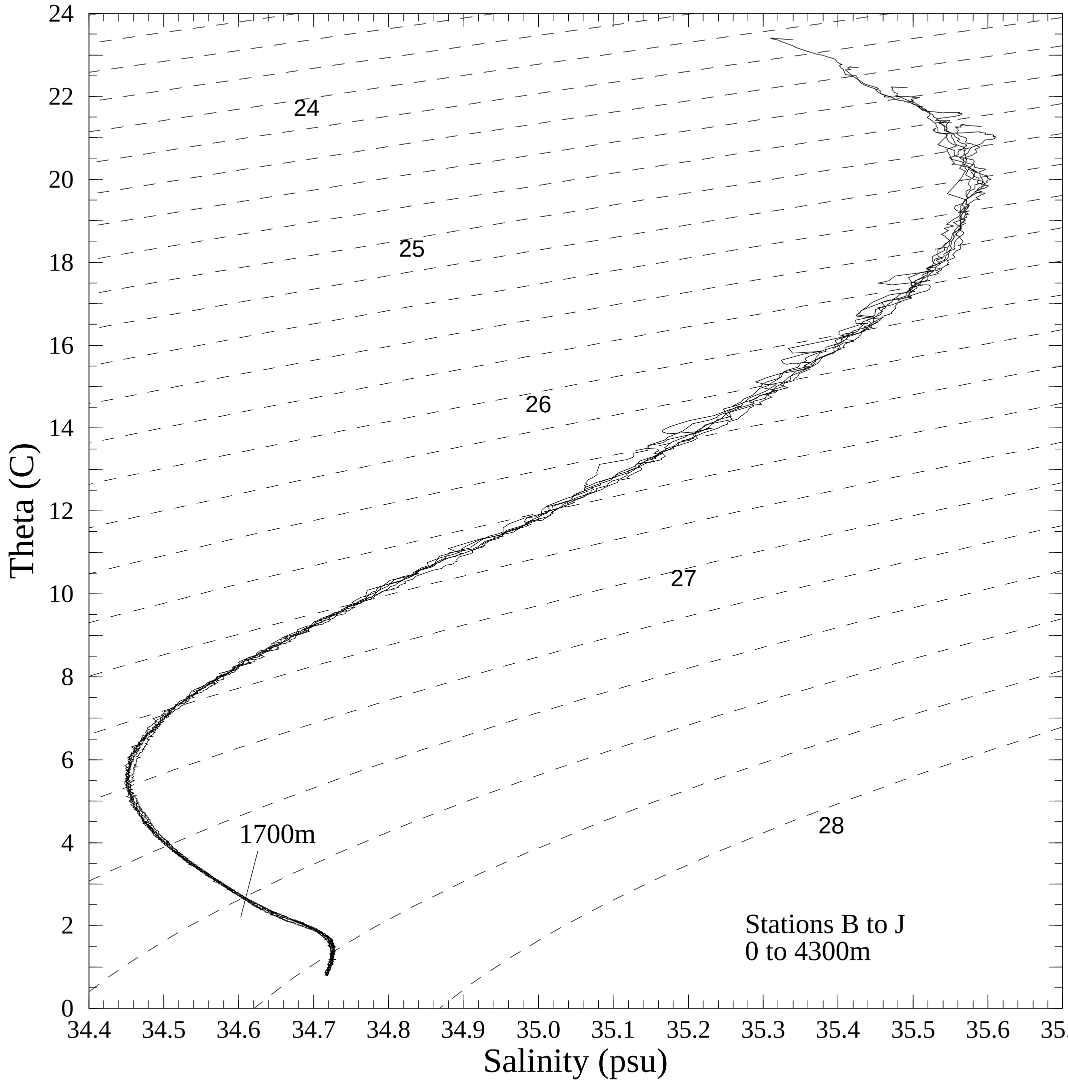

Figure 4.7: **:** Θ–S relations for stations B to J, from Fr0791. Depth range is from the surface to a maximum of 4300 m. The position of 1700 m is approximate. Dashed lines are σ_θ isopycnals. The deep S–max core is Antarctic Circumpolar Water (near $\sigma_\theta = 27.8$).

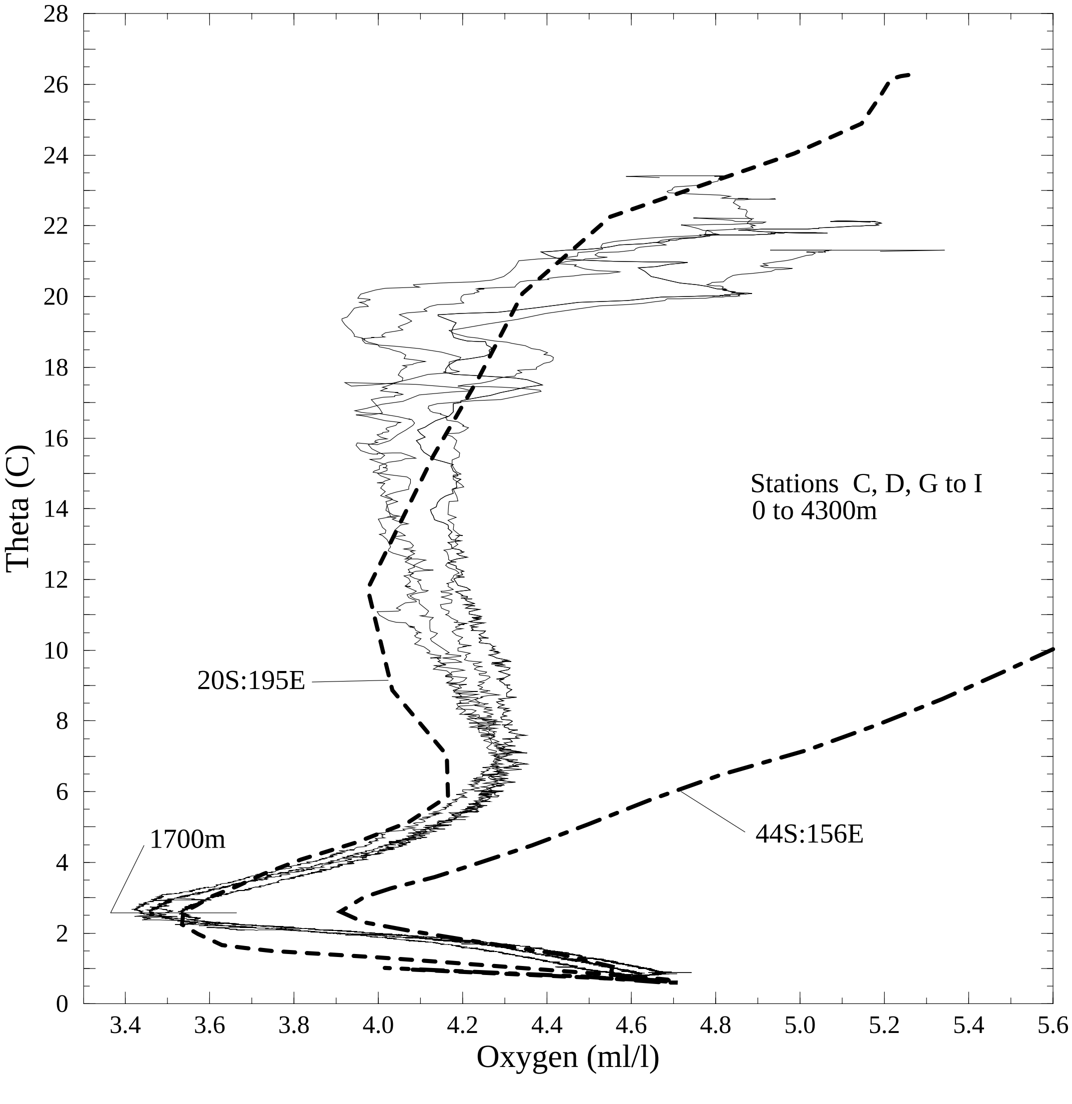

Figure 4.8: **:** Θ–O_2 relations for stations C, D, G to I, from Fr0791. Depth range is from the surface to a maximum of $4300\,m$. Corresponding relations from two SPAC sites are shown dashed. The O–min core at $1700\,m$ is Central Deep Water.

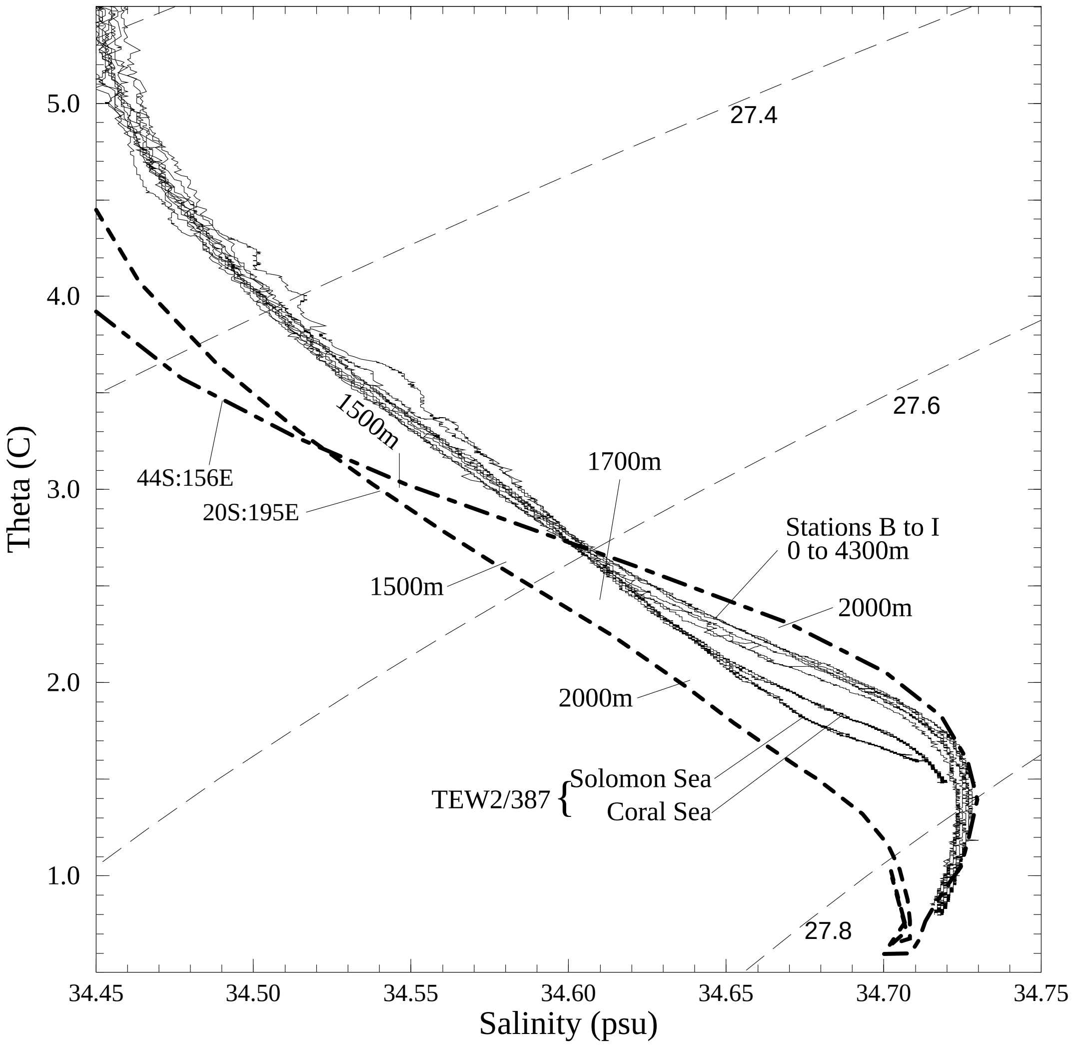

Figure 4.9: **:** Θ–S relations for stations B to I from Fr0791, and four stations from TEW2/387 in the Coral and Solomon Seas. Depth range is from 900 m to a maximum of 4300 m. Corresponding relations from two SPAC sites are shown dashed. This is the deep water tail of Fig. 4.7.

as Antarctic Circumpolar Water. Alternatively, the S–max core and modified Antarctic Bottom Water are often collectively termed Lower Circumpolar Water. The deepest waters of the Coral Sea Basin have salinities close to the S–max of Antarctic Circumpolar Water, which are larger than subpycnocline salinities found in the nearby open South Pacific. Thus, Coral Sea Basin water originates from the southern limits of the Tasman Sea and from the Southern Ocean. Pickard *et al.* (1977) note that there is no significant local production of water types in the Coral Sea, so the S–max water of the Coral Sea Basin is unlikely to be the result of subduction from local thermocline waters: the local thermocline has strong stability. Low latitude South Pacific water (SPAC line for 20°S in Fig. 4.9) between $900\,m$ and $2000\,m$ is actually denser than Central Deep Water from the Tasman Sea, indicating that this depth range in the Coral Sea may only involve mixing and not subduction. Of course, depth positions on property profiles can vary considerably between samples. Central Deep Water and Antarctic Circumpolar Water are denser below about $2000\,m$ and so subduction is likely.

Combining the results of Chapter 3, SPAC data and the findings above, a simple schematic can be constructed to show the basic flow regime of the Tasman and Coral Seas. Fig. 4.10 is a depth–latitude section showing the basic water types and their movements. The view is from the east looking towards Australia. The westwards (into the page) flowing SEC bifurcates at the Australian coast, with the bifurcation latitude being depth dependent, and then forms the EAC and NGCU. Inflowing SEC waters are confined above about $1700\,m$ due to the Kermadec Ridge, which runs meridionally from New Zealand to 17°S:186°E. Currents composed of Central Deep Water and Antarctic Circumpolar Water flow northwards into the Coral Sea, below $1700\,m$, where they then mix with low latitude water. Antarctic Circumpolar Water is denser than the low latitude waters at the same depth and so it sinks to the bottoms of the Coral and Solomon Sea Basins. Wyrtki (1961b) estimates the rate of subduction to be $0.04\,Sv$, although his value for turbulent vertical eddy diffusivity is only an order of magnitude estimate. An upper limit can be found from the deep velocities in Fig. 4.5 and the geometry of the Bellona Channel, which links the Tasman and Coral Sea Basins. The average width of the channel is about $38\,km$ between $2000\,m$ and $2700\,m$, and the due north velocity at $2350\,m$ in Fig. 4.5 is no larger than $6\,cm\,s^{-1}$. Thus, a maximum of $1.6\,Sv$ is available for subduction, which is still quite small in comparison with

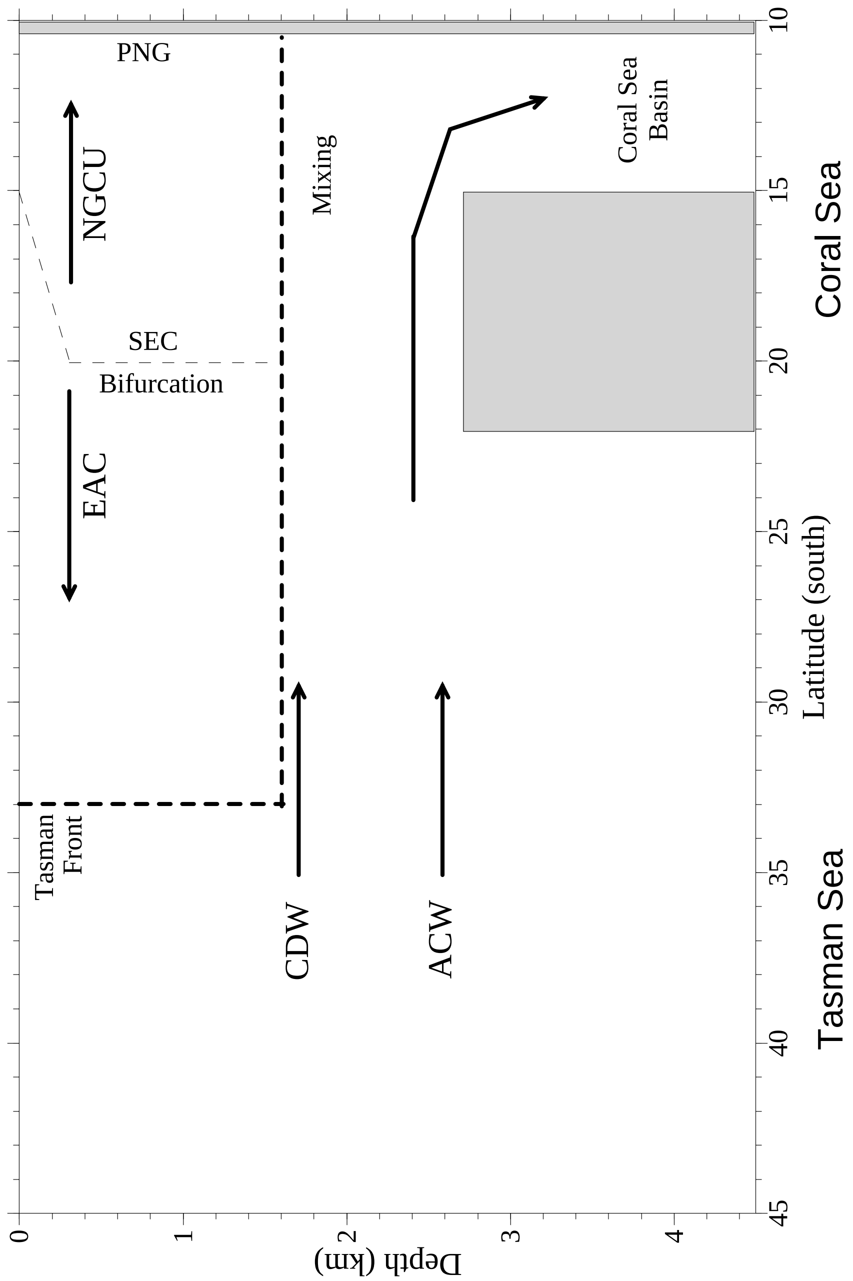

Figure 4.10: **:** [rotated] Schematic of open ocean sources for water types found in the Tasman and Coral Seas. View is from the east, looking towards Australia. The SEC flows into the page, and its depth dependent bifurcation latitude is shown approximately. Antarctic Circumpolar Water (ACW) is sufficiently dense to sink to the bottom of the Coral Sea Basin, but Central Deep Water (CDW) is likely to subduct only below 2000 m.

North Atlantic and Antarctic subduction rates. The northwards flow of Central Deep Water, however, could be much larger since the total channel width is about 200 km in the 1500–2000 m range. If the inflow of Central Deep Water into the Coral Sea is, for example, 4 Sv then there must be a similar influx of low latitude open Pacific water to produce the observed property distributions. An influx of low latitude water could occur through a deep (2700 m) channel at 11°S:163°E (Cape Johnson Trench, SOPAC charts).

4.2.4 EAC for Ga0260

Fig. 4.11 shows thermal wind isotachs of the zonal transect, at 30.3°S (Coffs Harbour), analysed by Thompson & Veronis (1980). The view is looking towards due north and positive (solid) velocities imply southwards flow (out of the page). Thermal wind profiles have been integrated from the bottom (max 4060 db) with V_B assumed to be zero. Stations Ga0260–100 and Ga0260–103 lie near the 1300 km position on the baseline in Fig. 4.11, so are outside of the region of interest. The station spacings on this transect are not less than 136 km, giving less resolution than is desirable. The first and second stations are 34 km and 170 km directly east of the Australian 200 m isobath, respectively. This places the mid–point of the first pair at 103 km east of the 200 m isobath, which is some distance east of the EAC's expected position. The mid–point of the second pair lies 230 km east of the 200 m isobath, yet there is an intense southwards flow here, of up to 45 $cm\,s^{-1}$. An upper limit for its e–folding width is 150 km. The southwards flux is 29 Sv (0/4060 db) and the current is bordered to the east by the Lord Howe Rise. Part of a strong northwards flow has been captured in the data of the first station pair, at 100 km on the baseline, where the peak velocity is 21 $cm\,s^{-1}$ at the surface. Thompson & Veronis gave a rough figure of 10 Sv for this northwards flow, using the $\sigma_\theta = 27.5$ surface as a reference pressure. Estimates for the present spline fits are 7.5 Sv for 0/3604 db, and 9.1 Sv, from the above mentioned isopycnal to the surface.

All stations between Australia and the Lord Howe Rise have very similar tracer properties and differences are obvious only in the mixed layer. The properties are similar to the extent that the coarse vertical resolution (of samples) will allow. Deep tracers to the east of the rise show, understandably, no presence

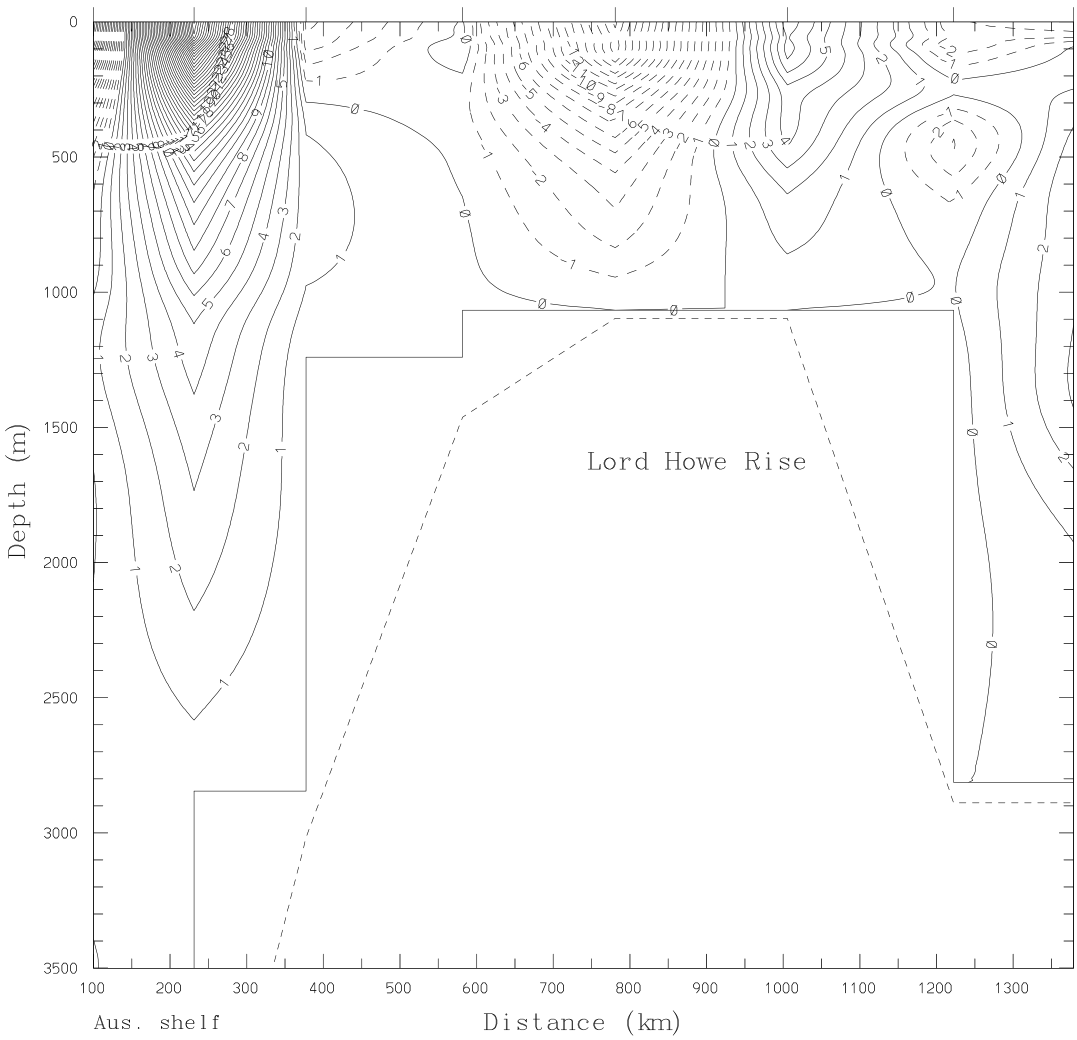

Figure 4.11: **:** Thermal wind isotachs derived from the 30°S transect of Ga0260, constructed from bottom casts (max 4060 db). The view is looking towards due north, from the Tasman Sea. Baseline shows the distance eastwards from the 200 m isobath at the Australian shelf. Positive (solid) lines imply southwards flow, i.e., out of the page. CI is 1 $cm\,s^{-1}$. The strong southwards flow at 230 km carries 29 Sv. See Fig. 4.5 caption for other details.

of Antarctic Circumpolar Water since this region is bordered to the east by the Kermadec Ridge.

4.3 Methods for Smagorinsky Mixing

A restart file at the end of the free–thermocline phase is integrated separately for a further three years, using SM and constant annually–averaged forcing. The 12:1 acceleration is retained for all extra world model runs, in this chapter. SM is similar to LM (i.e., ∇^2) but the effective viscosity and diffusivity coefficients adjust dynamically to the model's fields at each time step. The resulting coefficients are much smaller than those of LM, in the open ocean. The dimensionless wavenumber coefficient c is set to 0.3 [Eqns. (2.36) and (2.37)] to control inaccuracies in the stream function, but the model remains stable for values less than 0.15. Another separate run is commenced from the original restart file, retaining BM, but with smaller viscosity and diffusivity coefficients than those used in the free–thermocline and seasonally forced phases. Viscosity and diffusivity coefficients for the two extra world model runs are summarized in Table 4.1. Horizontal mixing coefficients for the extra BM run are set only large enough to suppress long–term instabilities, and so the stream function field is rather noisy, perhaps because of the relatively large number of islands. While "checker–boarding" of the stream function is commonly associated with LM, the present BM results display a similar grid resolution problem in the vicinity of Madagascar, which is included as a separate island. Results for LM presented below are from year five of the free–thermocline phase.

Closure	A_m	A_h	K_m	K_h
LM (m^2s^{-1})	6000	1000	10^{-3}	2.1×10^{-5} to 1.8×10^{-4}
BM (m^4s^{-1})	-4.0×10^{12}	-4.0×10^{12}	10^{-3} (m^2s^{-1})	" " (m^2s^{-1})
SM (m^2s^{-1})	5000 to 5 approx.	5000 to 10 approx.	10^{-3}	" "

Table 4.1: **:** Viscosity and diffusivity coefficients used for the three closure schemes of the extra runs. A implies horizontal, K implies vertical, m and h imply momentum and temperature–salinity, respectively. Limits for the effective Smagorinsky mixing coefficients are approximate, since statistics were kept only for limited areas and time steps.

4.4 Model Stream Function Results

Figs. 4.12 to 4.14 show the barotropic stream function for the LM, BM and SM runs, respectively, over the Tasman and Coral Seas. For the three cases, the stream function value for the Australia–PNG coastline is about $-16\,Sv$, i.e., the Indonesian throughflow (IT). The throughflows observed in Figs. 4.12 to 4.14 have nearly the same value merely by coincidence; these are instantaneous values at the time of the model's data output. The choice of horizontal mixing appears to have no discernible effect on the IT.

The EAC in Fig. 4.12 (LM) is observed to form near 20°S at the Australian coast, gaining most of its mass from the portion of the SEC flowing south of New Caledonia. The EAC proceeds southwards along the shelf edge to about 38°S, where it then departs and flows in a northeastly direction to the north coast of New Zealand. The stream function value along the Australian coast is $-16\,Sv$. For the purposes of this work, the Sverdrup component of the model EAC is defined to be the difference in stream function values between the Australian coast and 30°S:170°E. (This is probably a poor use of the term "Sverdrup", but better terminology does not exist.) The peak EAC flux is defined to be the stream function difference between the Australian coast and the most negative value not more than $300\,km$ off the coast. The Sverdrup component of the EAC is $18\,Sv$ and the peak flux is $27\,Sv$, using the above definitions. Flow above $200\,m$ tends to depart the coast closer to 33°S, while deeper portions of the EAC depart near 40°S. New Zealand's stream function value is $-14\,Sv$ which implies a nett northward flux of about $2\,Sv$ into the Tasman Sea from the Southern Ocean. No strong northward current is apparent immediately seawards of the EAC and the overall shape of the gyre is very much in line with conventional expectations.

Fig. 4.13 shows the stream function at the end of the extra BM run. There is more mesoscale variability compared with Fig. 4.12 and a tight anticyclonic (counterclockwise) loop is evident at 34°S. The loop is substantially barotropic and is in good agreement with historical observations (e.g., Hamon, 1961, 1965). The small anticyclonic gyre at the coast near 40°S is not a rudimentary ring since it is more than $1300\,m$ deep. In fact, the EAC loop has never undergone a pinch–off in any of the modelling work; the horizontal grid spacing is a little too coarse for this to occur. The bulk of the EAC departs the shelf near 33°S

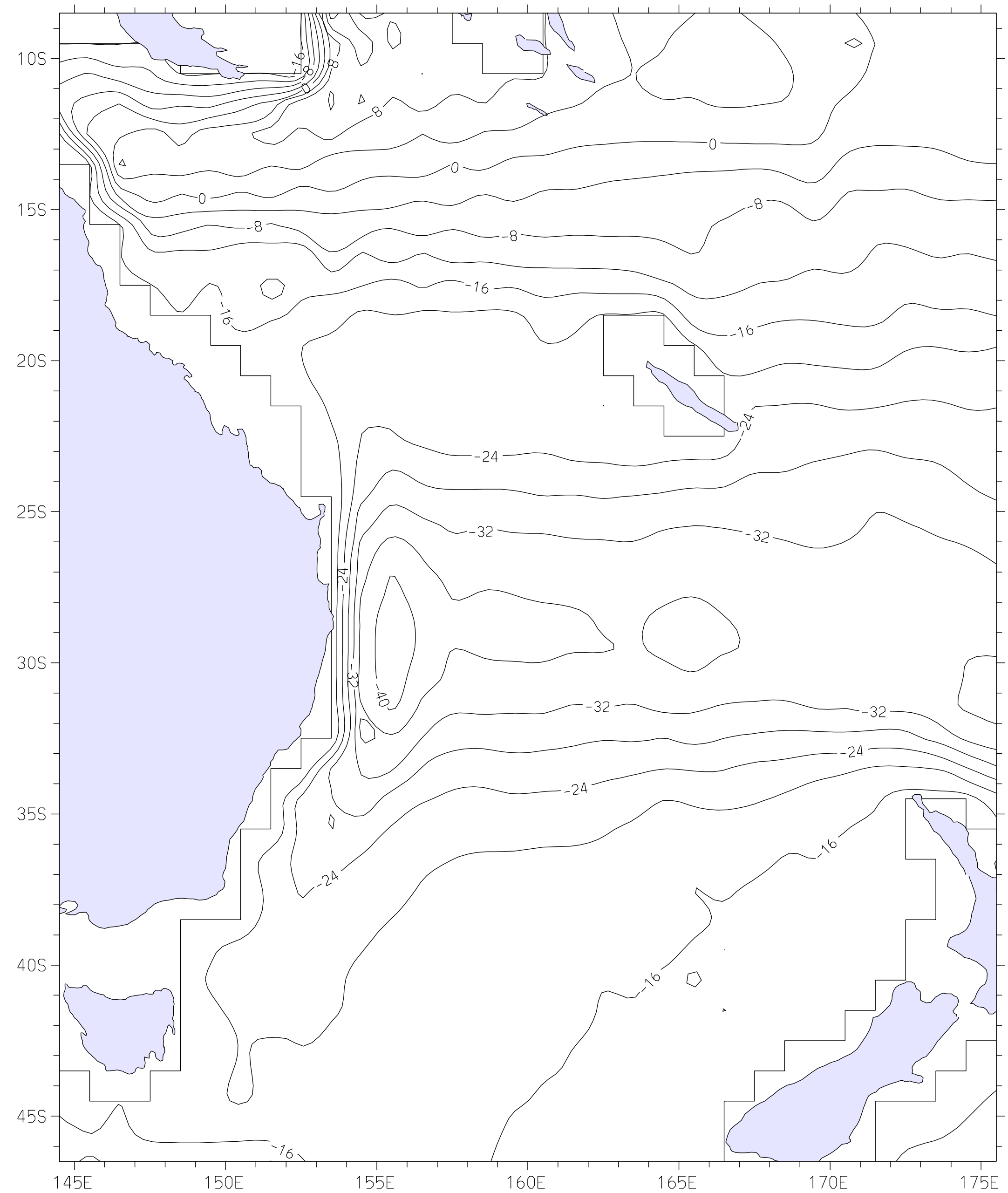

Figure 4.12: **:** Stream function results, over the Tasman Sea, for Laplacian mixing. Values for Australia, New Zealand and New Caledonia are −16.2, −14.5 and −20.0 Sv, respectively. CI is 4 Sv.

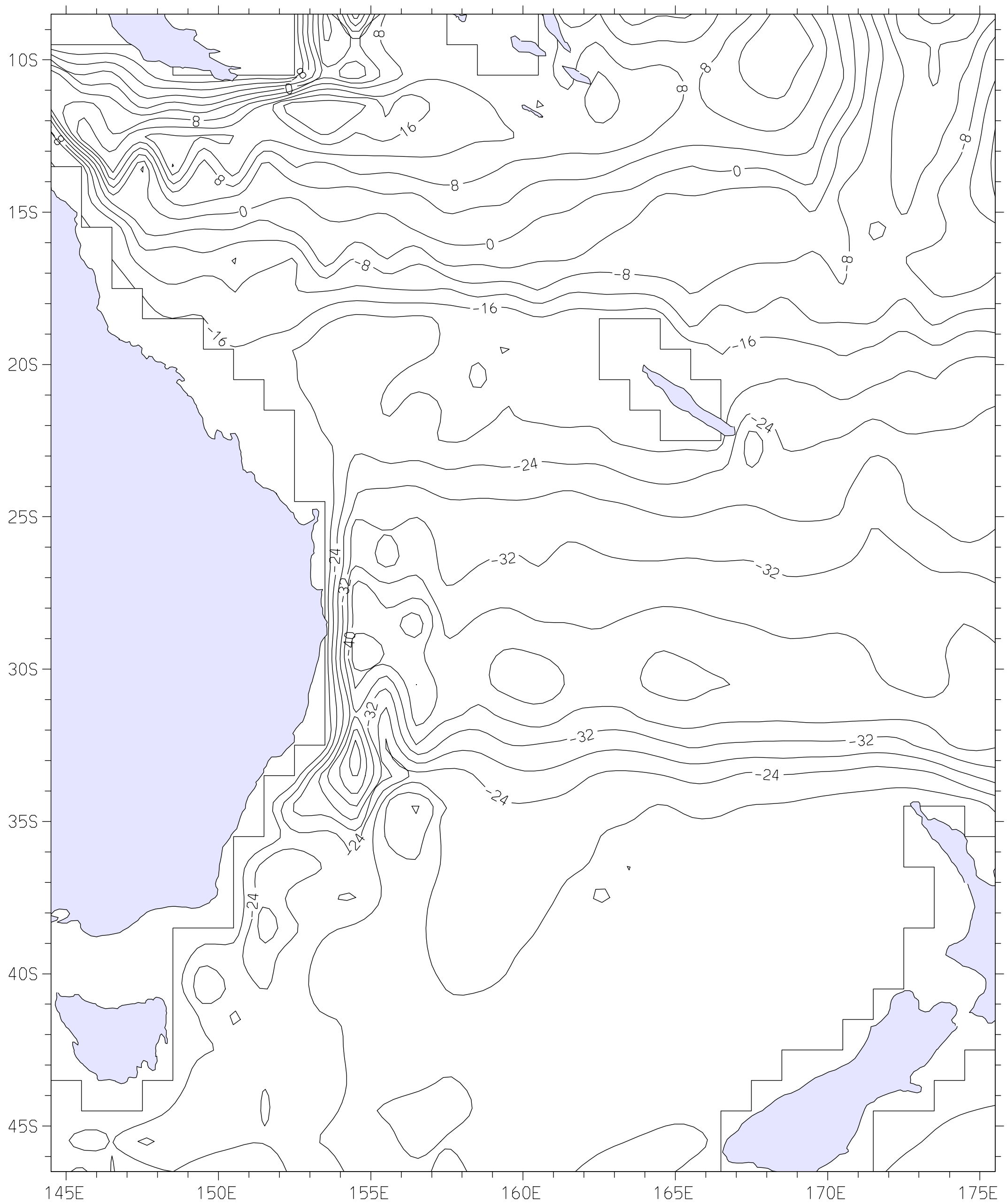

Figure 4.13: **:** Stream function results, over the Tasman Sea, for the extra biharmonic mixing run.Values for Australia, New Zealand and New Caledonia are -16.2, -16.9 and $-18.6\,Sv$, respectively. CI is $4\,Sv$.

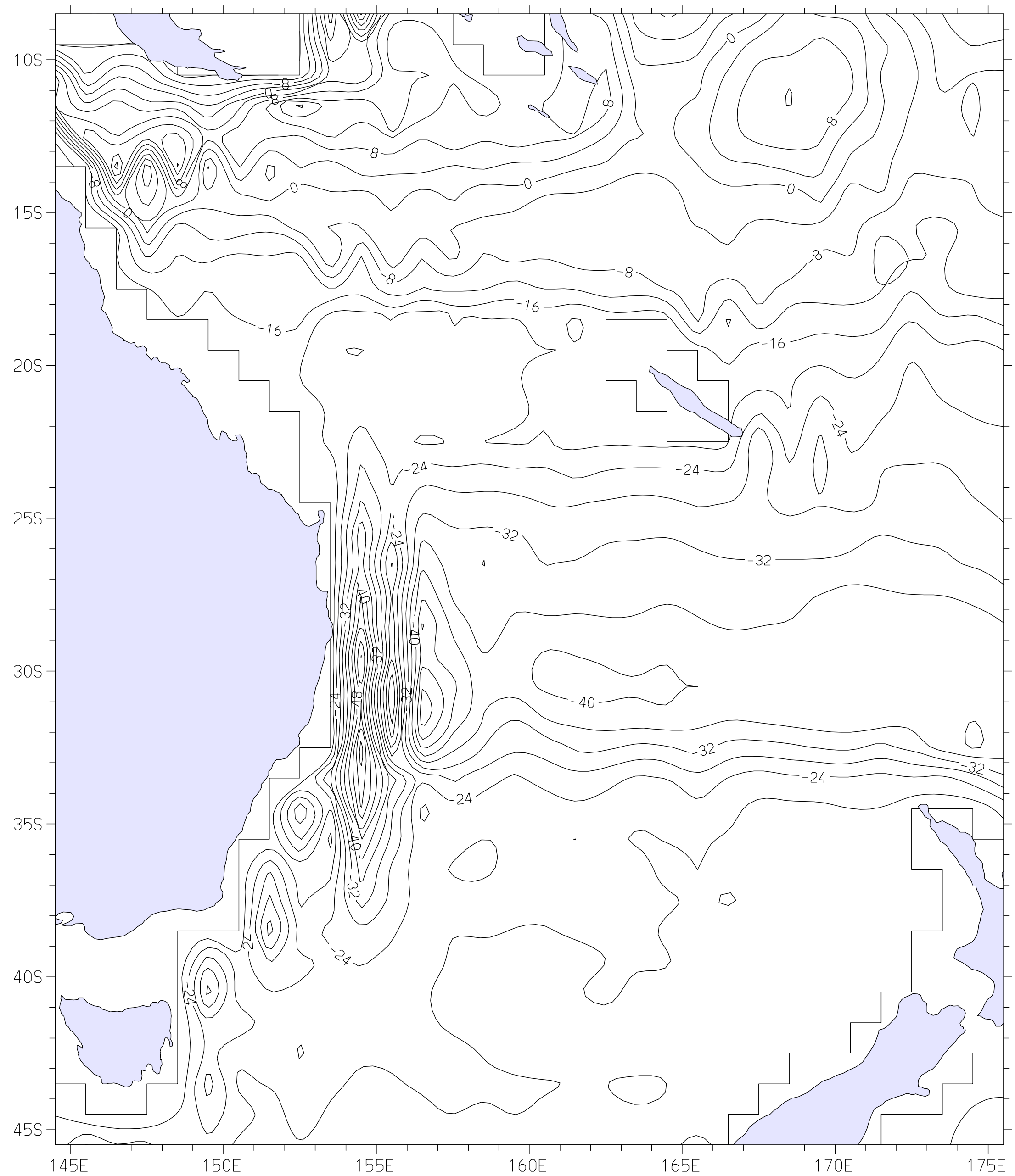

Figure 4.14: **:** Stream function results, over the Tasman Sea, for the Smagorinsky mixing run. Values for Australia, New Zealand and New Caledonia are -16.3, -17.0 and $-18.6\,Sv$, respectively. CI is $4\,Sv$.

and flows zonally towards New Zealand, east of 157°E A further 4 Sv continues along the shelf to Tasmania and then departs towards the southern tip of New Zealand; this current's axis is about 1300 m deep. It is important to keep in mind that the stream function is the depth–averaged flow and that the velocity fields at various depths can be quite different. The EAC Sverdrup and peak fluxes are 23 Sv and 32 Sv, respectively. The stream function values of Australia and New Zealand are -16 and $-17\,Sv$, respectively, which implies a nett flux of 1 Sv from the Tasman Sea to the Southern Ocean. In the depth–averaged sense this outflux re–enters the South Pacific east of New Zealand.

Fig. 4.14 shows the stream function at the end of the SM run. Mesoscale activity has increased further still but the three rings along the shelf, south of 35°S, are again well below the pycnocline. The anticyclonic loop, manifest with BM, has greatly intensified to become several elongated gyres that are almost separate from the main open ocean gyre further to the east. The gyre closest to the Australian coast is anticyclonic (counterclockwise) and thus produces an EAC which correctly flows southwards. Using the same definitions as above, the Sverdrup and peak fluxes of the EAC are 22 Sv and 47 Sv, respectively. At its outer edge, the recirculation gyre closest to the coast has a northwards flux of 44 Sv at 32°S, and 18 Sv at 27°S. The seawards transects in Figs. 4.3 and 4.4 show 23 Sv flowing northwards at 25°S. The system of gyres will be referred to as the East Australian Current Recirculation Region (EACRR). The stream function values of Australia and New Zealand are -16 and $-17\,Sv$, respectively, which implies a nett flux of about 1 Sv from the Tasman Sea to the Southern Ocean. The switch to SM causes an increase of mesoscale activity within all of the world's western boundary currents, but it is only the EAC which undergoes such a radical change in its *overall* flow regime. Very similar recirculation gyres develop over a limited latitudinal region of the North Brazil Current, shown in Fig. 4.15. The entry latitude of the current is about 15°S and the departure latitude is roughly 5°N. The entry and departure latitudes are rather poorly defined since the North Brazil Current's corresponding open ocean gyre is almost non–existent. (This is often postulated to be due to the shallow inflow and deep outflow of the Atlantic, e.g., Gordon, 1986.) The section of the model coastline where the North Brazil Current recirculation gyres occur is perfectly meridional, as is the section of Australia's coast where the EACRR develops.

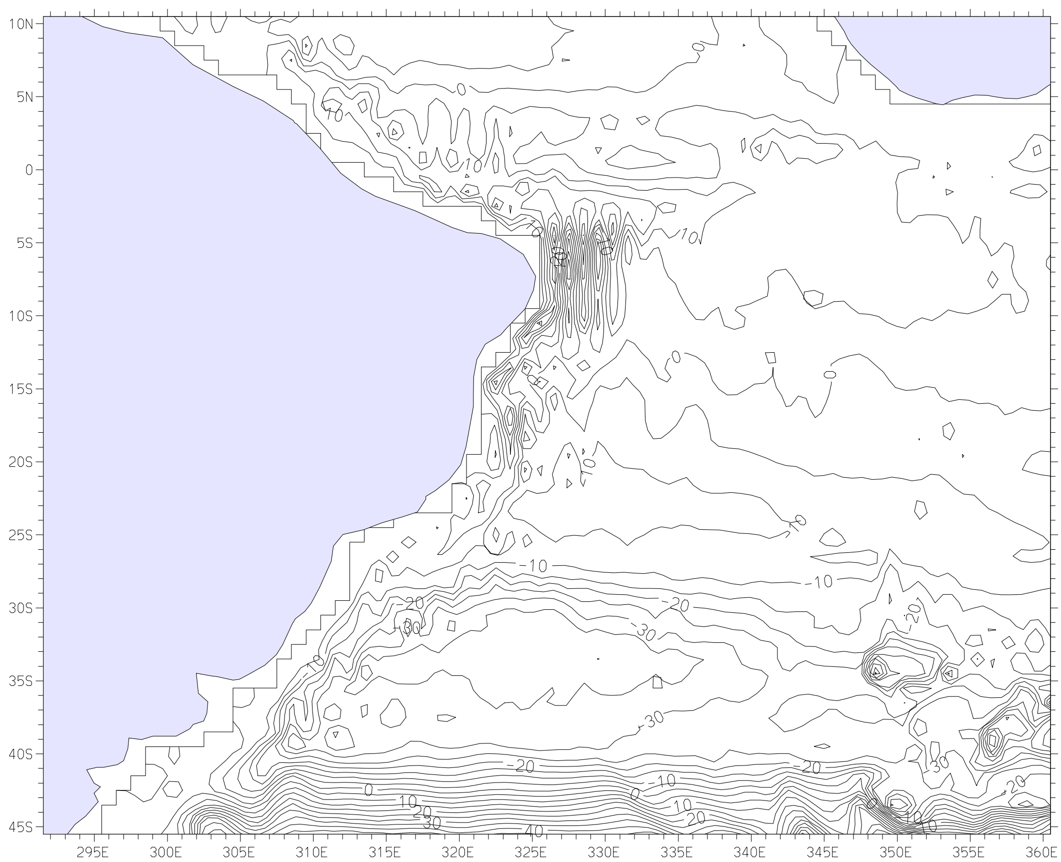

Figure 4.15: : Stream function results for the Smagorinsky mixing run, over the South Atlantic. CI is $5\,Sv$. The North Brazil Current begins near 15°S and departs at about 5°N. Recirculation gyres occur near 7°S.

4.5 North Pacific Model

Several models, based on the North Pacific have been constructed, using the MOM–1.0 code, to examine any possible link between the formation of the intense recirculation gyres and the orientation of the western boundary. Using a North Pacific domain is cheaper in machine time than a world configuration, and is equally effective for examining the dynamics. The implementations are similar to the world model, but with simple closed boundaries and a constant ocean depth of 4900 m. Model A of the North Pacific (NPA) has a rectangular domain with boundaries at 0°N to 50°N and 130°E to 250°E, a 1° horizontal resolution and seventeen depth layers. Model B (NPB) is the same but its western boundary consists of two sections at a gradient of 1:2 with respect to meridians (i.e., an included angle of 26.6°). The climatologies are derived from the Levitus data, and from the Hellerman & Rosenstein data, but the spin–up methods are a little different from that of the world model. Several separate runs are made for both NPA and NPB, for cases of fixed and seasonally varying wind stress, and for various values of bottom friction. The surface tracer forcing is simply held constant for all runs, based on the annually–averaged Levitus data. The time stepping is synchronous for all runs, and in all phases of integration. This is done to determine if the 12:1 acceleration used in the world model could be responsible for the intense recirculation gyres. The first four years of integration use relaxation constants of 35 days at the surface and 360 days at all other levels, to bring the model tracer fields to within 1% of the Levitus data. A further four years are performed with only relaxation in the surface layer, while all layers below the surface are fully prognostic. SM is used for all runs and phases of NPA and NPB. The SM wavenumber coefficient is the same as for the world model, namely 0.3.

Fig. 4.16 shows the stream function for the western half of NPA's domain, at the end of the four year prognostic phase. This case uses a fixed annually–averaged wind stress and a bottom friction coefficient of 1.2×10^{-3}. There is a pronounced recirculation region at the western boundary with gyres considerably more intense than those found in the world model. The gyre closest to the western boundary is anticyclonic (clockwise), thus correctly producing a polewards western boundary current (i.e., the Kuroshio). Clearly, the accelerated time stepping technique is not the cause of the recirculation gyres in the world model. Con-

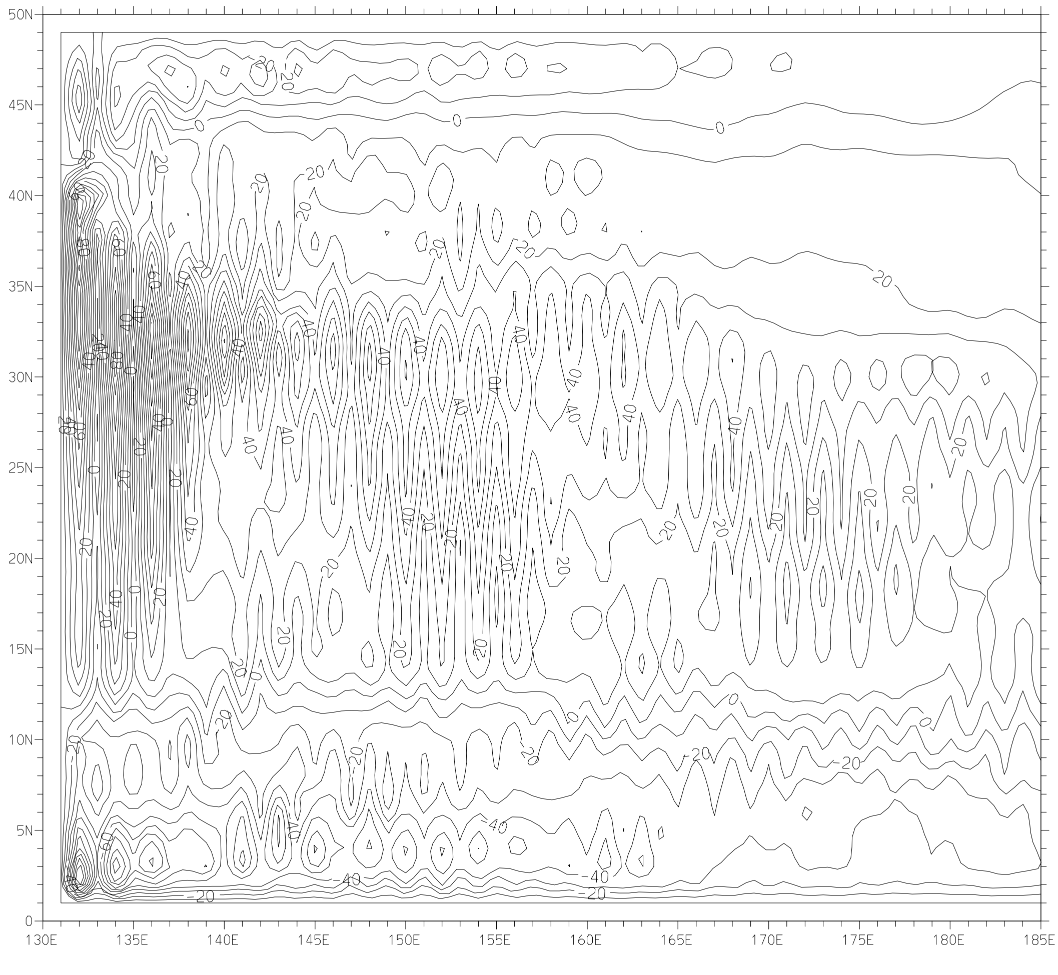

Figure 4.16: **:** Stream function results for model A of the North Pacific. CI is $10\,Sv$. The western boundary is perfectly meridional. The three large gyres closest to the western boundary are all anticyclonic (clockwise). Thus, the 'Kuroshio' flows to the north.

touring this field is problematic and so the figures are not particularly clear. The three most intense gyres at the western boundary each have barotropic fluxes exceeding 100 Sv and their rotational senses are all anticyclonic. There are smaller elongated gyres interposed between the larger ones, with cyclonic rotations and fluxes of up to 35 Sv.

Other intense gyres (Fig. 4.16 contour interval is 10 Sv) are observed many thousands of kilometres to the east of the boundary current region. Time–lapse images show these gyres to be moving *eastwards* at approximately 6 $cm\, s^{-1}$, while slowly dissipating. This velocity is quite similar to the predicted group velocity of *westward* propagating nondispersive midlatitude Rossby waves. These open ocean gyres are apparent in the pressure field only at depths below the pycnocline. The surface and thermocline pressure distributions show gyre activity to no more than 1200 km from the western boundary. At 5000 km from the western boundary the gyres are still propagating eastwards with the same group velocity, but only at abyssal depths. Fig. 4.17 shows the surface pressure, near the western boundary, for the NPA run with fixed wind stress.

A second run of NPA, but with a seasonally varying wind stress, gives intense gyres within a few hundred kilometres of the western boundary and only very weak abyssal gyres to a maximum of 1200 km eastwards. The surface pressure field (not shown) exhibits elongated gyre patterns extending less than 300 km offshore. A third run of NPA, using a fixed wind stress and large bottom friction (3×10^{-3}) yields boundary gyres less intense than the first run (Fig. 4.16) but a little more intense than those of the time varying wind stress run. A fourth run of NPA includes two deep meridional ridges in the bathymetry, 700 km offshore from the western boundary. All surface forcing is fixed in time and there is no bottom friction. The resulting gyres are confined between the western boundary and the ridges. Smaller abyssal gyres are generated on the eastern sides of the ridges, and propagate eastwards.

Two barotropic models of the North Pacific have been constructed (no results displayed here) to see if Haney & Wright's quasigeostrophic model results can be emulated by primitive equation implementations. A fifth run of NPA is performed, using SM, and the density of all tracer grid points is set to a single constant value, i.e., with no internal density structure. Recirculation gyres do not occur and the stream function is smoothly distributed, similar to those found

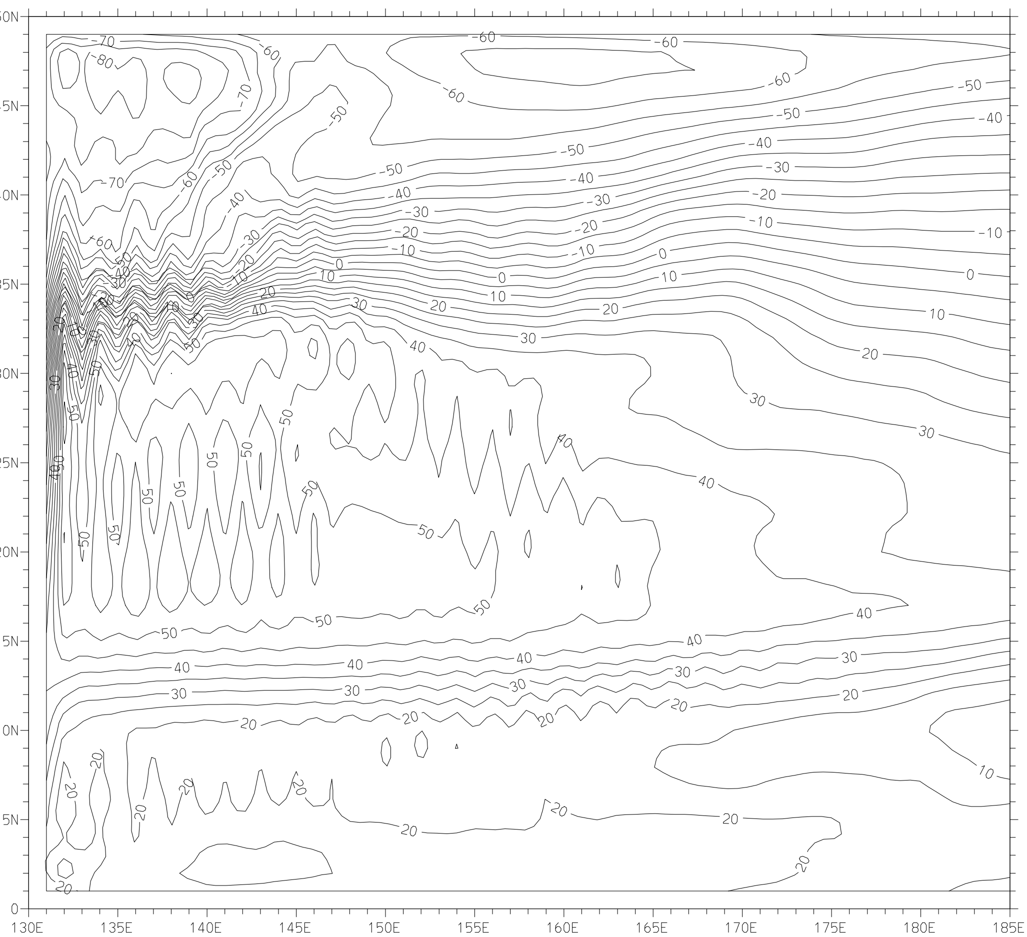

Figure 4.17: **:** North Pacific model A surface pressure variation (mb), for fixed wind stress. CI is $5\,mb$.

in simple classical Munk models (e.g., Pedlosky, 1987, Fig. 5.4.4). The second barotropic model has one layer, a horizontal resolution of $1/3°$ and a horizontally constant density field. Its resulting stream function field is qualitatively identical to that of the barotropic seventeen layer model, as expected.

Fig. 4.18 shows the resulting stream function for NPB, using a fixed wind stress and no bottom friction. Elongated gyres are not apparent but there are intense gyres with radii equal to the grid spacing, and a staggered distribution that is coincident with the stepped western boundary. Clearly, the grid spacing is much too coarse to resolve the intrinsic dynamics found here. Small gyres are observed several thousand kilometres offshore, but these are relatively weak and are well below the pycnocline. Varying the wind stress seasonally for NPB confines the mesoscale gyres to within $300\,km$ of the western boundary. In additional simulations with NPB, the gyres begin to link up as the boundary is rotated towards perfect meridional alignment, and form the 'super eddies' evident in NPA and the world model.

4.6 Internal Structure of the EAC System

This section provides a detailed examination of the internal structure of the Tasman Sea area, from the results of the extra SM run of the world model.

Fig. 4.19 shows the predicted surface pressure distribution over the Tasman Sea, from the SM run of the world model. This is the surface pressure corresponding to the stream function field of Fig. 4.14. Contours show the pressure variation in $2\,mb$ intervals, about a global mean which is arbitrarily set to zero. The position of Lord Howe Island is shown by the solid triangle. The model rigid–lid surface pressure p_s should be a good approximation to the surface elevation η of the real ocean, via the hydrostatic relation $\eta = p_s/\rho g$. However, large discrepancies are possible under certain conditions (Dukowicz & Smith, 1992; Smith *et al.*, 1992). The model p_s is reconstructed from the time derivative of the stream function, and the subsurface pressure fields are found by integrating the hydrostatic relation downwards, using p_s as the constant of integration. Densities are calculated from the model's equation of state, which is derived from the JPOTS standard (UNESCO, 1981). An alternative would be to calculate the surface steric height relative to some reference pressure, which would allow direct com-

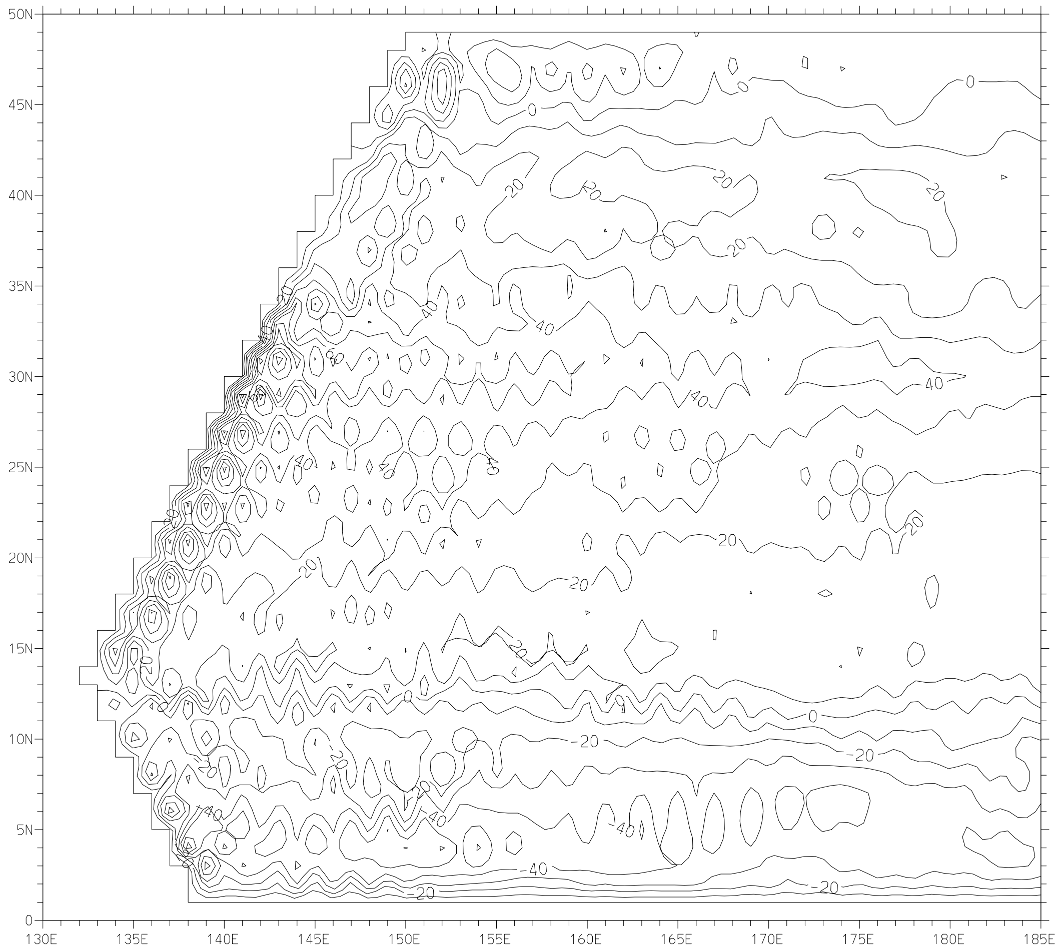

Figure 4.18: **:** Stream function results for model B of the North Pacific. CI is 10 Sv. The western boundary is at a gradient of 1:2 with meridians. The 'Kuroshio' flows to the north.

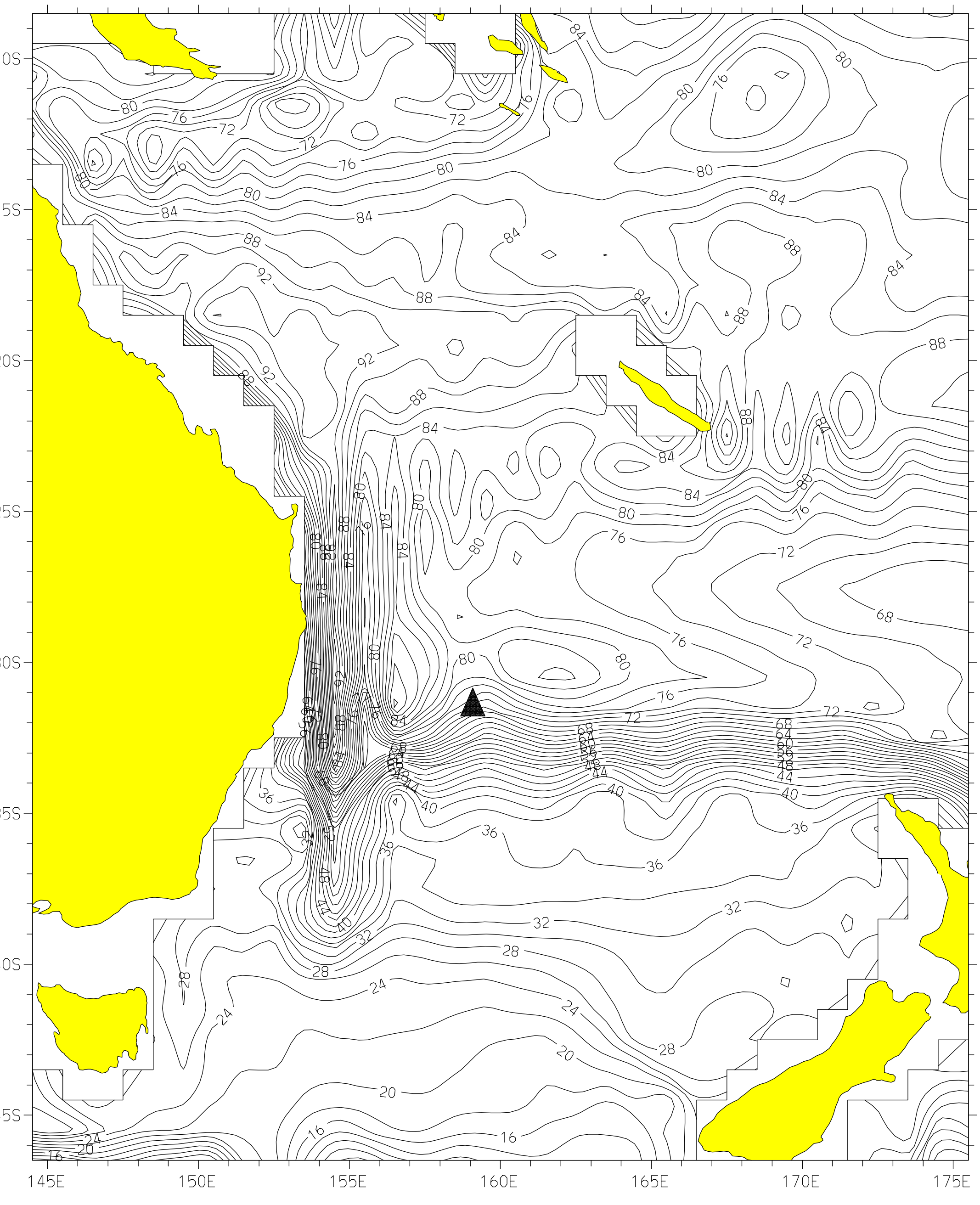

Figure 4.19: **:** Surface pressure variation (mb) for the Smagorinsky mixing run. CI is $2\,mb$. Triangle denotes Lord Howe I. (31.5°S:159°E).

parison with observed steric heights, but the variable bathymetry of the region makes this less attractive. The absolute surface elevation is directly comparable with satellite altimetry data. The pressure distribution is rather noisy along some of the coastlines, but could be improved by using a nine–point stencil to solve the stream function's Poisson equation. This unfortunately causes a compensating increase in the stream function's noise level (§2.6).

The zonal pressure ridge extending from the Australian coast to the northern tip of New Zealand is generally too intense compared to historical observations. It is too strong in the biharmonic and Laplacian cases, as well. The pressure fall is still 40–50 mb per 400 km well offshore. While such gradients have been observed close the Australian coast (e.g., Hamon, 1965), the model ridge is too intense to be realistic (Godfrey, private communication).

The southwards flowing EAC is evident in Fig. 4.19, and the divergence of pressure contours along the coastline is the mechanism which drives western boundary currents, i.e., cross–isobar acceleration. The EACRR is evident in the surface pressure and extends nearly 500 km directly offshore. The EAC departs the Australian coast at about 33°S, circulates around a tight loop and then flows zonally towards New Zealand, east of 157°E, to form the Tasman Front (Warren, 1970). This zonal front has its largest pressure gradients at the surface and is quite weak below the pycnocline. Several world model runs have been performed with New Zealand shifted northwards and southwards by 400 km, wherein the latitude of the Tasman Front changes commensurately, and it remains zonal. Moving New Zealand has no effect on the EACRR which retains its position along the perfectly meridional section of the Australian coast. Ageostrophic velocities in the EAC are directed southwards along the Australian coast, in the same direction as the main flow, and are about 2% of the total velocity: see Fig. 4.20. The comparatively strong ageostrophic velocities in the Tasman Front are also very coherent with the direction of the main flow, being towards New Zealand, thus implying at least some inertiality for this current.

There is a weak near surface eastwards current, originating from the northern limit of the EACRR (24°S, Fig. 4.19), that flows towards New Caledonia. This is joined by some water flowing northwards over a convoluted path from the Tasman Front, and the resulting current intensifies while flowing eastwards away from New Caledonia. The zonal current eventually disperses into the tropical

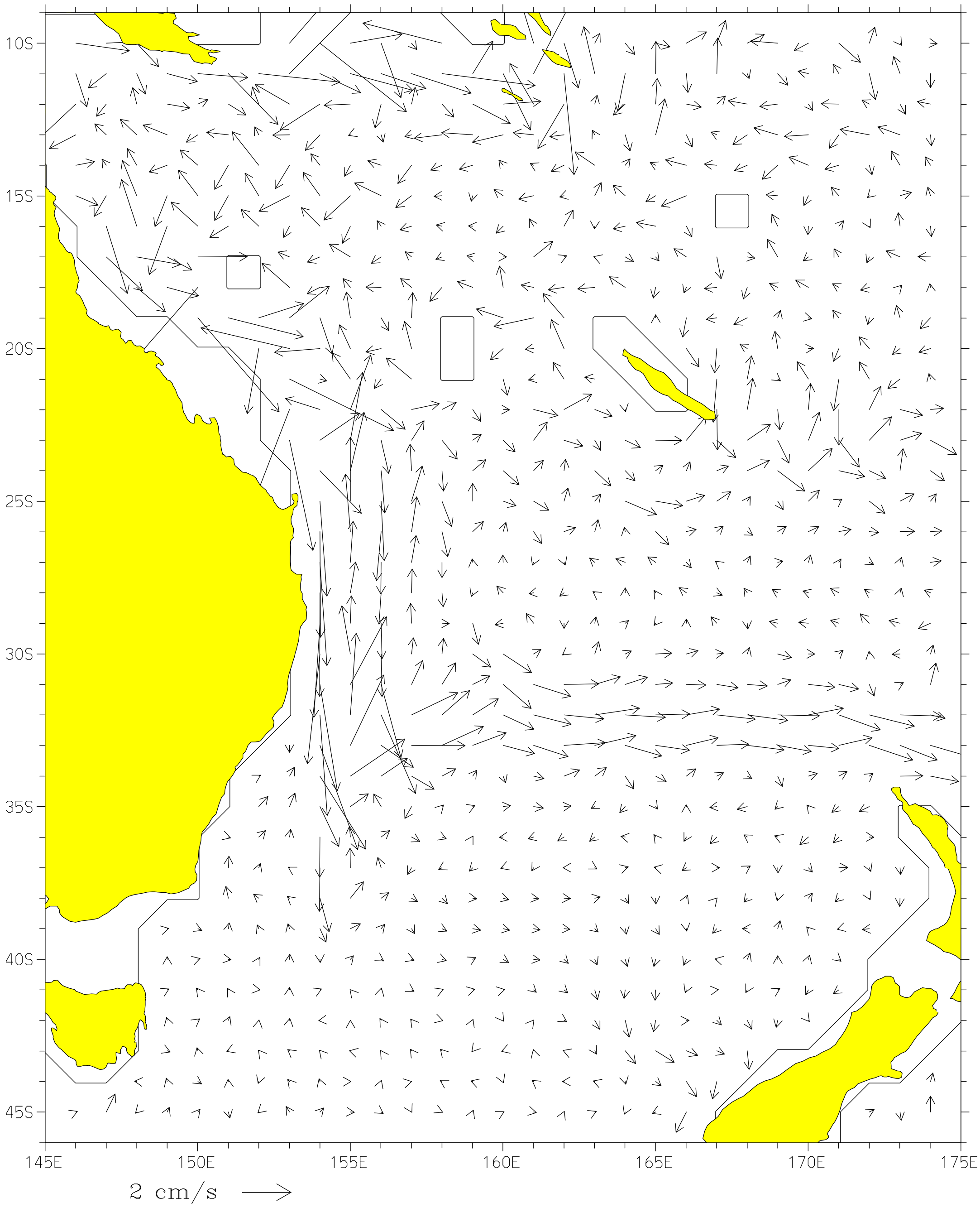

Figure 4.20: **:** Ageostrophic velocities at 210.5 m for the Smagorinsky mixing run. Ageostrophic velocities in the Tasman Front are in the same direction as the total flow, and are about one third of those for the EAC, adjacent to the Australian coast.

gyre further to the north: see Figs. 5.3 and 5.20.

Fig. 4.21 shows the pressure variation at 210.50 m. The variation is relative to the model's global average of 216.01 db, at this geometric depth. The northward flowing current at the northern end of the EACRR ($\sim 24°$S) feeds directly back into the EAC, unlike the corresponding surface flow in Fig. 4.19. There is also inflow originating from south of New Caledonia, rather than the near surface outflows implied by the surface pressure. The Tasman Front's cross–stream pressure gradient is smaller than the EAC's, but because of its small latitudinal range the isobars effectively constitute streamlines.

Fig. 4.22 shows the pressure variation at 896.50 m, about the global average of 922.13 db at this depth. The northwards and southwards flows of the EACRR are now similar in magnitude, with most of the influx arriving from south of New Caledonia; the Kermadec Ridge is deeper near New Zealand than it is further to the north. The Tasman Front's cross–stream pressure gradient is now much smaller than the corresponding gradient at 210 m in Fig. 4.21. A polewards current, evident along the southern Australian shelf edge, turns westwards at the southern tip of Tasmania. This southbound current originates from the EACRR and the SEC inflow towards Australia at 25°S. More detailed analyses of the model's pressure field show that the southbound current exists only between depths of 750 m and 1800 m, and carries roughly 5 Sv. The bifurcation latitude of the SEC at the Australian shelf is about 24°S, and the northwards branch (NGCU) is evident flowing towards PNG.

Fig. 4.23 shows the pressure variation at 1636.00 m, about the global average of 1686.16 db at this depth. The northern and southern areas of the EACRR are similar in magnitude and two deep gyres are evident further to the south. Below about 1600 m the SEC inflow is prevented from entering the Tasman Sea by the Kermadec Ridge and Lord Howe Rise. Anticyclonic rings are evident south of 34°S. The rings are still apparent below this depth (not shown) but the southbound flow towards Tasmania is not. Gyres within the EACRR gradually weaken in magnitude as the seafloor is approached, but even there, their associated pressure gradients are still a good deal larger than those in the open Pacific. Lord Howe Rise represents a bathymetric restriction to the EACRR, and considering the North Pacific model results, this is the reason why the EACRR gyres are weakened at these depths. The bottom friction is also probably weakening the

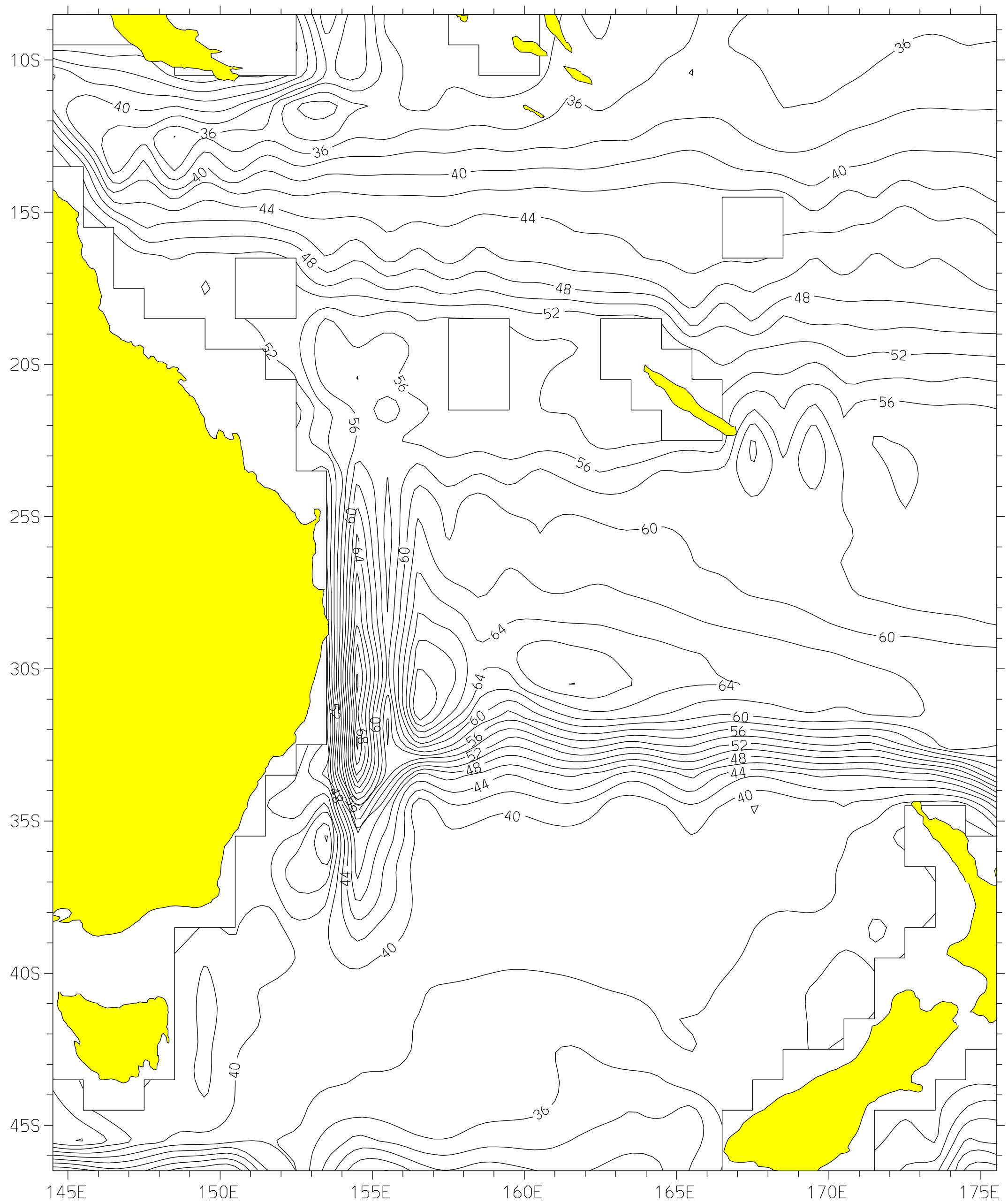

Figure 4.21: **:** Pressure variation (mb) at $210.50\,m$ for the Smagorinsky mixing run. Global average is $216.01\,db$. CI is $2\,mb$. At this depth the bulk of the EAC departs the Australian coast at 33°S and flows directly towards the north coast of New Zealand, forming the Tasman Front.

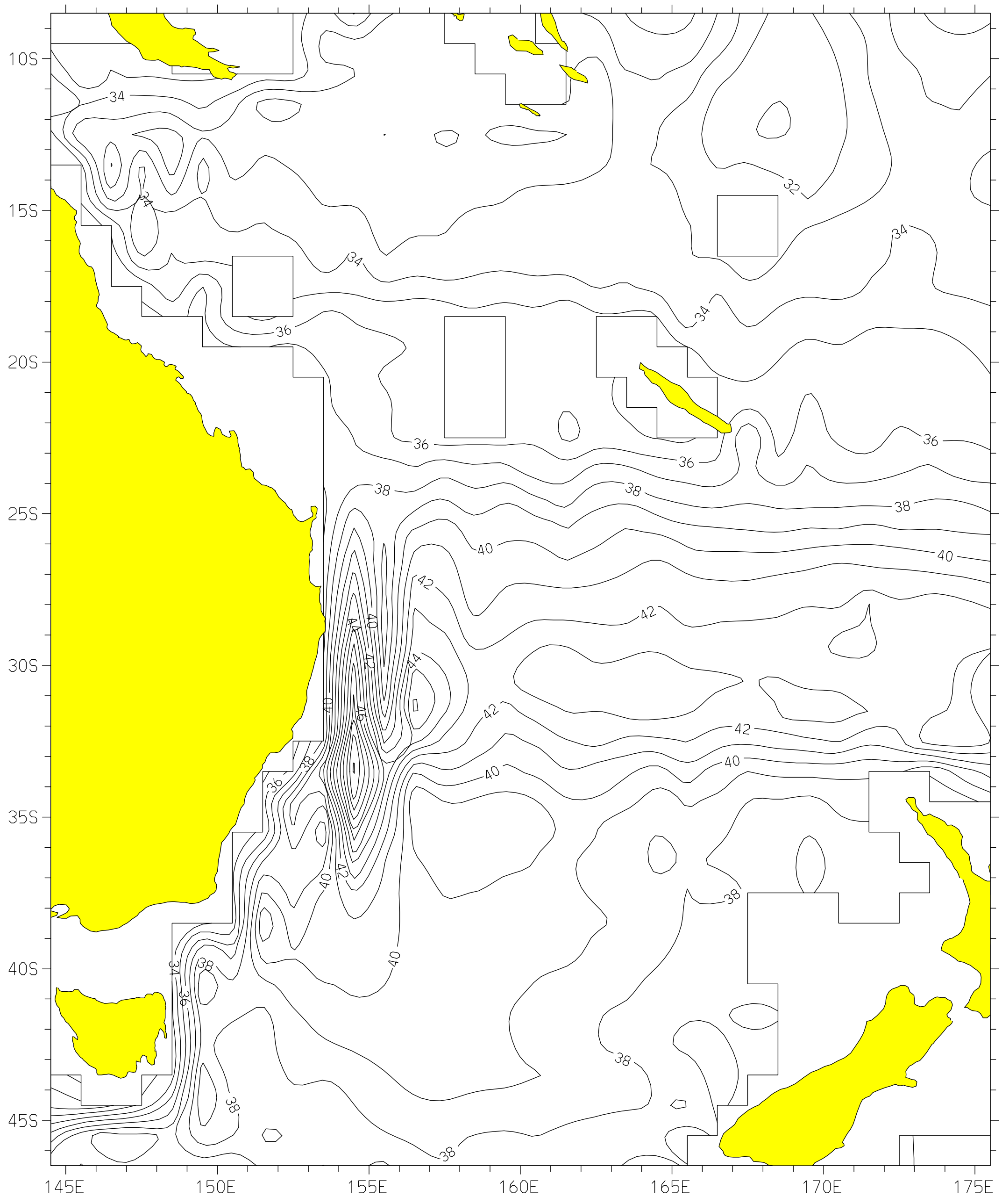

Figure 4.22: **:** Pressure variation (mb) at $896.50\,m$ for the Smagorinsky mixing run. Global average is $922.13\,db$. CI is $1\,mb$. The SEC bifurcation lies near 24°S at the Australian shelf. A significant current flows southwards from the EACRR, rounds the southern tip of Tasmania, and is eventually entrained in to the ACC further to the south.

Figure 4.23: **:** Pressure variation (mb) at $1636.00\,m$ for the Smagorinsky mixing run. Global average is $1686.16\,db$. CI is $0.5\,mb$. The Lord Howe Rise completely blocks zonal flows between Australia and New Zealand. EACRR gyres and the southwards current are the most dominant features at this depth, in the Tasman Sea.

abyssal flows.

Fig. 4.24 shows the velocity field at 2120 m. The Bellona Channel (21°S:-155°E) has an equatorwards flow along its eastern flank and a polewards flow along its western flank. The nett flow through the channel, between 1400 m and the bottom, is 0.5 Sv to the south and the oppositely directed currents carry about 2.5 Sv each. A weak anticyclonic nett circulation is just perceptible in the Coral Sea, as is observed in field data. The seasonally forced phase of the world model, using BM, shows a deep (1200–2700 m) southwards current through the Bellona Channel, with a flux of about 2 Sv (Fig. 3.43a,b). All deep velocities within the channel are directed southwards, so preventing Central Deep Water and Antarctic Circumpolar Water from entering the Coral Sea Basin. This deep current enters the Coral Sea from the open Pacific via the channels at the northwestern and southeastern ends of the Solomons. The deep current also causes a strong anticyclonic circulation below 1200 m in the Coral Sea Basin. Such a strong, pervasive influx of low latitude water cannot occur in reality since the water property data obtained during Fr0791, at depth around the Bellona Channel, show only Central Deep Water and Antarctic Circumpolar Water. Thus, SM produces results which are in better agreement with observations, for the deep source waters of the Tasman and Coral Seas. It is the oppositely directed currents in the Bellona Channel, with SM, that drive the deep anticyclonic circulation in the Coral Sea. The BM results are simply not correct for the deep waters of this area. As a further contrast, LM yields relatively stagnant deep waters in the Tasman and Coral Seas.

Fig. 4.25 shows the model velocity field at 3300 m for the Tasman Abyssal Plain and areas to the south. The ACC flows through the abyssal gap between the Macquarie–Balleny and South Tasmania Ridges. Model abyssal velocities within the EACRR attain a maximum magnitude of only 6 $cm\,s^{-1}$, being much weaker than the 35 $cm\,s^{-1}$ jets measured by Mulhearn *et al.* (1986). However, this is still an improvement over the BM velocities of 0.5 $cm\,s^{-1}$. Mulhearn *et al.* find the intermittent jets are composed of relatively cold water, which is most likely to be modified Antarctic Bottom Water originating from the ACC further to the south.

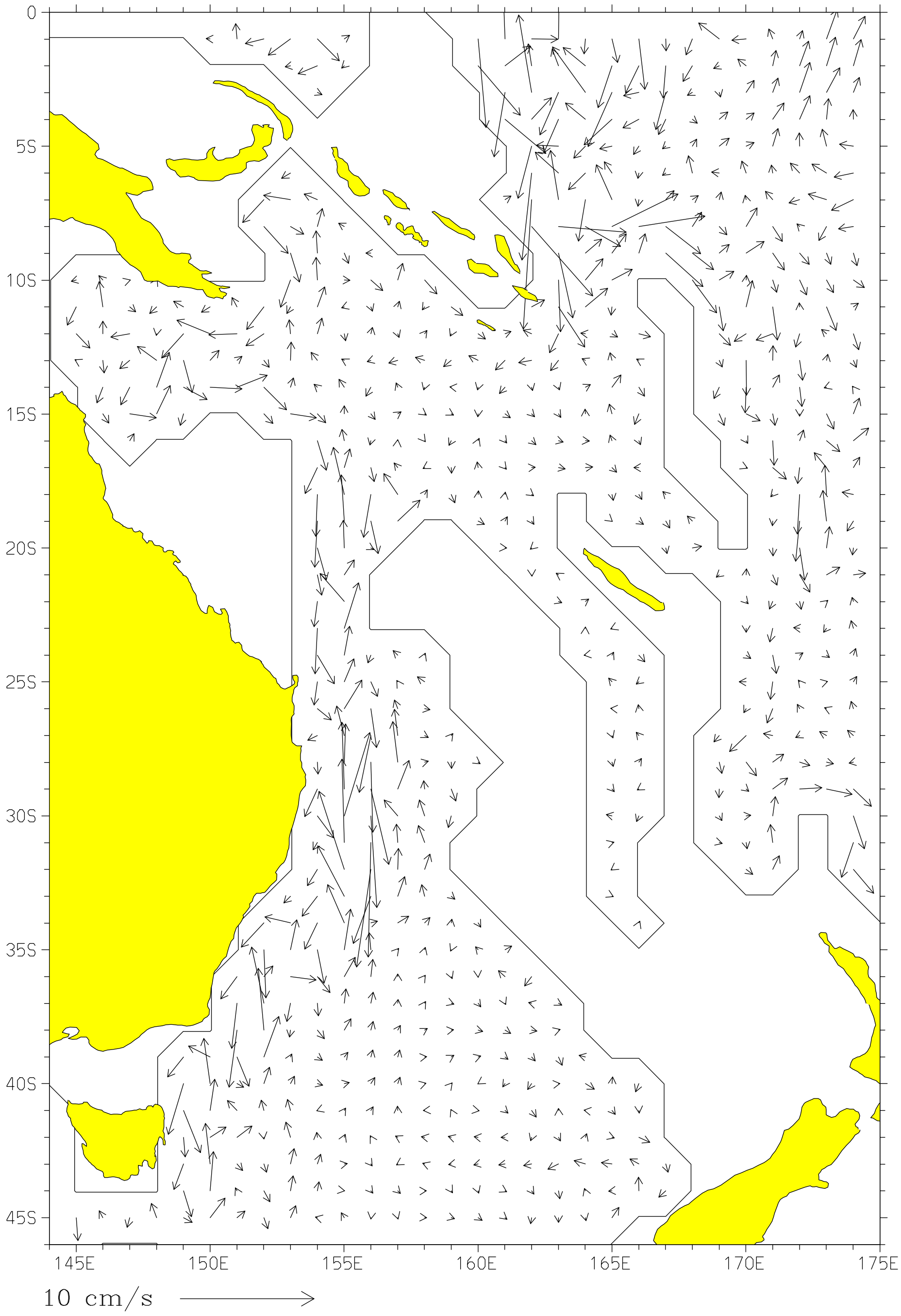

Figure 4.24: **:** Velocities at 2120 m (level 13) for the Smagorinsky mixing run. The EACRR drives two oppositely directed currents through the Bellona Channel at 21°S:154°E. Another strong current is visible heading southwards along the eastern flank of the Ontong Java Plateau (8°S:162°E), but only 0.5 Sv enters the Coral Sea below 1400 m.

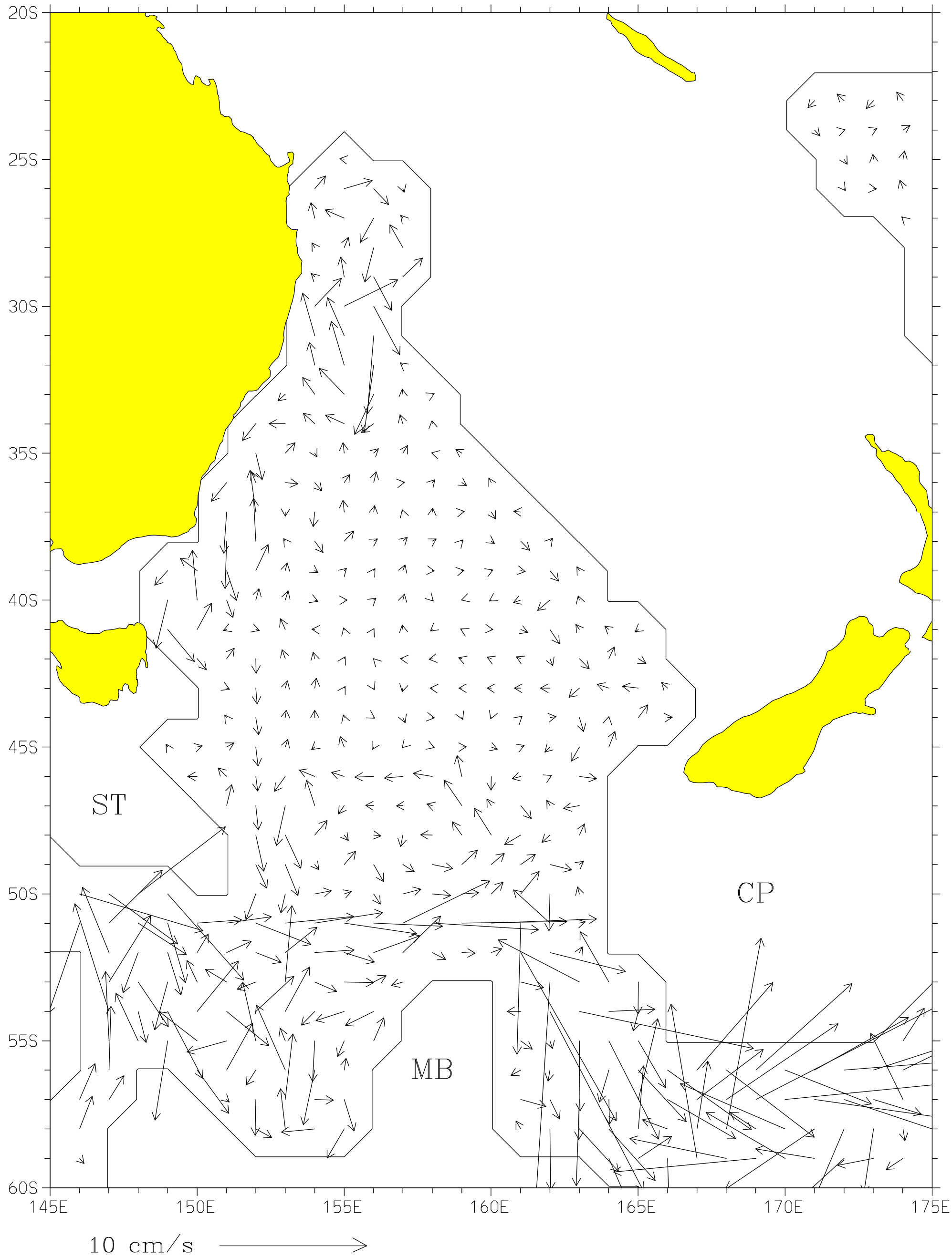

Figure 4.25: **:** Velocities at 3288 m (level 15) for the Smagorinsky mixing run. EACRR peak speeds are $6\,cm\,s^{-1}$. The ACC flows between the Macquarie–Balleny Ridge (MB), the South Tasmania Ridge (ST) and the Campbell Plateau (CP). Its peak speeds are $17\,cm\,s^{-1}$.

4.7 Analysis of the EACRR

The large differences between the results of the three mixing schemes clearly demonstrate the importance of correctly parameterizing friction, notably within western boundary current regions. The elongated gyres found in Fig. 4.16 show a layering of oppositely circulating gyres against the coast, and is somewhat indicative of a standing wave system. Planetary waves associated with western boundary currents are, of course, dispersive with eastward group velocities. Some further insight can be gained into the existence of the oppositely directed layered jets by examining the vorticity balance close to the oceanic western boundary. To render the analysis tractable, it is assumed that advective nonlinearities, zonal velocities and the wind stress are of no consequence in this region. Diffusion of planetary vorticity by lateral viscosity, using a polyharmonic operator and the β–plane approximation, is simplified to:

$$\frac{\partial^2 v}{\partial t \partial x} + (-1)^{n+1} A_m \frac{\partial^{2n}}{\partial x^{2n}} (\frac{\partial v}{\partial x}) = \frac{\partial}{\partial t}(\beta(y - y_0) + f_0) \tag{4.1}$$

where x, y are the eastward and northward coordinates, v is the northward material velocity, t is time, A_m (> 0) is the eddy viscosity coefficient and $n = (1, 2, 3, ...)$. β is f_y at the nominal latitude y_0, with f_0 being the nominal Coriolis factor. For the time invariant case ($\partial_t v = 0$), eqn. (4.1) reduces to the boundary value problem:

$$(-1)^{n+1} A_m \frac{d^{2n+1} v}{dx^{2n+1}} - \beta v = 0 \tag{4.2}$$

Clearly, for a nontrivial solution some sort of friction is essential. The characteristic equation for (4.2) is

$$r^{2n+1} - \alpha = 0 \qquad \text{where} \qquad \alpha = [(-1)^{n+1} \beta / A_m]^{\frac{1}{2n+1}} \tag{4.3}$$

and the roots are

$$r_k = \alpha \exp\{\frac{i\, 2\pi k}{2n+1}\} \qquad \text{for} \qquad k = 0, \pm 1, ..., \pm n \tag{4.4}$$

The roots are symmetrically distributed around the α-circle, and occur as conjugate pairs and one real value. Suitable boundary conditions for the problem are:

$$v(0) = 0 \qquad \text{(i.e., no–slip)} \tag{4.5}$$

$$v(x) \sim 0 \qquad \text{as} \qquad x \to \infty \tag{4.6}$$

$$\int_0^\infty v\, dx = -F \tag{4.7}$$

where F is the northwards open ocean Sverdrup flux at the nominal latitude. Cases for slip at the coast are treated in a similar fashion. Killworth (1993) shows that a wide range of diffusion operators are capable of providing boundary current solutions which can match any open ocean requirements, at least in mathematical models. The analysis here merely investigates the behaviour of v at a particular latitude, and it must be remembered that F will vary with latitude. Hence, $v(x)$ is actually $v(x, y)$ or $v(x, F)$. A little work shows that n conjugate pairs can always be discarded, and the solution of (4.2) is given by

$$\begin{aligned} v(x) \; = \; & G \exp\{\alpha\, x\} + \sum_m \exp\{x\alpha \cos(\frac{2\pi m}{2n+1})\}(H_m \cos(x\alpha \sin\{\frac{2\pi m}{2n+1}\}) + \; ... \\ & I_m \sin(x\alpha \sin\{\frac{2\pi m}{2n+1}\})) \end{aligned} \tag{4.8}$$

where G, and the H_m and I_m are purely real. For odd n, m takes integer values from $(n+1)/2$ to n, and from 1 to $n/2$ when n is even. For odd n and the no–slip condition, G must be zero since $\alpha > 0$, and the H_m must sum to zero. For even n, G will generally not be zero. The mode number m takes only one value for both LM and BM; thus H_1 and G are always zero for LM. If F is zero then LM must yield $v(x) = 0$, but v need not be zero for higher orders. Therefore, there is a fundamental difference in behaviour between ∇^2 and higher order polyharmonic operators.

Eqn. (4.8) gives the solution in terms of a linear combination of discrete standing short planetary waves, each with different wavelengths and decay rates. Generally, shorter wavelengths correspond to lower decay rates in the eastwards direction. The mode which offers the greatest number of flow reversals inside its own e-folding distance corresponds to the root which is closest to, but still to the left of the imaginary axis. This has mode number $m = (n+1)/2$ for odd n, and $m = n/2$ when n is even. For ∇^4, this is the $m = 2$ mode and there are 6.2 flow reversals within its e-folding distance. For this to occur, only I_2 and possibly G are permitted to be non–zero.

Only one degree of freedom is left, namely boundary condition (4.7), so that $v(x)$ is uniquely determined only if m takes no more than one value. This is true for ∇^2 and ∇^4, but higher orders require more conditions. This does not pose a problem when polyharmonic diffusion is used in general circulation models, but it is reasonable to expect that the solution in the neighbourhoods of western boundaries will become progressively more sensitive as n is increased. In fact, non–determinism is a useful attribute for the problem since it implies that western boundary currents are controlled by the open ocean flow regime, and not the reverse (Killworth, 1993). Of course, the analysis above has ignored advective nonlinearities which may radically alter boundary current behaviour by inducing substantial zonal velocities close to the coast.

From the sine term in (4.8), the x-distance between oppositely directed jets (i.e., one half of an x-direction wavelength) is

$$W_j \;=\; \frac{\pi}{\alpha}\csc\left(2\pi\frac{m-1}{2n+1}\right) \tag{4.9}$$

The exponential term gives the e-folding length scale for v, moving eastwards away from the coast:

$$W_e \;=\; \frac{1}{\alpha}\sec\left(2\pi\frac{m-1}{2n+1}\right) \tag{4.10}$$

Thus, W_j and W_e are closely related via α and the mode number m. The BM operator is capable of producing six flow reversals within the largest e–folding distance, but the total width of the corresponding recirculation region is still comparable with the classical Munk scaling length (i.e., that for ∇^2) of about $60\,km$. A $500\,km$ wide recirculation region would require much higher order polyharmonic operators, but even then, there is certainly no guarantee that it would develop. In any event, polyharmonic operators, or a linear combination of them, cannot parameterize possible large–scale nonlinear behaviour.

SM is a more realistic parameterization of Reynolds stresses, and so has more physical legitimacy than polyharmonic operators. The effective Laplacian viscosity coefficient is, for the one dimensional SM case:

$$A_m \;=\; s\,|\frac{dv}{dx}| \tag{4.11}$$

where s is an empirical constant. This is formulated as a stress tensor for higher dimensions. In numerical schemes, s is replaced by $\frac{1}{2}(c\,\Delta x)^2$, where c is a dimensionless constant. Eqn. (4.2) becomes

$$\frac{d^2}{dx^2}\left[s\,|\frac{dv}{dx}|\,\frac{dv}{dx}\right] - \beta v \;=\; 0 \tag{4.12}$$

A natural scaling distance L_s is readily shown to be $\{c\,V_0(\Delta x)^2/2\beta\}^{1/4}$, where V_0 is a nominal velocity. Whether this scaling distance is indicative of W_j or W_e

is uncertain. V_0 needs to be specified and cannot be derived from other natural scales. For $c = 0.3$, $\Delta x = 100\,km$ and $V_0 = 1\,m\,s^{-1}$, L_s is $93\,km$ at 30°S.

Analytic solutions to (4.12) are not forthcoming so numerical examination is the only possible course. The commonly available shooting methods fail to produce a bounded solution for (4.12); the DE is too stiff. Two–point boundary methods produce sets of nonlinear coupled equations, for which the Newton–Raphson method diverges. The Laplacian problem (Eqn. (4.2) with $n = 1$ and non–dimensionalized) is soluble with a simple shooting method, but it is still quite stiff. With sufficient machine precision (64 bits), it can be solved with Runge–Kutta integration, with the shots being controlled by a Newton–Raphson scheme. $v'(0)$ is used as the adjustable parameter in the Newton–Raphson root finder, and needs to be determined to about nine significant digits for an acceptable solution. The domain of integration should not be more than about thirty times the Munk length scale. The time variable SM problem can be recast in stream function–vorticity (ψ–ζ) form:

$$\frac{\partial \zeta}{\partial t} = \frac{\partial^2}{\partial x^2}(s\,|\zeta|\zeta) - \beta\frac{\partial \psi}{\partial x} \qquad (4.13)$$

However, all of the usual methods for solving initial value transport–diffusion problems fail to remain stable. Thus, it is not known if (4.12) has solutions which "wiggle" away from the boundary.

4.8 Discussion

One of the most intriguing observations of the EAC's volume flux is the $10\,Sv$ northwards estimate given by Thompson & Veronis (1980). The mid–point of their first two hydrographic stations was $103\,km$ from the $200\,m$ isobath, so that the EAC was probably missed. Fig. 4.11 shows part of a strong northwards current at the first station pair, and this could well be part of the eastern region of an elongated recirculation gyre: perhaps the one closest to the Australian shelf. Thus, they find an 'EAC' apparently flowing northwards. Interestingly, they state in their conclusions:

> *A synoptic data set (taken in late March 1960) indicates a well–established cyclonic gyre in the Coral Sea and a weak, disordered cir-*

culation in the Tasman Sea, with essentially no East Australian Current. The nearly synoptic set yields an EAC, but we have suggested that this feature is a result of having replaced the stations that include the outflow of the cyclonic gyre in the Coral Sea with new stations that do not contain the outflow.

The Coral Sea cyclonic gyre that they refer to is the NGCU.

If the predicted EACRR actually exists, then different sets of hydrographic stations, with slightly different station positions or times, could well yield very different flux estimates for the EAC and the Tasman Sea. Intense and narrow currents with abrupt reversals of direction, measured at different times and positions, would cause the 'EAC' nett flux to *appear* to be highly variable. The wind–driven flow arriving at the Australian coast need not be highly variable. For example, the EAC volume flux could easily appear to vary, in time, from $50\,Sv$ southwards to a lesser amount northwards. The very large variations of EAC fluxes reported by Boland & Hamon (1970) are unexpected at midlatitudes since the response time of long Rossby waves to variations of the wind stress is of order decades. In any event, the Kermadec Ridge poses a substantial barrier to such wave motions, making their influence on EAC variability less likely.

The observed absence of a much warmer pool of water lying equatorwards from the Tasman Front may be due to homogenization of temperatures by the EACRR. The elongated gyres could rapidly transport higher latitude waters back to lower latitudes, and vice–versa, yielding relatively constant temperatures and salinities over the entire EACRR. Intense jets of cold water at about $4700\,m$ are reported by Mulhearn *et al.* (1986) near 34°S at the Australian shelf. The model results (Fig. 4.25) give some indication that these cold jets are modified Antarctic Bottom Water being entrained into the EACRR. The $100\,Sv$ estimate for a warm–cored eddy, given by Lilley *et al.* (1986), is larger than the model's peak EACRR flux of $47\,Sv$. If $100\,Sv$ is reasonably accurate, then the model's wavenumber coefficient is too large: reducing it will require a finer resolution grid.

Lord Howe Island lies near the junction of the EACRR and the Tasman Front (Fig. 4.19). The observed large sea level variations could well be due to slow meanders of the Tasman Front and to variability of the intense EACRR gyres.

The island is a little too far to the east of the Australian coast ($590\,km$) for any possible coastal trapped waves to effect such large variations of its nearby sea level.

Linear theory predicts a much slower eastward propagation of short internal Rossby waves at midlatitudes, and their dissipation is rapid in the presence of friction. The minimum time required for such a wave packet to cross a basin of width L is (e.g., Anderson & Gill, 1975, Eqn. 7.4):

$$T_{min} \;=\; 8L\{\left(\frac{2\pi}{\lambda}\right)^2 + a^2\}/\beta \tag{4.14}$$

where $1/a$ is the deformation radius and λ is the meridional wavelength. Taking values of $1/a = 50\,km$ and λ unbounded, T_{min} for the North Pacific basin ($L = 10000\,km$) is $\sim$100 years. The group velocity is $0.3\,cm\,s^{-1}$ to the east. (The barotropic mode can cross in $\sim$90 days, although this mode is of little consequence in the real ocean.) These wave motions are dispersive, evanescent in the presence of friction and in reality are likely to exist only near meridional western boundaries. The eastward propagation rate of the recirculation region in model NPA is $6\,cm\,s^{-1}$, which is very similar in magnitude to the westward group velocity of long internal waves. Thus, the existence of the 'super eddies' is reliant, in some way, on nonlinearities and perhaps on large intermodal cascades of energy. Theoretical analysis of the dynamics of such motions is difficult and far from complete.

It has not yet determined why SM produces intense recirculation gyres at nearly perfectly meridional western boundaries, nor the reason why these gyres are capable of propagating eastwards with a coherent large–scale pattern. Simple baroclinic instability has horizontal scales comparable with the local internal deformation radius, and is unlikely to be influenced by the orientation of a boundary many thousands of kilometres distant. Lighthill (1969, p. 81) finds nothing unusual about the orientation of western boundaries with respect to the eastwards propagation of short Rossby waves. His analysis involves only linear dynamics, and so there is a little more evidence that the predicted gyres are the result of nonlinearities. Since the gyres propagate well below the pycnocline, where little kinetic energy is initially available, one can postulate that the gyres gain their kinetic energy from other modes, i.e., from the potential energy of the water column above. In a sense, they could be regarded as Huygens 'wavelets'. Each small eastwards displacement of an individual wave front creates a new wave front that is aligned with the old one, while the necessary kinetic energy is obtained from some other source.

Reznik *et al.* (1993) analyse nonlinear interactions of resonant triads, for spherical Rossby waves, and find that the probability of resonance increases for progressively larger horizontal wavenumbers. Substantial interwave energy cascades are possible for *approximate* resonance conditions between short waves. The model gyres have zonal wavelengths comparable with eastward propagating Rossby waves, although the model grid spacing is a little too coarse to truly resolve them. The model gyres are prone to dissipation by seasonal variations of the wind stress, but not nearly to the same degree as the short Rossby waves of linear dynamics. A possibility is that the model gyres are highly dissipative, but extract energy from the water column at a sufficient rate to overcome the loss of kinetic energy. While short Rossby waves are strongly evanescent, the model gyres can, under certain conditions, maintain relatively coherent patterns for many thousands of kilometres away from a western boundary.

Haney & Wright's (viscosity) diffusion operator was effectively that in (4.11), but included background Laplacian diffusion. If the background coefficient was set too small, intense recirculation gyres developed throughout the model domain, and they reasonably assert this to be a false computational mode. This behaviour cannot be termed a computational instability since the models remain stable. The barotropic versions of the North Pacific primitive equation model do not show such computational modes, and there is little qualitative difference between the LM, BM and SM results. Gyres develop only when there is stratification, and only along meridional western boundaries. The model gyres are prone to dissipation with friction and variable surface forcing, a characteristic of short planetary waves, as well. While it is easy to contemptuously dismiss the SM model results as numerical artifacts, it should be kept in mind that the LM and BM results are simply quite wrong in the light of the observations presented here. It is not asserted here that computational modes are not involved, but there does appear to be at least some realistic behaviour in the primitive equation models. The author is keen to see other investigators reproduce the results of the present models, using different codes and formulations. The integration time for the world model SM run is fairly brief, but if run for longer periods the EACRR should spread eastwards to the Lord Howe Rise. The EACRR gyres in Fig. 4.14 have not spread far enough eastwards to be fully consistent with the Ga0260 results (Fig. 4.11), and with the very large sea level variability observed at Lord Howe Island. However, lengthy accelerated SM runs with constant forcing are of questionable value, since seasonal forcing affects the eastwards propagation of the western boundary gyres. Sufficient machine time for a synchronous seasonally forced run of the world model, using SM, is not yet available.

Chapter 5

Global and Indonesian Throughflow Model Results

The main finding covered in this chapter is the Indonesian throughflow (IT) sensitivity to the Antarctic Circumpolar Current (ACC). The low latitude flows for the Pacific are examined, to show their relationship to the Coral Sea area and the seasonal reversals north of Papua New Guinea (PNG). Also, the usual global analyses are briefly presented for completeness: overturning stream functions and poleward tracer transports.

5.1 Global Stream Function, Pressure and TS

The scalar fields presented in this section are from the average of years seven and eight of the seasonally forced phase, unless otherwise stated. Figures are split into eastern and western hemispheres, to allow for clarity. The stream function and pressure fields are lightly smoothed to remove noise, which is confined to certain areas such as Madagascar, the east coast of Africa and the Philippines.

Fig. 5.1 shows the global stream function contoured at intervals of $10\,Sv$. The extreme values of the field are $191\,Sv$ (Southern Ocean, 200°E) and $-105\,Sv$ (Agulhas). The IT is $14.4\,Sv$. The ACC is steered by topography but not to the same extent as it is in models with finer grid resolutions, such as FRAM (Webb *et al.*, 1991). The ACC average volume flux for years seven and eight is $173\,Sv$, and is still slowly increasing (Fig. 5.2). It flows in close proximity to the Agulhas at the southern tip of Africa, and strongly intensifies around Campbell Plateau (170°E) and the Falklands Plateau (310°E). The Kuroshio peak flux is $100\,Sv$ but its

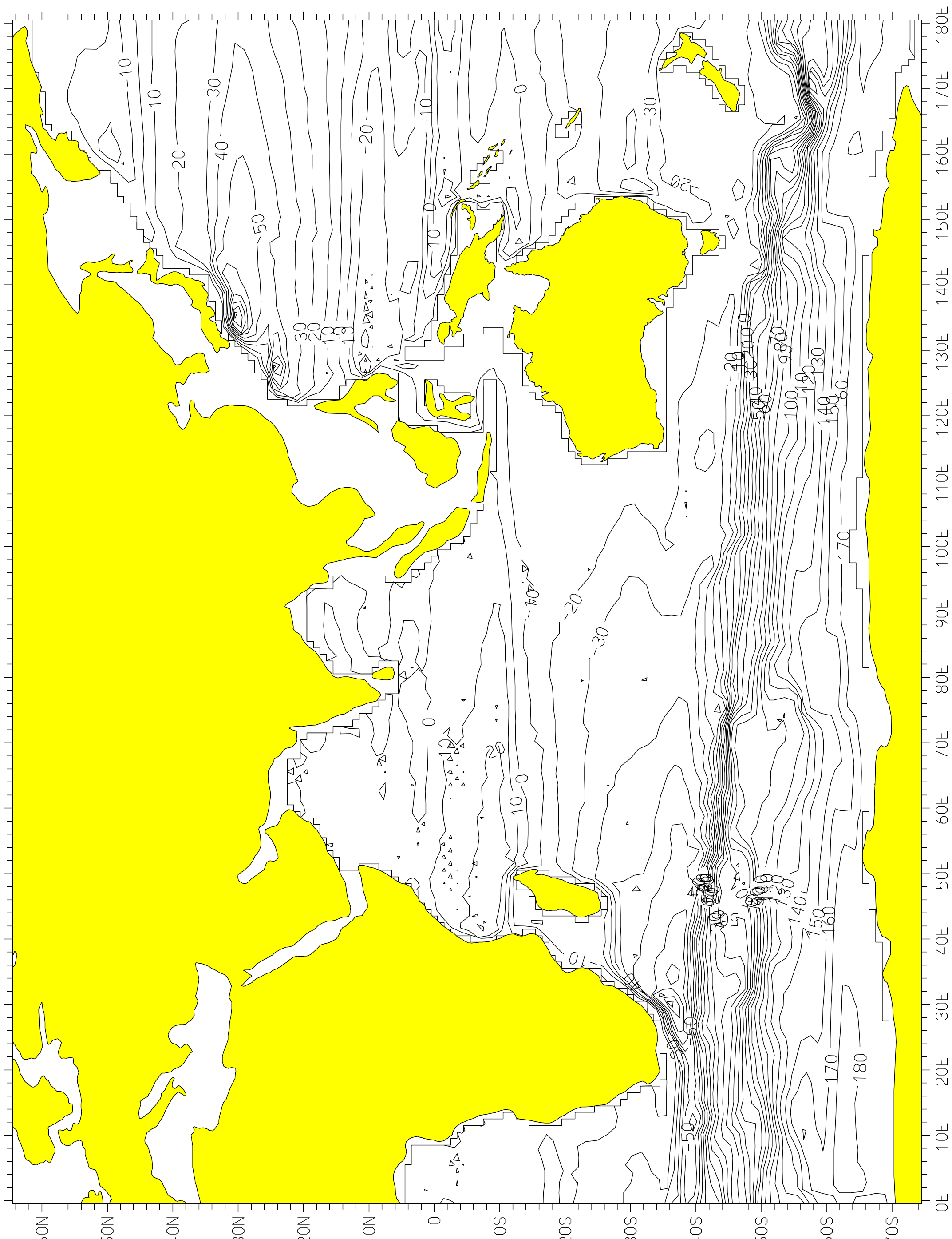

Figure 5.1: **a:** [rotated] Global stream function (Sv) averaged over years seven and eight, eastern hemisphere. CI is $10\,Sv$. The ACC is $173.0\,Sv$, and is seen to been steered by topography to some extent. It flows in close proximity to the Agulhas (25°E) and intensifies around Campbell Plateau (170°E). The IT is $14.4\,Sv$.

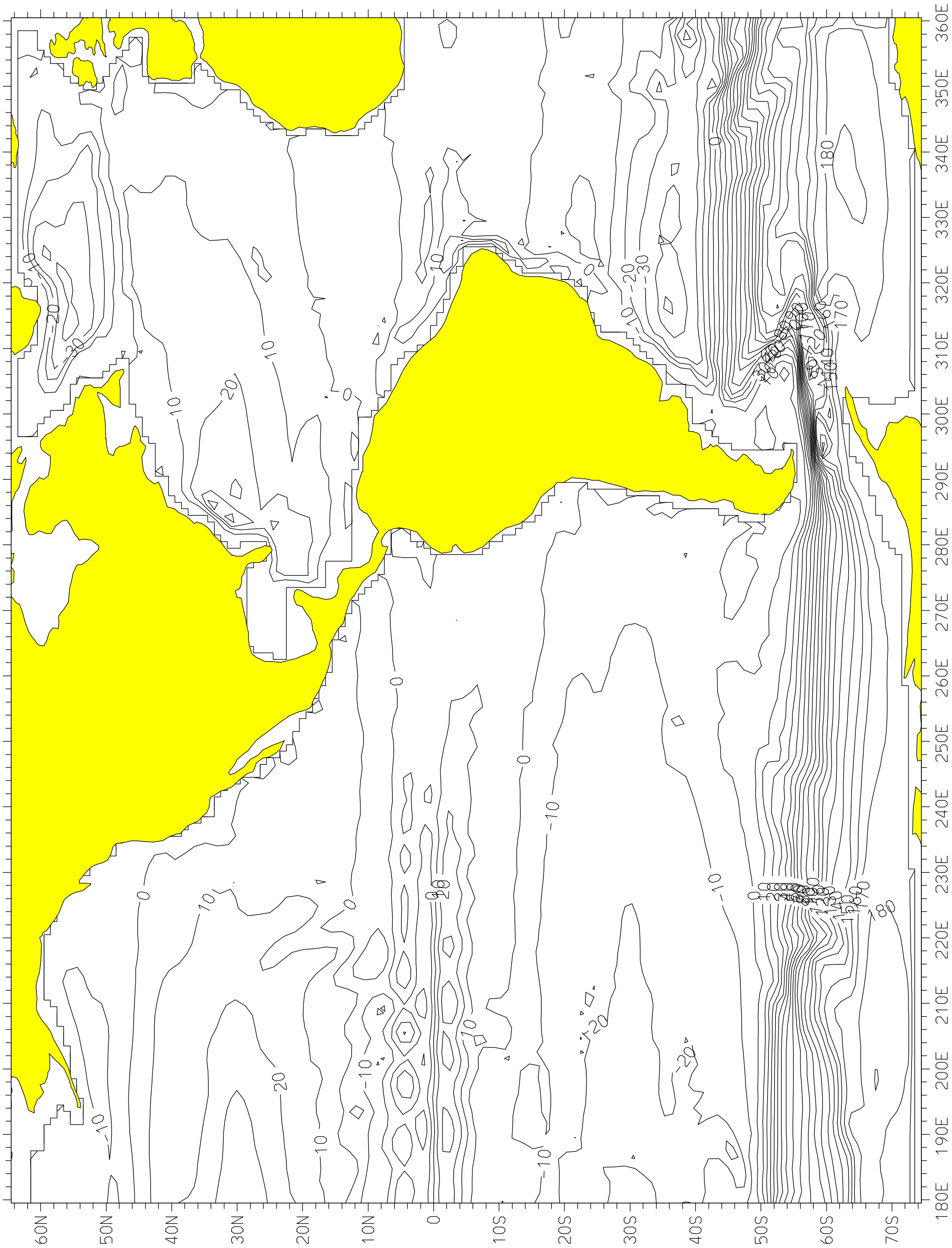

Figure 5.1b: [rotated] Global stream function (Sv) averaged over years seven and eight, western hemisphere. CI is $10\,Sv$.

Sverdrup component is not more than $60\,Sv$. The Gulf Stream is unrealistically weak at $30\,Sv$, which is a common result for (global) primitive equation models. The central Pacific is comparatively structureless but instantaneous snapshots show intense localized seasonal flows, of up to $25\,Sv$.

Fig. 5.2 shows the time variation the ACC and IT fluxes, over years four to eight. Values have been recorded each time step (one hour) and then filtered, since the Euler backward time step (13:1) tends to spike the internal and external fields with near inertial frequencies. Convective adjustments in the Southern Ocean also contribute to high frequency variability (cf. Fig. 5.16). The ACC is still slowly rising, as it does in all phases of the intergration, while the IT has no obvious decreasing trend. Their peak fluxes are in phase, occurring during the austral winter. The ACC flux reaches a minimum for short periods, while the IT peaks exist only for relatively short periods.

Fig. 5.3 shows the surface pressure variation about the global mean, which is arbitrarily set to $0\,db$. The range is from $-181\,mb$ (Weddell Sea, 335°E) to $193\,mb$ (Kuroshio). The mean surface elevations of the Pacific and Indian Oceans are about $30\,cm$ (i.e., mb) higher than the mean elevation for the Atlantic. The North Equatorial Current (NEC) is clearly delineated, but the NGCU is barely evident. Isobars in the central and eastern South Pacific tend to cross the equator rather than forming the closed loops of North Pacific central gyre. Midlatitude gyres are not particularly evident in the Indian or South Atlantic and this is due, no doubt, to the IT and Agulhas retroflection. These flows are shallow and will have a substantial effect on the surface pressure. The warm water carried into the Indian Ocean by the IT establishes a surface height gradient along the west Australian coast that extends westwards to Africa. This obscures the expected gyre pattern at the surface, but not in deeper waters.

Fig. 5.4 shows the pressure variation at $210.50\,m$, about the global mean of $216.01\,db$. The range is from $-141\,mb$ to $147\,mb$. There are no extreme differences from patterns in the surface pressure field. The NGCU is more apparent, whereas the NEC is not obvious. Isobars in the southern Indian and South Pacific now show stronger tendencies to form closed gyres, in comparison with the surface pressure. At 42°S, $8\,Sv$ of the South Pacific's inflow (IT is $14.4\,Sv$) is supplied between the surface and $115\,m$ (levels 1–4), and this the reason for the differences between the external and thermocline pressures of the South Pacific.

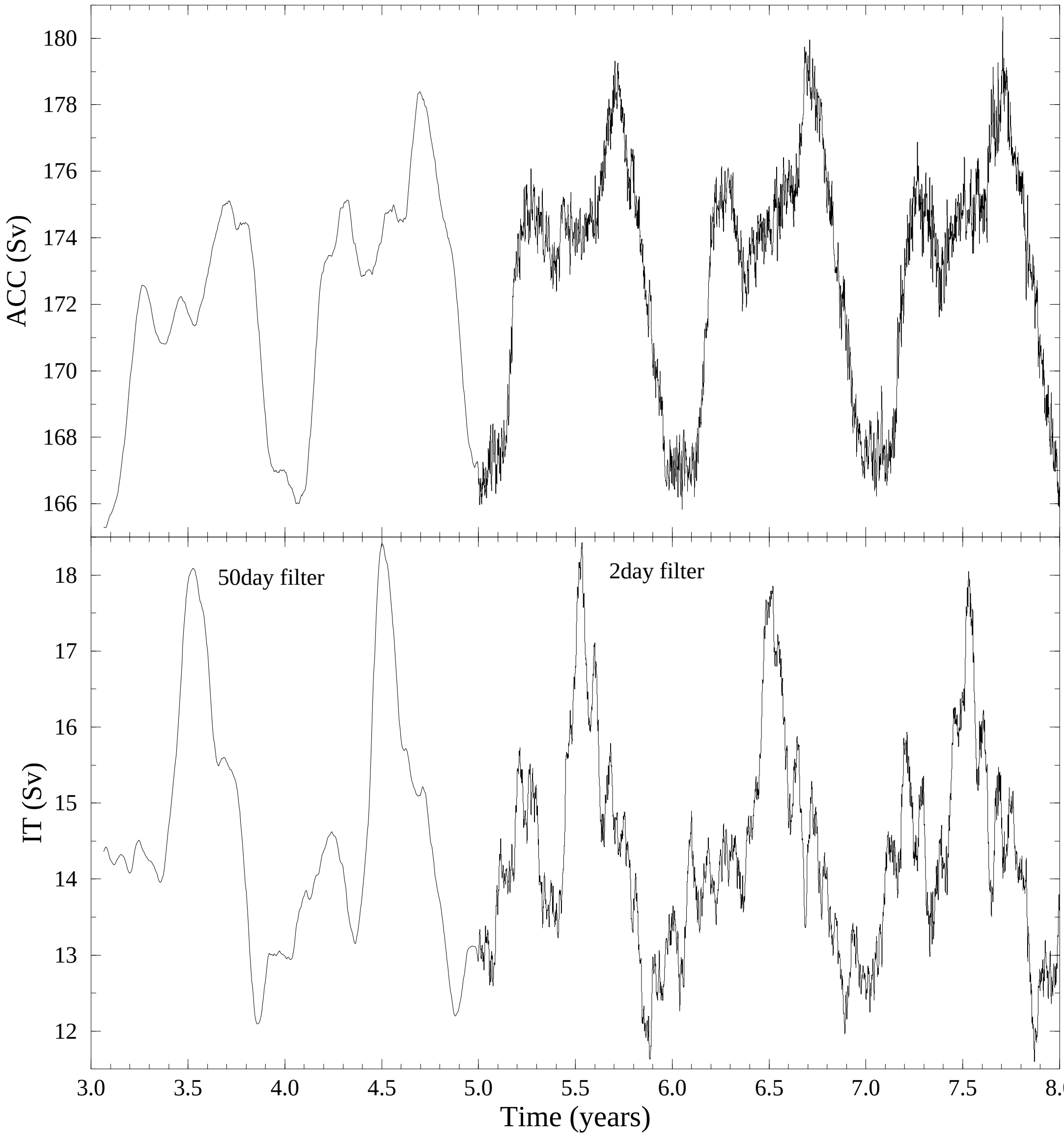

Figure 5.2: **:** Antarctic Circumpolar Current (ACC) and Indonesian throughflow (IT) for years four to eight of the seasonally forced phase. Values are recorded every model time step (one hour), but the above are filtered, as noted in the IT panel.

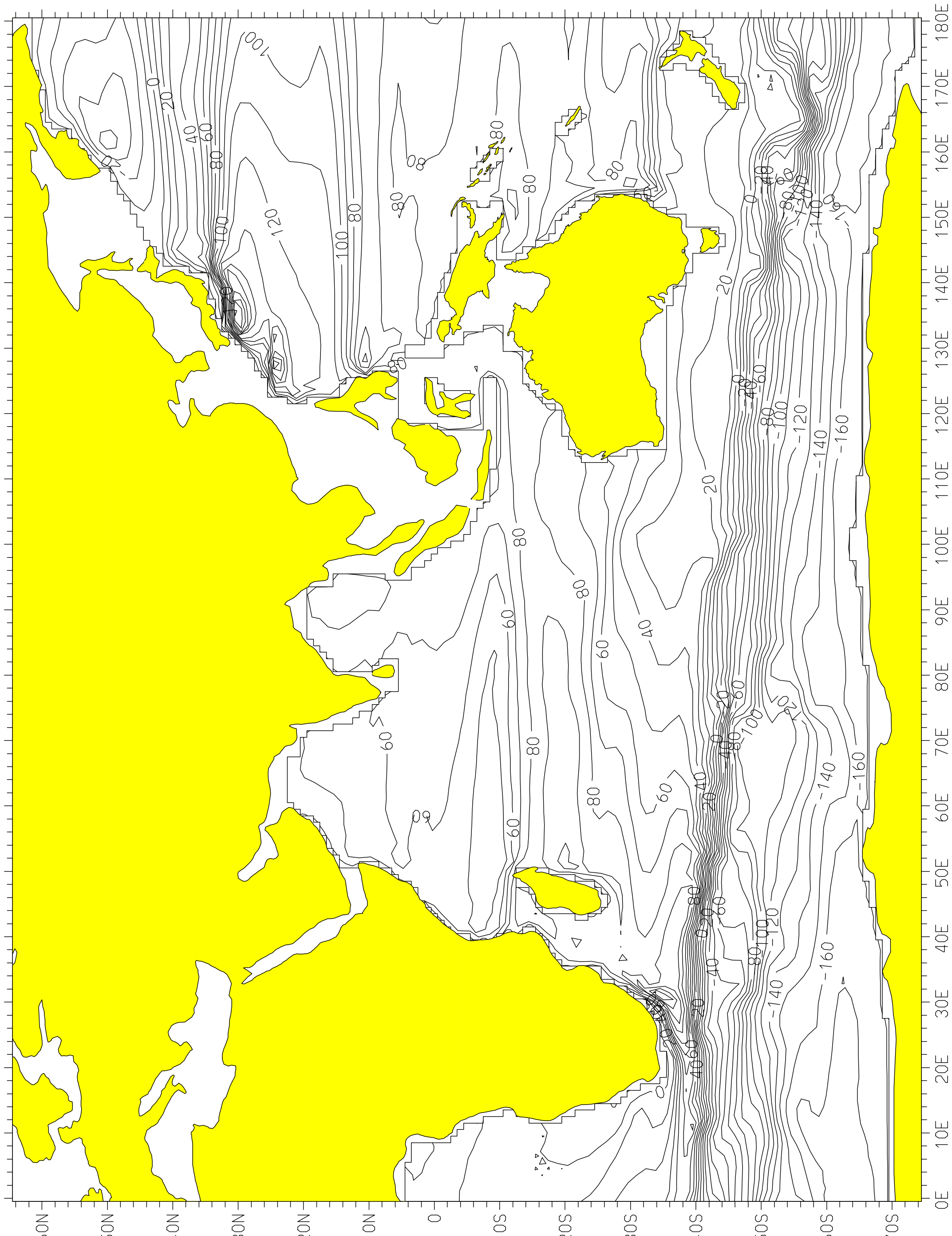

Figure 5.3: **a:** [rotated] Global average surface pressure (mb) variation, eastern hemisphere. CI is $10\,mb$.

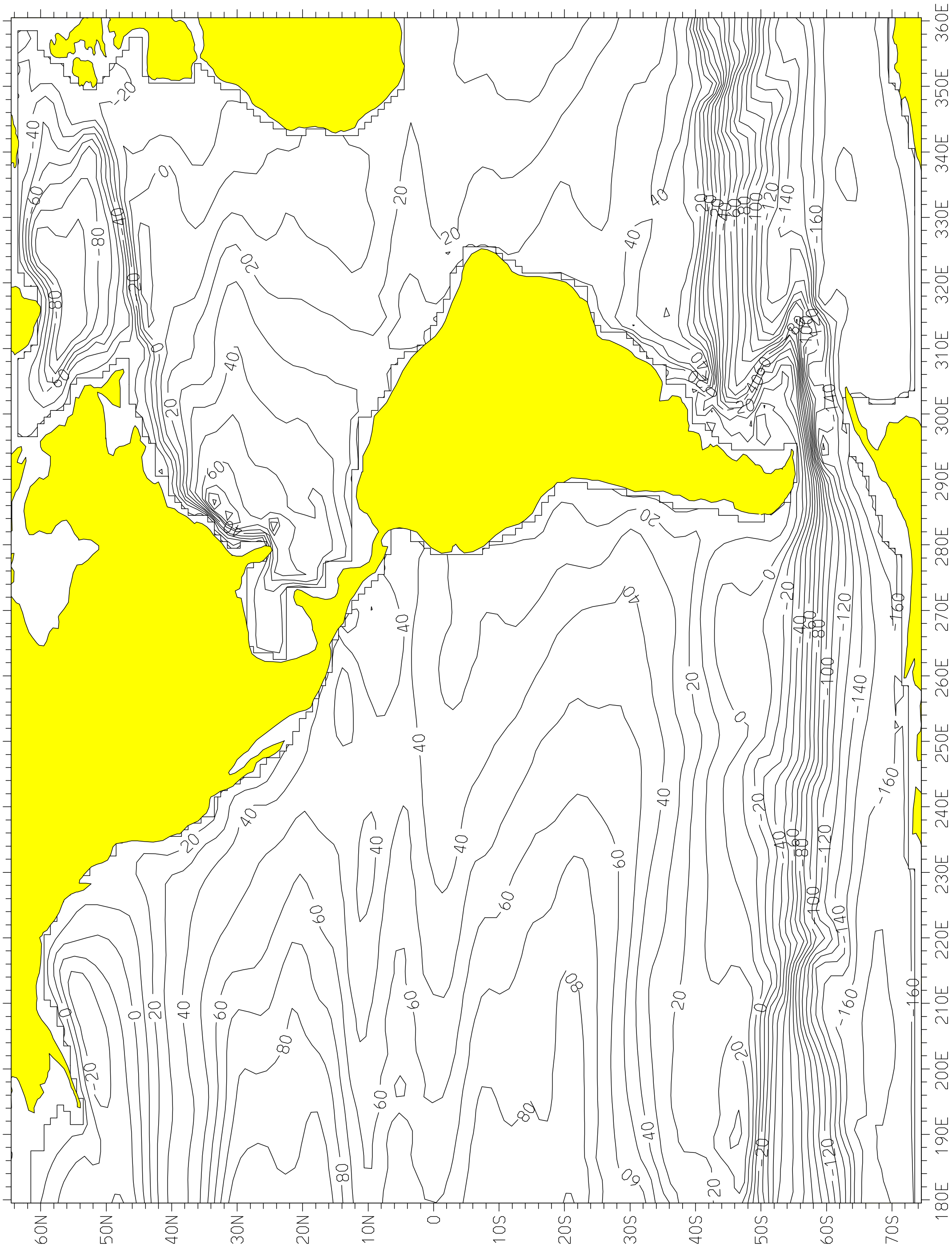

Figure 5.3b: [rotated] Global average surface pressure (mb) variation, western hemisphere. CI is $10\,mb$.

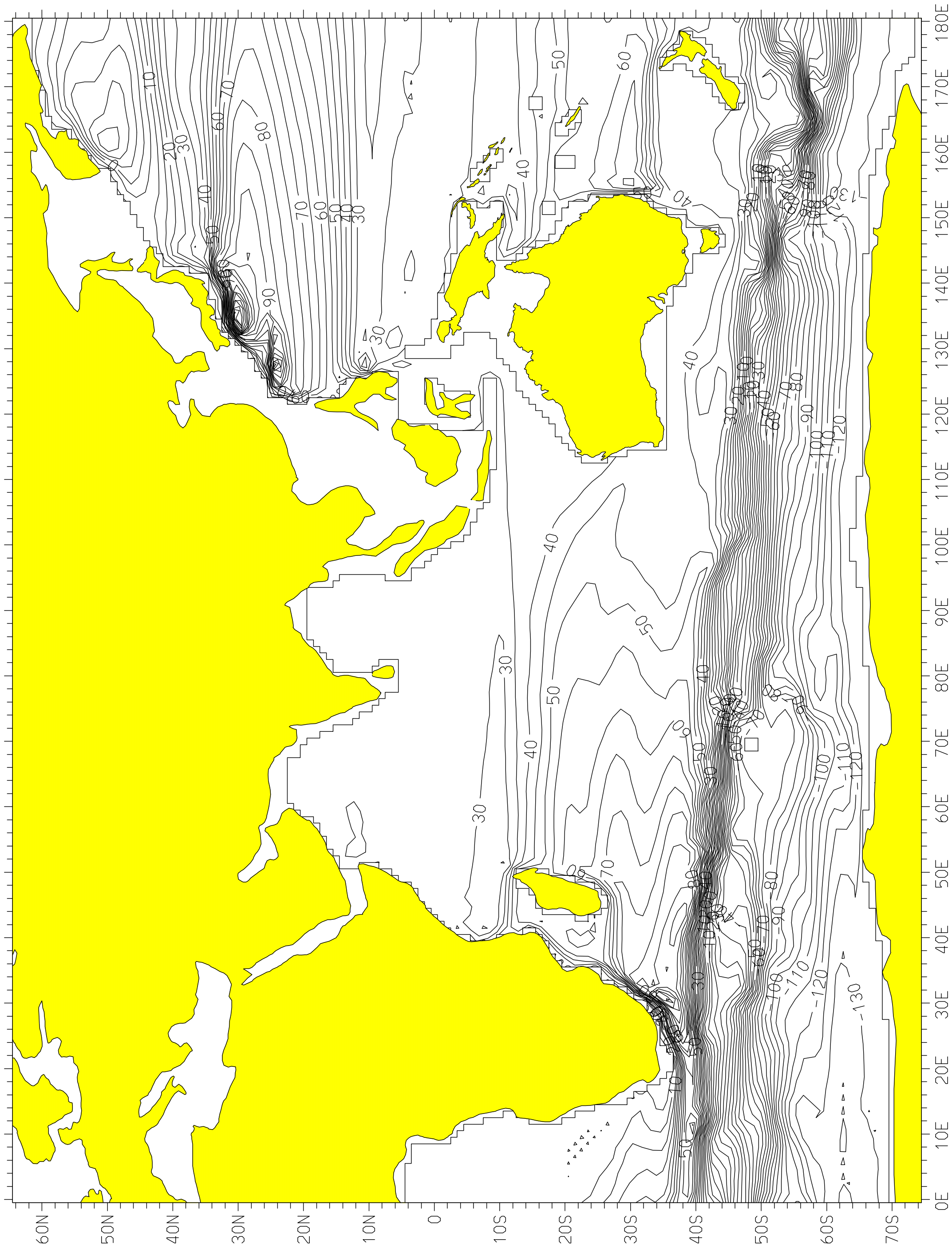

Figure 5.4: **a:** [rotated] Global average pressure variation (mb) at $210.50\,m$, eastern hemisphere. CI is $5\,mb$. Mean pressure is $216.01\,db$ at this geometric depth.

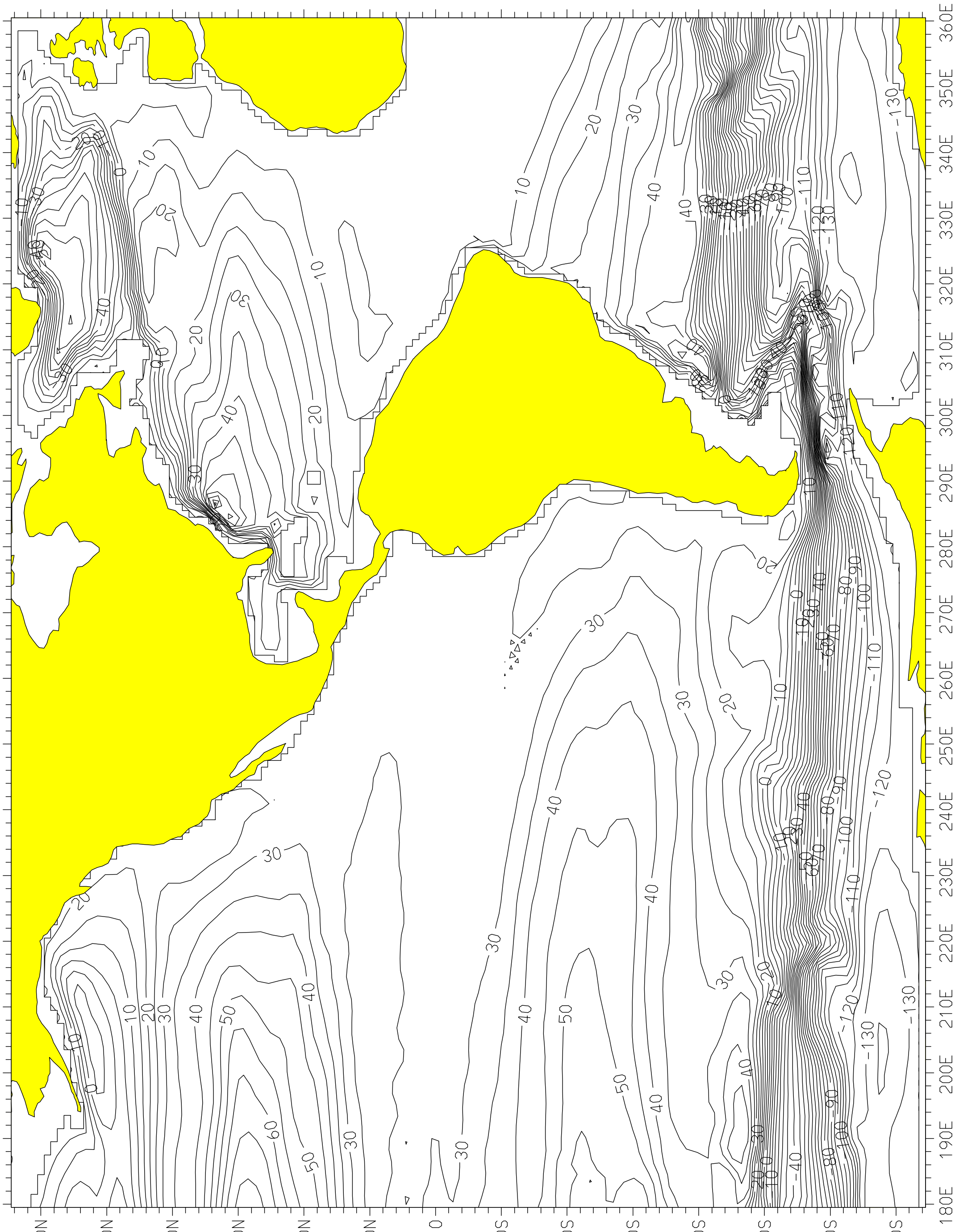

Figure 5.4b: [rotated] Global average pressure variation (mb) at $210.50\,m$, western hemisphere. CI is $5\,mb$.

Fig. 5.5 shows the global surface temperature distribution, and may be viewed in conjunction with Fig. 5.6, which shows the corresponding anomalies relative to the Levitus data. The most noticeable gradients occur at the southern tip of Africa, between the Kuroshio and Oyashio, and between the Gulf Stream and Labrador Current. Thermal fronts are only slightly sharper than for the Levitus set. During the spin–up phase, high latitude surface temperatures were generally too high by over 2°C but this discrepancy reduces to less than 1°C at the end of the seasonally forced phase. The model's Western Warm Pool is quite similar to the Levitus set, but its equatorial temperatures near 250°E are colder than the corresponding Levitus data, by more than 4°C. Here, the model has 'unsmoothed' the Levitus data to produce sharper gradients, although its temperatures are too cool by 1–2°C to be realistic (cf. Fig. 1.12 of Philander, 1990). Atlantic temperatures, over nearly all areas, show smaller differences from the Levitus set.

Fig. 5.6 shows the average (years seven and eight) surface temperature anomalies relative to the annually-averaged Levitus data. Differences from the annually-averaged Levitus data are generally about ±0.5°C, except in certain localized areas. The Agulhas retroflection, Kuroshio, Gulf Stream and Brazil–Malvinas–confluence areas have differences of up to ±4°C, but these are merely the effects of the model 'unsmoothing' the Levitus data. The Labrador Current region, around the southern tip of Greenland, is too warm by up to 3°C and is probably caused by the 65°N wall. The most notable discrepancies in the open ocean, occur in the equatorial bands of the Pacific and Atlantic. While zonal strips of cooler equatorial water have been eliminated in the smoothed Levitus data, the model yields waters which are too cold by 1–2°C, as mentioned above. The anomalies with the Levitus data will be proportional to the surface heat flux, but only in the limit of an equilibrium being attained. Positive anomalies imply a flux from the ocean to the atmosphere. Once a thermohaline equilibrium is attained (the model is far from this) the internal heat transports of Fig 5.29 will be in balance with the surface anomalies.

Fig. 5.7 shows the surface salinity (averaged over years seven and eight of the seasonally forced phase). Model salinities differ little from the Levitus set, and the largest discrepancies, being no larger than $0.3\,psu$, are confined to a few localized areas. These are the Gulf of Guinea, Bay of Bengal, Arabian Sea and the

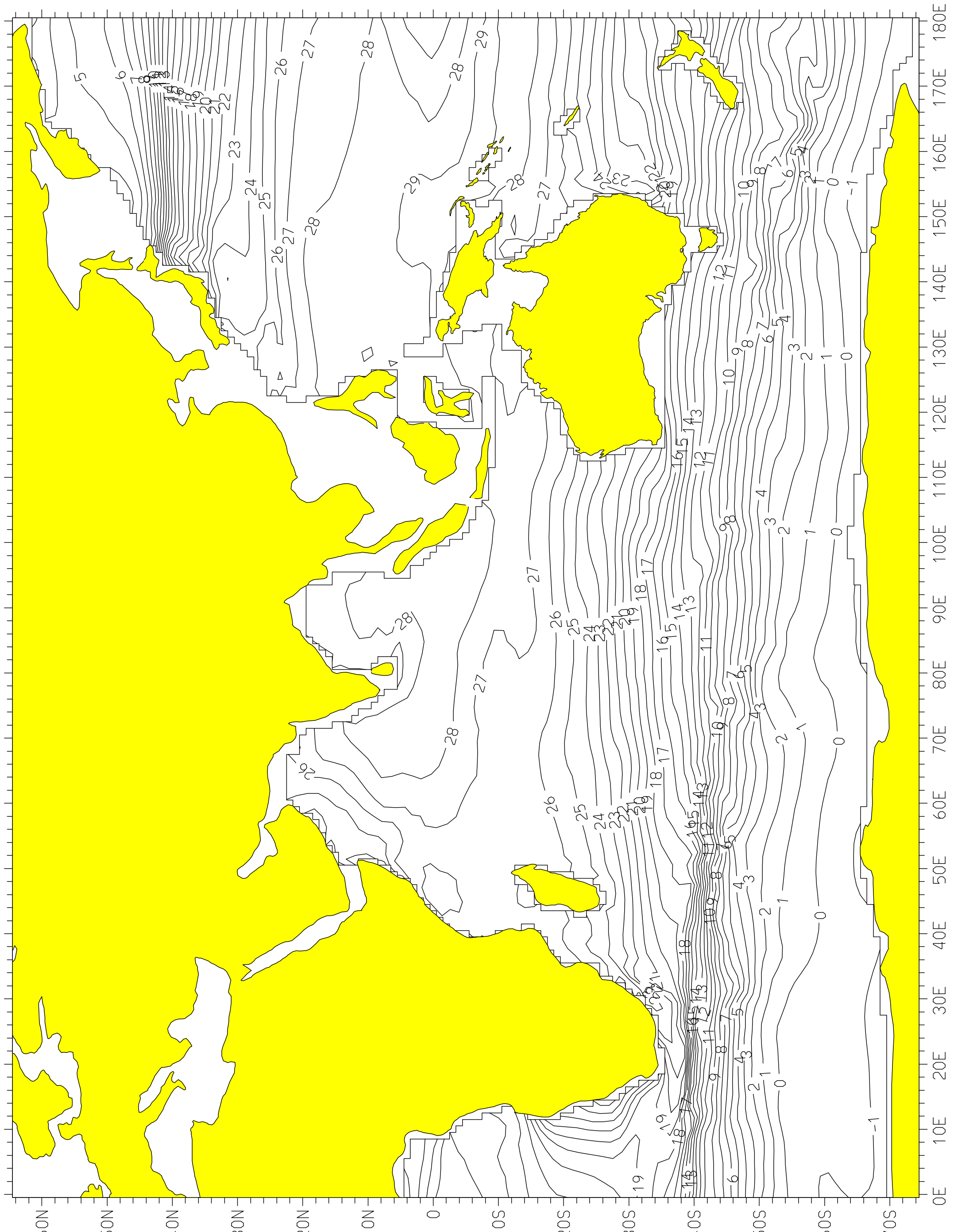

Figure 5.5: **a:** [rotated] Global average surface temperature (°C), eastern hemisphere. CI is 1°C.

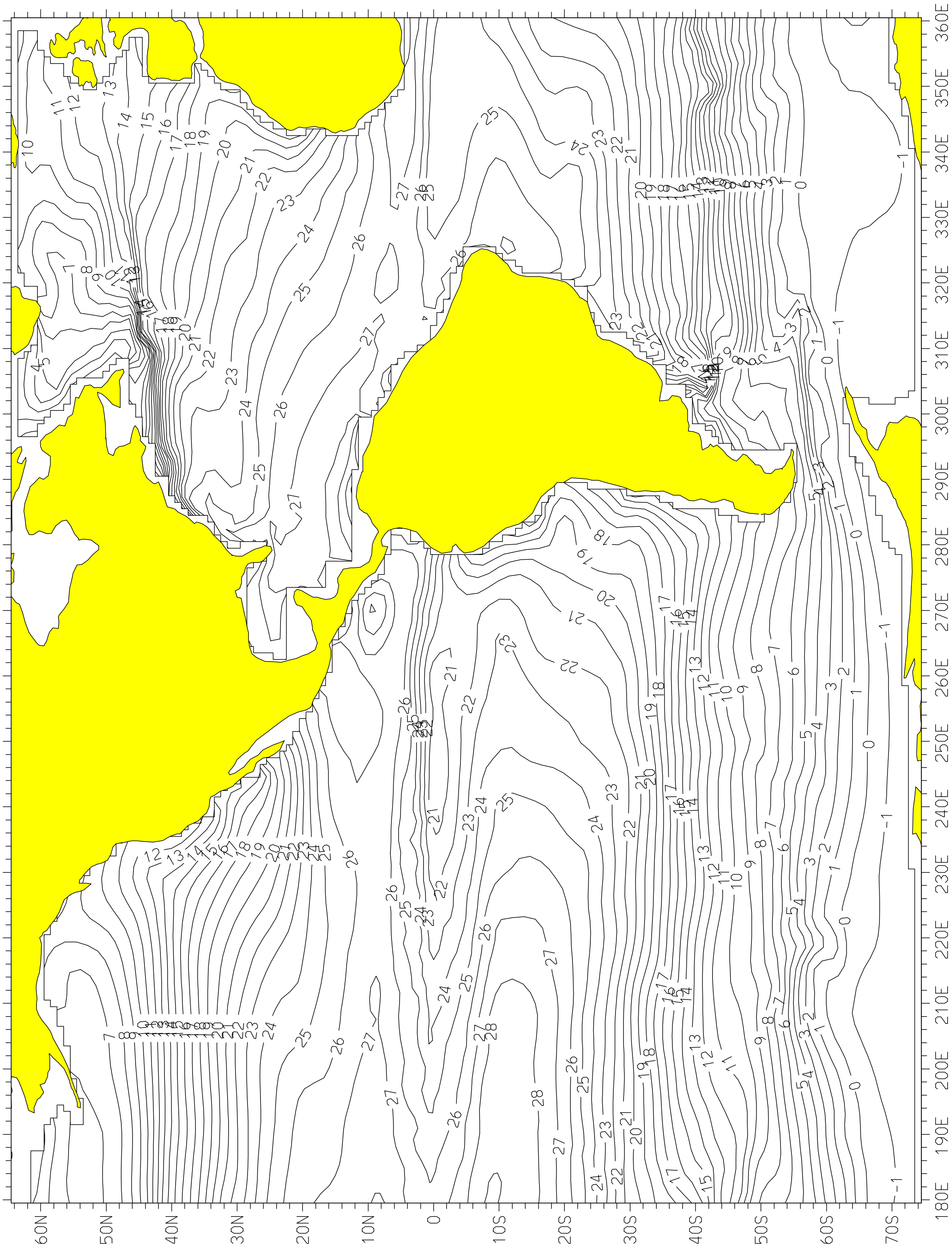

Figure 5.5b: [rotated] Global average surface temperature (°C), western hemisphere. CI is 1°C.

Figure 5.6: **a:** [rotated] Global average surface temperature anomalies (°C), relative to the annually–averaged Levitus data: eastern hemisphere. CI is 0.5°C.

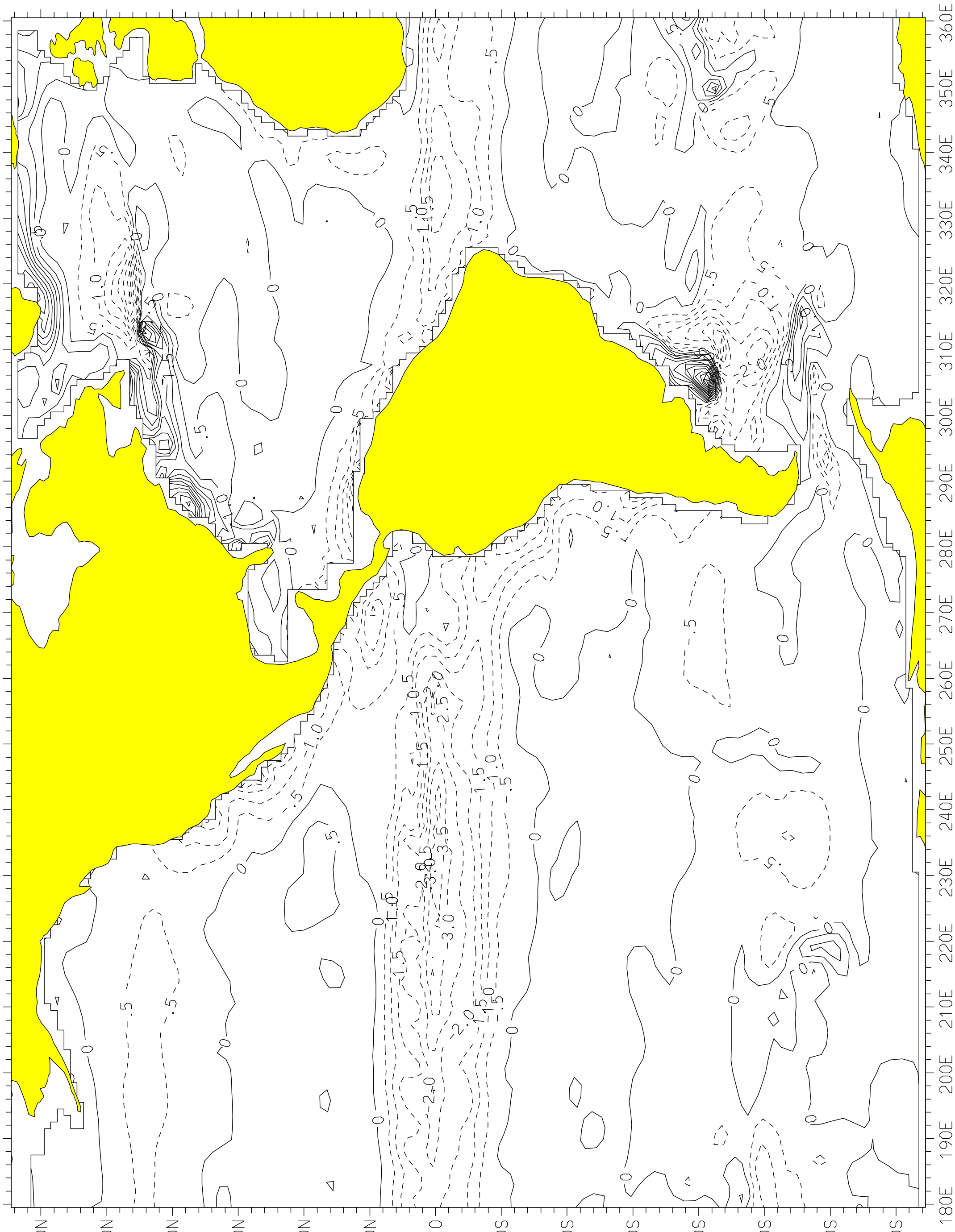

Figure 5.6b: [rotated] Global average surface temperature anomalies (°C), relative to the annually–averaged Levitus data: western hemisphere. CI is 0.5°C.

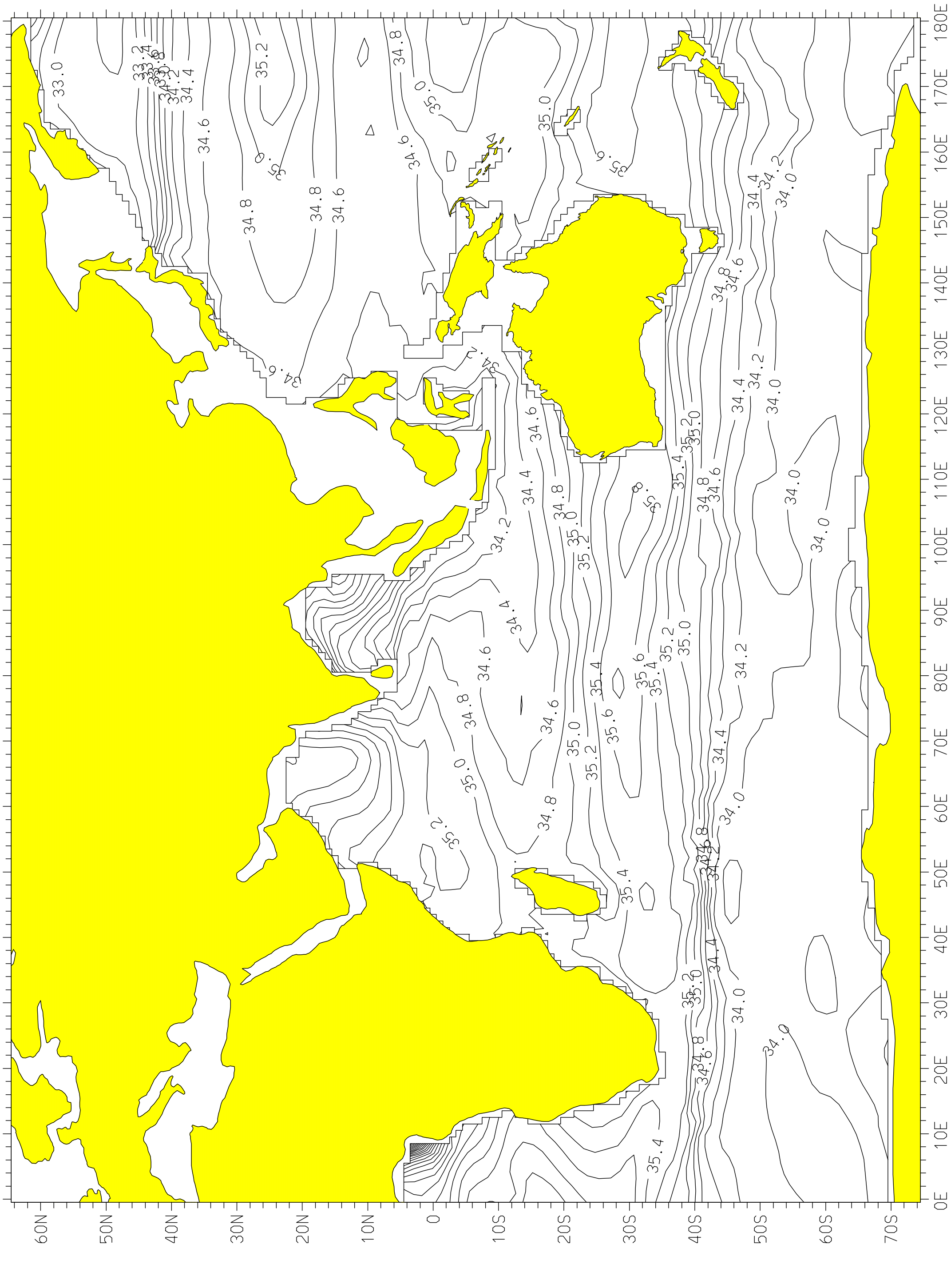

Figure 5.7: **a:** [rotated] Global average surface saltinity (psu), eastern hemisphere. CI is $0.2\,psu$.

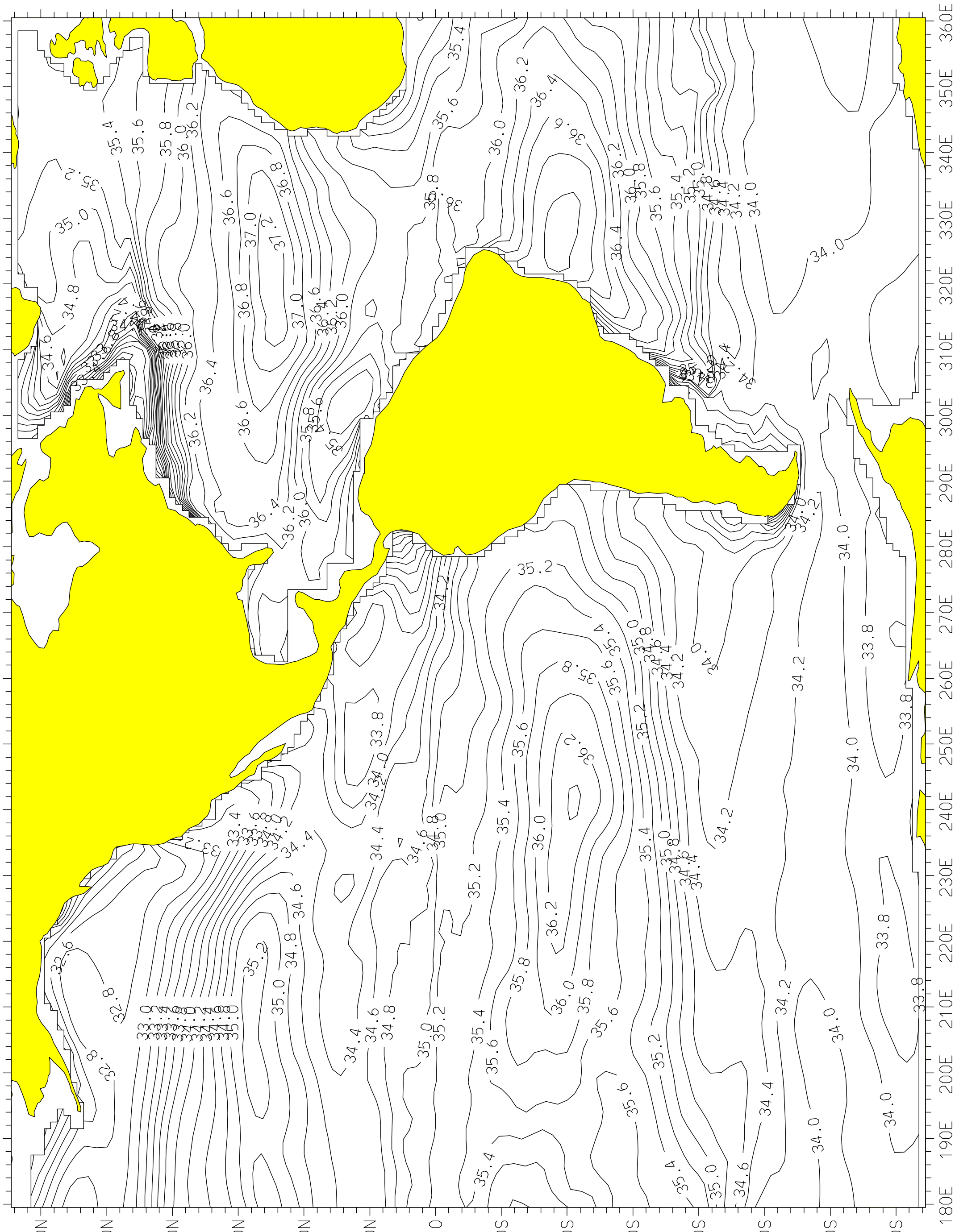

Figure 5.7b: [rotated] Global average surface saltinity (*psu*), western hemisphere. CI is $0.2\,psu$.

eastern and western coasts of South America, south of 40°S. Surface salinities in these areas are affected by eastern boundary upwelling, overturning, evaporation, land–based ice melt and river runoff. These areas are small and are covered by comparatively few grid points, so incorporating the above dynamics into a 1° model is not worthwhile (eastern boundary upwelling is, of course, present).

Fig. 5.8 shows the global temperature field at 210.5 m (level 6). Model thermal gradients around western boundary current departure areas are noticeably sharper than the Levitus data, i.e., there has a good deal more 'unsmoothing' at this depth, in comparison with the surface temperatures. Apart from this, the discrepancies with the Levitus data are similar to surface anomalies. The area west of Greenland has the largest discrepancy, being about 3°C warmer than the Levitus data, and is probably caused by the wall at 65°N preventing the cooling influence of Polar waters. Waters within 1500 km of the Gulf Stream are too warm by up to 2°C, and this may be partially due to the 65°N boundary. However, it is due, more likely, to the model's finite vertical layer resolution, and to the crude vertical mixing dynamics. Similar warming, of about 2°C, is observed along the 'cold dome' separating the Pacific NEC from the NECC. At this depth, the cold pool near 10°N:230°E is in good agreement with the Levitus set, within ~ 0.4°C. A zonal band of 20°C water lies along 20°S in the Indian Ocean, being about 1.3°C warmer than the Levitus data. All of the discrepancies mentioned above are characteristic of ocean general circulation models, and, hopefully, with improving grid resolutions, will become smaller.

Fig. 5.9 shows the global salinity field at 210.5 m (level 6). Like the temperature distribution, haline gradients in the vicinity of western boundary current departure latitudes are a good deal sharper than the Levitus data. The Pacific EUC haline gradient is comparable with Atlantic haline gradients. This gradient is heavily smoothed in the Levitus data and merges with the low latitude South Pacific salinity distribution. At 200°E, the model EUC haline gradient is distinct from the South Pacific gradient. Philander (1990, §2.8) discusses the importance of vertical mixing and turbulence in eroding the haline core of the Pacific EUC, and considers this to be more significant than role played by horizontal mixing. Salinities in the northwestern North Pacific, within 800 km of Alaska and Canada, are up to 0.5 psu higher than the Levitus data, this being one of two notable salinity discrepancies. The second is a strong salinity gradient in the Gulf of Guinea,

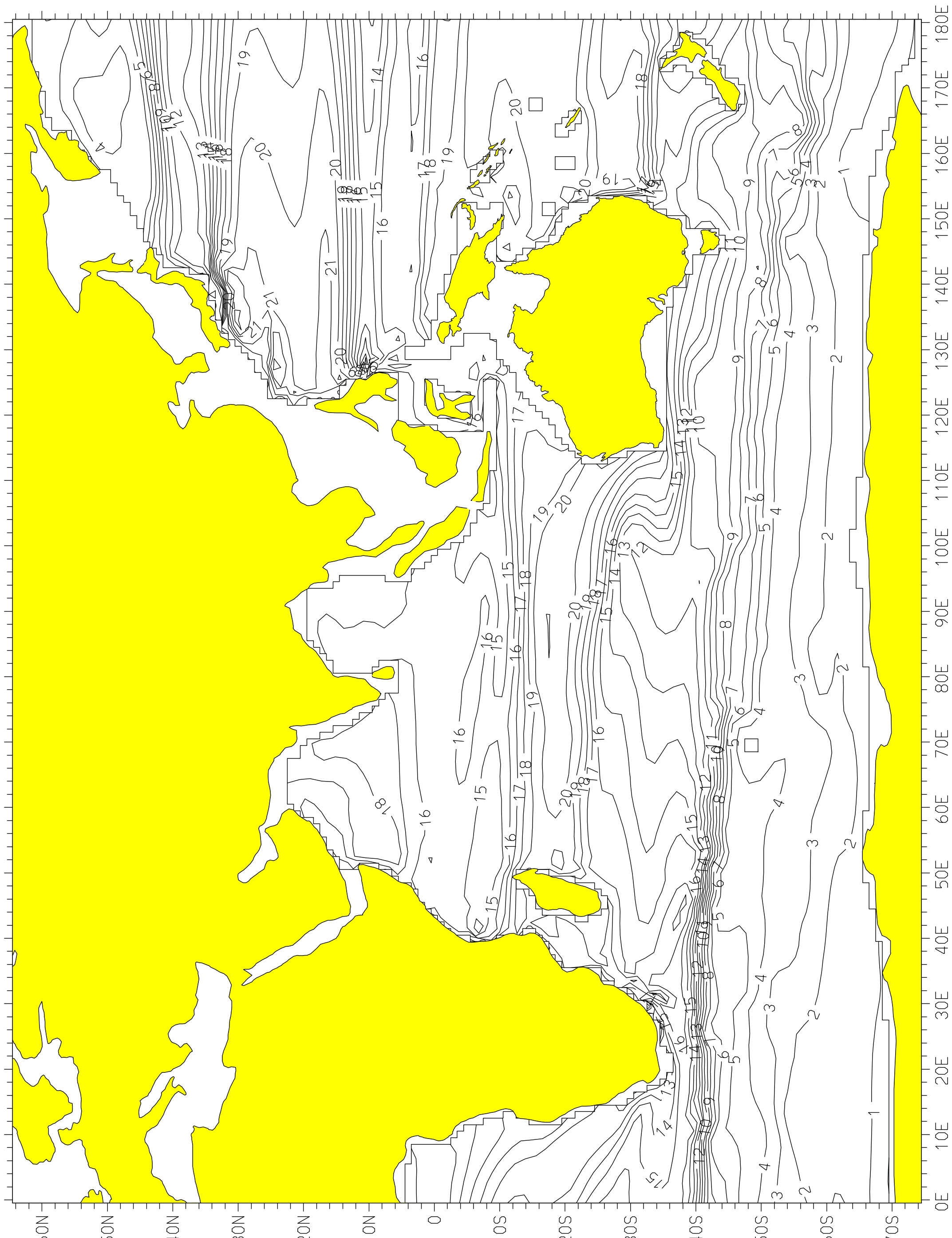

Figure 5.8: **a:** [rotated] Global average temperature at 210 m, eastern hemisphere. CI is 1°C.

Figure 5.8b: [rotated] Global average temperature at 210 m, western hemisphere. CI is 1°C.

Figure 5.9: **a:** [rotated] Global average saltinity (psu) at $210\,m$, eastern hemisphere. CI is $0.1\,psu$.

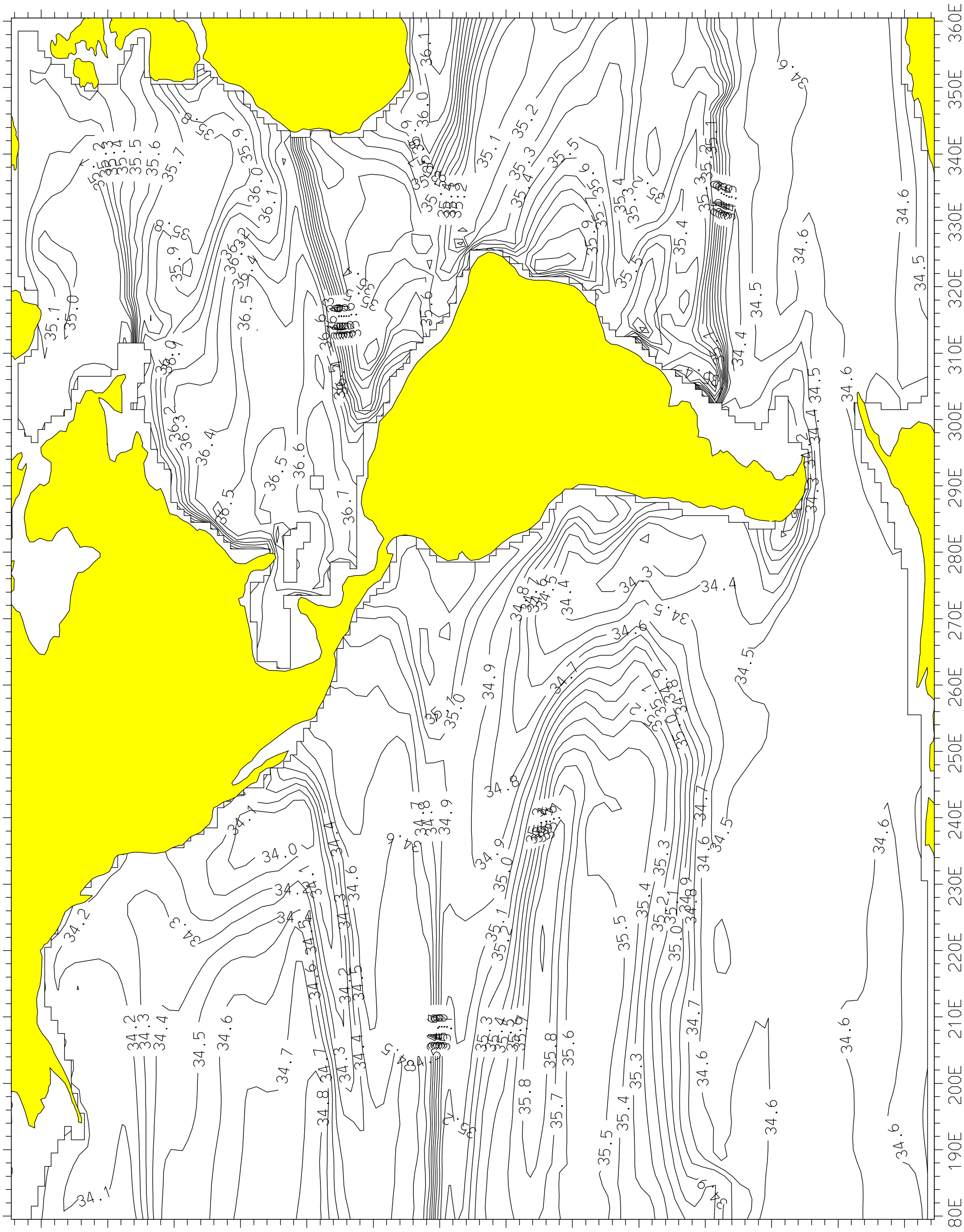

Figure 5.9b: [rotated] Global average saltinity (psu) at $210\,m$, western hemisphere. CI is $0.1\,psu$.

where salinities are up to $0.5\,psu$ higher than for the same depth range in the Levitus set.

5.2 Indonesian Throughflow

5.2.1 Indonesian Outflow and South Pacific Inflow

Fig. 5.10(a) shows the zonally–averaged flux versus depth histogram for the South Pacific inflow at 42°S, which supplies the IT. There is 16.8 Sv entering the Pacific between the surface and 751 m (levels 1 to 9), i.e., within the thermocline. Of that inflow, 6.8 Sv is entering within the 0–27 m (level 1) depth range. Between 751 m and 3610 m (levels 10 to 15), there is 6.9 Sv exiting southwards into the Southern Ocean. Between 3610 m and the bottom at 4900 m (levels 16 and 17), there is 4.5 Sv of Lower Circumpolar Water and Antarctic Bottom Water entering the South Pacific. Summing over all depths, the total is 14.4 Sv flowing northwards into the Pacific. The vertical distribution appears to imply that the 4.5 Sv of bottom water entering the Pacific entirely exits as deep water, along with 2.4 Sv of thermocline water. This is true in the sense of mean circulation, but it does not exclude the possibility that some bottom water remains in the Pacific and upwells to the near surface. A heat/salt budget could be used to examine this further.

Panel (b) of Fig. 5.10 shows the corresponding flux histogram for the IT, averaged across the passages at 8°S (see Fig. 5.19). Of the 14.4 Sv flowing southwards, 10.7 Sv is confined above 365 m (bottom of level 7). Flows between 365 m and 751 m (bottom of level 9) are insignificant. There is an additional 3.6 Sv flowing southwards between 751 m and 1412 m (levels 10 and 11), which is the sill depth. The near surface 10.6 Sv southwards flow is in keeping with the observations of Fieux *et al.* (1993), although they find 23 Sv for this depth range. They observe about 2 Sv flowing northwards below the thermocline, and they also show tracer properties in the northern Indonesian waters (Pacific side) to be consistent with this. The model's 3.6 Sv southwards flow, not an uncommon result for general circulation models, is therefore incorrect in the light of this observation. Relaxation is present in the model from levels 10 to the bottom, and this could be a cause for the questionable 3.6 Sv southwards flow. However, fully prognostic models can (usually) have a southwards throughflow at these depths, e.g., Hirst & Godfrey (1993). In the present model, the extra throughflow originates from a zonal mean westwards flow along the Pacific equator, over this particular depth range.

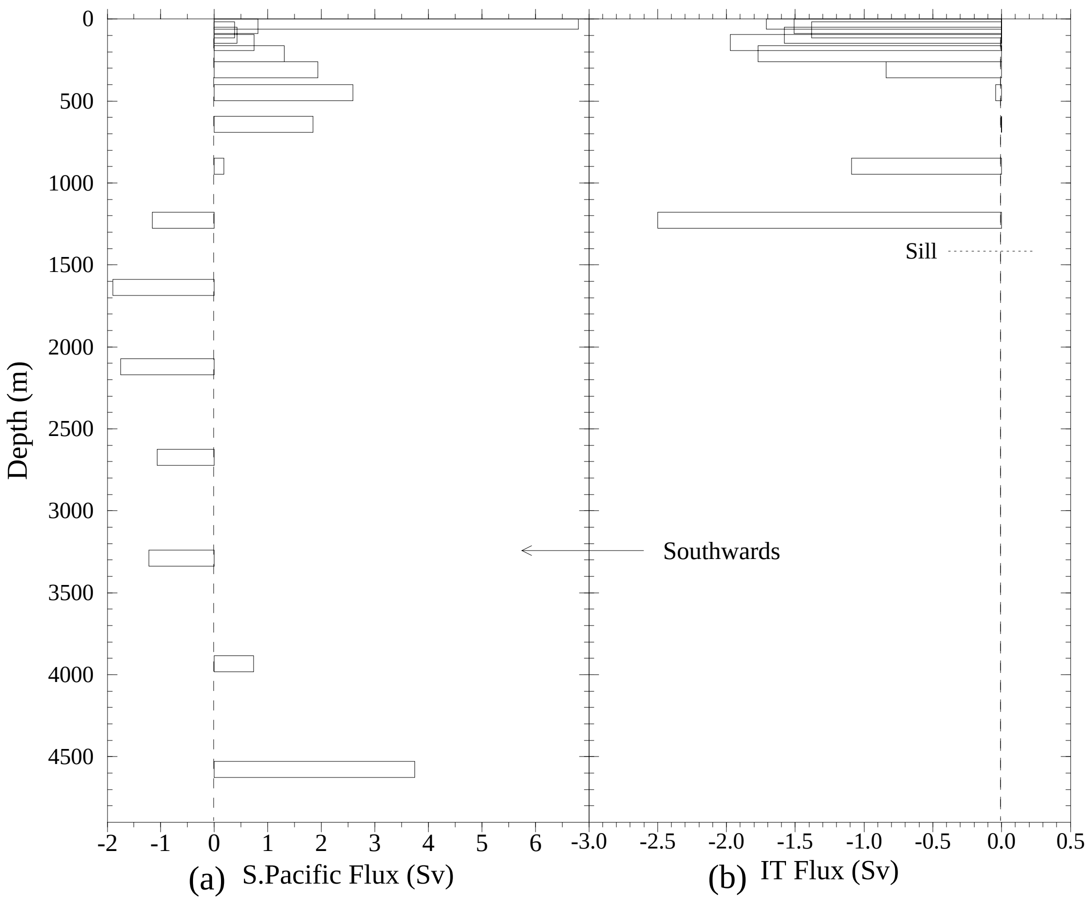

Figure 5.10: **:** (a) South Pacific volume inflow zonally averaged at 42°S, and (b) Indonesian throughflow zonally averaged across the passage at 8°S.

Figs. 5.11 and 5.12 show zonally averaged T and S versus depth, for 42°S in the Pacific and 8°S across the Indonesian passages, respectively. The total northwards flux of oceanic heat across 42°S, relative to the Standard Ocean, is $0.60\,pW$. The corresponding southwards flux of heat via the Indonesian passages is $1.06\,pW$. Thus in the model, the Pacific supplies a nett $0.46\,pW$ for its throughflow waters, via the surface and deep temperature relaxation. The northwards flux of salt across 42°S is $-8.88\,kt\,s^{-1}$, relative to the Standard Ocean, or a total of $494.77\,kt\,s^{-1}$ northwards. The southwards flux of salt through the Indonesian passages is $-6.96\,kt\,s^{-1}$, relative to the Standard Ocean, or a total of $496.69\,kt\,s^{-1}$ southwards. The discrepancy is $+1.91\,kt\,s^{-1}$, equating to a freshwater influx of $0.067\,Sv$ into the Pacific. The surface tracer relaxation removes the salt excess.

Figs. 5.13, 5.14 and 5.15 show the zonal internal distribution of flux, T and S for the 42°S parallel across the South Pacific. It is of interest to examine not only the depth distribution of the Pacific inflow but also the horizontal spatial distribution. To examine the internal distribution of volume influx, the cumulative flux statistic is defined. Starting at the first ocean grid point on the west coast (Tasmania in this case), the northwards fluxes (v component) for each velocity grid point are integrated over a desired depth range. The partial sums are then integrated while proceeding zonally from the west coast to the east coast (South America in this case). The final value at the west coast is the nett northwards flow, over the given depth range. The partial sums form a continuous function, except where the path of integration crosses islands (New Zealand in this case), and the function's gradient is proportional to the mean northwards velocity, for the given depth range.

Fig. 5.13 shows the cumulative flux and TS across 42°S over the depth range 0–751 m (levels 1 to 9). There is $16.8\,Sv$ flowing northwards (cf. Fig. 5.10), distributed nearly evenly between 200°E and 285°E (South America). The EAC transports about $2\,Sv$ southwards next to the Tasmanian coast, but there is a compensating northwards flow of nearly $5\,Sv$ into the open Tasman Sea. There is a weak southwards flow of $2.5\,Sv$ on New Zealand's east coast, with the water being comparatively warm and salty. This is the East Auckland Current and is sourced from the Tasman Front, which is in turn sourced from the EAC. Between New Zealand and South America, temperature and salinity fall considerably. Fig. 5.14 shows the cumulative flux and TS across 42°S over the depth range

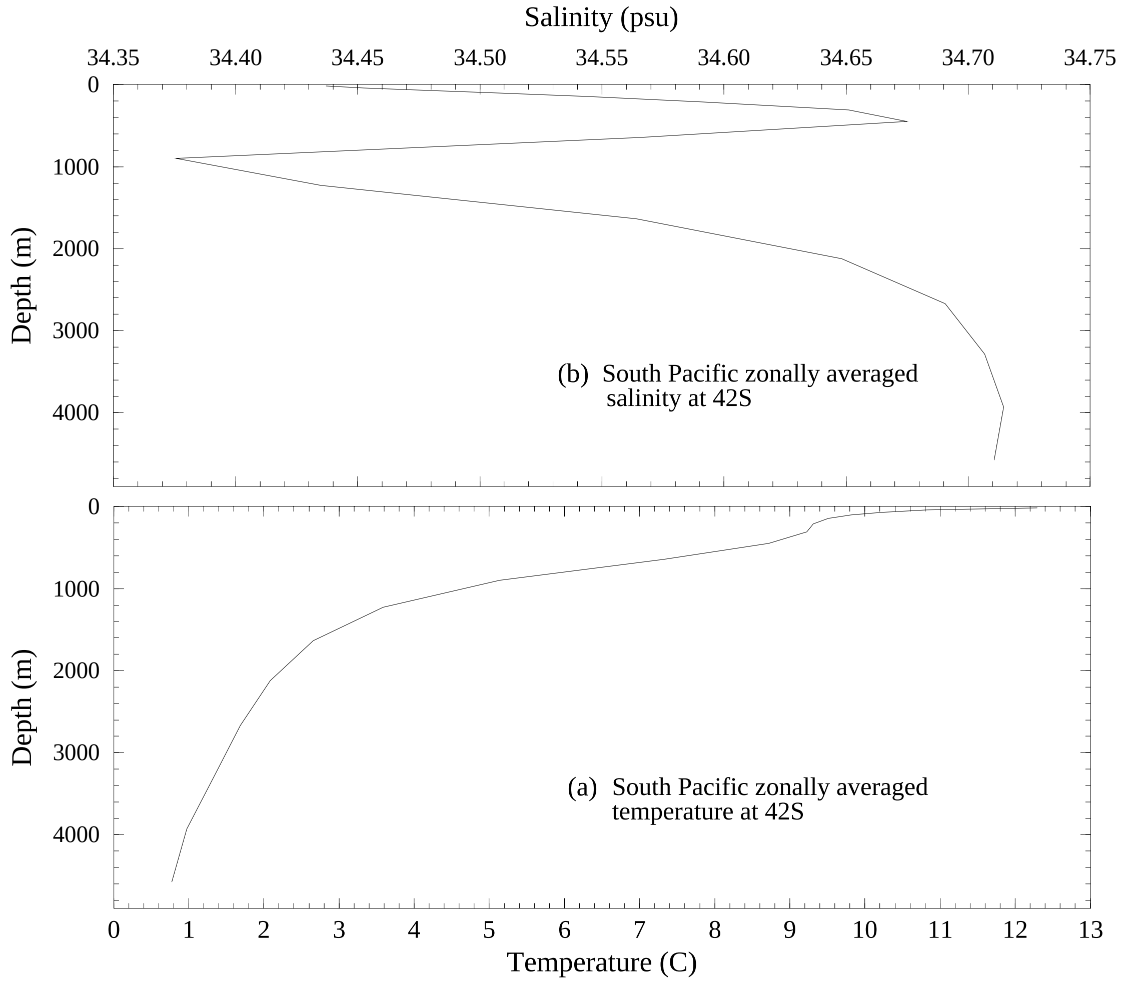

Figure 5.11: **:** South Pacific tracers zonally averaged at 42°S, (a) average temperature and (b) average salinity.

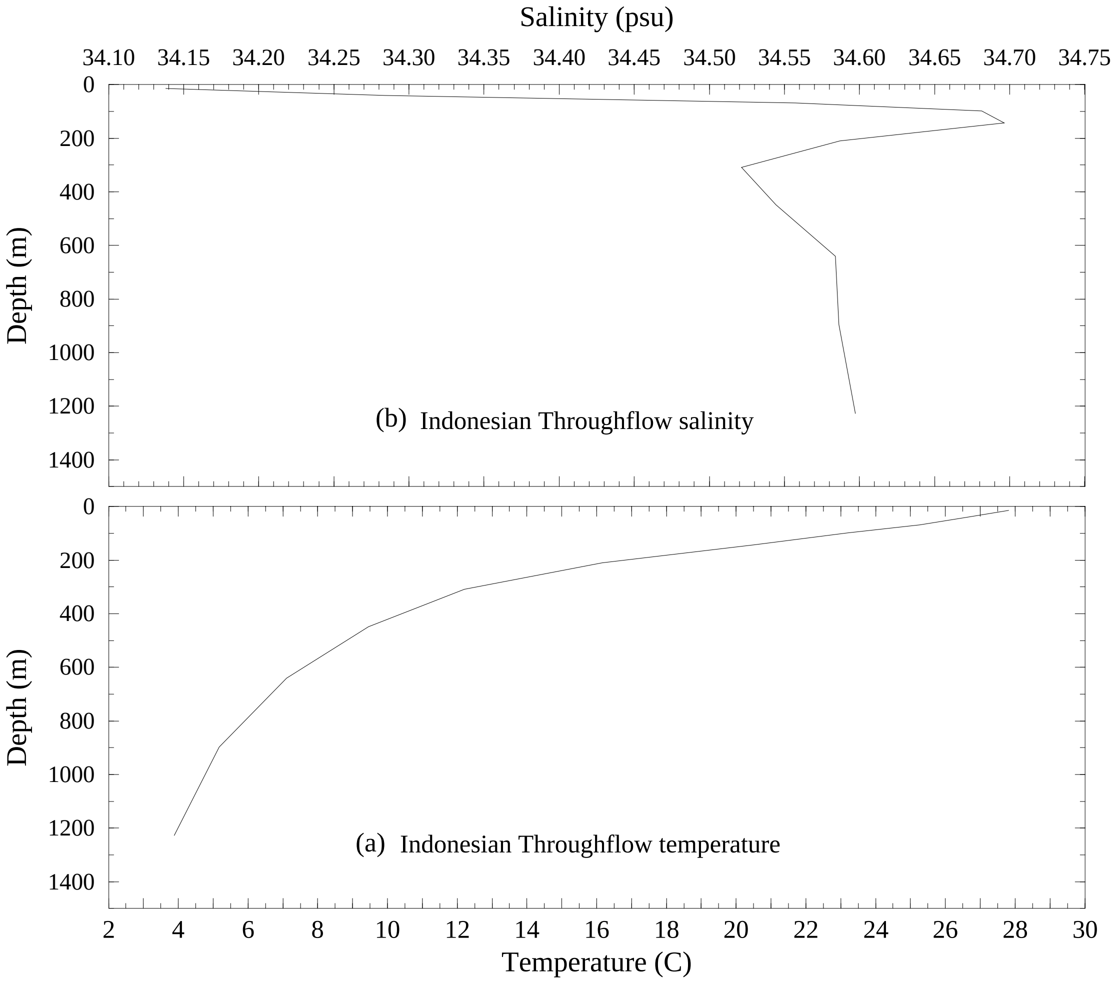

Figure 5.12: **:** Indonesian passages tracers zonally averaged at 8°S, (a) average temperature and (b) average salinity.

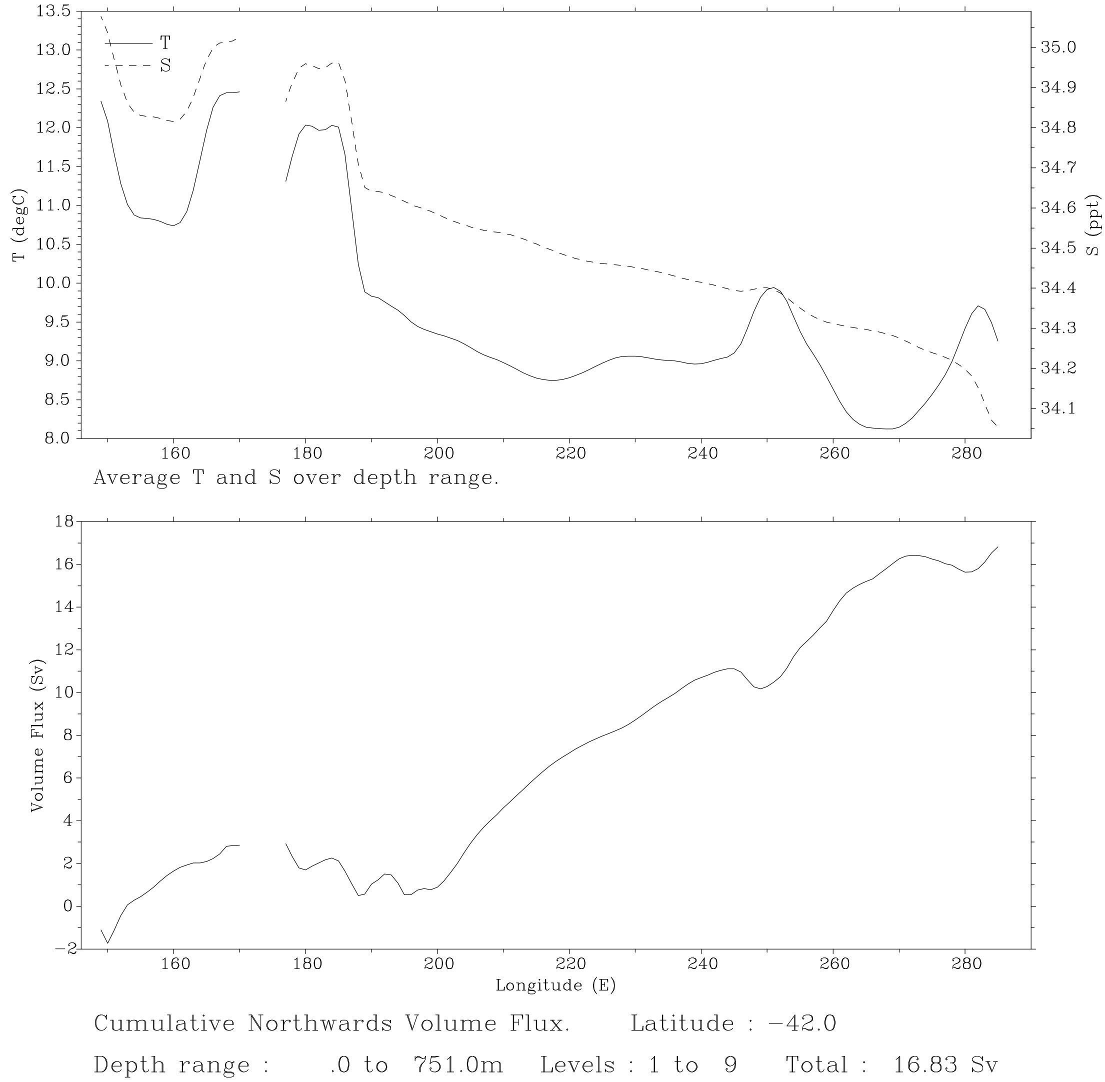

Figure 5.13: **:** Cumulative volume flux and tracers along 42°S in the South Pacific. Depth range is 0–751 m (levels 1–9). Volume fluxes and tracers are averaged over the given depth range. Volume flux is integrated from the western boundary. The nett inflow/outflow for the depth range is the integrated flux value at the eastern boundary.

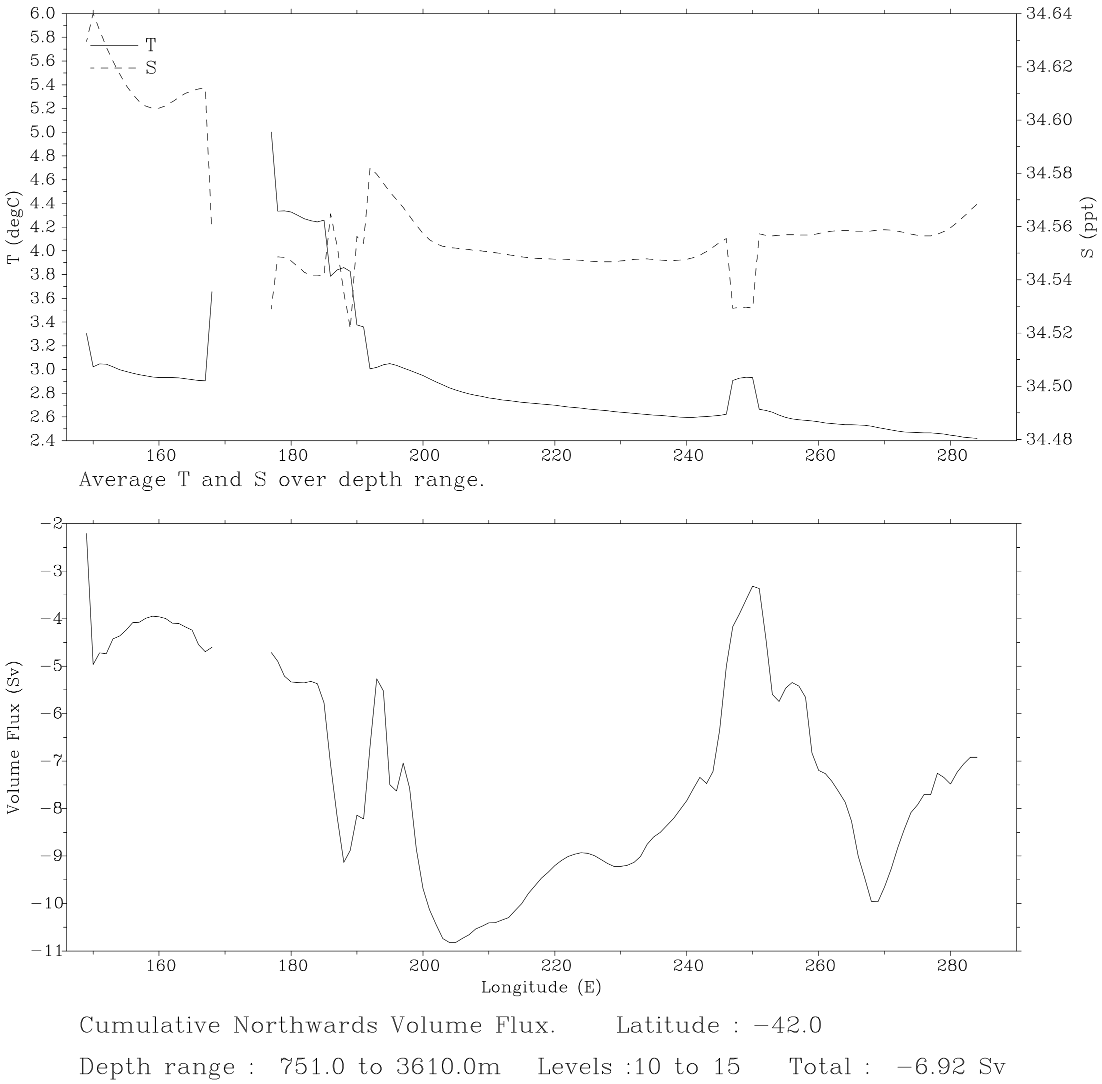

Figure 5.14: **:** Cumulative volume flux and tracers along 42°S in the South Pacific. Depth range is 751–3610 m (levels 10–15).

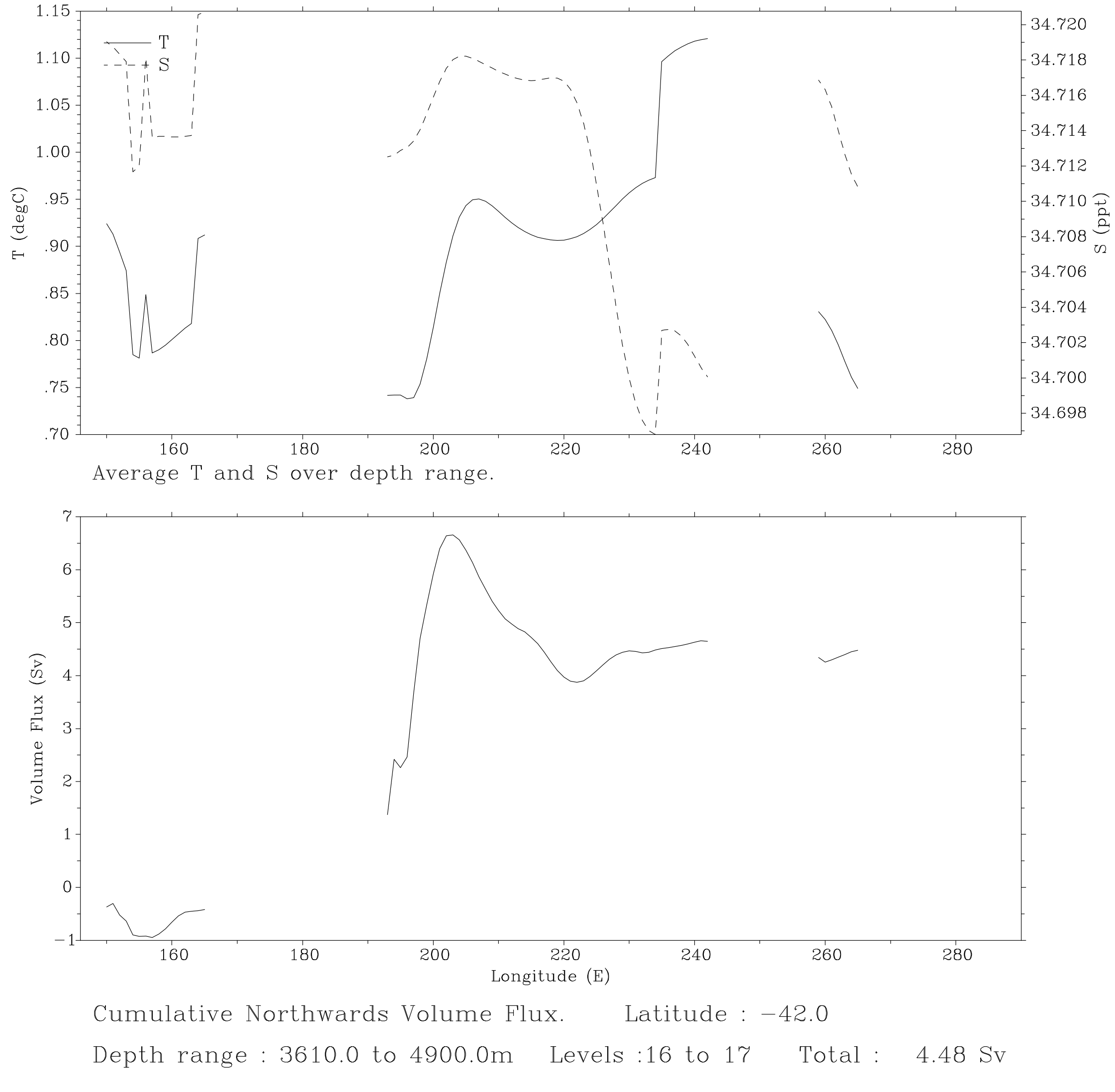

Figure 5.15: **:** Cumulative volume flux and tracers along 42°S in the South Pacific. Depth range is 3610–4900 m (levels 16 & 17).

751–3610 m (levels 10 to 15); this is the depth range for the southwards flow of 6.9 Sv in Fig. 5.10. There is a southwards flow of 11.8 Sv between the Tasmanian coast and 205°E, and a northwards flow of 8.9 Sv between that longitude and the Pacific–Antarctic Ridge (250°E). There is a strong southwards flow east of the ridge and velocity distributions show considerable steering (not shown). Fig. 5.15 shows the cumulative flux and TS across 42°S over the depth range 3610–4900 m (levels 16 and 17). The total northwards flow is 4.5 Sv, occurring mostly along the eastern flank of the Chatham Rise (195°E). This is the deep western boundary current reported by Stommel *et al.* (1973) and Taft *et al.* (1992). The model boundary current is carrying 7.6 Sv, in fair agreement with the 9 Sv of Taft *et al.*, but 2.7 Sv flows southwards, further to the east. Only the abyssal plain between the Chatham Rise and the Pacific–Antarctic Ridge has a sufficiently wide and deep sill to its north to permit an exit of water into the central Pacific.

5.2.2 Robustness of Model Indonesian Throughflow

The reason for the existence of the IT and its strength have been topics of debate for several decades. Theories of thermohaline circulation propose that some of the North Atlantic Deep Water present in the Southern Ocean, and some Antarctic water from several levels, are upwelled in the Pacific and that this mass exits the Pacific via the Indonesian passages (Gordon, 1986). Whether such upwelled waters may drive the throughflow or simply utilize it in a passive way has not been shown. Sverdrupian theories propose that the IT is driven by the South Pacific wind stress, since the area averaged wind stress curl over Australia–PNG's zonal projection across the South Pacific has a residual of about 17 Sv to the north. New Zealand needs to be included in the calculation, as well (Godfrey, 1989). Godfrey's prediction of 17 Sv for the average throughflow seems quite reasonable although a minor difficulty arises since the flow should come entirely from the South Pacific, whereas observations show it comes almost exclusively from the North Pacific (Fieux *et al.*, 1993; Godfrey *et al.*, 1993; Levitus, 1982). (The basic Sverdrup relations are covered in Appendix A.)

An unexpected model result, and somewhat in contention with Sverdrupian ideas, shows that the IT is quite sensitive to modifications of the ACC. An initial world model configuration had the southern wall at 64°S, which is well to the south of the Pacific and the strong westerlies over the Southern Ocean. The resulting throughflow seemed reasonable at $\sim 15\,Sv$ during the diagnostic phase. However, during free–thermocline runs, with annually–averaged climatologies and forcing, the fluxes of both the ACC and IT decreased in strength. Fig. 5.16 shows the ACC and IT fluxes for a particular run of this model. The ACC increases rapidly during the first year, and approaches a steady value. As soon as the thermocline relaxation is removed it begins to fall steadily. For some runs (not shown) it reached a near steady value of $125\,Sv$ after more than a decade, but the 64°S model was not run for longer than this to see if the ACC would eventually rise. The tendency for the ACC to decrease was very much counter to the usual results; it is normally too large in general circulation models. A great deal of the available machine time was used in many test runs of the 64°S model, with different parameters, in an attempt to determine why the ACC and IT were giving unusual results. The IT reaches $19\,Sv$ within nine months and then falls to $13\,Sv$ by the third year. It has several falls and a slight rise during the diagnostic phase, and is $10.8\,Sv$ at the end of this particular run. The IT flux–time profile for the current model, i.e., wall at 75°S, is similar, but the mean only falls to about $16\,Sv$ during the free–thermocline phase. The high frequency (weeks) variation is, however, much larger at $\pm 3\,Sv$, and similarly for the ACC.

Placing the wall at 75°S completely alleviates the IT robustness problem, and the IT remains steady during the switch over to the free–thermocline phase. The ACC's long–term trend is to slowly rise during all phases, whereas it slowly fell after the diagnostic spin–up phase of the 64°S configuration. Moving the wall further southwards, so that all of the Ross and Weddell Seas are covered, may slightly change the results yet again. The ACC flow path, implied by the Levitus data, is confined north of 64°S except for a small portion of it near the Ross Sea, that deviates a little southwards of this latitude. This small part of the ACC was truncated in the climatology of the 64°S world model. If the IT is actually driven only by the mid and low latitude South Pacific wind stress then truncating a small part of the ACC should have little effect. Running the 64°S configuration for many decades, with a large acceleration, may see the IT slowly rise again, as the ACC's climatology recovers from the truncation, but such a run has not been performed. In a further experiment, with the wall at 64°S, the truncated climatology was compressed into the southernmost few latitude rows

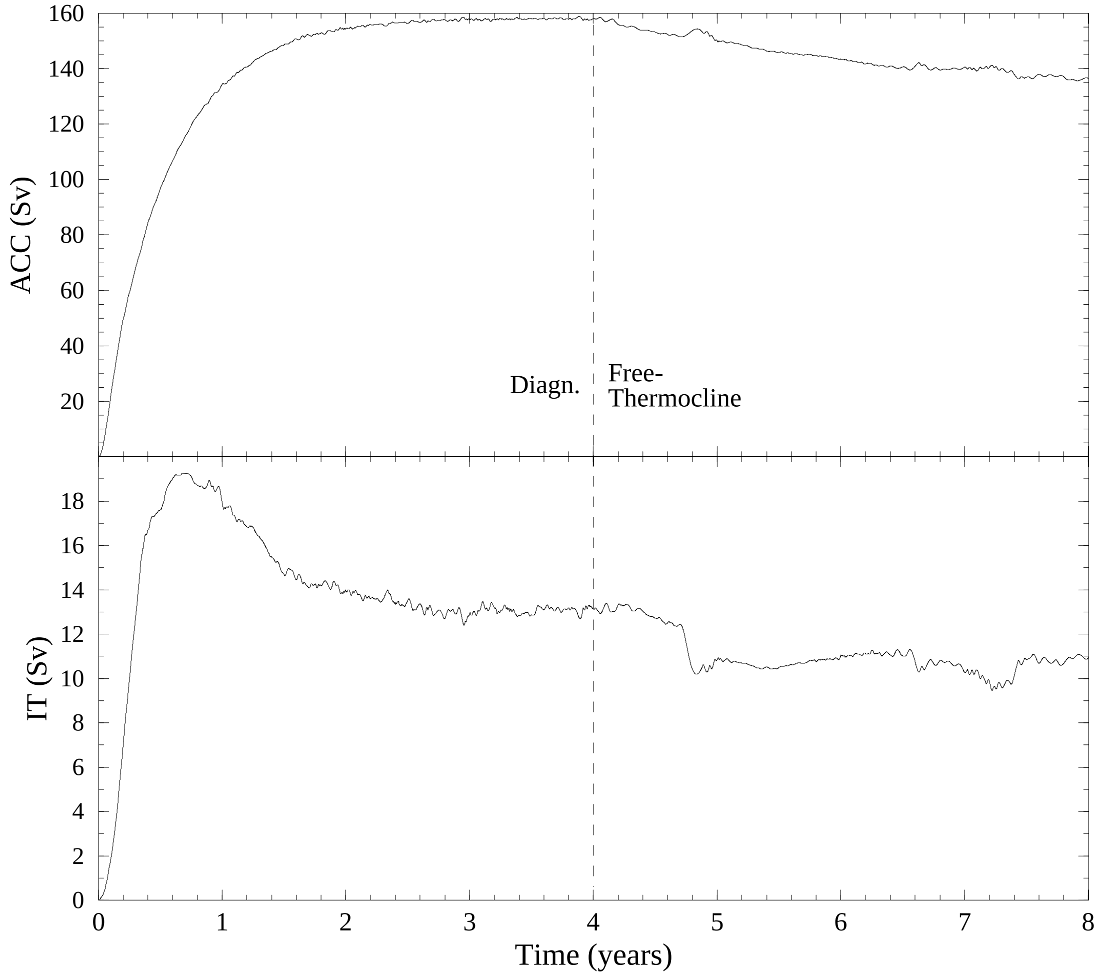

Figure 5.16: **:** Indonesian throughflow (IT) and Antarctic Circumpolar Current (ACC) volume fluxes during a spin–up of the 64°S world model. The acceleration is 12:1 during the diagnostic phase and 80:1 thereafter.

and the throughflow robustness problem was again alleviated.

Sverdrup models, such as Godfrey's, have an arbitrary depth–averaged pressure specified at some point, e.g., the southern tip of South America, and line integrals are commenced from this point to yield the global depth–averaged pressure field. One of the most frequently recurring problems is a large pressure drop in the ACC as it traverses Drake Passage. This must occur since the pressure field is conservative and the Southern Ocean has cyclic continuity. This difficulty is usually explained in terms of a hydraulic head caused by the bathymetry of Drake Passage. An equally valid possibility is that the portion of ACC which forms the Malvinas Current rapidly reduces the pressure head via western boundary dynamics. Some subsurface western boundary behaviour could also occur in the deep channels further to the southwest. In this sense, the ACC is an open ocean gyre while the Malvinas Current is its corresponding western boundary current. The ACC may also undergo some (weak) boundary current dynamics in the vicinity of Campbell Plateau, immediately to the south of New Zealand. These two areas are usually included in the integrals, but this may violate the basic assumptions of Sverdrup models. The ACC also flows in close proximity to the southern tip of Africa where it has a strong interaction with the Agulhas Current, possibly being slightly nonlinear in the sense of Sverdrupian dynamics, and it no doubt has a strong influence on the local depth–averaged pressure. If it is assumed that the ACC sets, or at least has a substantial influence over, the pressure field at the southern tips of both Africa and South America, then the pressure difference between these two points is fixed mainly by the ACC. (Truncating a small part of the ACC in the Ross Sea should have the effect of slightly reducing the pressure difference between Africa and South America.)

In a Sverdrup model (e.g., Godfrey's Fig. 3), the depth–averaged pressure at the southern tip of Africa is determined by a zonal integral starting from the east coast of Australia (boundary E_3). The pressure at the southern tip of Australia is determined by a similar zonal integral from New Zealand's east coast (boundary E_2), which is in turn found from a zonal integral beginning at South America's east coast (E_1). Fig. 5.1a shows the model ACC is steered by the Kerguelen platform and the Crozet Ridge, to the southeast of Africa, and that the Agulhas essentially joins the ACC, after its retroflection. Around Campbell Plateau, the ACC undergoes an abrupt southwards and then northwards meander, which will have a substantial effect on the depth–integrated pressure in the vicinity of New Zealand. The path of the ACC between Africa and New Zealand is quite close to the integration path mentioned above, and it can be argued that the ACC may be as equally influential as the wind stress, in setting the pressure difference between South America and Africa, or perhaps even more influential.

Other integration paths can be selected around the Pacific and Indian Oceans, via the Indonesian passages, for which the pressure variations will be caused by their corresponding wind stresses. The pressure distribution along the lengthy western coast of the Americas is determined only by the alongshore component of the wind stress. For example, integrating from the southern tip of South America, around the Pacific and Indian rims to the southern tip of Africa will also yield a pressure difference, but it is very unlikely that it will be the same as the difference set by the ACC. Since the pressure field must be single valued, this discrepancy needs be eliminated by some mechanism along the Pacific-Indian rim, or whichever path of integration is used. An extraneous western boundary current, or a hydraulic step, could easily eliminate the pressure discrepancy by producing a flow towards Africa if the discrepancy is positive, or towards South America if negative. Any hydraulic steps are likely to be associated with a sill or restricted passages. An extraneous western boundary current needs to be associated with a coastline but not necessarily the Pacific rim; the northern Irian Jayan coast would be equally satisfactory. The boundary current would not be directly affected by latitudes of zero wind stress curl. The characteristics mentioned above are observed in the intense flows though the Indonesian passages (Wyrtki, 1961a). Since virtually all the water that flows southwards through the Indonesian passages originates from the North Pacific it is reasonable to assume, within the framework of the present argument, that an extraneous boundary current exists on the Pacific rim in Indonesian waters—actually through the deeper passages just offshore.

A (large) seasonal modulation of the IT should occur as the pressure discrepancy fluctuates, due to the seasonal fluctuations in the Pacific–wide wind stress and to the smaller seasonal variations of the ACC. The variability of the IT could be determined by complex interactions and variabilities, not only over the South Pacific, but over most of the world's oceanic regions. During the diagnostic spin–up phase of the 75°S world model, the IT varies erratically by $\pm 3\,Sv$ on a time scale of months and the ACC also has a similar variability of $\pm 4\,Sv$. The 64°S model also shows this feature but the variations are much smaller, less than $\pm 1\,Sv$. As far as can be determined, the erratic variations are due to wave activity generated by convective adjustment events near Antarctica. The Levitus data have areas of spurious TS values in abyssal waters around the Antarctic shelf, and this problem is rectified either by setting such values inland, by clamping them within certain limits, or by some other method. For the 64°S configuration, the rates of decrease of the ACC and IT are sensitive to the way in which the spurious TS values are dealt with. Generally, changing the latitudinal position of the southern wall causes larger variations of the ACC and IT but, in comparison, the spurious TS values are not insignificant contributors. The 75°S model had the greatest requirement for the TS problem to be rectified, since more spurious values were included in the domain. Most of the problematic ocean points were set inland while others had their TS values clamped. Density inversions were eliminated from the TS climatology prepared for the model. Nevertheless, weak inversions do begin to occur as integration proceeds, and so convective adjustment is activated regularly. These adjustment events presumably yield propagating disturbances within the ACC, which in turn perturb the IT.

It is quite important to properly prepare the Levitus data for use in primitive equation models, especially the abyssal TS values in the Southern Ocean. Deep waters around the Sulu Sea in the Philippines also need to be carefully screened before use, although resulting errors appear to be localized. Mediterranean water 'floating' at about $1300\,m$ in the eastern Atlantic should not be modified or clamped in any way.

Pressure discrepancies may well exist for the Atlantic, since the eastwards Africa–to–South America pressure change, set by the ACC, is identical to that obtained in going eastwards from South America to Africa. The wind stress over the entire Atlantic is unlikely to produce exactly the same ACC pressure difference that exists between the tips of South America and Africa, and the mechanism which overcomes this discrepancy may be that part of the Agulhas which does not completely retroflect, but rather flows into the Atlantic. A more quantitative argument is needed here since the Brazil–Malvinas confluence is expected to cause a large pressure drop in the ACC; it is likely to be undergoing some western boundary intensification in that region.

Several variations of the model bathymetry around the Indonesian passages have been implemented, with some islands either present or removed, to determine if friction plays a key role in the throughflow. Admittedly, a 1° grid is incapable of realistically representing the true bathymetry, but the sill is always set to a realistic depth of 1412 m. Variations of island positions do not cause any discernible changes to the nett throughflow, nor to its composition, but with the single exception of Halmahera Island. This island serves to deflect the NGCU northwards during the southern winter, to its departure latitude of 2°N, so that it never directly participates in the throughflow. Moving the island southwards by only one grid point causes the NGCU to participate significantly in the wintertime IT. This tends to be water deeper than the V–max core of the NGCU. For this case, the NGCU and Mindanao currents coalesce, changing the composition of the throughflow, but the nett flux remains about the same. To minimize the stream function errors caused by an over abundance of islands, Halmahera has finally been included as an 'L'–shaped extension at the western end of the Irian Jayan coast. (As a separate island it needs to be separated by at least two ocean grid points from the Irian Jayan coast, a little excessive compared with the actual width of the channel.) Using the ideas above, the NGCU could act as an extraneous boundary current supplying the IT if it were not for the presence of Halmahera. Godfrey *et al.* (1993) compare the Semtner & Chervin model with a coarse resolution model (Hirst & Godfrey, 1993) and discuss various aspects relating to the presence of Halmahera.

Figs. 5.17 and 5.18 show instantaneous snapshots of the barotropic stream function and the salinity (210 m) distribution for the Indonesian passages, respectively, during August-8 (i.e., August of year eight of the seasonally forced phase). There is strong retroflection at Halmahera's east coast only during the austral winter, and is at its most intense during this month. Stream function isopleths show 30 Sv (IT is 16 Sv) being deflected to the east by 'Halmahera', at 2°N:131°E. The depth–averaged flow immediately north of PNG has a localized recirculation of about 15 Sv while another 30 Sv of the retroflected current flows into the North Pacific tropical gyre. The retroflected high salinity core of the NGCU does not merge with the North Pacific tropical gyre but flows due east along 1°N. The strong meridional salinity gradient in Fig. 5.18 follows the 1°N parallel eastwards to at least 220°E. The model NGCU's V–max core, at a

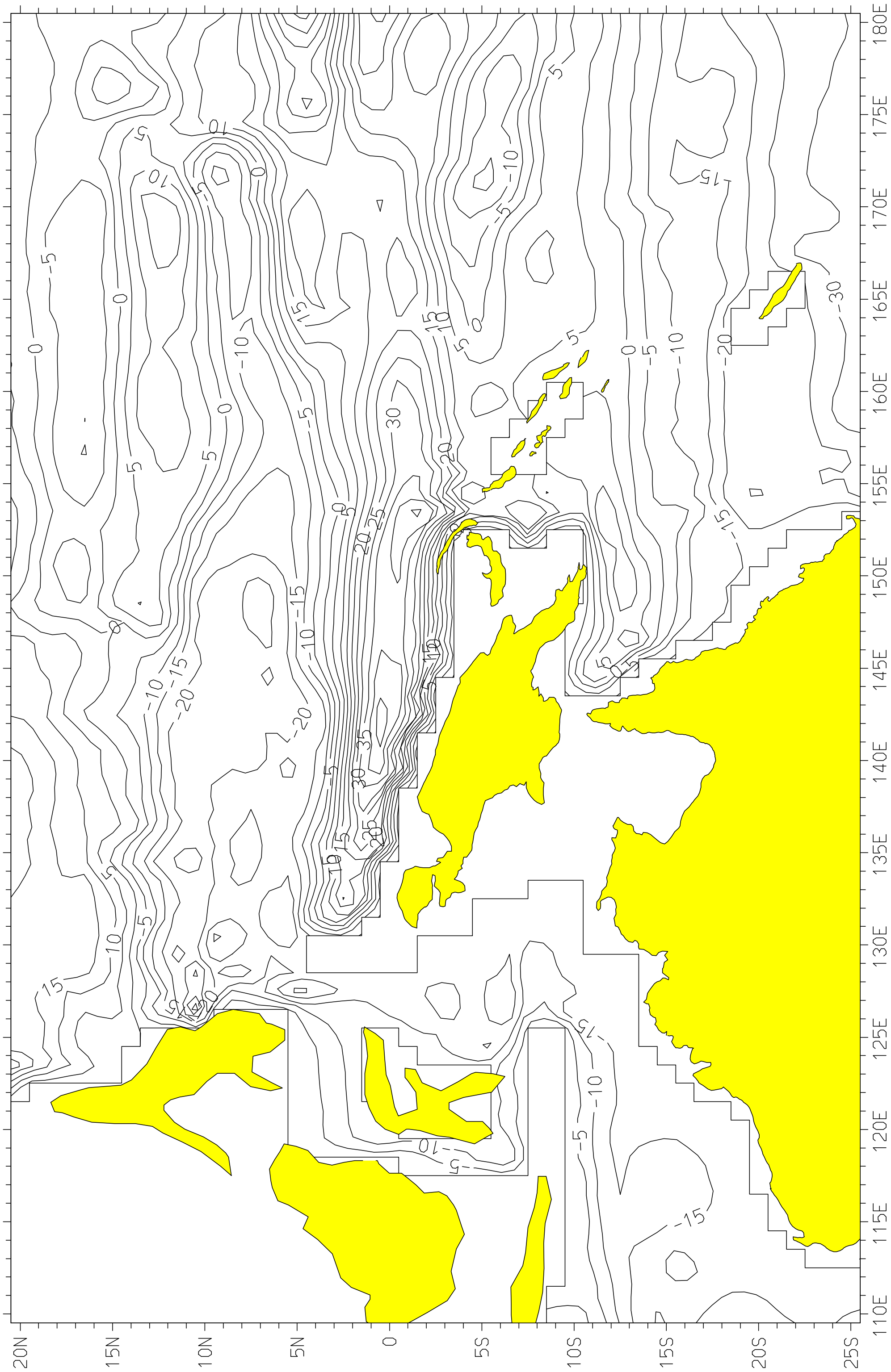

Figure 5.17: **:** [rotated] Instantaneous barotropic stream function (Sv) during August-8 for the Indonesian passages area. CI is $5\,Sv$ and the Indonesian Throughflow is $15.7\,Sv$. Results have been lightly smoothed to remove computational noise ("checker boarding"), thus causing some streamlines to terminate on land boundaries.

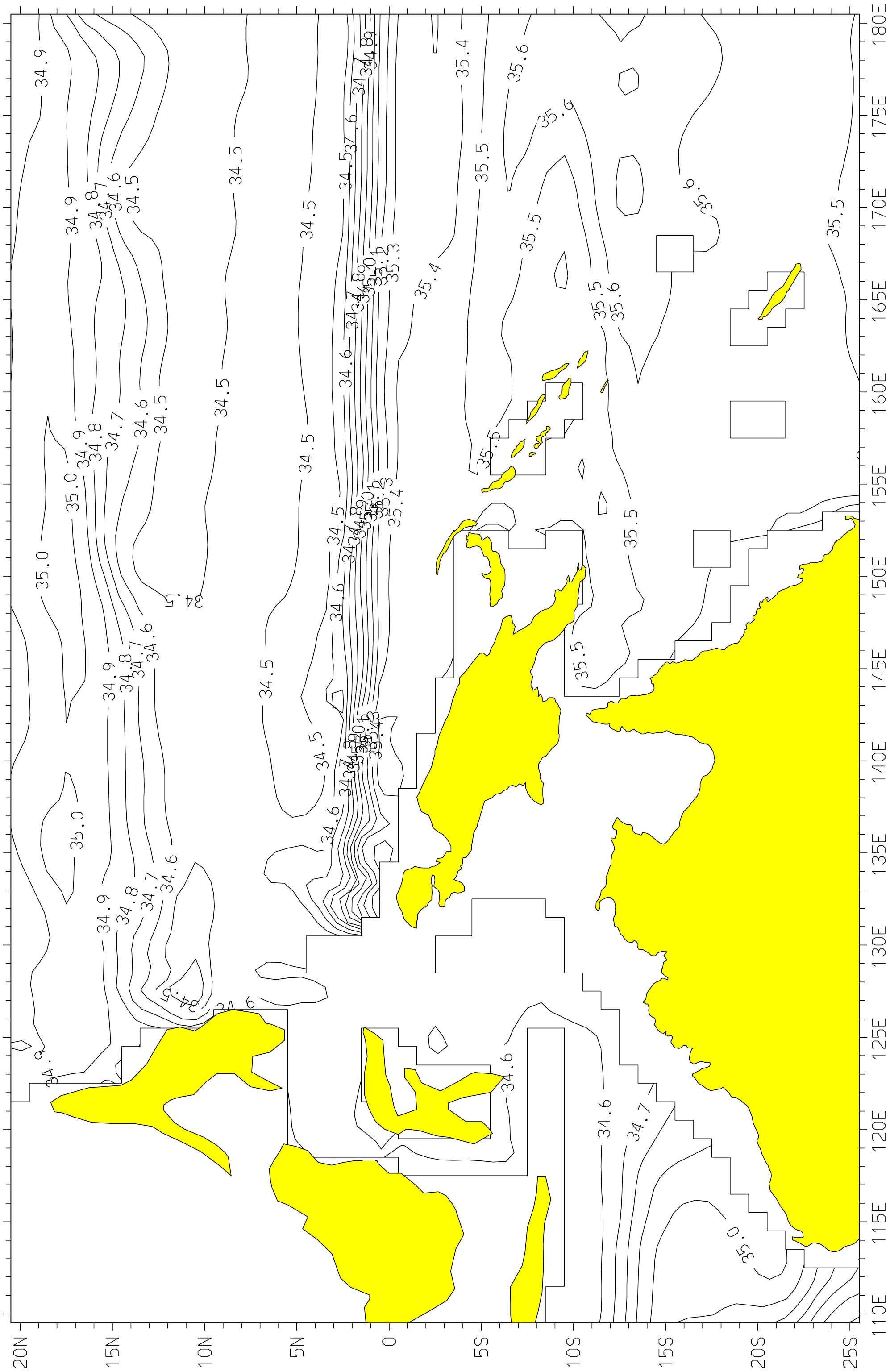

Figure 5.18: **:** [rotated] Instantaneous salinity (psu) distribution at 210.5 m (level 6) during August-8 for the Indonesian passages area. The salinity variation across the Equatorial Undercurrent is 0.9 psu.

depth of $\sim$200 m, forms the EUC after it retroflects at 'Halmahera'. The NGCU is observed to be the source of the EUC (Tsuchiya, 1968 & 1981; Lindstrom *et al.*, 1987; Tsuchiya *et al.*, 1987), but the finer details of the flow path along the north coasts of PNG and Irian Jaya, and the seasonal variation, are yet to be established. The model EUC eventually diffuses into the South Pacific tropical gyre and, to a lesser extent, into the North Pacific tropical gyre at 230–250°E.

Fig. 5.19 shows the velocity field of the Indonesian passages at 67.5 m, averaged over years seven and eight. The IT is supplied entirely from the Mindanao Current, which flows southwards along the Philippines east coast. The main path is though Makassar St., although the true path through the passages is not known with any certainty.

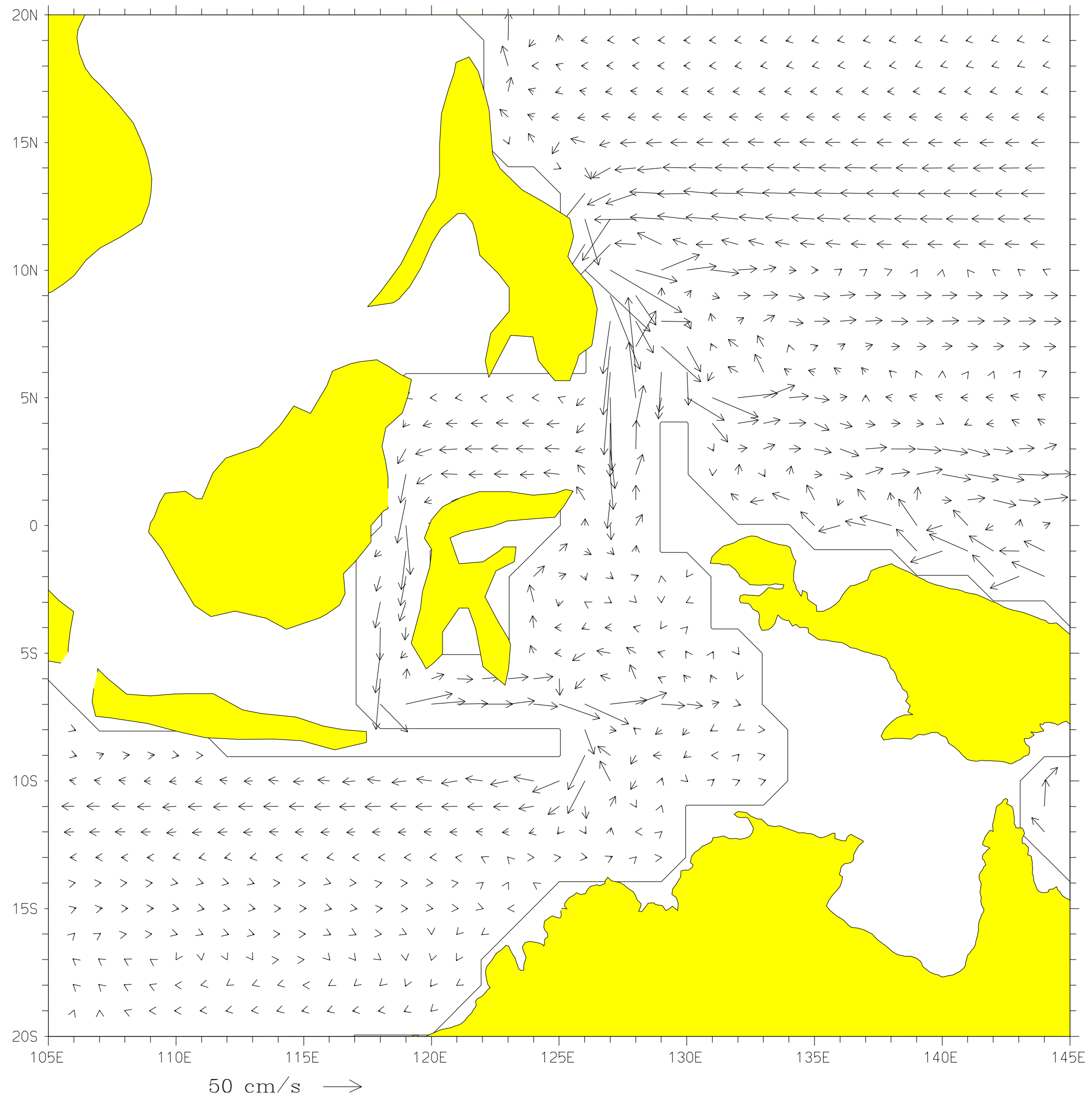

Figure 5.19: **:** Indonesian passages velocity field at 67.5 m (level 3) averaged over years seven and eight of the seasonally forced phase. The IT is supplied by the Mindanao Current flowing southwards along Mindanao I. The NGCU retroflects at 134°E.

5.3 Low Latitude Pacific Currents

This section details the currents of the low latitude Pacific, for various depths, and its bearing on the Coral and Solomon Seas. Results are from the average of years seven and eight of the seasonally forced phase, unless otherwise stated.

Fig. 5.20 (a and b) shows velocities at 67.5 m (level 3). The magnitude scaling is set to show open ocean currents and so clamping to a maximum of $10\,cm\,s^{-1}$ is necessary. In the ranges 225–255°E, and 3–20°S, a zonal westwards flow is observed, which is the beginning of the South Equatorial Current (SEC). At 220°E a distinct separation of SEC flows is evident, near 9°S, and this becomes more pronounced as the SEC proceeds westwards. By 200°E a significant eastwards flow is interposed between the two separated paths of the SEC, and this eastwards flow is commonly termed the South Equatorial Countercurrent (SECC). There are occasionally differences in the naming of the SEC, or rather its latitudinal position. The SECC has its origins along the eastern flank of the Solomon Islands. More than half of the water of the northern branch of the SEC, at about 4°S, turns to the southeast along the islands and forms the SECC. The remainder of the SEC northern branch, which lies between 6°S and 2°S, continues on towards Halmahera. The southern branch of the SEC flows into the Coral Sea, bifurcating around islands, which leave distinct zonal bands in the velocity field.

The North Equatorial Current (NEC) lies between 10°N and 18°N, and the North Equatorial Countercurrent (NECC) lies in the 5°N to 10°N latitudinal range. A strong westwards flow between roughly 2°N and 5°N, and no more than three grid points wide, is found across most of the Pacific. This is the counterpart of the northern branch of the SEC, and there is qualitative symmetry about the equator. The shallower flows of the Equatorial Undercurrent (EUC) are visible across most of the Pacific, covering no more than two grid points in width.

From 185°E and further eastwards, the dividing latitude between the SEC and eastwards flows, further to the south, is 21°S. Flows south of 21°S, in the central South Pacific, are entirely eastwards and they do not form a closed gyre pattern with the EAC (see also Fig. 5.3). This flow field permits the 6.8 Sv surface inflow into the Pacific (Fig. 5.10), and is closely linked to the IT. Velocities at the southern tip of New Caledonia are strongly eastwards.

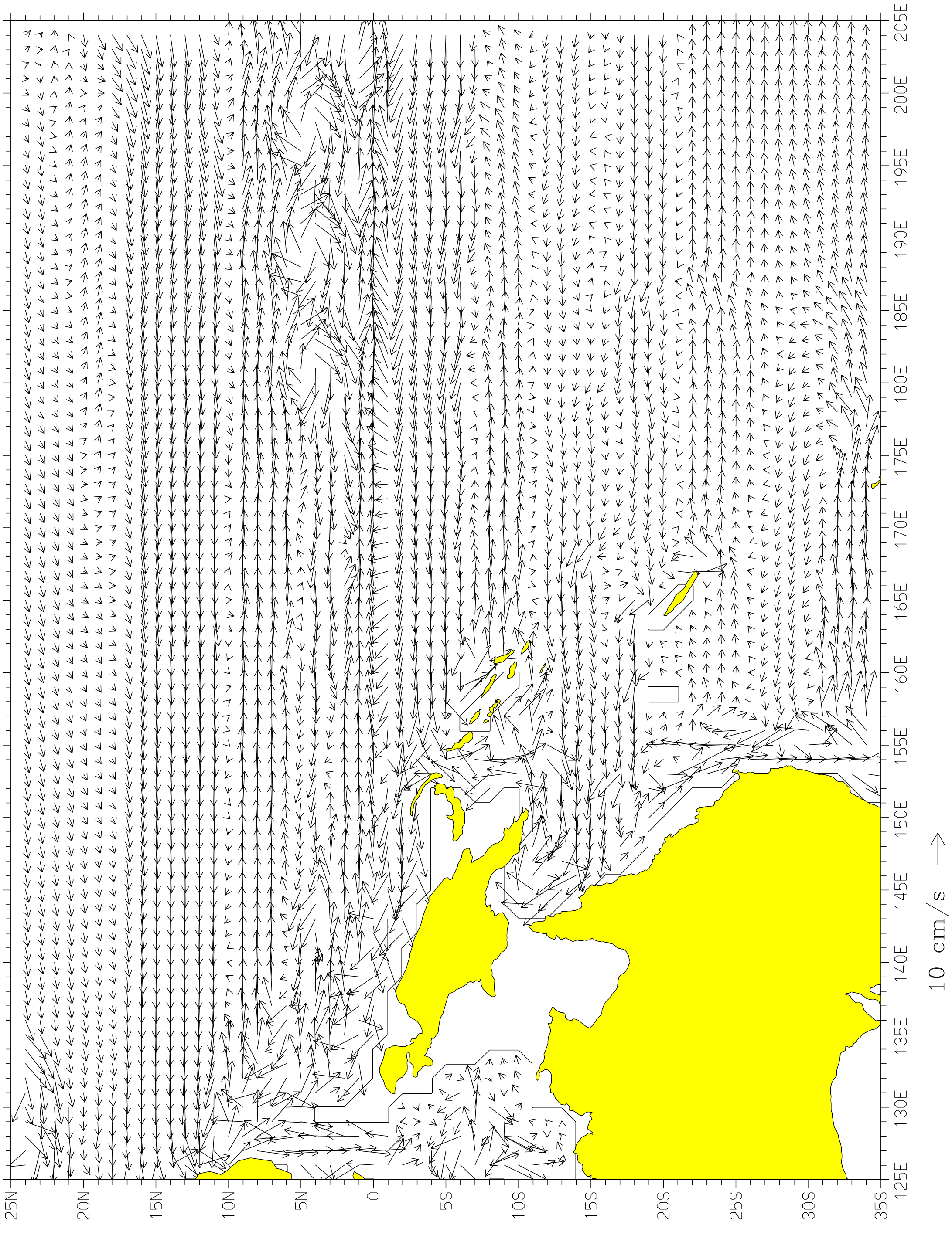

Figure 5.20: **a:** Velocities at $67.5\,m$ for the low latitude western Pacific, averaged over years seven and eight of the seasonally forced phase. Velocities are clamped to a maximum of $10\,cm\,s^{-1}$. Western boundary and equatorial currents are not in proportion.

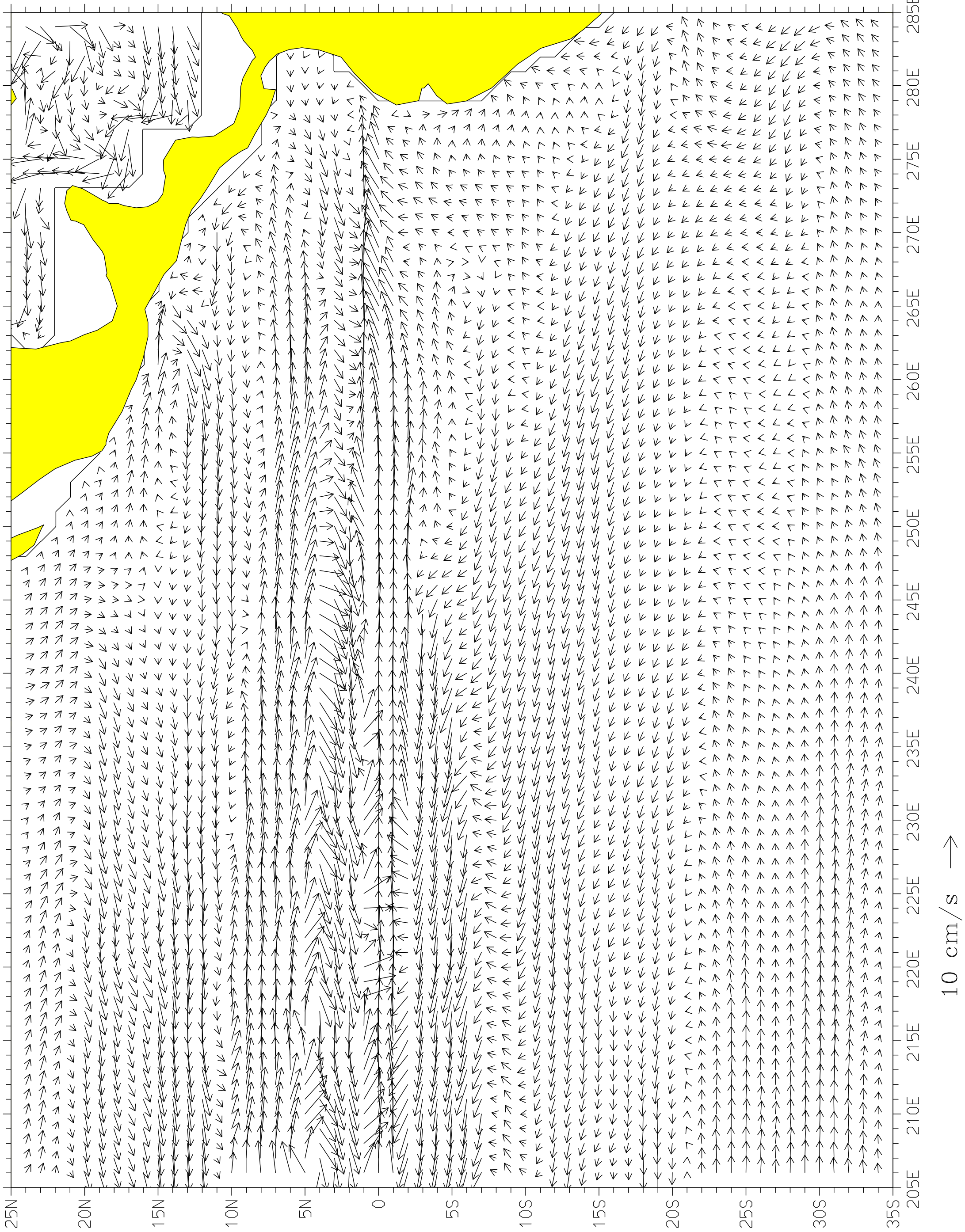

Figure 5.20b: Velocities at $67.5\,m$, eastern Pacific, clamped to $10\,cm\,s^{-1}$.

Fig. 5.21 shows velocities at $210.5\,m$ (level 6). The EUC is much stronger at this depth and is up to five grid points wide, about the equator. It can be traced from the north coast of Irian Jaya to 255°E. The SEC is still split into two branches but the bifurcation does not occur until it has reached 180°E. Flows at the southern tip of New Caledonia are westwards, and are supplied by the SEC. The SECC is not evident, but the NECC, which is only just distinct from the EUC, exists across the entire North Pacific,

Fig. 5.22 shows velocities at $1636.0\,m$ (level 12). There is strong residual wave activity (not eliminated by the two year average) in the eastern equatorial region and in areas around 15°N:215°E; the South Pacific is more sedate. There is generally a southwards flow along the Australia–PNG east coast. A strong westwards flow at 2°N bifurcates north of Irian Jaya, forming a southeastwards western boundary current along PNG's north coast. Here, mean flows above $1400\,m$ are westwards.

Fig. 5.23 shows the strong seasonal reversal (a and b, respectively) of the velocity field in the western equatorial Pacific, at $1636.0\,m$ (level 12). During summer (Fig. 5.23a) the flow along PNG's north coast is strongly to the east, and this current continues on to 175°E. It is supplied mostly by a westwards flow at 3°N, that retroflects on the north coast of Irian Jaya. During winter, a strong westwards equatorial current intercepts the northern Irian Jayan coast, and then retroflects mainly back into the open North Pacific, while a lesser amount continues towards the Philippines. The flow immediately north of New Ireland is weakly eastwards but, in reality, this may well be dependent on the local bathymetry.

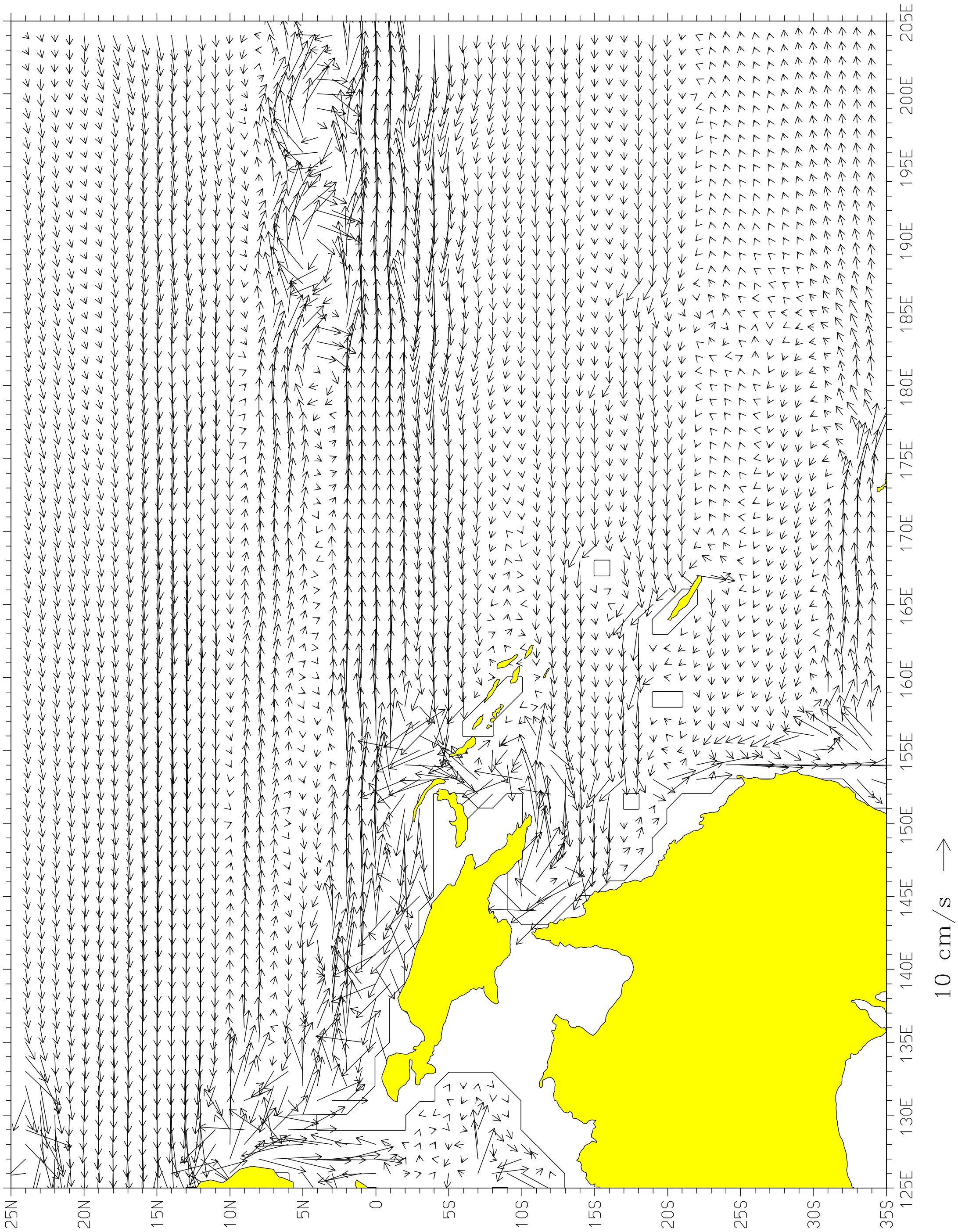

Figure 5.21: **a:** Average velocities at 210.5 m for the low latitude western Pacific. Clamped to a maximum of 15 $cm\, s^{-1}$.

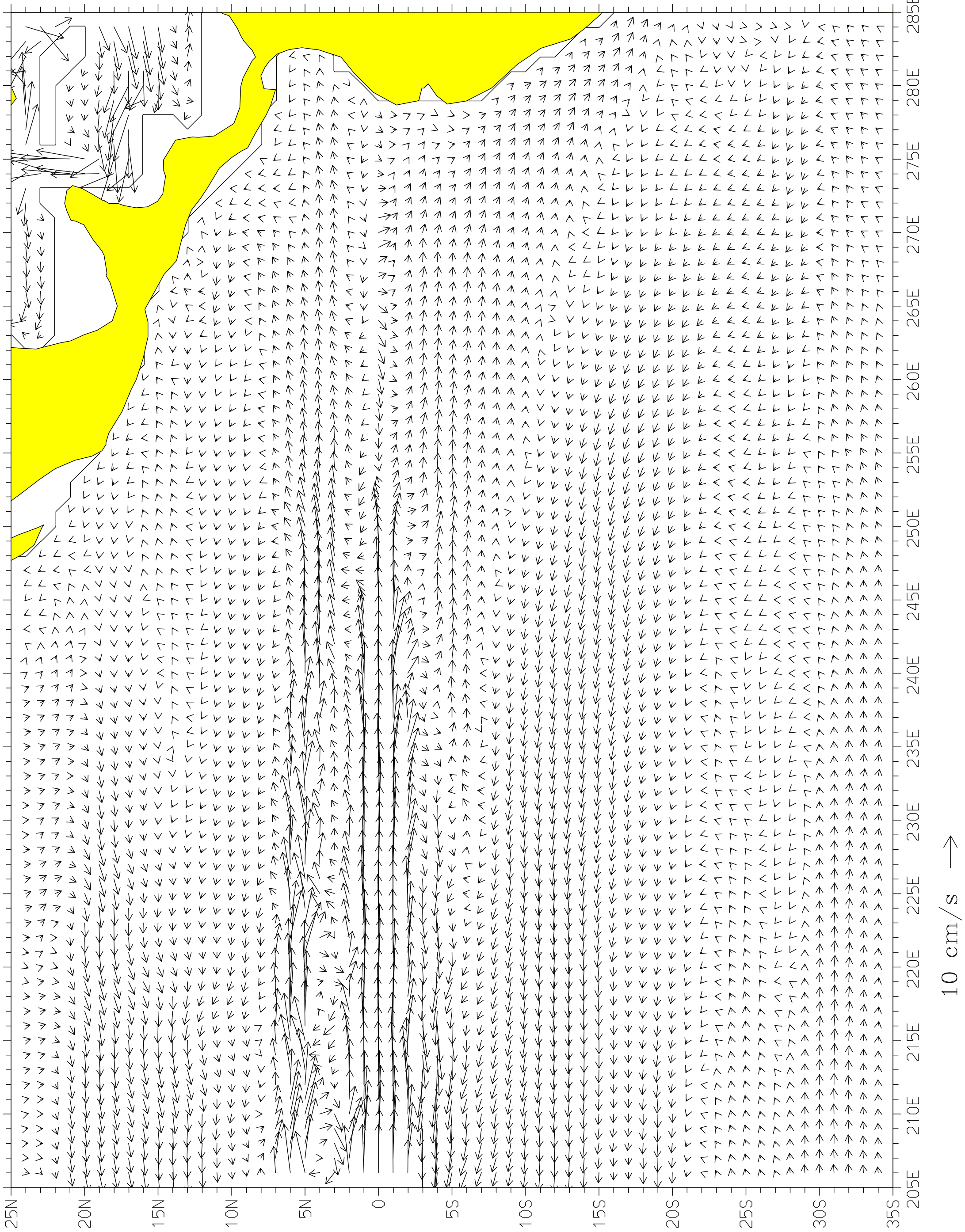

Figure 5.21b: Velocities at $210.5\,m$, eastern Pacific, clamped to $15\,cm\,s^{-1}$.

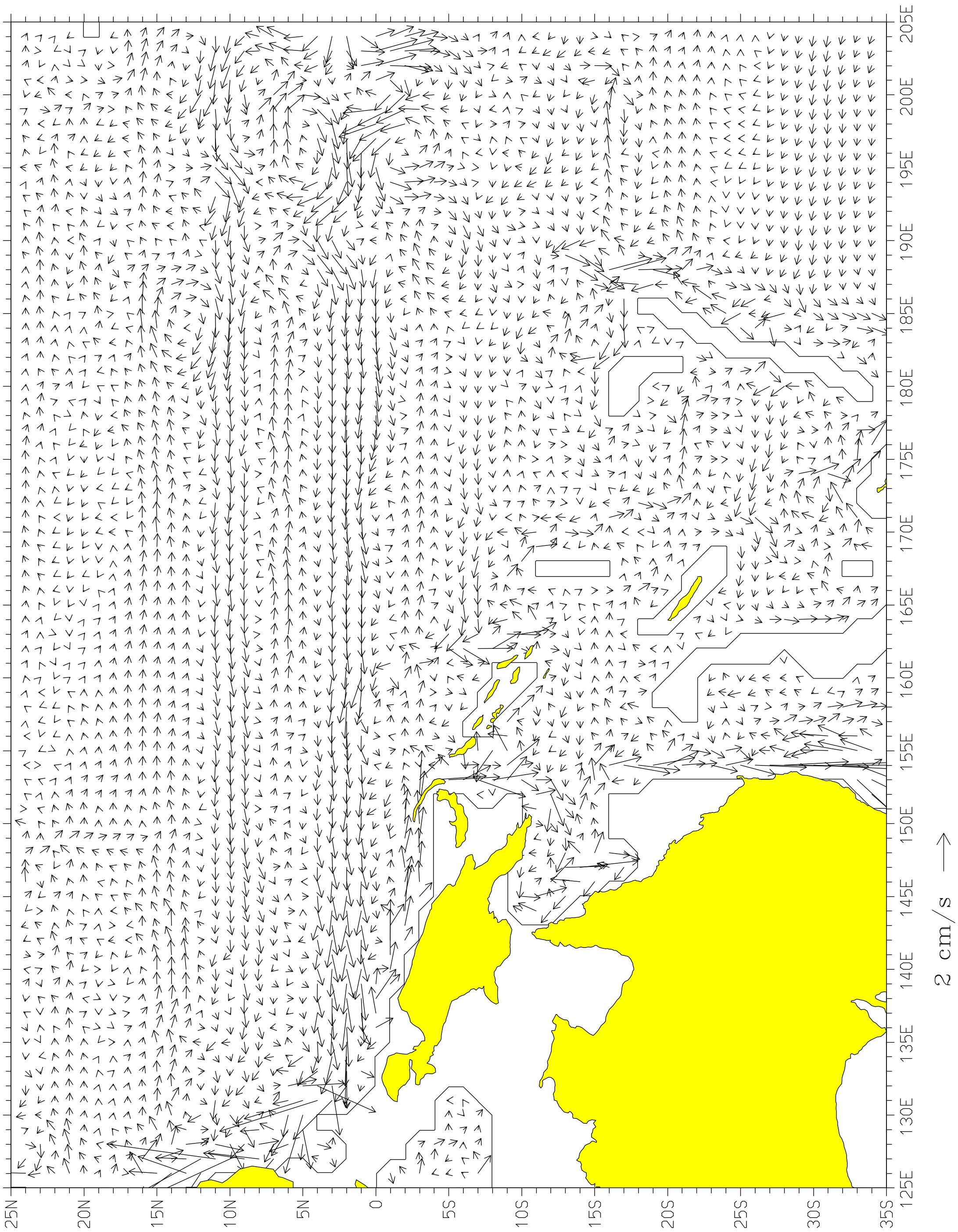

Figure 5.22: **a:** Average velocities at 1636.0 m for the low latitude western Pacific.

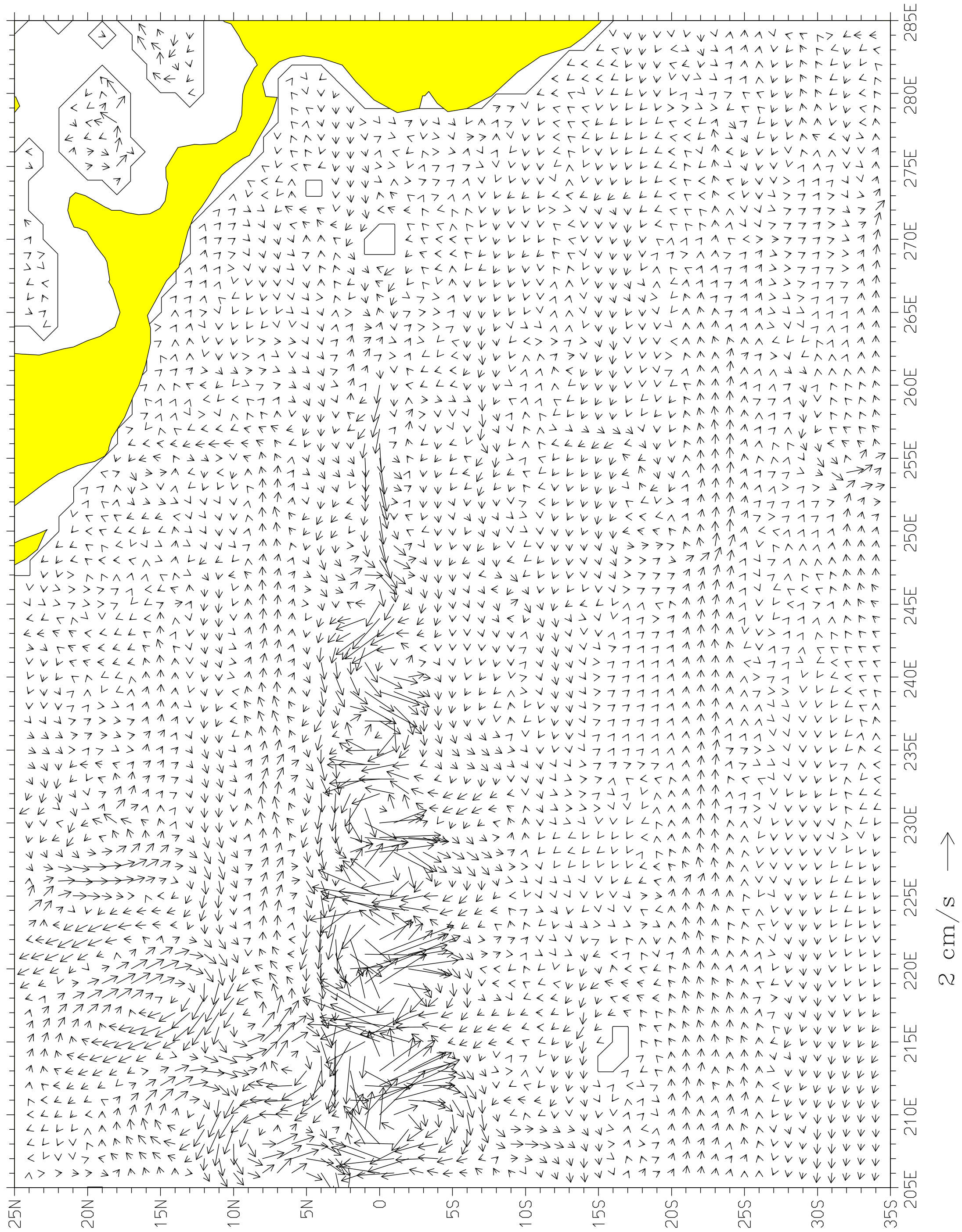

Figure 5.22b: Velocities at $1636.0\,m$, eastern Pacific.

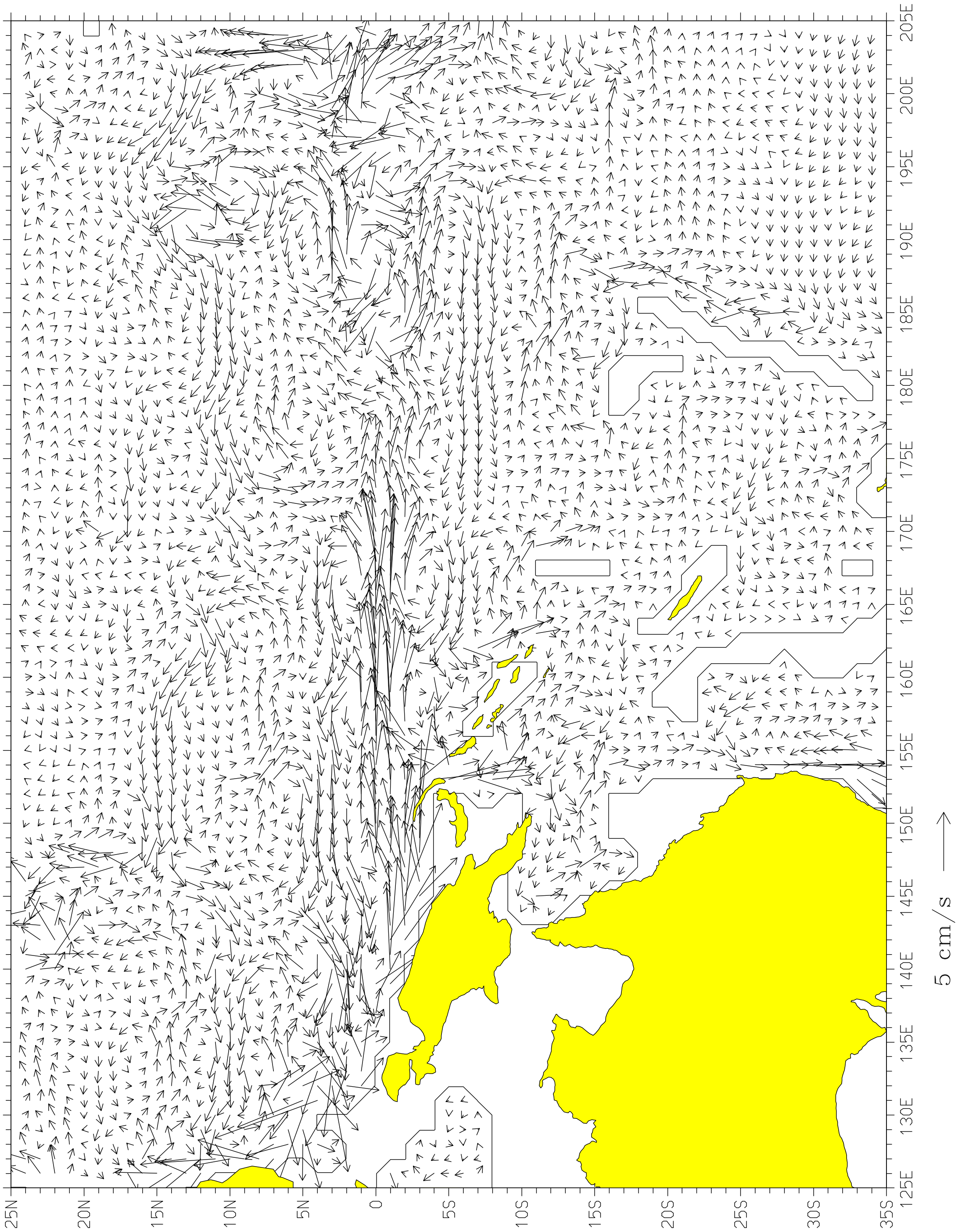

Figure 5.23: **a:** Velocities at 1636.0 m, western Pacific for January-8. There is a strong *eastwards* flow, along PNG's north coast, that then follows the equator to about 180°E.

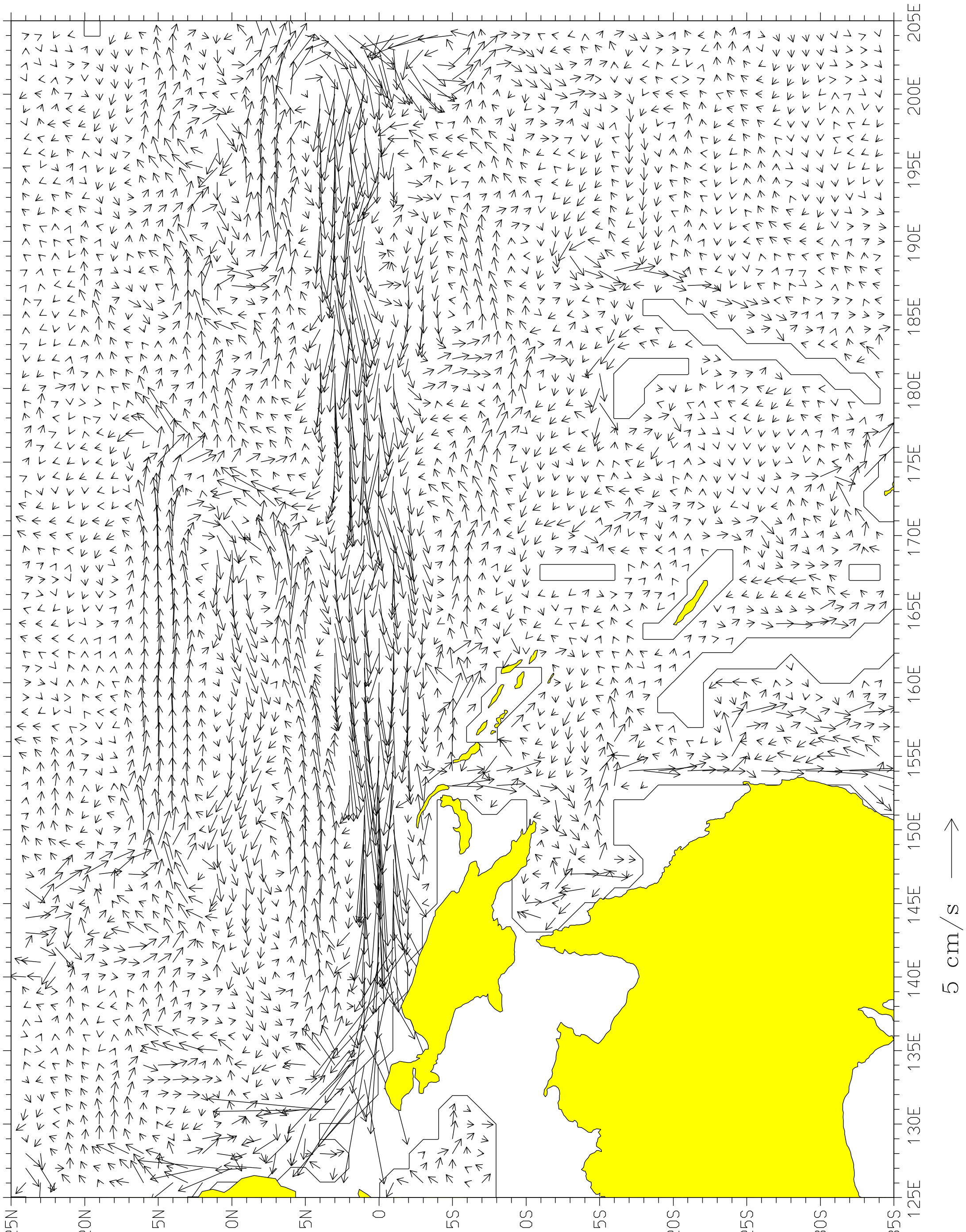

Figure 5.23b: Velocities at $1636.0\,m$, western Pacific for July-8. There is a strong *westwards* flow, along PNG's north coast, that originates from 3°N:200°E. Flows further to the east are more incoherent (cf. Fig. 5.22b).

5.3.1 Low Latitude Pacific Zonal Isotachs

This section presents a series of contour plots of the seasonal zonal component isotachs for the low latitude Pacific, and complements the previous section.

Figs. 5.24a to 5.24f show the seasonal variation of low latitude zonal component isotachs, at 170°E, over the depth range 0–641 m (levels 1–9). Fig. 5.24g shows the average for years seven and eight of the seasonally forced phase. The equatorial currents and countercurrents are labelled in the figures, except for the northern branch of the SEC (2–6°S) and its northern hemisphere counterpart (2–5°N). In the text of this section, they will temporarily be referred to as the SECb and NECb, respectively. The SECb and NECb are permanent features, at this longitude, and both currents separate the SECC and NECC from the EUC, respectively. Both the SEC and SECb are a little stronger in the austral winter but the overall seasonal variation, in strength and latitudinal position, is not large. The SECC is also reasonably constant. It is strong in March-8 and weak in May-8, but this is more a reflection of higher frequency wave activity than a true seasonal variation. The NEC and NECC do have a more noticeable variation, being stronger in the boreal winter. The NECC is apparently absent in July-8, but again this is due to higher frequency wave activity.

The EUC has a distinct seasonal variation, in the strength and depth of its V-max core. The trend is for it to be deeper and weaker during the austral summer, and shallower and stronger during winter. In January-8, the core is 31 $cm\,s^{-1}$ at a depth of 210 m, and in July-8 it is 84 $cm\,s^{-1}$ at 100 m. While some of this variation may be due directly to equatorial dynamics, the EUC is closely linked to the NGCU and is very likely to be influenced by seasonal variations in the South Pacific (§3.7).

Figs. 5.25a to 5.25f show the same seasonal isotachs as Figs. 5.24a to 5.24f, but over the depth range 0–3932.5 m (levels 1 to 16). For clarity, all magnitudes are clamped to 20 $cm\,s^{-1}$. Fig. 5.25g shows isotachs for the average of years seven and eight of the seasonally forced phase. The most noticeable seasonal variation for deep waters occurs directly beneath the EUC. From 700 m down to about 2500 m, the seasonal trend is for strong eastward flows during the austral summer and strong westward flows during winter. The 1636 m velocity fields are shown in Figs. 5.23a and 5.23b. The annually–averaged (years seven and

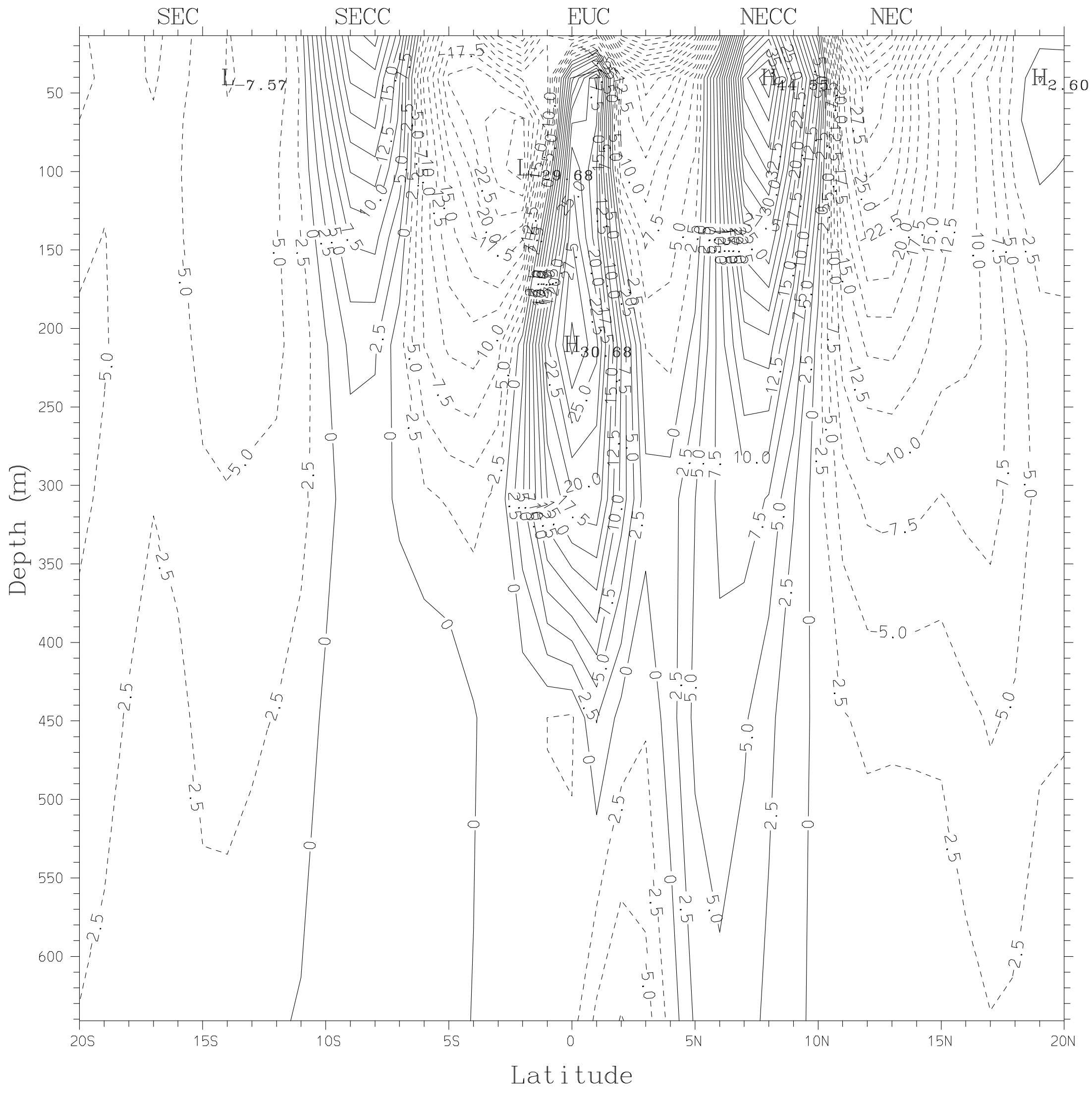

Figure 5.24: **a:** Zonal component isotachs ($cm\,s^{-1}$) at 170°E, January-8. Depth range is 0–641 m, levels 1–9. CI is 2.5 $cm\,s^{-1}$. EUC core is 31 $cm\,s^{-1}$ at 210 m.

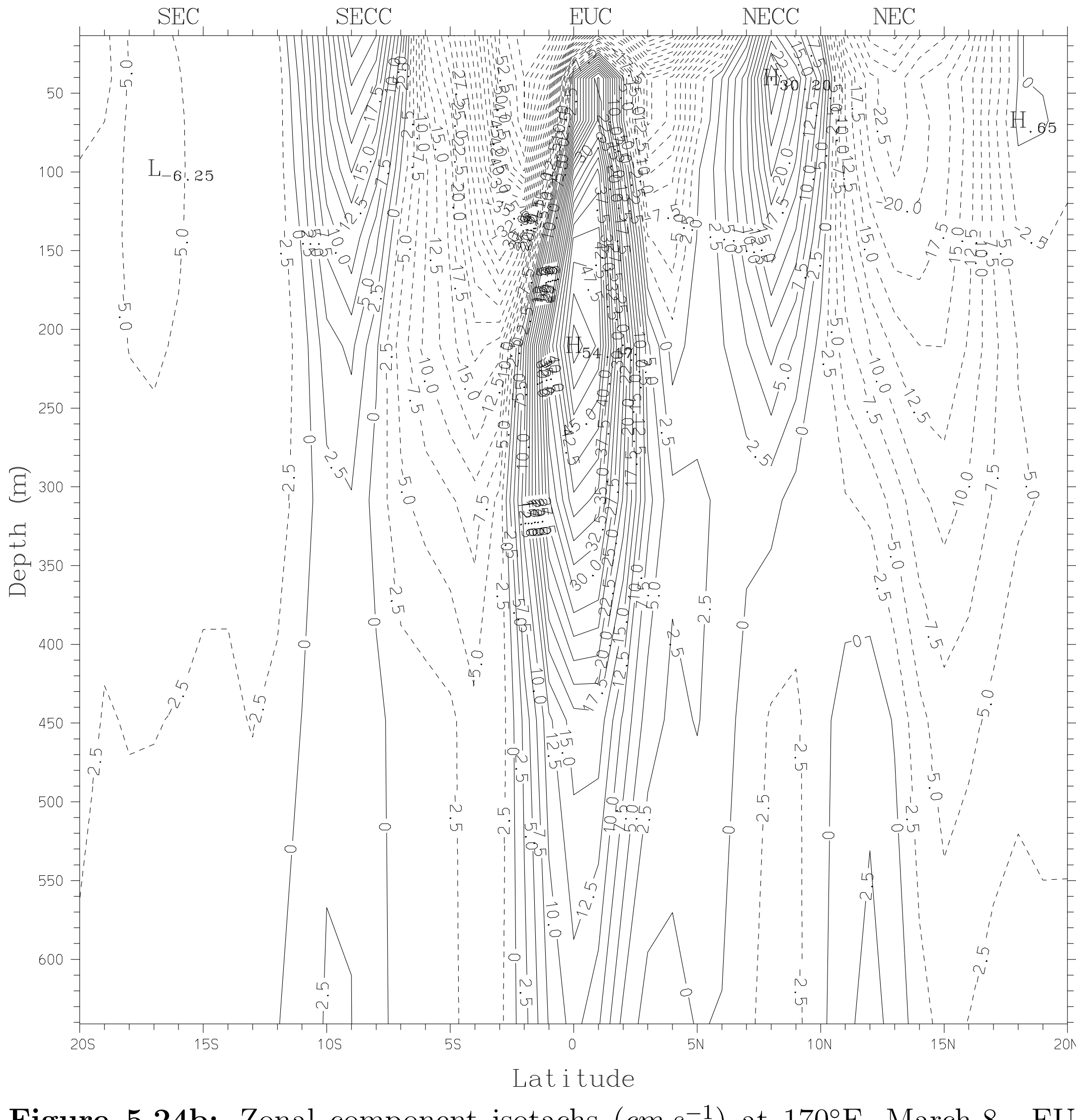

Figure 5.24b: Zonal component isotachs ($cm\,s^{-1}$) at 170°E, March-8. EUC core is $54\,cm\,s^{-1}$ at $210\,m$.

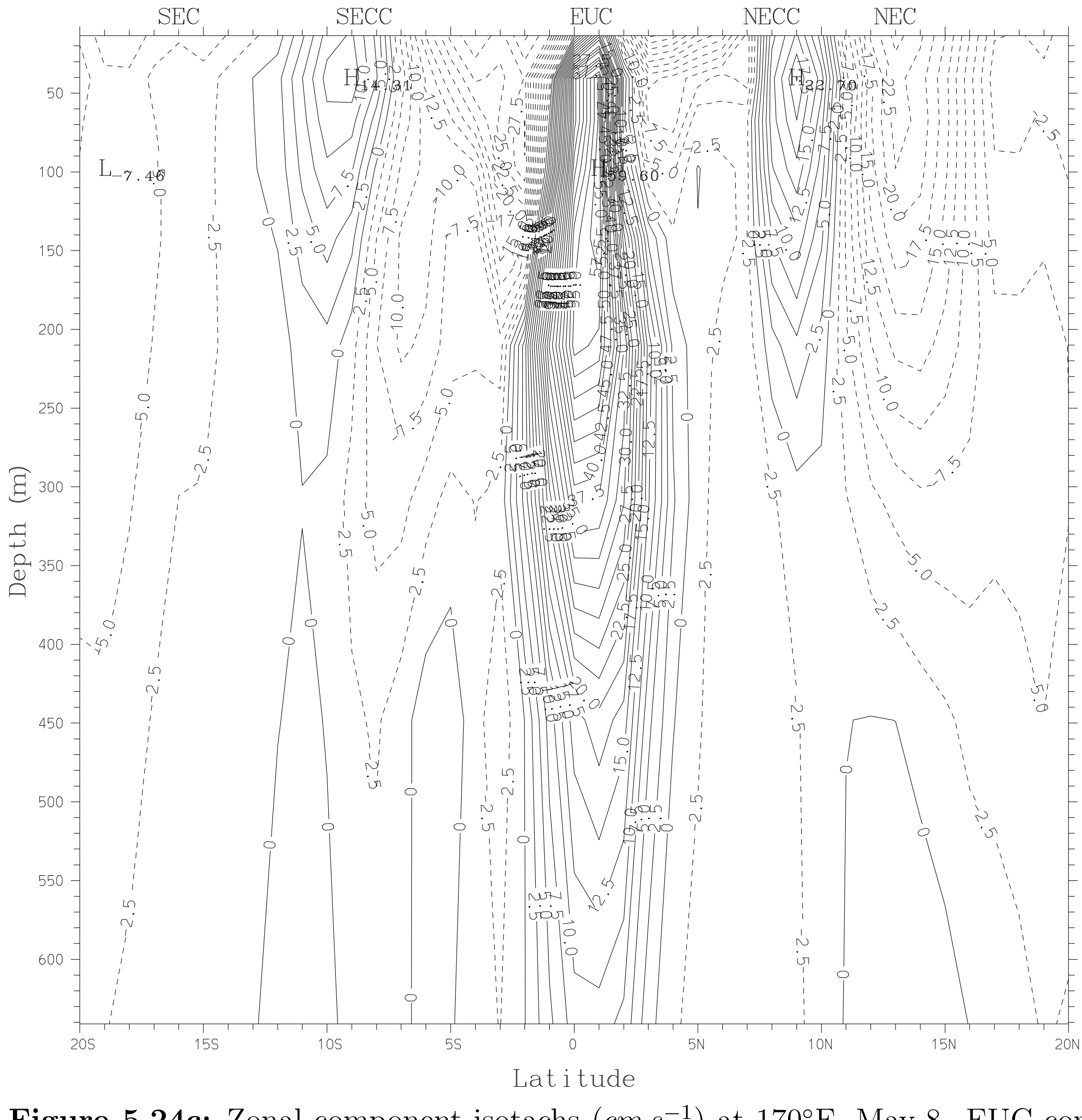

Figure 5.24c: Zonal component isotachs ($cm\,s^{-1}$) at 170°E, May-8. EUC core is $59\,cm\,s^{-1}$ at $180\,m$.

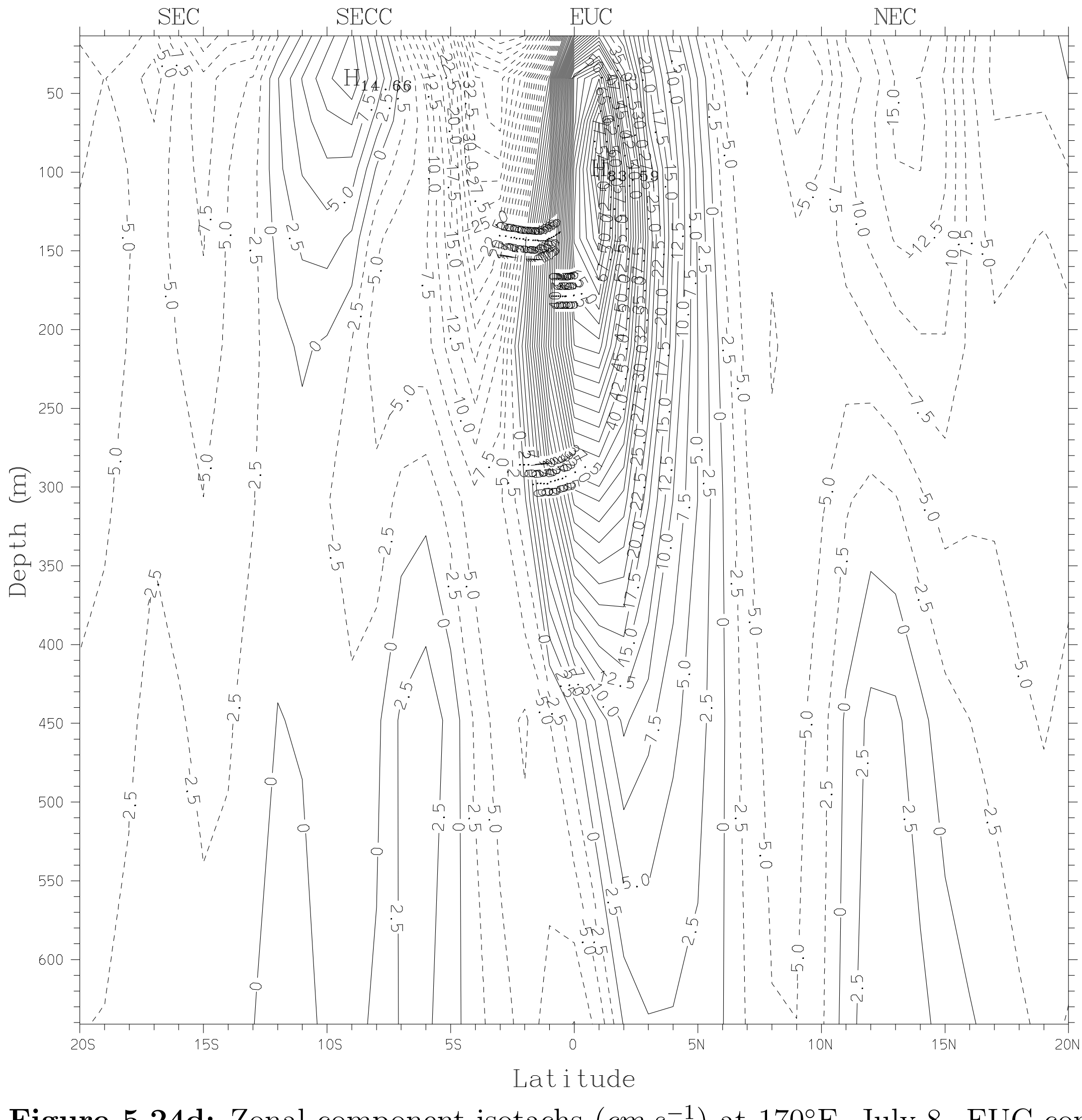

Figure 5.24d: Zonal component isotachs ($cm\,s^{-1}$) at 170°E, July-8. EUC core is $84\,cm\,s^{-1}$ at $100\,m$. The NECC is either not present or is not distinct from the EUC.

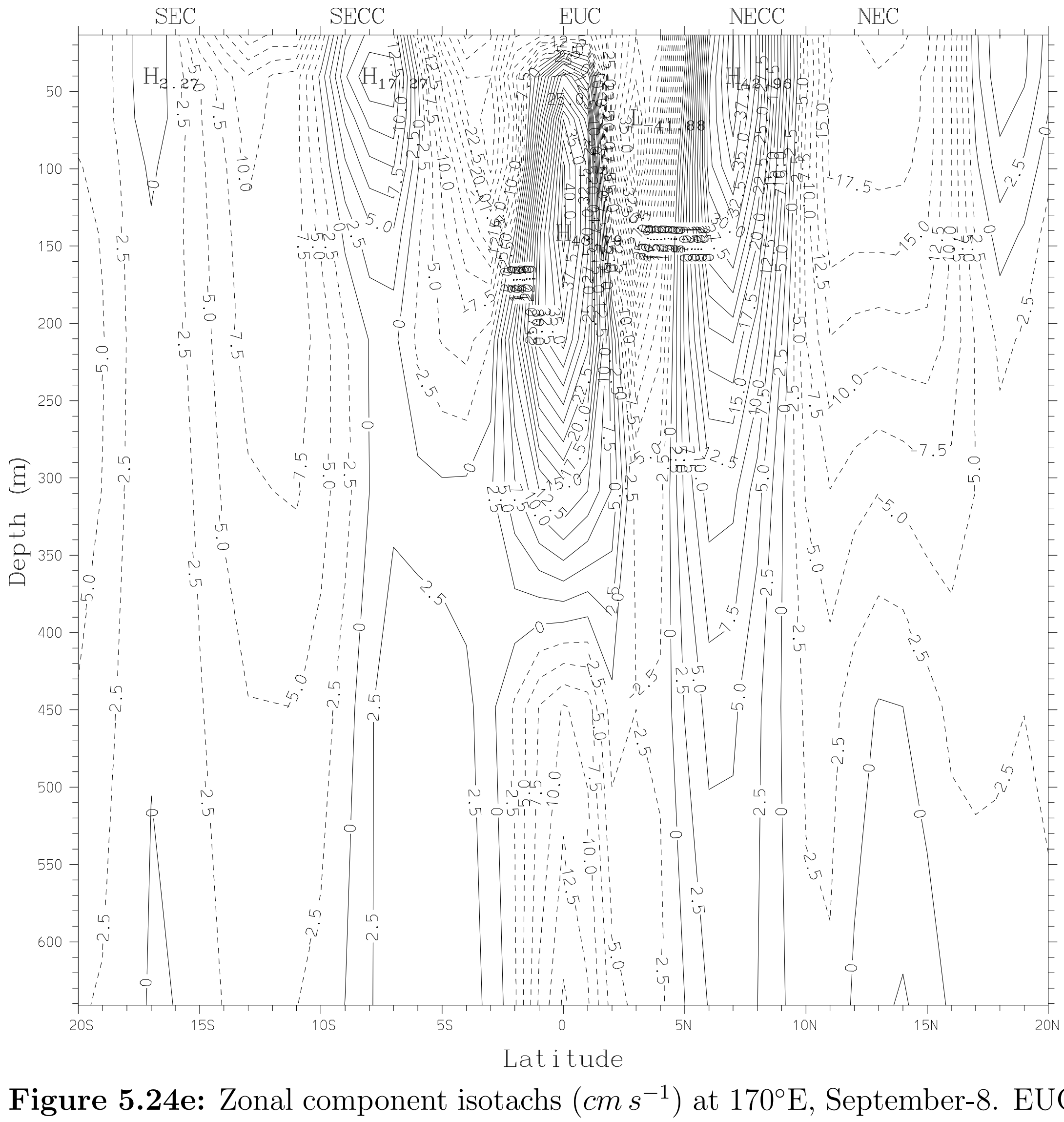

Figure 5.24e: Zonal component isotachs ($cm\,s^{-1}$) at 170°E, September-8. EUC core is $43\,cm\,s^{-1}$ at $140\,m$.

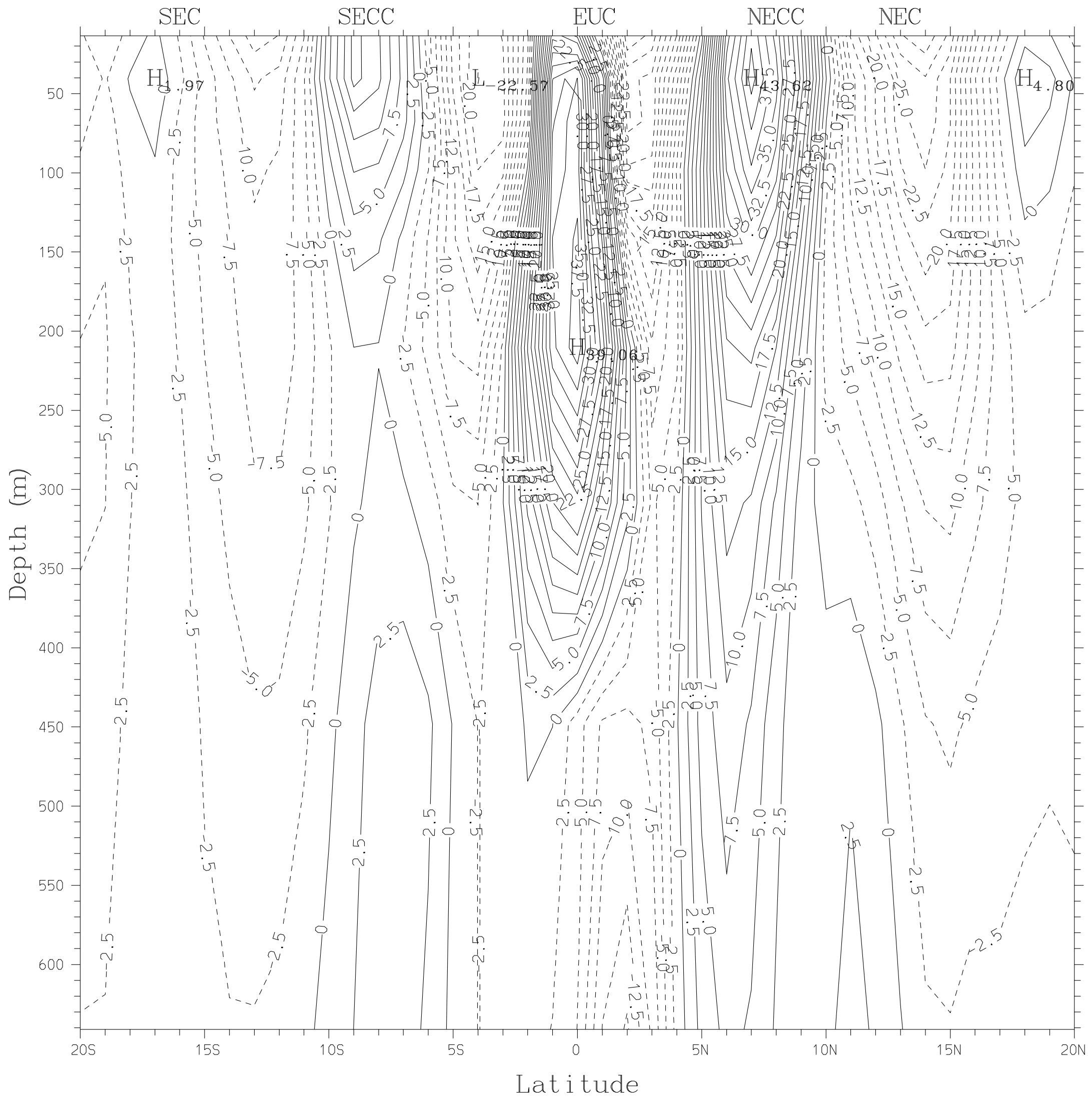

Figure 5.24f: Zonal component isotachs ($cm\,s^{-1}$) at 170°E, November-8. EUC core is $39\,cm\,s^{-1}$ at $210\,m$.

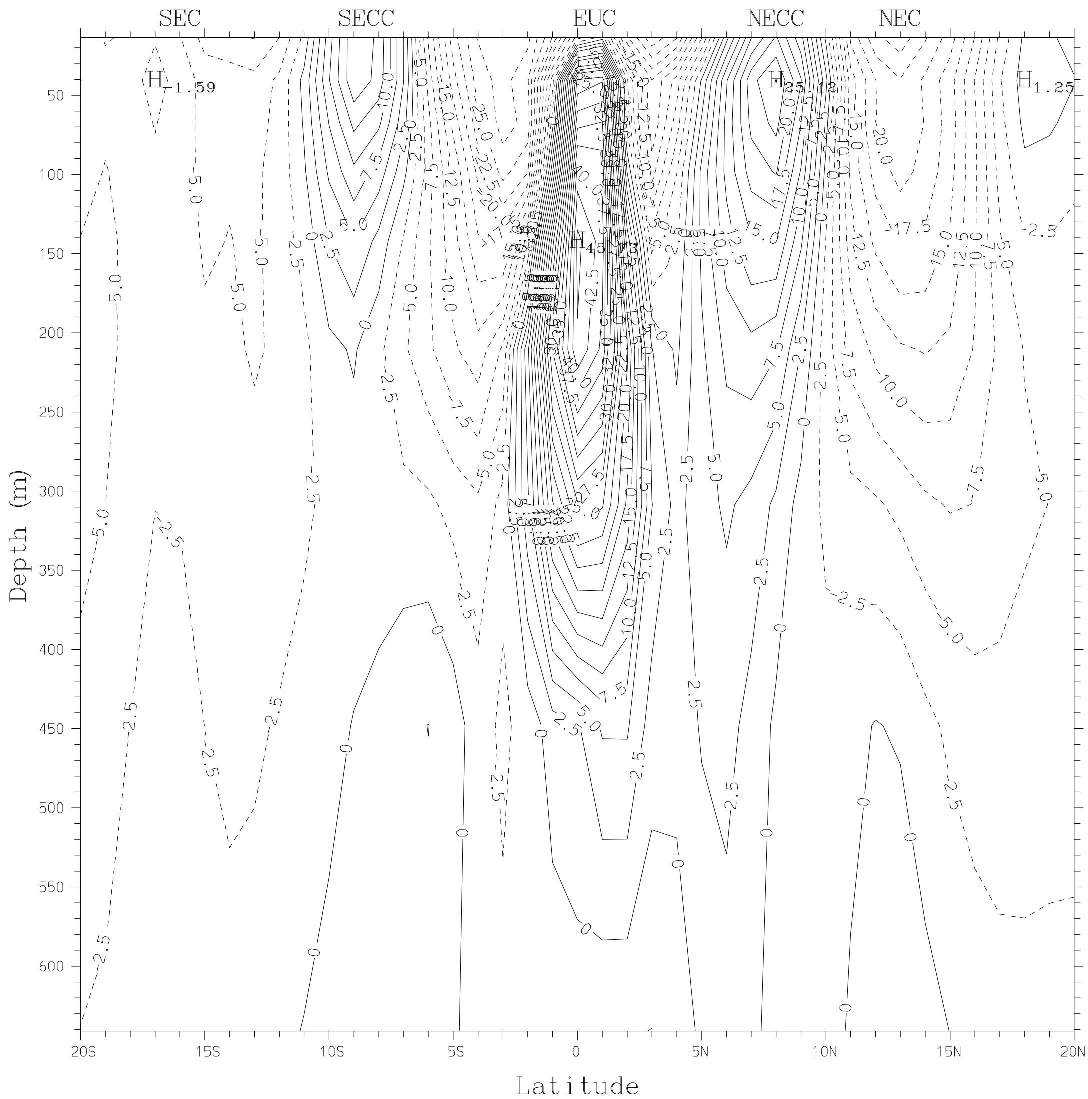

Figure 5.24g: Zonal component isotachs ($cm\,s^{-1}$) at 170°E, averaged over years seven and eight. EUC core is $46\,cm\,s^{-1}$ at $150\,m$.

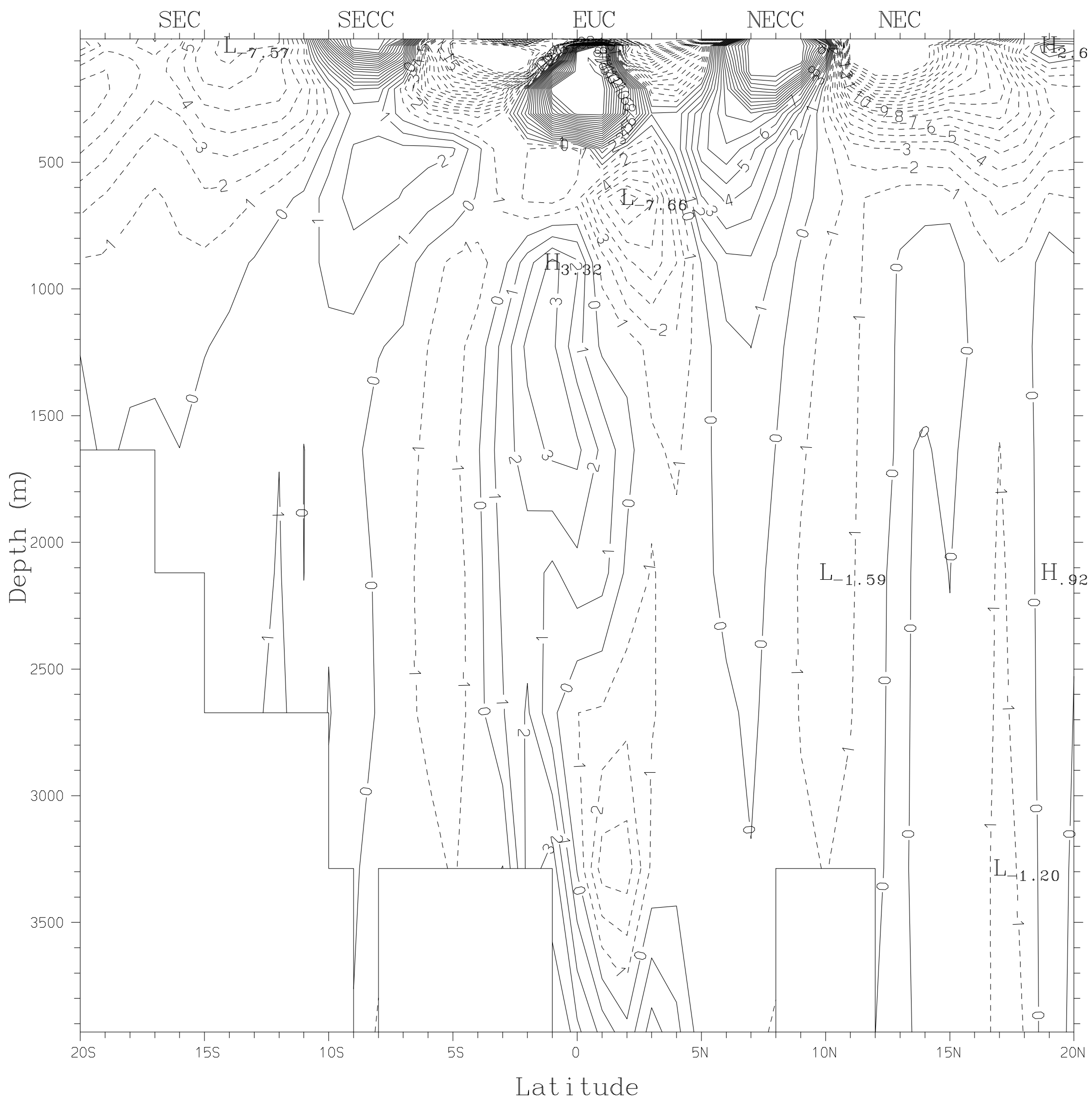

Figure 5.25: **a:** Zonal component isotachs ($cm\,s^{-1}$) at 170°E, January-8. Depth range is 0–3932.5 m, levels 1–16. CI is $1\,cm\,s^{-1}$. Clamped to $\pm 20\,cm\,s^{-1}$.

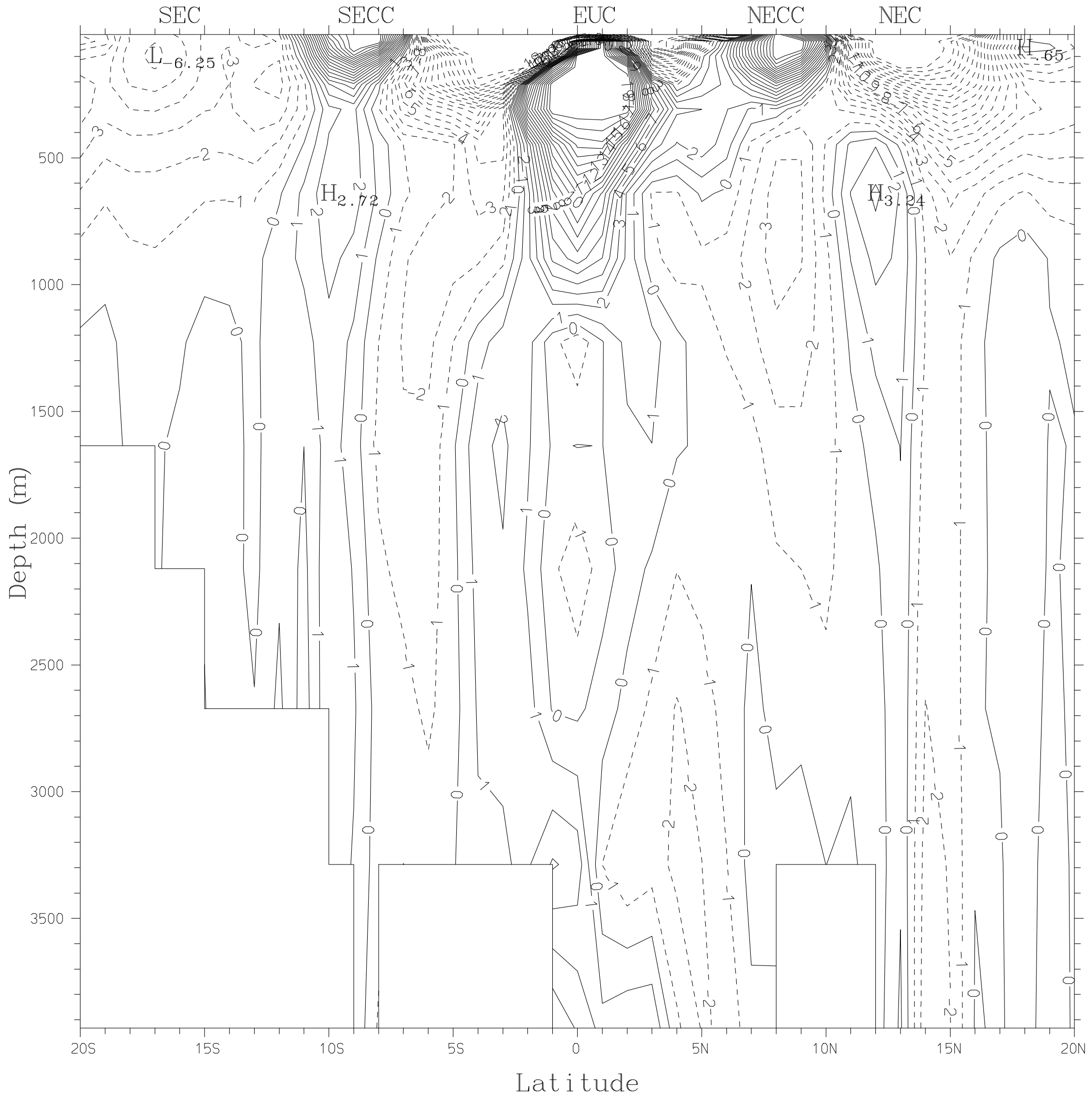

Figure 5.25b: Zonal component isotachs ($cm\, s^{-1}$) at 170°E, March-8. Clamped to $\pm 20\, cm\, s^{-1}$.

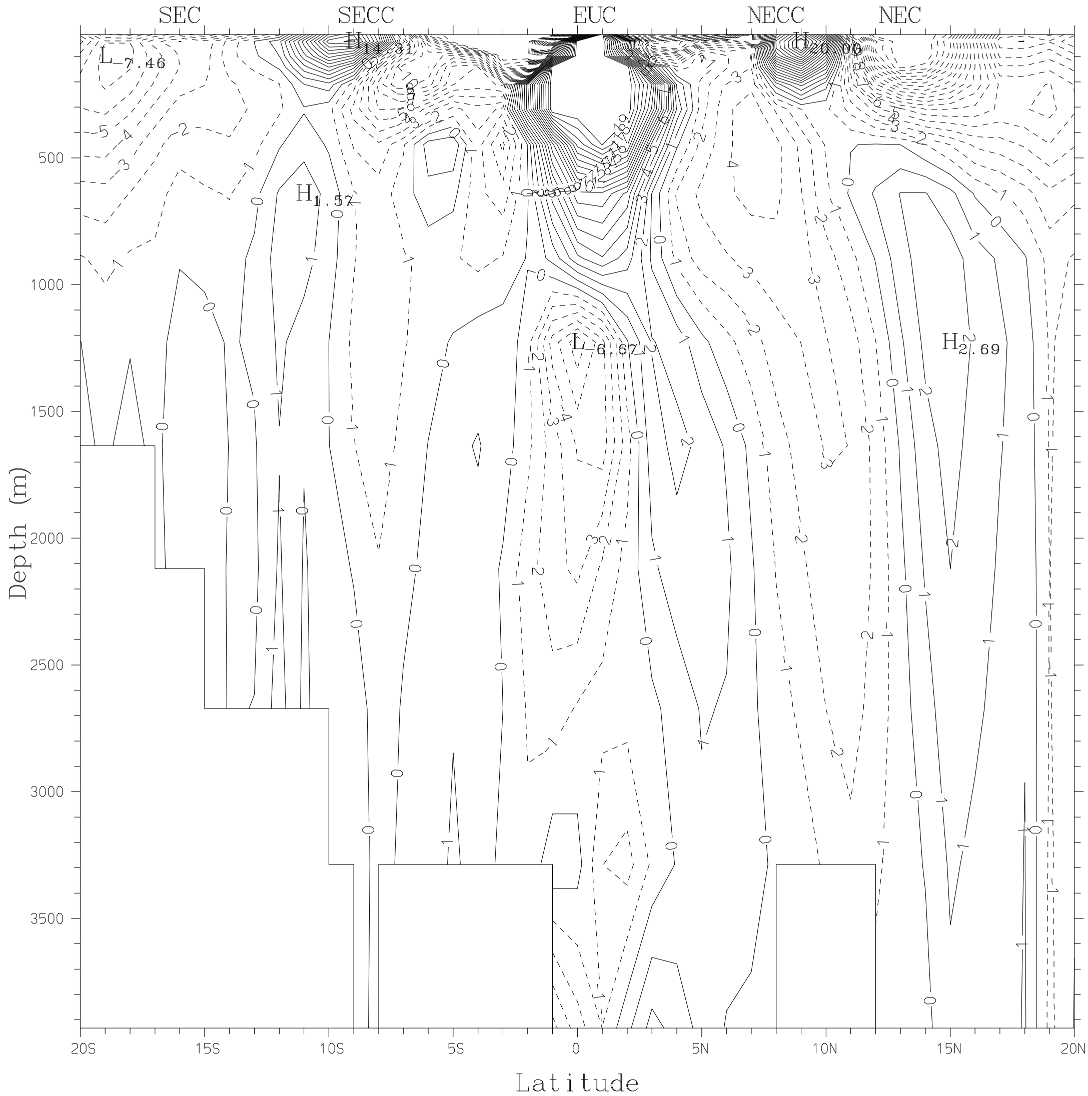

Figure 5.25c: Zonal component isotachs ($cm\,s^{-1}$) at 170°E, May-8. Clamped to $\pm 20\,cm\,s^{-1}$.

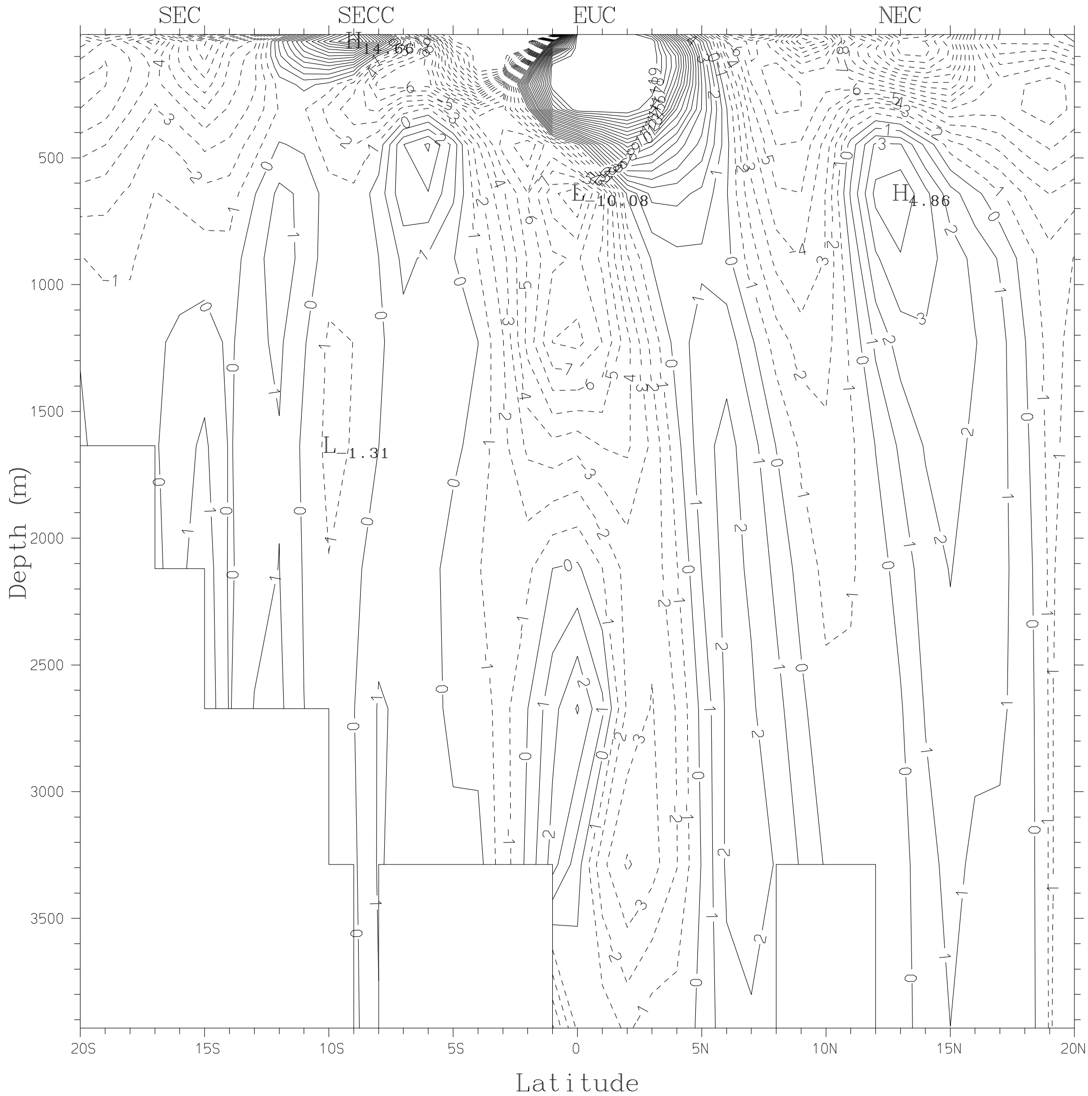

Figure 5.25d: Zonal component isotachs ($cm\,s^{-1}$) at 170°E, July-8. Clamped to $\pm 20\,cm\,s^{-1}$.

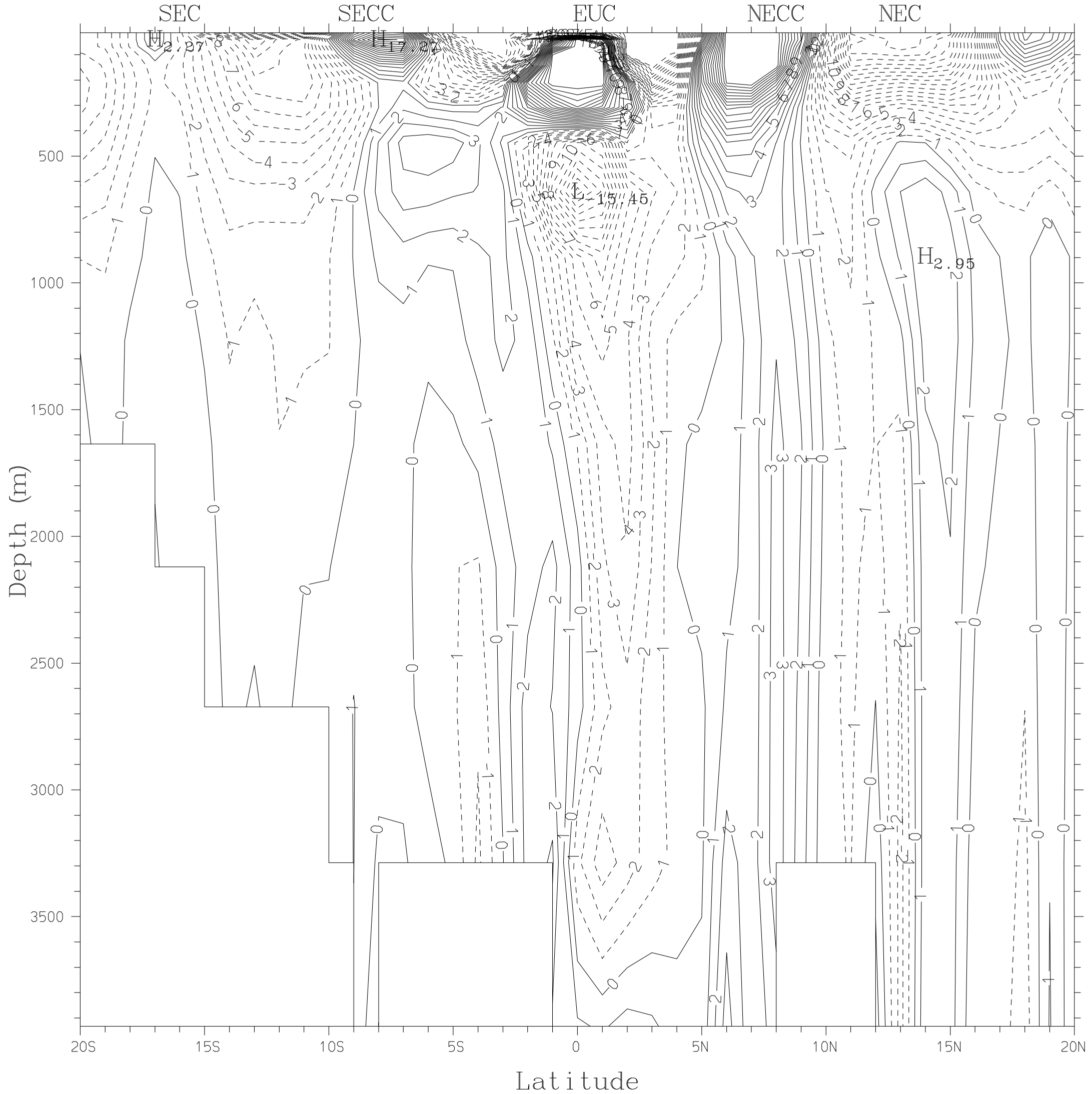

Figure 5.25e: Zonal component isotachs ($cm\,s^{-1}$) at 170°E, September-8. Clamped to $\pm 20\,cm\,s^{-1}$.

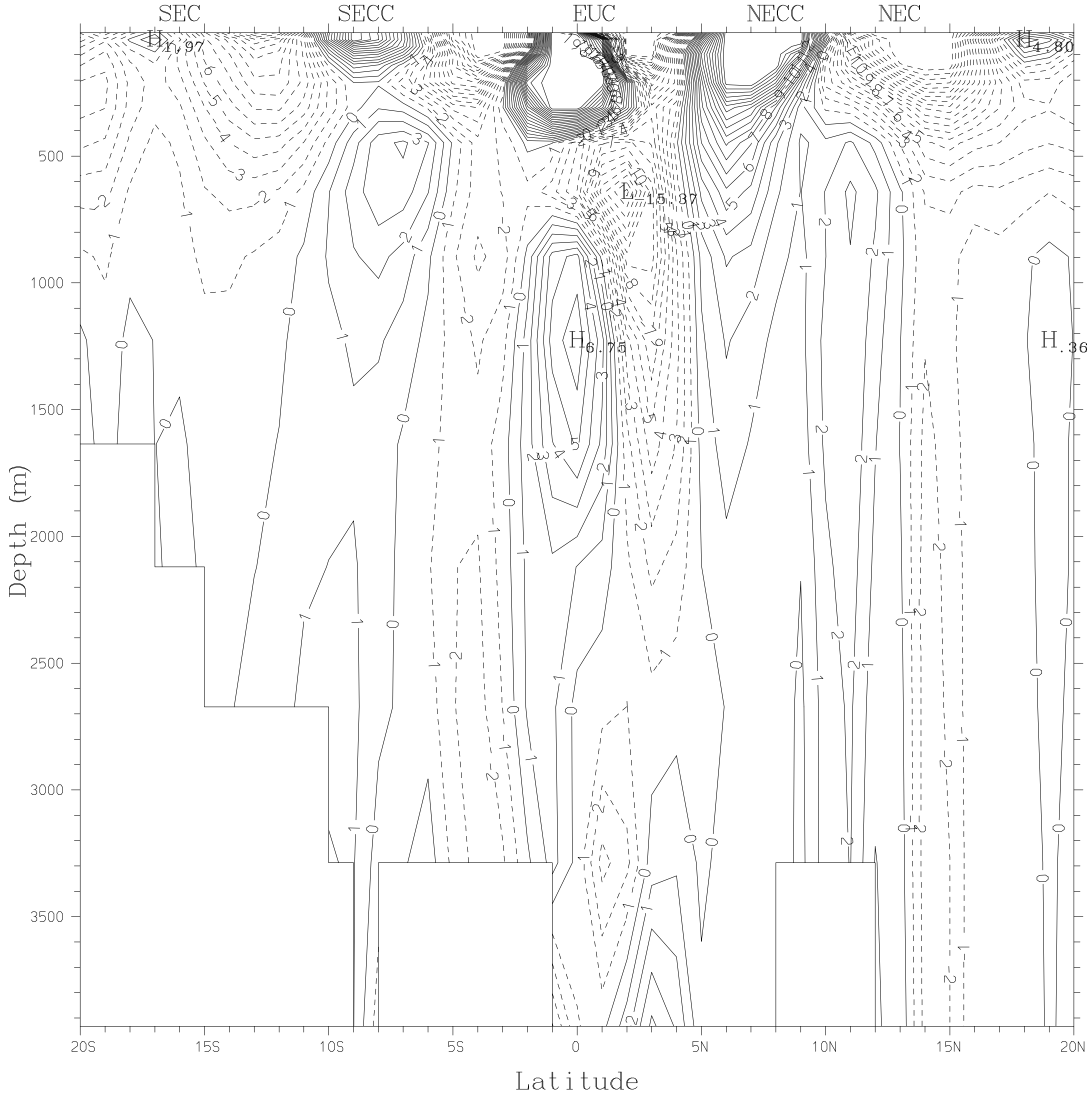

Figure 5.25f: Zonal component isotachs ($cm\,s^{-1}$) at 170°E, November-8. Clamped to $\pm 20\,cm\,s^{-1}$.

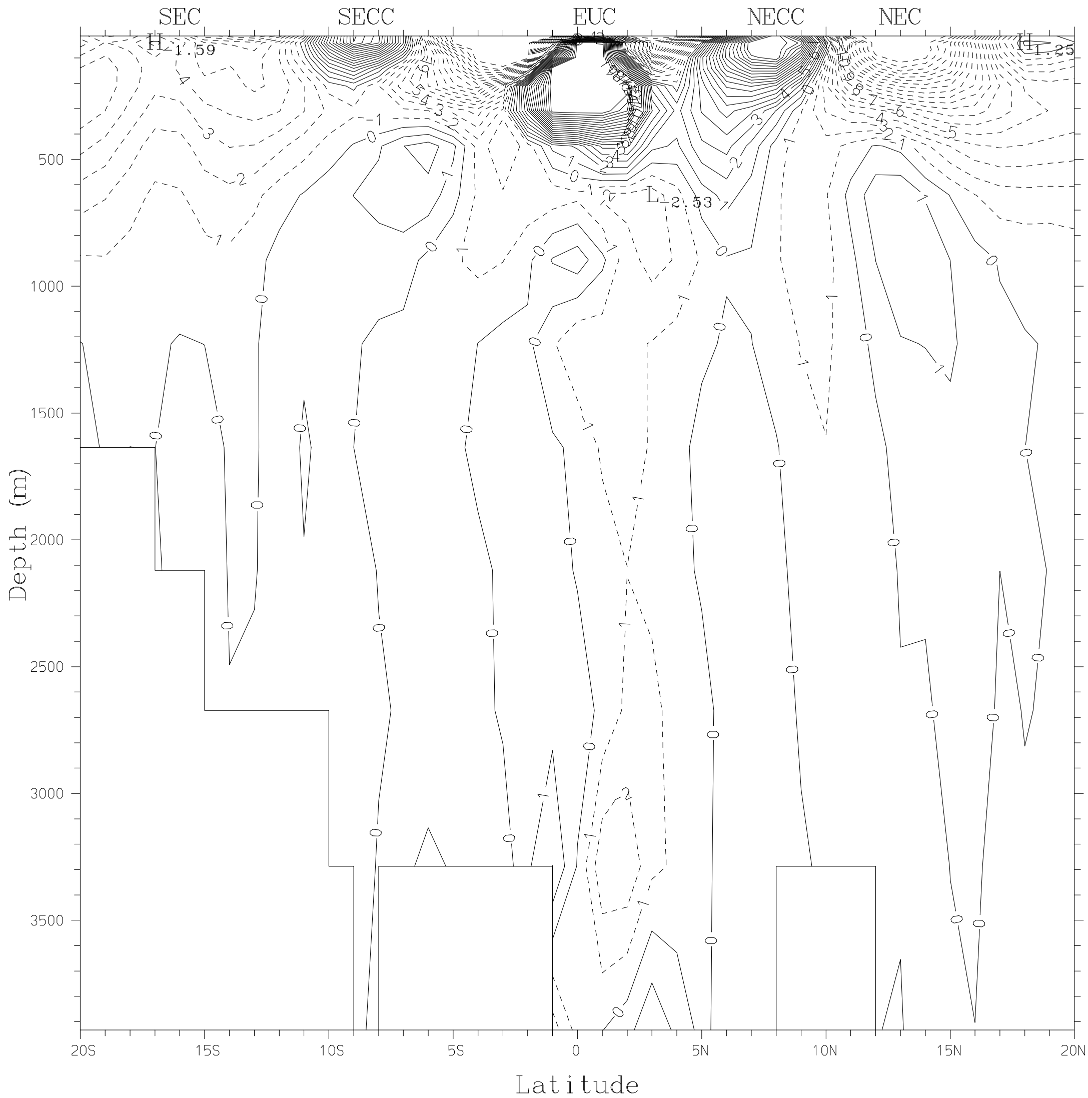

Figure 5.25g: Zonal component isotachs ($cm\,s^{-1}$) at 170°E, averaged over years seven and eight. Depth range is 0–3932.5 m, levels 1–16. CI is 1 $cm\,s^{-1}$. Clamped to $\pm 20\,cm\,s^{-1}$.

eight) deep isotachs in Fig. 5.25g are a good deal smaller than the instantaneous seasonal isotachs, demonstrating the rapid variability of equatorial flows.

5.4 Overturning and Tracer Transports

This section presents overturning stream functions and the global meridional tracer transports. This results can be used to gauge the effects of the vertical tracer diffusity scheme (§2.2). The definitions of these quantities appear in Appendix B, although the accompanying discussions are beyond the scope of this short section and the reader is referred to Cummins *et al.* (1990) and Weaver & Sarachik (1990), as examples.

Fig. 5.26 shows the global overturning stream function, averaged over years seven and eight. The function is defined so that an advected particle has the more negative isopleth on its left hand side. The most intense cell is centred at 45°S, being $200\,m$ deep. This is now known as the Deacon Cell (England, 1992), and is considered to be the result of the northwards Ekman drift of cold polar waters, which then subduct below warmer midlatitude waters. The interpretation of overturning stream functions is a subject of debate, and unambiguous conclusions cannot be made (e.g., Killworth, 1992). The $+11.32\,Sv$ cell at 40°N is due to subduction in the North Atlantic. There is a $-17.15\,Sv$ cell at the equator ($3700\,m$ deep), and Weaver & Sarachik (1990) argue that such an equatorial cell can be the result of a purely computational mode, if the vertical diffusivity coefficient is not sufficiently large (grid Peclet and Reynolds numbers > 2). This cell is very intense ($-65\,Sv$) during the diagnostic phase but decays to about $-10\,Sv$ during the free–thermocline run. At the end of seasonal forcing it has intensified to $-17\,Sv$. The grid Peclet number limit can be exceeded in the instantaneous fields, in a few locations, but not in the time averaged fields. Semtner & Chervin (1992) also obtain this cell, using a different vertical diffusivity scheme. In fact, Fig. 5.26 is barely different from their Fig. 9c, except for the depth scaling. A weak cell of $-1.7\,Sv$ at the southern wall produces Antarctic Bottom Water.

Fig. 5.27 shows the Pacific–Indian overturning stream function, averaged over years seven and eight. Differences from Semtner & Chervin's results are a little larger than for the global results, but are still not sufficiently different to give any clear indication as to whether or not the present vertical mixing scheme is

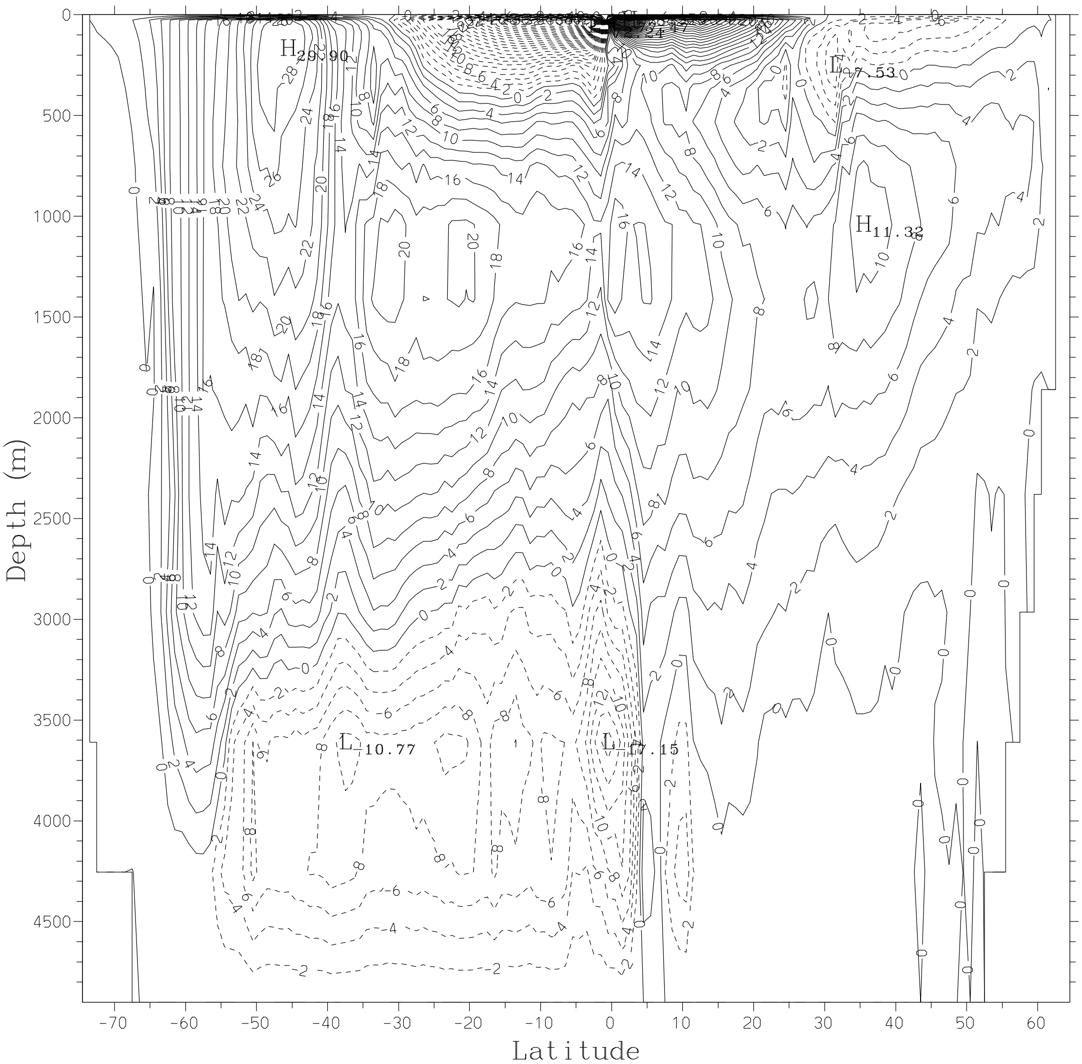

Figure 5.26: **:** Global meridional overturning stream function (Sv), averaged over years seven and eight of the seasonally forced phase. CI is $2\,Sv$. An advected particle has the more negative stream function on its left hand side. Antarctic Bottom Water production is $1.7\,Sv$.

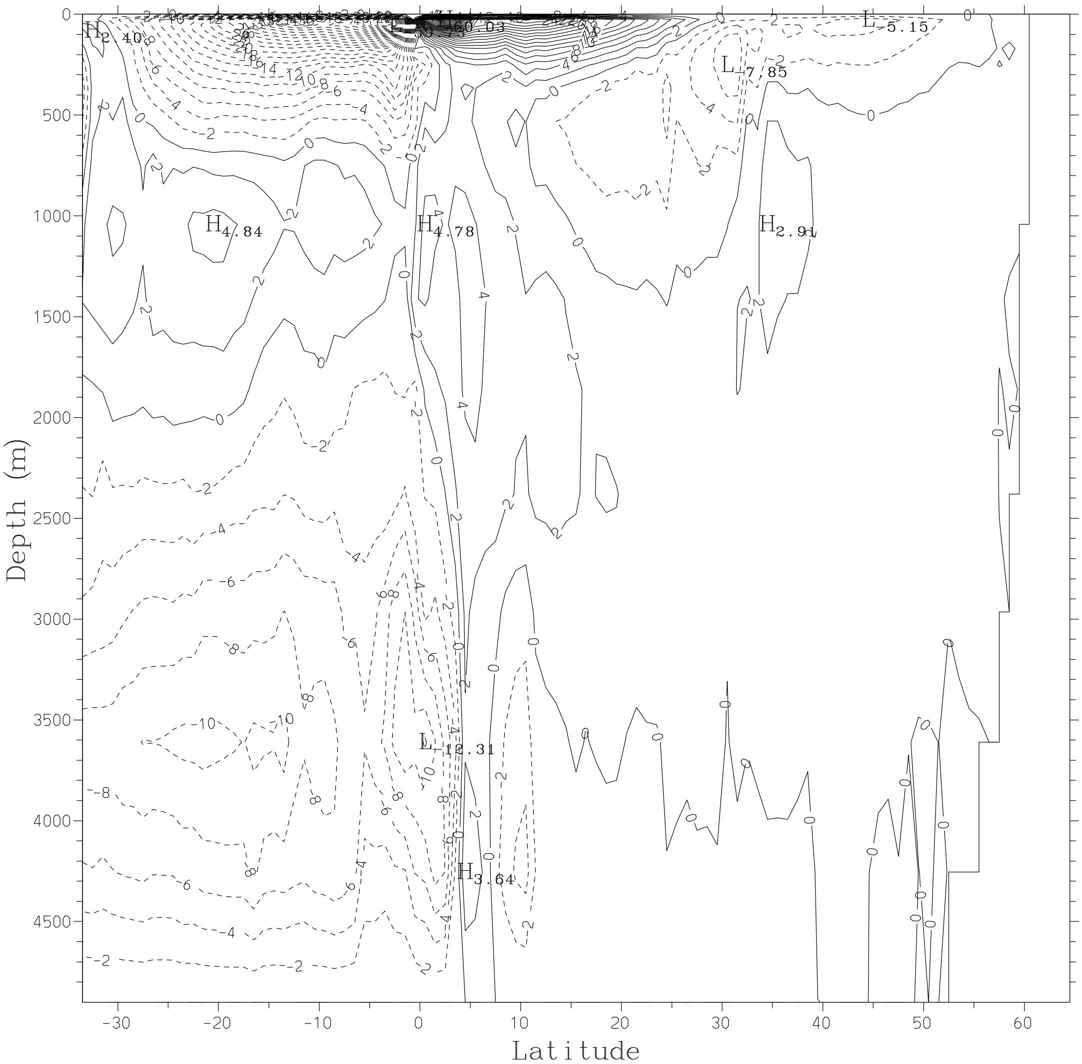

Figure 5.27: : Pacific–Indian meridional overturning stream function (Sv), averaged over years seven and eight of the seasonally forced phase. CI is $2\,Sv$.

better, or worse, than others. Both models show the North Pacific to be relatively stagnant, in the zonally averaged sense, with respect to deep overturning.

Fig. 5.28 shows the overturning stream function for the Atlantic, averaged over years seven and eight. The results are virtually identical to those of Semtner & Chervin (1992, their Fig 9a). Some $8.7\,Sv$ subducts in the North Atlantic, and the total overturning is a little over $18\,Sv$.

Fig. 5.29 shows the global meridional transports of heat and salt, averaged over years seven and eight. The total polewards heat flux between 50°S and the southern wall is simply too small to be realistic, and is the usual result for general circulation models. This small value is due, no doubt, to the comparatively small vertical diffusivity coefficients in the thermocline (Table 2.1), but the trade–off has been to help preserve the thermocline structure (F. Bryan, 1987; K. Bryan, 1991). Cummins *et al.* (1990) note that their dynamically adjusting coefficients can give quite different heat transports for the Southern Ocean, and could be calibrated to give reasonable results. The only qualitative difference between the present results and those of Semtner & Chervin (1992) is the 'eddy' (e.g., Cox, 1984) salt transport, which is somewhat larger than theirs.

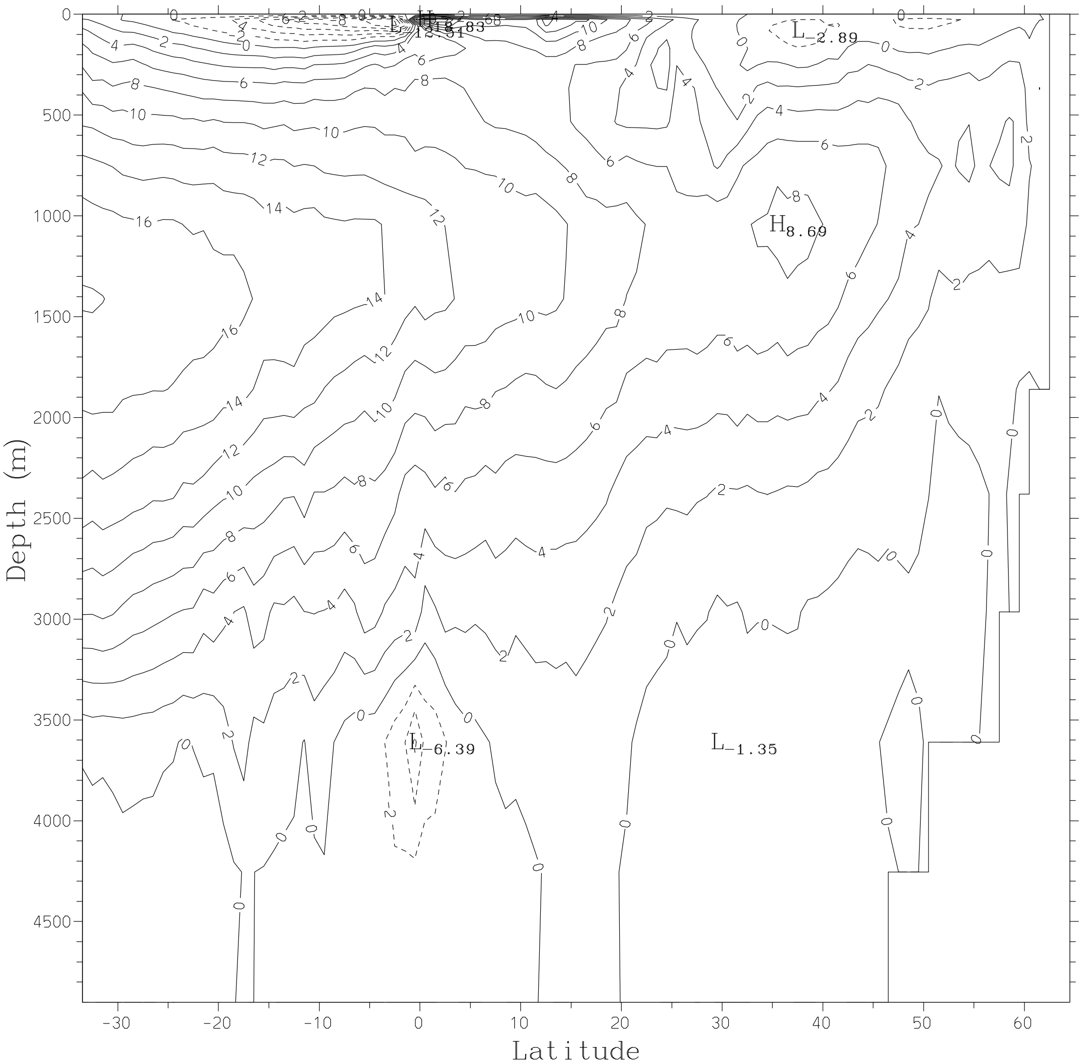

Figure 5.28: **:** Atlantic meridional overturning stream function (Sv), averaged over years seven and eight of the seasonally forced phase. CI is $2\,Sv$.

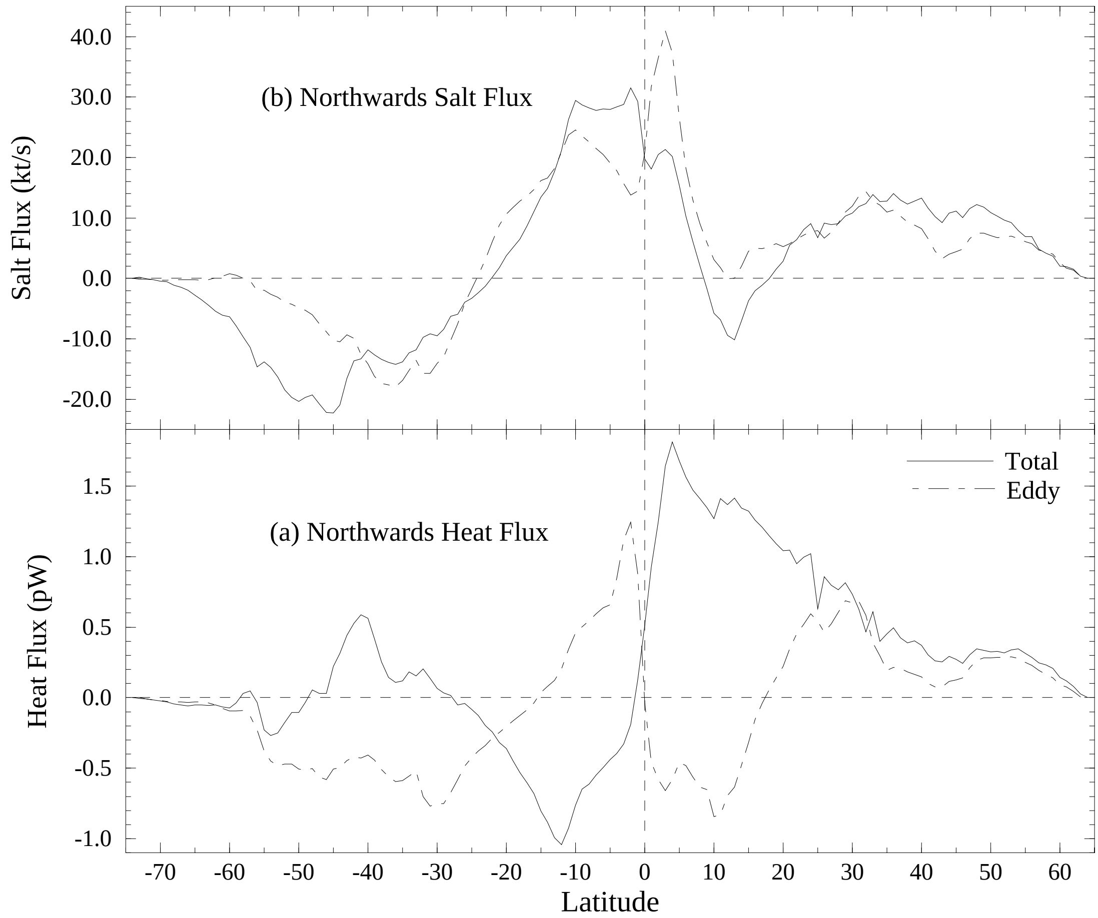

Figure 5.29: **:** Global meridional (a) heat ($peta\,Watts$) and (b) salt fluxes ($10^6\,kg\,\mathrm{s}^{-1}$), averaged over years seven and eight of the seasonally forced phase.

5.5 Overall Conclusions

The three main findings of this thesis are summarized below, beginning with the most important. Of course, all conclusions drawn from field observations must take precedence over the modelling work, wherever there are discrepancies. For example, the model predicts that strong westward fluxes should exist along the north coast of New Ireland, during the late austral winter, yet the few observations (Butt & Lindstrom, 1993) in the area show fluxes of only $\sim 3\,Sv$ westwards. In this case, the modelling work at least provides some clues as to how future surveys should be conducted in this area, notably for reference pressures. If the predicted seasonal reversals of deep equatorial flows, west of the Date Line, are correct, then CTD bottom casts will be necessary for fair flux estimates.

The study of the oceans usually involves only zeroth order experiments, that is, pure observations, and the real oceans cannot be 'poked' and 'prodded' in the same way as for model oceans. For example, it is unlikely that the IT sensitivity to the ACC could have ever been determined from pure observations.

The observational confirmation of the existence of the NGCU, along the southern coast of PNG, is the most significant facet of the results presented in this work. While previous reports (e.g., Thompson & Veronis, 1980) give indications of strong northward flows into the Solomon Sea, none of these discuss the NGCU in terms of being a true western boundary current, to the best of the author's knowledge. The NGCU is commonly found in large domain general circulation models, with varying predictions of its volume flux, and it is fair to say, for this feature, that the models are ahead of empirical knowledge.

In the model, the sensitivity of the IT to modifications of the ACC is an intriguing characteristic, and needs to be examined further, with other codes and dynamical formulations. Placing the southern wall at 64°S, and simply truncating the Southern Ocean climatology is just sufficient to demonstrate the sensitivity, while moving the wall further northwards causes larger reductions of both the IT and ACC fluxes.

Regions of recirculation along meridional western boundaries, using Smagorinsky mixing, is the most speculative model prediction presented here, although there is corroboration from limited field data. Recent improvements in the accuracy of satellite altimetry measurements will permit the confirmation, or refutation, of such flow patterns in the surface elevations of the EAC. If such flows exist only below the pycnocline, in the EAC area, then many more CTD bottom cast data, and deep mooring data, will be needed to observe this feature. The most promising observation presented here, in favour of Smagorinsky mixing, is that of the bottom water composition of the Coral and Solomon Sea Basins. Smagorinsky mixing predicts a northwards flow of deep Tasman Sea water (i.e., Southern Ocean water) into these basins, whereas the corresponding Laplacian and biharmonic mixing results are categorically wrong.

The bifurcation of the model SEC into two distinct flow paths, with the SECC being interposed, is an unexpected model result and sufficient historical TS data should exist to confirm or refute this prediction. Existing altimetry data will be too inaccurate, considering the low latitudes involved, while data to be obtained in the near future should be more than acceptable. Comparison of the model equatorial zonal isotachs with Fig. 10 of Kessler & Taft (1987) is encouraging for confirming the SECb prediction, but the NECb is not apparent. Should this model prediction come to fruition, a change in the naming scheme would be advantageous. Suggestions are: the *South Equatorial Current* for the branch closest to the equator, and the *South Tropical Current* for the poleward branch (cf. Donguy & Henin, 1975b; Rougerie & Donguy, 1975). The term "equatorial" is best reserved for regimes that lie within 2.4 internal radii from the equator, i.e., $\sim 600\,km$ (cf. Killworth, 1991).

Appendix A

Basic Sverdrup Integrals

A full analysis of Sverdrup models is beyond the scope of this section. Thus, only the basic relations (Godfrey, 1989) used for line integrals are covered. The ocean is assumed to be motionless below some (large) depth Z, and the depth–averaged flow between the surface and Z is assumed to obey the geostrophic relations, and to be non–divergent:

$$\begin{aligned} -fV &= -g\frac{\partial P}{\partial x} + \frac{1}{\rho_0}\tau^x - X && \text{(A.1)} \\ fU &= -g\frac{\partial P}{\partial y} + \frac{1}{\rho_0}\tau^y - Y && \text{(A.2)} \\ \frac{\partial U}{\partial x} + \frac{\partial V}{\partial y} &= a^{-1}\, V \tan\phi && \text{(A.3)} \end{aligned}$$

Here, x, y imply east and west directions, respectively; U, V are the depth–integrated x and y direction velocity components, respectively; f is the Coriolis parameter, and g is gravitational acceleration. ϕ is latitude and a is the earth's radius. P is the depth–integrated pressure between the surface and Z; X and Y are parameterizations of total frictional stresses in the x and y directions, respectively, and τ^x and τ^y are the wind stress components. It is assumed that the ocean is of uniform density ρ_0, and there is no gain or loss of mass through the bottom Z surface or side–walls, i.e., no normal flow at side–walls. All submarine ridges are assumed to lie below the depth Z. X and Y are usually set to zero, *except* in western boundary current regions, which are considered to be infinitesimally thin.

The variation of P along any eastern boundary path l (strictly, any non–

western boundary) is assumed to be given by

$$\frac{\partial P}{\partial l} = \frac{\tau^l}{g\rho_0} \qquad \text{giving} \qquad P_B - P_A = \frac{1}{g\rho_0}\int_A^B \tau^l \, dl \tag{A.4}$$

where τ^l is the alongshore wind stress, and A and B are any two points lying on the simply connected eastern boundary (Fig. A.1); the path of integration must not pass through a western boundary region. Within the ocean interior, the Sverdrup relation holds for V, viz:

$$\beta V = \frac{1}{\rho_0}\left(\frac{\partial \tau^y}{\partial x} - \frac{\partial \tau^x}{\partial y}\right) \tag{A.5}$$

where $\beta = \partial_y f$. Combining (A.1) and (A.5) gives a relation for zonal pressure differences; point C lies due west of B (i.e., same latitude) and is in the open ocean:

$$P_C - P_B = \frac{1}{g\rho_0}\int_B^C \left[\tau^x + \frac{f}{\beta}\left(\frac{\partial \tau^y}{\partial x} - \frac{\partial \tau^x}{\partial y}\right)\right] dx. \tag{A.6}$$

The first term of the integrand represents the simple zonal wind setup and the second term is the geostrophic pressure gradient of the northwards Sverdrup flow. Let point D lie at the corresponding western boundary and at (nearly) the same latitude as C and B.

$$P_D - P_B = \frac{fT_0}{g} + \int_D^B \frac{\tau^l}{g\rho_0} dl \tag{A.7}$$

where T_0 is the total mass flux across D–B and τ^l is the along–path (zonal) wind stress. Strictly, the integration path must be normal to the coast when it crosses any western boundary current, but these regions are assumed to be 'thin' and so f does not change. Also, here, the wind stress is not significant.

If the ocean is semi–enclosed, e.g., the North Pacific, then T_0 is zero. If D lies on the western boundary of an island, then T_0 is the total northwards flux (open ocean and western boundary current). In this case, the value of T_0 is constant over the area included by the island's zonal projection to the eastern boundary. The first step in finding the global P field is to calculate T_0 for every island. Let points N and S lie at the northern and southern tips of an island, respectively, and let E and F lie at the same respective latitudes on the closest eastern boundary. The difference between P_N and P_S can be found from (A.4) and (A.7), and also independently from (A.4) along the island's own east coast. Thus, T_0 can be immediately calculated:

$$T_0 = \frac{1}{\rho_0(f_N - f_S)} \oint_{NEFSN} \tau^l \, dl. \tag{A.8}$$

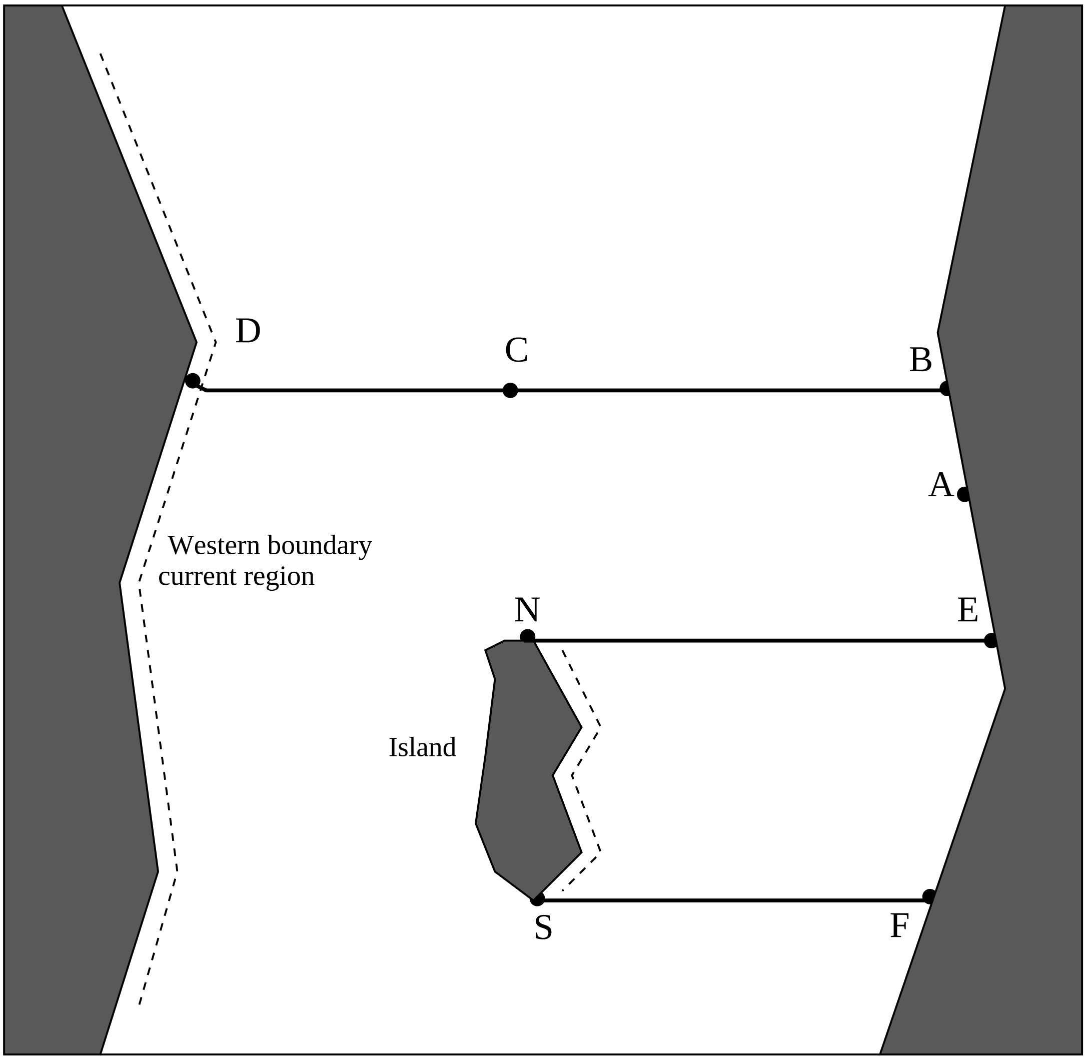

Figure A.1: **:** Line integral paths for Sverdrup relations. Points A, B, E and F lie on the eastern boundary, and C lies in the open ocean. D is at the western boundary coast, inshore from the boundary current region. N and S lie at the northern and southern tips of the island, respectively, as close as possible to the island's own western boundary.

The path segment S–N lies along the island's east coast.

The global P field may now be calculated using (A.4), (A.6), (A.7) and the set of T_0 values. Once an arbitrary reference point is chosen on an eastern boundary, say the tip of South America, P along the eastern boundary can be found from (A.4). P for the open Pacific, i.e., up to, but excluding western boundary regions, is then found from (A.6). Pressure variations across western boundary currents are then found from (A.7), using the previously computed T_0 values, if the western boundary current is associated with an island. Thus, the along–shore pressure variations within western boundary regions are found. Once the pressure variation along an island's east coast is known (directly from (A.4)), the same procedure is used for the area to the east of the island. There is a more complicated case where the eastwards zonal projections of two islands overlap, such as Australia and New Zealand, and the solution method is given by Godfrey (1989).

The barotropic stream function is found for the open ocean in a similar way, although it is actually a little easier to find. The stream function along the coastline of Americas–Europe–Africa–Asia is arbitrarily set to zero, and the coastlines of all islands are given their appropriate T_0 values. Eqn. (A.5) is then integrated westwards away from each eastern boundary point, up to the first ocean point at the corresponding western boundary. Since the coastline value was set previously, either to 0 or to T_0, the boundary current mass flux is automatically implied.

For simple versions of Sverdrup models, it is assumed that the open ocean flows are determined entirely by the wind stress, and that nonlinearities occur only within western boundary currents. This may not be an accurate assumption at high latitudes, especially for the ACC, where bathymetric steering may be quite substantial. It is also assumed that there is no mass exchange though the reference surface at depth Z, and this is not necessarily a good approximation for the real oceans, the North Atlantic and high–latitude Southern Ocean being two possible examples.

Appendix B

Overturning and Poleward Transports

Variables not defined below may be found in the first few sections of Chapter 2. For compactness, e and w subscripts/limits shall imply eastern and western boundaries, respectively. For cyclic continuity boundaries, e and w are the same ocean point and corresponding zonal integral paths are assumed to circuit the globe. All integrands are assumed to be zero when inland.

In a similar fashion to the definition of the barotropic stream function (with rigid–lid condition), meridional and zonal overturning stream functions can be defined in the ϕ–z and λ–z planes. The continuity equation in spherical coordinates is

$$\frac{\partial u}{\partial \lambda} + \frac{\partial}{\partial \phi}(v \cos\phi) + a \cos\phi \frac{\partial w}{\partial z} = 0 \tag{B.1}$$

where a is the earth's radius. Zonally integrating (B.1), from either land or cyclic boundaries, gives

$$\int_w^e \frac{\partial}{\partial \phi}(v \cos\phi)\, d\lambda + a \cos\phi \int_w^e \frac{\partial w}{\partial z}\, d\lambda = 0. \tag{B.2}$$

The $\partial_\lambda u$ term in (B.1) vanishes since u_w and u_e are zero inland, or equal for cyclic boundaries. Moving the partial derivatives outside of the integrals in (B.2) gives an equation of the form

$$\frac{\partial A}{\partial \phi} + \frac{\partial B}{\partial z} = 0. \tag{B.3}$$

A function Φ may defined such that $\partial_z \Phi = -A$ and $\partial_\phi \Phi = B$, and (B.3) is immediately satisfied. The meridional overturing stream function Φ is found by performing either of the following integrals:

$$\Phi(\phi, z) = -\int_{-H}^{z} \int_{w}^{e} va\cos\phi \, d\lambda \, dz' \tag{B.4}$$

$$\Phi(\phi, z) = \int_{south}^{\phi} \int_{w}^{e} wa^2 \cos\phi' \, d\lambda \, d\phi'. \tag{B.5}$$

Eqn. (B.4) is preferred since w is not carried explicitly in the model, nor dumped in the snapshots, and finding it requires extra calculations. The zonal overturning stream function (generally of less interest) is found in a similar fashion to the above.

The *total* northwards meridional transports of heat and salt, respectively, are defined as

$$F_H(\phi) = \rho_0 C_p \int_{-H}^{0} \int_{w}^{e} \left(vT - \frac{k_h}{a} \frac{\partial T}{\partial \phi} \right) a\cos\phi \; d\lambda \, dz \tag{B.6}$$

$$F_S(\phi) = \rho_0 10^{-3} \int_{-H}^{0} \int_{w}^{e} \left(vS - \frac{k_h}{a} \frac{\partial S}{\partial \phi} \right) a\cos\phi \; d\lambda \, dz \tag{B.7}$$

where T is temperature (°C), S is salinity (psu) relative to the Standard Ocean, k_h is the vertical tracer diffusivity, ρ_0 is a nominal density, and C_p is the specific heat of sea water at a constant pressure, and is taken to be constant at $4.186\, kJ\, l^{-1}$ (Pacanowski *et al.*, 1991). Model salinity S is measured relative to the Standard Ocean (i.e., difference from $35\, psu$), and salt transport values are usually left in these units.

Correspondingly, *eddy* transports are defined as (e.g., Cox, 1984)

$$E_H(\phi) = \rho_0 C_p \int_{-H}^{0} \left(\overline{vT} - \frac{\overline{v}\,\overline{T}}{L} \right) dz \tag{B.8}$$

$$E_S(\phi) = \rho_0 10^{-3} \int_{-H}^{0} \left(\overline{vS} - \frac{\overline{v}\,\overline{S}}{L} \right) dz \tag{B.9}$$

where $$\overline{X} = \int_{w}^{e} X\, a\cos\phi \, d\lambda.$$

L is the length of the zonal integration path, at depth z, excluding portions inland. Other types of meridional transport quantities are routinely calculated in the running model, such as Ekman, mean, advective and diffusive transports.

References

1. Anderson D.L.T. and A.E. Gill (1975), Spin–up of a stratified ocean, with applications to upwelling. *Deep–Sea Research*, **22**, 583–596.

2. Andrews J.C and P. Scully-Power (1976), The structure of an East Australian Current anticyclonic eddy. *Journal of Physical Oceanography*, **6**, 756–765.

3. Andrews J.C. and S. Clegg (1989), Coral Sea circulation and transport deduced from modal information models. *Deep–Sea Research*, **36**, 957–974.

4. Arakawa A. (1966), Computational design for long-term numerical integration of the equations of fluid motion: two-dimensional incompressible flow. *Journal of Computational Physics* , **1** (1), 119–143.

5. Arakawa A. and V.R. Lamb (1977), Computational design of the basic dynamical processes of the UCLA general circulation model. *Methods in Computational Physics*, **17**, 174–256.

6. Bennett A.F. and P.E. Kloeden (1981), The ill-posedness of open ocean models. *Journal of Physical Oceanography*, **11**, 1027–1029.

7. Bennett A.F. (1983), The South Pacific including the East Australian Current. In: *Eddies in Marine Science*, A.R. Robinson, editor, Springer Verlag, ISBN 0-387-12253-2, 219–244.

8. Bindoff N.L. and C. Wunsch (1992), Comparison of synoptic and climatologically mapped sections of the South Pacific Ocean. *Journal of Climate*, **5**, 631–645.

9. Boland F.M. and B.V. Hamon (1970), The East Australian Current, 1965–1968. *Deep–Sea Research*, **17**, 777–794.

10. Boning C.W., R. Dorscher and R.G. Budich (1991), Seasonal transport variation in the western subtropical North Atlantic: experiments with an eddy resolving model. *Journal of Physical Oceanography*, **21**, 1271–1289.

11. Bryan K. and M. Cox (1968), A nonlinear model of an ocean driven by wind and differential heating: part I. description of the three-dimensional velocity and density fields. *Journal of the Atmospheric Sciences*, **25** (6), 945–967.

12. Bryan K. and M. Cox (1968), A nonlinear model of an ocean driven by wind and differential heating: part II. an analysis of the heat, vorticity and energy balance. *Journal of the Atmospheric Sciences*, **25** (6), 968–978.

13. Bryan K. (1969), A numerical method for the study of the circulation of the world ocean. *Journal of Computational Physics*, **4**, 347–376.

14. Bryan K. (1984), Accelerating the convergence to equilibrium of ocean-climate models. *Journal of Physical Oceanography*, **14**, 666–673.

15. Bryan K. (1991), Poleward heat transport in the ocean. *Tellus*, **43AB**, 104–115.

16. Bryan F.O. and W.R. Holland (1989), A high resolution simulation of the wind and thermohaline driven circulation in the North Atlantic Ocean. In *Parameterization of the small-scale processes, Proceedings of the 'Aka Huliko'a Hawaiian winter workshop*, eds. P. Muller & D. Henderson, 99–115. University of Hawaii, 1989.

17. Bryan F.O. (1987), Parameter sensitivity of primitive equation ocean general circulation models. *Journal of Physical Oceanography*, **17**, 970–985.

18. Bryan F.O. (1986), High-latitude salinity effects and interhemispheric thermohaline circulations. *Nature*, **323**, 301–305.

19. Butt J. and E. Lindstrom (1993), Currents off the east coast of New Ireland, Papua New Guinea and their relevance to regional undercurrents in the western equatorial Pacific Ocean. *Journal of Geophysical Research*, in the press.

20. Camerlengo A.L. and J.J. O'Brien (1980), Open boundary conditions in rotating fluids. *Journal of Computational Physics*, **35**, 12–35.

21. Charney J.G., R. Fjortoft and J. von Neumann (1950), Numerical integration of the barotropic vorticity equation. *Tellus*, **2**, 237–254.

22. Church J.A. (1987), The East Australian Current adjacent to the Great Barrier Reef. *Australian Journal of Marine and Freshwater Research*, **38**, 671–683.

23. Church J.A. and F.M. Boland (1983), A permanent undercurrent adjacent to the Great Barrier Reef. *Journal of Physical Oceanography*, **13** (9), 1747–1749.

24. Courant R., K. Friedrichs and H. Lewy (1928), Über die partiellen Differenzengleichungen der Mathematischen Physik. *Mathematische Annalen*, 32–74.

25. Cox M. (1984), *A primitive equation, 3-dimensional model of the ocean.* Technical Report No. 1, Geophysical Fluid Dynamics Laboratories/NOAA, Princeton University.

26. Cox M. (1987), Isopycnal mixing schemes. *Ocean Modelling*, **74**, 1–5, June 1987.

27. Creswell G.R. and R. Legeckis (1986), Eddies off southeastern Australia, *Deep–Sea Research*, **33**, 1527–1562.

28. Cummins P.F., G. Holloway and A.E. Gargett (1990), Sensitivity of the GFDL ocean general circulation model to a parameterization of vertical diffusion. *Journal of Physical Oceanography*, **20**, 817–830.

29. Deardorff J.W. (1973), The use of subgrid transport equations in a three–dimensional model of atmospheric turbulence. *Journal of Fluids Engineering*, **95**, 429–438.

30. Donguy J.R., C. Oudot and F. Rougerie (1970), Circulation superficielle et subsuperficielle en Mer du Corail et à 170°E. *Cah. O.R.S.T.O.M., Sér Océanogr.*, **8**, 3–20.

31. Donguy J.R. and C. Henin (1975a), Surface waters in the north of the Coral Sea. *Australian Journal of Marine and Freshwater Research*, **26**, 293–296.

32. Donguy J.R. and C. Henin (1975b), Evidence of the South Tropical Countercurrent in the Coral Sea. *Australian Journal of Marine and Freshwater Research*, **26**, 405–409.

33. Dukowicz J.K. and R.D. Smith (1992), Implicit free–surface method for the Bryan–Cox–Semtner ocean model. *Journal of Geophysical Research*, under consideration, 1992.

34. Edwards R.J. (1979), *Tasman and Coral Sea Ten Year Mean Temperature and Salinity Fields, 1967–1976.* Report No. 88, CSIRO, Division of Fisheries and Oceanography.

35. England M.H. (1992), On the formation of Antarctic Intermediate Water and bottom water in ocean general circulation models. *Journal of Physical Oceanography*, **22**, 918–926.

36. ETOPO5, Earth topographic data set (1978), NOAA/National Geophysical Data Center, Marine Geology and Geophysics Division (E/GC3).

37. Fieux M., C. Andrie, P. Delecluse, A.G. Ilahude, A. Kartavtseff, F. Mantisi, R. Molcard and J.C. Swallow (1993), Measurements within the Pacific-Indian ocean throughflow region. *Deep–Sea Research*, in the press.

38. Fr0791, expedition of *R.V. Franklin* in September 1991. Chief Scientist: Dr. D.M. Burrage, Australian Institute of Marine Science, PMB 3 Townsville MC QLD 4810 Australia. Cruise reports, and data available from: CSIRO Division of Oceanography, GPO Box 1538 Hobart TAS 7001 Australia.

39. Gill A.E. (1982), *Atmosphere–Ocean Dynamics.* Academic Press, ISBN 0-12-283522-0.

40. Godfrey J.S. (1973), Comparison of the East Australian Current with the western boundary flow in Bryan and Cox's (1968) numerical ocean model. *Deep–Sea Research*, **20**, 1059–1076.

41. Godfrey J.S. and T.J. Golding (1981), The Sverdrup relation in the Indian Ocean and the effect of the Pacific–Indian oceans throughflow on Indian Ocean circulation and on the East Australian Current. *Journal of Physical Oceanography*, **11**, 771–779.

42. Godfrey J.S. (1989), A Sverdrup model of the depth-integrated flow for the world ocean allowing for island circulations. *Geophysical and Astrophysical Fluid Dynamics*, **45**, 89–112.

43. Godfrey J.S., K. Ridgway, G. Meyers and R. Bailey (1989), *Sea Level and Thermal Response to the 1986–1987 ENSO Event in the Far Western Pacific.* Proc. TOGA-CORE Workshop, Nouméa, May 1989.
(In preparation for *Journal of Physical Oceanography.*)

44. Godfrey J.S. and A.J. Weaver (1991), Is the Leeuwin Current driven by Pacific winds and heating? *Progress in Oceanography*, **27**, 225–272.

45. Godfrey J.S., A.C. Hirst and J. Wilkin (1993), Why does the Indonesian throughflow appear to originate from the North Pacific? *Journal of Physical Oceanography*, **23**, 1087–1098.

46. Gordon A. (1986), Interocean exchange of thermocline water. *Journal of Geophysical Research*, **91** , 5037–5046.

47. Hamon B.V. (1961), *The structure of the east Australian current.* Technical Paper No. 11, CSIRO, Division of Fisheries and Oceanography.

48. Hamon B.V. (1965), The East Australian Current, 1960–1964. *Deep–Sea Research*, **12**, 899–921.

49. Hamon B.V. (1968), Spectrum of sea level at Lord Howe Island in relation to circulation. *Journal of Geophysical Research*, **73**, 6925–6927.

50. Haney R.L. (1971), Surface thermal boundary conditions for ocean circulation models. *Journal of Physical Oceanography*, **1**, 241–248.

51. Haney R.L. and J.M. Wright (1975), The relationship between the grid size and the coefficient of nonlinear lateral eddy viscosity in numerical ocean circulation models. *Journal of Computational Physics*, **19**, 257–266.

52. Heath R.A. (1985), Large-scale influence of the New Zealand seafloor topography on western boundary currents of the south Pacific. *Australian Journal of Marine and Freshwater Research*, **36**, 15–22.

53. Hellerman S. and M. Rosenstein (1983), Normal monthly wind stress over the world ocean with error estimates. *Journal of Physical Oceanography*, **13**, 1093–1104.

54. Highley E. (1967), *Oceanic circulation patterns off the east coast of Australia.* Technical Paper No. 23, CSIRO, Division of Fisheries and Oceanography.

55. Hirst A.C. and J.S. Godfrey (1993), The role of the Indonesian throughflow in a global ocean GCM. *Journal of Physical Oceanography*, **23**, 1057–1086.

56. Hughes R.D., D.M. Burrage and L. Bode (1994) The east Australian currents. Under consideration by *Journal of Physical Oceanography*

57. Hughes R.D., D.M. Burrage and L. Bode (1993), A western boundary current along the coast of Papua New Guinea. Under consideration by *Deep–Sea Research.*

58. Inoue M. and S.E. Welsh (1993), Modelling seasonal variability in the wind–driven upper layer circulation in the Indo-Pacific region. *Journal of Physical Oceanography*, **23**, 1411–1436.

59. Kamenkovitch V.M. (1962), *Trudy Instituta Okeanologii,* Akad. Nauk SSSR, **56**, 241 pp.

60. Kessler W.S. and B.A. Taft (1987), Dynamic heights and zonal geostrophic transports in the central tropical Pacific. *Journal of Physical Oceanography*, **17**, 97–122.

61. Killworth P.D. (1987), Topographic instabilities in level model OGCMs. *Ocean Modelling*, **75** (9), November 1987.

62. Killworth P.D. (1991), Cross–equatorial geostrophic adjustment. *Journal of Physical Oceanography*, **21**, 1581–1601.

63. Killworth P.D., D. Stainforth, D.J. Webb and S.M. Paterson (1991), The development of a free–surface Bryan-Cox-Semtner ocean model. *Journal of Physical Oceanography*, **21**, 1333–1348.

64. Killworth P.D. (1992), An equivalent barotropic mode in the Fine Resolution Antarctic Model. *Journal of Physical Oceanography*, **22**, 1379–1387.

65. Killworth P.D. (1993), On the role of dissipation in inertial western boundary currents. *Journal of Physical Oceanography*, **23**, 539–553.

66. Legeckis R., W. Pichel and G. Nesterczuk (1983), Equatorial long waves in geostationary satellite observations and in a multi–channel sea surface temperature analysis. *Bulletin of the American Meteorological Society*, **64**, 133–139.

67. Levitus S. (1982), *Climatological atlas of the world ocean.* NOAA Prof. Paper 13. Geophysical Fluid Dynamics Laboratory/NOAA Princeton University.

68. Lighthill M.J. (1969), Dynamic response of the Indian Ocean to onset of the Southwest Monsoon. *Philosophical Transactions of the Royal Society of London*, **A265**, 45–92.

69. Lilley F.E.M., J.H. Filloux, N.L. Bindoff, I.J. Ferguson and P.J. Mulhearn (1986), Barotropic flow of a warm–core ring from seafloor electric measurements. *Journal of Geophysical Research*, **91** (C11), 12979–12984.

70. Lindstrom E., R. Lukas, R. Fine, E. Firing, S. Godfrey, G. Meyers and M. Tsuchiya (1987), The western equatorial Pacific ocean circulation study. *Nature*, **330**, 533–537.

71. Lindstrom E., J. Butt, R. Lukas and J.S. Godfrey (1990), The flow through Vitiaz Strait and St. George's Channel, Papua New Guinea. In: *The Physical Oceanography of Sea Straits*, L.J. Pratt, editor, Kluwer Acad. Pub., 171–189.

72. Luyten J.R., Pedlosky J. and H. Stommel (1982), The ventilated thermocline. *Journal of Physical Oceanography*, **13**, 292–309.

73. Mangum L., J. Lynch, K. McTaggart, L. Stratton and S. Hayes (1991), *CTD/O_2 Data Measurements Collected on TEW (Transport of Equatorial Waters).* NOAA Data Report ERL PMEL-33.

74. Margolin L. (1978), A method for treating hourglass patterns. In: *Numerical Methods in Laminar and Turbulent Flow*, Vol. 5 Pt. 1, C. Taylor, W.C. Habashi and M.M. Hafex, editors, Pineridge Press, Swansea UK.

75. Meyers G. (1980), Do Sverdrup transports account for the Pacific North Equatorial Countercurrent? *Journal of Geophysical Research*, **85**, 1073–1075.

76. Meyers G., R. Bailey and T. Worby (1991), *Seasonal Variations of Major Currents in the Tropical Indian Ocean Observed by Expendable Bathythermograph.* (IAPSO Abstract, IUGG XX General Assembly, Vienna, August 1991).

77. Mulhearn P.J., J.H. Filloux, F.E.M. Lilley, N.L. Bindoff and I.J. Ferguson (1986), Abyssal current during the formation of a warm–core ring in the East Australian Current. *Deep–Sea Research*, **33**, 1563–1576.

78. Oberhuber J.M. (1988), *An atlas based on the COADS data Set: The budgets of heat, bouancy, and turbulent kinetic energy at the surface of the global ocean.* Report 15, Max Planck Institute fur Meteorolgy, Hamburg.

79. Pacanowski R.C., K.W. Dixon and A. Rosati (1991), *GFDL Modular Ocean Model Users Guide V 1.0*. Ocean Group Technical Report No. 2, Geophysical Fluid Dynamics Laboratories/NOAA, Princeton University.

80. Pacanowski R.C. and S.G. Philander (1981), Parameterization of vertical mixing in numerical models of tropical seas. *Journal of Physical Oceanography*, **11**, 1443–1451.

81. Pedlosky J. (1986), *Geophysical Fluid Dynamics.* Springer Verlag, ISBN 0-387-96388-X.

82. Pedlosky J. (1991), The link between western boundary currents and equatorial undercurrents. *Journal of Physical Oceanography*, **21**, 1553–1558.

83. Philander S.G. (1990), *El Niño, la Niña, and the Southern Oscillation.* Academic Press, ISBN 0-12-553235-0.

84. Pickard G.L., J.R. Donguy, C. Henin and F. Rougerie (1977), *A Review of the Physical Oceanography of the Great Barrier Reef and Western Coral Sea.* Australian Institute of Marine Science Monograph Series, Vol 2.

85. Reid J.L. (1986), On the total geostrophic circulation of the South Pacific Ocean: flow patterns, tracers, and transports. *Progress in Oceanography*, **27**, 111–124.

86. Reznik G.M., L.I. Piterbarg and E.A. Kartashova (1993), Nonlinear interactions of spherical Rossby modes. *Dynamics of Atmospheres and Oceans*, **18**, 235–252.

87. Robinson A.R. and L.J. Walstad (1987), The Harvard open ocean model: calibration and application to dynamical processes, forecasting, and data assimilation studies. *Applied Numercal Mathematics*, **3** (1–2), 89–131.

88. Rochford D.J. (1959), *The primary external water masses of the Tasman and Coral Seas*. Report No. 16, CSIRO Division of Fisheries and Oceanography.

89. Rochford D.J. (1960a), The intermediate depth waters of the Tasman and Coral Seas. I. The 27.20 σ_t surface. *Australian Journal of Marine and Freshwater Research*, **11**, 127–147.

90. Rochford D.J. (1960b), The intermediate depth waters of the Tasman and Coral Seas. II. The 26.80 σ_t surface. *Australian Journal of Marine and Freshwater Research*, **11**, 148–165.

91. Rosati A. and M. Miyakoda (1988), A general circulation model for upper ocean simulation. *Journal of Physical Oceanography*, **18**, 1601–1626.

92. Rougerie F. & J.R. Donguy (1975), La Mer du Corail en régime d'alizé de sud–est. *Cah. O.R.S.T.O.M., Sér Océanogr.*, **13** , 49–67.

93. Scully-Power P.D. (1973), Coral Sea flow budgets in winter. *Australian Journal of Marine and Freshwater Research*, **24**, 203–215.

94. Semtner A.J. and R.M. Chervin (1988), A simulation of the global ocean circulation with resolved eddies. *Journal of Geophysical Research*, **93**, 15502–15522.

95. Semtner A.J. and R.M. Chervin (1992), Ocean general circulation from a global eddy-resolving model. *Journal of Geophysical Research*, **97**, 5493–5550.

96. Smagorinsky J. (1963), General circulation experiments with the primitive equations: I. The basic experiment. *Monthly Weather Review*, **91**, 99–164.

97. Smagorinsky J. (1993), Historical remarks on nonlinear viscosity. In *Large Eddy Simulations of Comples Engineering and Geophysical Flows*, eds. B. Galperin and S.A. Orszag, 3–35. Cambridge University Press.

98. Smith R.D., J.K. Dukowicz and R.C. Malone (1992), Parallel ocean general circulation modeling. *Physica D*, **60**, 38–61.

99. Spall M.A. and W.R. Holland (1991), A nested primitive equation model for oceanic applications. *Journal of Physical Oceanography*, **21**, 205–220.

100. Stevens D.P. (1990), On open boundary conditions for three dimensional primitive equation ocean circulation models. *Geophysical and Astrophysical Fluid Dynamics*, **51**, 103–133.

101. Stommel H., E.D. Stroupe, J.L. Reid and B.A. Warren (1973), Transpacific hydrographic sections at latitudes 43°S and 28°S: the SCORPIO expedition. *Deep–Sea Research*, **20**, 1–8.

102. Stuiver M. and P.D. Quay (1983), Abyssal Water Carbon–14 Distribution and the age of the world oceans. *Science*, **219**, 849–851.

103. de Szoeke R.A. (1987), On the wind–driven circulation of the South Pacific. *Journal of Physical Oceanography*, **17**, 613–630.

104. Taft B.A., S.P. Hayes, G.E. Friederich and L.A. Codispoti (1991), Flow of abyssal water into the Samoa passage. *Deep–Sea Research*, **38** suppl. 1, S103–S128.

105. Takahashi T. (1960), Existence of a *contra solem* vortical motion in the Coral Sea. *Records of Oceanographic Works in Japan*, **5** (2), 52–54.

106. Takano K. (1974), *A general circulation model for the world ocean.* Technical Report No. 8, Department of Meteorology, University of California Los Angeles.

107. Thompson R.O.R.Y. and G. Veronis (1980), Transport calculations in the Tasman and Coral Seas. *Deep–Sea Research*, **27A**, 303–323.

108. Tsuchiya M. (1968), *Johns Hopkins Institute Oceanography Study No. 4.*

109. Tsuchiya M. (1981), The origin of the Pacific equatorial 13°C water. *Journal of Physical Oceanography*, **11**, 794–812.

110. Tsuchiya M., R. Lukas, R. Fine, E. Firing and E. Lindstrom (1989), Source waters of the Pacific equatorial undercurrent. *Progress in Oceanography*, **23**, 101–147.

111. UNESCO (1981) *Tenth Report of the Joint Panel on Oceanographic Tables and Standards.* UNESCO Technical Papers in Marine Science, No. 36, UNESCO, Paris.

112. Warren B.A. (1970), General circulation of the South Pacific. In: *Scientific Exploration of the South Pacific*, W.S. Wooster, editor, N.A. Science, Washington, p. 33.

113. Weaver A.J. and E.S. Sarachik (1990), On the importance of vertical resolution in certain ocean general circulation models. *Journal of Physical Oceanography*, **20**, 600–609.

114. Webb D.J. and the FRAM group (1991), An eddy resolving model of the southern ocean. *EOS, Transactions of the American Geophysical Union*, **72**, 169–175.

115. Wolanski E., P. Ridd and M. Inoue (1988), Currents through Torres Strait. *Journal of Physical Oceanography*, **18**, 1535–1545.

116. Wunsch C. (1978), The North Atlantic general circulation west of 50°W determined by inverse methods. *Reviews of Geophysics and Space Physics*, **16**, 583–620.

117. Wyrtki K. (1960), *Surface circulation in the Coral and Tasman Seas*. CSIRO Division of Fisheries and Oceanography, Technical Paper 8.

118. Wyrtki K. (1961a), *Physical oceanography of southeast Asian waters.* NAGA Report Vol. 2, Scripps Institute of Oceanography.

119. Wyrtki K. (1961b), The flow of water into the deep–sea basins of the western South Pacific. *Australian Journal of Marine and Freshwater Research*, **12**, 1–16.

120. Wyrtki K. (1962a), The subsurface water masses in the western South Pacific. *Australian Journal of Marine and Freshwater Research*, **13**, 18–47.

121. Wyrtki K. (1962b), Geopotential topographies and associated circulation in the western South Pacific Ocean. *Australian Journal of Marine and Freshwater Research*, **13**, 89–105.

122. Wyrtki K. (1975), Fluctuations of the dynamic topography in the Pacific Ocean. *Journal of Physical Oceanography*, **5**, 450–459.

123. Yamanaka H. (1973), Surface currents in the western Pacific ocean as seen from the drift of tuna longline gear. *Bulletin of the Far Seas Fisheries Research Laboratories* (Japan), **9**, 19–43.